Biological multi-functionalization and surface nanopatterning of biomaterials

Zhe Annie Cheng

THÈSE

PRÉSENTÉE A

L'UNIVERSITÉ BORDEAUX 1

ÉCOLE DOCTORALE DES SCIENCES CHIMIQUES

Par Zhe (Annie) CHENG

POUR OBTENIR LE GRADE DE

DOCTEUR

SPÉCIALITÉ : POLYMÈRES

Biological Multi-Functionalization and Surface Nanopatterning of Biomaterials

Directeurs de thèse : Mme. Marie-Christine DURRIEU & M. Alain M. JONAS

Soutenue le : 10 décembre, 2013

Devant la commission d'examen formée de :

Mme. MIGONNEY, Véronique	Professeur de l'Université Paris 13, France	Rapporteur
Mme. PICART, Catherine	Professeur de l'Université Grenoble INP, France	Rapporteur
M. GAIGNEAUX, Eric	Professeur de l'Université catholique de Louvain, Belgique	Examinateur
M. AYELA, Cédric	Chargé de Recherche CNRS, Bordeaux, France	Examinateur
Mme. FOULC, Marie-Pierre	Ingénieur de Recherche, Rescoll, Bordeaux, France	Examinateur
Mme. GLINEL, Karine	Professeur de l'Université catholique de Louvain, Belgique	Examinateur
M. JONAS, Alain	Professeur de l'Université catholique de Louvain, Belgique	Directeur
Mme. DURRIEU, Marie-Christine	Chargée de Recherche INSERM, Bordeaux, France	Directeur

This thesis work was carried out in the International Doctoral School in Functional Materials (IDS-FunMat) framework, and is the results of a collaboration between:

Université de Bordeaux 1
CNRS, Chimie et Biologie des Membranes et des Nanoobjets UMR5248
Institut Européen de Chimie et Biologie
2 Rue Robert Escarpit
33607 Pessac Cedex, France

Under the supervision of

Dr. Marie-Christine DURRIEU

and

Université catholique de Louvain
Institut de la Matière Condensée et des Nanosciences
Bio- and Soft Matter
1 Croix du Sud
B-1348 Louvain-la-Neuve, Belgium

Under the supervision of

Dr. Alain M. JONAS

and

Rescoll, Bordeaux (industry partner)

Acknowledgements

As I contemplate, at the end of my PhD studies, the ups and downs, the joys and struggles, the accomplishments and obstacles I've experienced these three fun and enduring years in Europe, I realized that this chapter of my life is not merely a journey of academic and professional endeavor, but also one of growth, transformation, and revelation. That is why I feel that it is necessary to thank not only those people who have made an impact in my career development, but also every individual who played a part in molding me (NIL reference, sorry, can't help it) into the way I am today. Therefore, please understand the reason for my very lengthy acknowledgement, every part of which I write with my most genuine gratitude.

The path of my PhD was made possible by the International Doctoral School in Functional Materials (IDS-FunMat) program and the two collaborating universities in my project, Université de Bordeaux 1 (UB1) in Bordeaux, France and Université catholique de Louvain (UCL) in Louvain-la-Neuve, Belgium. First and foremost I would like to convey my deepest thanks to my thesis supervisors, Dr. Marie-Christine Durrieu at UB1, and Dr. Alain Jonas and Dr. Karine Glinel at UCL. Marie has been kind and patient throughout my work, especially during the toughest periods of thesis-writing. She is supportive and always ready and willing to help in any situation, and her encouragements have given me a lot of confidence, even when I didn't think that I would be able to achieve my standards and expectations. To her I express my utmost respect and gratitude. In Belgium, I owe my thanks to Alain and Karine for making my integration in the lab very smooth and pleasant. I've learned a lot from Alain's efficiency and leadership as well as Karine's rigor and meticulousness. From the search for accommodation to the search for alternative methods of experimentation, their professional guidance has been an indispensable part in the course of my work.

In addition to my thesis supervisors, I would like to thank sincerely my senior, colleague, and friend, Dr. Omar Zouani. From the very beginning of my thesis, Omar has been helping me and guiding me in all aspects of cell culture and biological analysis. His insights and bright ideas are very valuable and I appreciate his enthusiasm and willingness to help. Without his advice, the completion of the thesis would have been much more difficult.

As my thesis was completed in a co-tutelle collaboration, I had the pleasure and honor of being part of three different laboratories. In France, I started my work at INSERM. I thank the director Dr. Joelle Amédée for the opportunity to work at INSERM, and I would also like to thank Christel Chanseau and Jérôme Kalisky for teaching me the methods of surface functionalization, as well as Lila Rami for helping with confocal microscopy and cell culture. In years 2 and 3, I joined the Institut Européen de la Chimie et Biologie (IECB) as part of Dr. Reiko Oda's research unit. I thank Dr. Oda for her extreme kindness in welcoming our group, special thanks to her for organizing the awesome parties at her house! At IECB, I am grateful to have met so many fun colleagues with whom I could not only discuss academic endeavors, but hang out and get to know as good friends. Special thanks to Dr. Yifeng Lei for her constant help in every aspect of my life in France, Dr. Rajat Kumar Das for his professional advice, encouragements, and love of chocolate; Dima Dedovets for his inquisitiveness, love of cats and photography, and putting up with my nonsense and thesis rants; Jiaji Cheng for his humor and teaching me so much about modern Chinese culture; Alexandre Cunha for helping me with my analysis and bringing so much joy to the lab; and Yi-Shiang Huang for discussions about cell culture and travel. Thanks also to Dr. Guillaume Le Saux, Alla Malinenko, Xiang Gao, Yutaka Okazaki, Dr. Emilie Pouget, Dr. Sylvain Nlate and other IECB colleagues, including Dr. Xiaoqian Xu, Xuesong Li, Xiang Wang, and Jun Zhou. In addition, I thank Philippe Legros of the Bordeaux Imaging Center for his help with confocal imaging, Florent Deliane at Rescoll for his detailed explanations of mechanical testing, Christine Labrugère for performing XPS in Bordeaux, and Martin Teichmann for allowing me to use his cell culture facilities.

In Belgium, I was part of the Institut de la Matière Condensée et des Nanosciences (IMCN), in the Bio- and Soft Matters (BSMA) division. Even though every stay at the lab was no more than 3 months, I am sincerely grateful for all the help I've received at UCL. I would like to thank Cédric Burhin for teaching me how to prepare and characterize my materials from the very basics, including nanoimprinting, silanization, functionalization, and X-ray reflectivity; André Crahay in WinFab for performing every oxygen plasma experiment and being such a kind and personable colleague; Amir Bahrami for the insightful conversations; Yang Li for the dinner talks, assisting me with various issues when I was not in Belgium, and enduring many inevitable struggles with

me; and Aurore Becquevort for helping with many administration issues. Thanks also to the IMCN colleagues with whom I've had regular interactions: Diana Ramirez Wong, Naresh Saha, Ronggang Cai, Delphine Magnin, Camille Marie, Nasima Afsharimani, Antony Fernandes, Ali Dirani, Alina Osypova, Ara Kim, Maryna Kuzminska, Florence Fioretti, and Hailu Gebru Kassa.

Being part of the IDS-FunMat program means that I got to meet many people from more fields of studies than I could name and originating from more diverse cultural backgrounds than I could imagine. During the three IDS-FunMat training schools, I had the opportunity to interact and make connections with each of these adorable colleagues, and I believe that these connections will be long-lasting even after we graduate. Thanks to all the IDS-FunMates for the FUN times outside of the labs, whether these are spontaneous location-based dinner gatherings, short weekend getaways, or personal interactions. In particular, I would like to thank Uyxing Vongsaysy for always believing in me and cheering me up with her dynamic personality. Also I owe my gratitude to Audrey Sidobre for being very kind and patient in helping me through every painstaking administrative process. Thanks also to Laurent Servant and Marianne Delmas for their help and support.

A significant part of my life in France is the Groupe Chrétien de Chinois (GCC), a Chinese Christian fellowship that has made me part of its family since October 2010. I really feel that God has prepared this home for me before I even stepped foot onto European soil, and He has sent me brothers and sisters to accompany me through troubles and struggles every step along the way. My PhD experiences would not be complete without this home away from home. I am indebted to Andy Cheung for his selfless contributions to the fellowship and to me during my first two years of studies. Andy's insurmountable patience, gentle words of wisdom and consolation, and silent, unnoticed prayers have been my encouragement through times of unbearable anxiety. Thank you so much, Andy, for pouring out your heart (and pouring out warm soup for me on cold winter nights!) In the GCC, I thank Yihua Lam and his family for their hospitality and care; Sharon Cheung for her optimistic attitude and making delicious desserts; Yuehong Zhu and Huiru Chen for being friends with whom I could share my joys and sorrows; Peiguang Wei for lending me an ear and for all the crazy laughter we shared; Sen Zhang for being our trustworthy and wise elder brother; Jinlong Wang for

being someone with whom I can discuss spiritual issues without hesitation; and Yan-Fang Chen for all those unplanned 5-hour chats, admitting that physicists are crazy (and actually being able to understand what it is like being a PhD student), trusting me, and being honest. Thanks also to Jade Blanche, Weiyun Yang, Xinning Wang, Chenggang Ma, Jiawei Shi, Shan Zhu, Siyao Liu, Xin Zhao, Linan Yao, Yuanjie Wang, Cindy Chan, Arting Wong, Ruru Yang, Mengmeng Hu, Junyang Cai, Kathryn Choi, and Regine Chang for their prayers and support.

My friends and family in Canada have never stopped supporting me, even though we are an ocean apart. Florence Kan is always there with the surprising super ability to absorb my rants and share my burdens, and how she is still not tired of my endless complaints is beyond my understanding. Others who have endured my rambles include Hong Hua, Richard Chou, Derek Ching, Oliver Poon, Geoff Lee, Candy Lee, and Chahat Kansal. I sincerely thank you all for being faithful friends throughout all these years and still keeping in touch often. Of course, I must thank my dad, my mom, and my sister Sherry for their love and encouragements. My family never doubted that I would succeed, and their confidence in me keeps me going no matter what hardships I am going through. Even at a distance, my parents always care for my well-being, and Sherry never fails to make me laugh with her silliness. I appreciate it very much!

Last but not least, I send my highest praise and thanksgiving to my Lord Jesus Christ who has granted me peace and joy and bestowed on me everything I have today.

Summary

Tissue engineering is an emerging field in contemporary health sciences that applies strategies to restore functions of damaged tissues. This goal can be achieved by delivering a combination of cells, biological factors, and a biomaterial scaffold on which these cells can adhere, organize, and develop to resemble native tissue. In the context of biomaterials, the optimization of surface interactions between biological components is important for sustaining an artificial environment capable of directing and maintaining favorable cell and tissue growth. Stem cells are often used for applications in tissue engineering due to their multipotent capacities, allowing cell differentiation to be precisely controlled. Herein, we designed and developed nanopatterned biomaterial surfaces that are modified with a bioactive motif with the objective of mimicking physiological extracellular matrices. In turn, we study specific stem cell interactions with our artificially fabricated environments.

We first created nanopatterned bioactive surfaces by combining nanofabrication and surface functionalization techniques. Nanoscale features were introduced on silicon, our base substrate, using nanoimprint lithography. A three-step chemical process was then applied to the nanopatterns, resulting in the local grafting of a cysteine-containing peptide in a continuous anti-fouling background. We characterized our surfaces using a series of techniques including fluorescence microscopy, X-ray photoelectron spectroscopy, X-ray reflectivity, atomic force microscopy, and contact angle analysis, which reveal information related to the surface, such as elemental composition, peptide layer thickness, grafting density, chemical topography, and surface energy.

Next, we studied human mesenchymal stem cell (hMSC) behavior on nanopatterned surfaces grafted with an adhesion-promoting peptide, RGD, in terms of adhesion, proliferation, and stem cell commitment. hMSCs showed different cytoskeletal organization, actin stress fiber arrangement, and focal adhesion (FA) maturation on nanopatterned surfaces compared with homogeneous RGD-grafted surfaces and bare silicon controls. In particular, FA area, distribution, and conformation were highly affected by the presence of nanopatterns, which in turn affect their maturation. The expression of a mesenchymal stem cell marker, STRO-1, also decreased on nanopatterns after hMSCs have been in culture for 4 weeks, which is a preliminary sign of cell

commitment. However, immunofluorescence evaluation of lineage-specific markers (osteoblasts, adipocytes, neurons, and chondrocytes) at 2 weeks post-culture failed to show hMSC differentiation into any particular type of mature phenotype.

Finally, we grafted a mimetic peptide of an important protein for bone development, bone morphogenetic protein 2 (mBMP-2), on our nanopatterns and studied the same hMSC behaviors in comparison with RGD. On mBMP-grafted surfaces, hMSCs take on a cytoskeletal organization that is radically different from that induced by RGD-grafted surfaces. More importantly, only point-like focal complexes were seen on mBMP-grafted surfaces while mature FA were absent, whether homogeneous or nanopatterned. This observation is in direct contrast with RGD, where FA maturation is prominent on RGD nanopatterns but limited on homogeneous surfaces. The assessment of hMSC osteospecific differentiation proves to be complicated as osterix and osteopontin show opposite trends in levels of expression. Thus the osteogenic capabilities of mBMP-2 cannot be precisely evaluated in this study.

In summary, the combination of nanoimprint lithography and surface functionalization is a unique way of presenting nanodistributed bioactivity on a material surface. This nanodistribution influences hMSC fate by altering its adhesive and commitment behaviors in remarkable ways that contribute to our understanding of cell-extracellular matrix interactions.

Keywords: nanoimprint lithography; surface functionalization; bioactivity; mesenchymal stem cell; focal adhesion; differentiation; tissue engineering

Résumé

L'ingénierie tissulaire, domaine en plein essor permet de construire des substituts biologiques afin de restaurer les fonctions normales d'organes dont les tissus sont endommagés ou détruits. Le plus grand défi de l'ingénierie tissulaire est donc de mimer ou recréer *in vitro* les modèles qui puissent être représentatifs de la situation existant *in vivo*. Cet objectif peut être atteint en associant une combinaison de cellules, des facteurs biologiques à un biomatériau sur lequel ces cellules peuvent adhérer, s'organiser, et se développer pour reconstruire le tissu natif. En ce qui concerne le biomatériau, l'optimisation des interactions de surface avec les facteurs biologiques est importante pour l'obtention d'un environnement artificiel capable de diriger et de maintenir un développement favorable des tissus. Les cellules souches sont souvent utilisées pour des applications en ingénierie tissulaire; elles sont multipotentes et en modifiant leur environnement, on peut espérer contrôler leur différenciation. L'objectif de notre travail de recherche était de concevoir et développer des surfaces de biomatériaux nanostructuréss fonctionnalisés avec un principe « bioactif » dans le but de comprendre les interactions cellules/Matrice ExtraCellulaire (MEC). Nous proposons d'étudier les interactions de Cellules Souches Mésenchymateuses avec les environnements artificiellement fabriqués.

Nous avons d'abord créé des surfaces bioactives nanostructurées en combinant la nanolithographie et la fonctionnalisation de surface. Des motifs nanométriques ont été introduits sur le silicium, notre substrat, en utilisant la lithographie par nanoimpression. Une méthode de fonctionnalisation a ensuite été appliquée en trois étapes sur ces systèmes nanolithographiés, en greffant localement un peptide par l'intermédiaire d'un résidu cystéine. Nous avons caractérisé les surfaces avec une série de techniques, notamment la microscopie à fluorescence, la spectroscopie de photo-électrons X, la réflectométrie des rayons-X, la microscopie à force atomique, et l'analyse d'angle de contact, dans le but de caractériser nos surfaces (la composition élémentaire, l'épaisseur de la couche de peptide, sa densité de greffage, la topographie, et l'énergie de surface ont été analysées).

Ensuite, nous avons étudié les comportements des cellules souches mésenchymateuses humaines (hMSC) sur ces surfaces bioactives nanostructures. Ces surfaces ont tout d'abord été greffées avec un peptide contenant la séquence RGD, un peptide qui favorise l'adhésion des cellules. Par rapport au silicium nu, le cytosquelette des hMSCs s'organise différemment avec les fibres de stress localisés sur les surfaces nanolithographiées par le RGD. La maturation des adhésions focales (AFs) est beaucoup plus importante sur les les systèmes nanolithographiés. En particulier, nous verrons que l'aire, la distribution, et l'orientation des AFs sont fortement affectées par la présence des nano-îlots lithographiés. L'expression de STRO-1, un marqueur des

cellules souches mésenchymateuses, a également diminué sur les systèmes nanolithographiés après la culture des hMSCs pendant 4 semaines, ce qui est un signe préliminaire de la différenciation des hMSCs. Toutefois, les résultats préliminaires obtenus dans l'optique d'évaluation de marqueurs immunofluorescence spécifique de la différenciation (les ostéoblastes, les adipocytes, les neurones, et les chondrocytes) à 2 semaines après la culture n'ont pas permis de montrer une différenciation spécifique dans un phénotype mature.

Enfin, nous avons greffé un peptide mimétique d'une protéine importante pour le développement des os, le « bone morphogenetic protein 2 » (mBMP-2), sur nos systèmes nanolithographiés et nous avons étudié le comportement des hMSCs et comparé ces résultats à ceux obtenus avec les matériaux fonctionnalisés avec le peptide RGD. Sur les surfaces greffées par le mBMP-2, les hMSCs prennent une organisation du cytosquelette qui est radicalement différente de celle induite par les surfaces greffées par le RGD. En plus, seuls des complexes focaux ponctuels sont observés sur les surfaces greffées par le mBMP-2, et les AFs matures sont absents, que ce soit sur les surfaces homogènes ou lithographiées. Cette observation est en contraste directe avec le RGD, où la maturation des AFs est clairement déterminée sur les matériaux bioactifs nanostructurés avec des peptides RGD mais limitée sur les surfaces homogènes. Les résultats préliminaires obtenus dans le cadre de l'évaluation de la différenciation ostéogénique des hMSCs sont compliqués à interpréter puisque l'osterix et l'osteopontin montrent des tendances opposées dans les niveaux d'expression. Ainsi, les capacités ostéogéniques de mBMP-2 ne peuvent être évaluées précisément dans cette étude.

En résumé, la combinaison de la lithographie par nanoimpression et la fonctionnalisation de surface nous a permis de créer une bioactivité selon un motif de distribution spatial nanométrique en surface d'un matériau (silicium). Cette nanodistribution influence de façon évidente les hMSCs en modifiant leur comportement (adhésion et différenciation) ce qui a contribué et ce qui contribuera à améliorer la compréhension des interactions des cellules avec la matrice extracellulaire.

Mots clés: lithographie par nanoimpression; fonctionnalisation de surface; bioactivité, cellule souche mésenchymateuse; adhésion focale; différenciation; ingénierie tissulaire

Table of Contents

List of Figures

List of Tables

General Introduction

The main goal of tissue engineering strategies is to restore the function of damaged tissues by delivering a combination of cells, biological factors, and a biomaterial scaffold on which these cells must adhere, organize, and develop to resemble native tissue. *In vivo*, the fates of the cells are determined by a complex interaction of nanoscale physical and chemical signals. In the case of bone tissue, cells evolve *in vivo* (adhesion, migration, differentiation) following biological signals they receive from their local environment – the extracellular matrix (ECM). The challenges lie, therefore, in synthesizing materials able to reproduce these signals likely to induce cells to elicit chosen responses, and in studying the impact of these synthetic ECMs on cell behavior. These studies are of particular importance in the field of stem cells for which the controlled differentiation protocols toward specific lineages has to be improved for their use in tissue engineering.

In this context, nanotechnologies undeniably represent excellent tools for producing structured materials that can mimic the ECM on the nanoscale and lead to bioactivity. In recent years, extreme miniaturization of micro- and nano-systems has presented interesting applications in biomedical engineering and the health sciences. These approaches have primarily been dominated by top-down approach coming from microelectronics, but should now be compared with more recent bottom-up approaches, inherited from chemistry and biology.

In parallel, important advances have been made in the field of biomaterials over the past few years, and most of these have been associated with rendering materials biologically active. It is as logical to develop biomaterials that are bioactive as it is to develop drugs that are bioactive. Pharmacological activity is based on the principles of biological recognition, for example, to competitively inhibit receptors or enzymes, to block binding sites, to regulate certain biological pathways, and so on. Only recently have novel bioactive biomaterials begun to make clinical impact, but given the relatively long cycle from concept to clinic, this is to be expected.

The study presented in this thesis is dedicated to developing nanostructured biomaterials using nanofabrication methods in order to study their impact on human mesenchymal stem cell (hMSC) adhesion and differentiation. Using silicon as the base substrate, we propose an integrated process combining top-down nanoimprint lithography (NIL) and bottom-up surface functionalization (ligands promoting cell

adhesion and/or differentiation) to synthesize bioactive nanostructured materials. These platforms allow cellular assays to be carried out for the investigation of hMSC-material nanointeraction. The first part of the surface modification process involves applying the template-based NIL technique. Due to the high throughput and versatility of NIL, a wide range of geometries and dimensions can be patterned for diverse applications. In our tissue engineering study, we successfully fabricated and characterized two types of nanodots ($D_{150}S_{350}$ – diameter of 150 nm with interdot gap width of 350 nm, and $D_{80}S_{110}$ – diameter of 80 nm with interdot gap width of 110 nm). These nanodots were subsequently functionalized with either a cell adhesion-promoting RGD peptide or a mimetic peptide of bone morphogenetic protein 2 (mBMP-2) through a three-step grafting procedure. Each step of the surface modification process was monitored through a variety of surface characterization techniques to ensure the validity of the protocol. These techniques include fluorescence microscopy, which confirms successful peptide grafting; X-ray reflectivity, which verifies monolayer thickness and molecular density; X-ray photoelectron spectroscopy, which examines elemental composition; confocal microscopy, which allows visual inspection of nanopatterned peptides; atomic force microscopy, which demonstrates chemical topography and compositional contrast; and goniometry, which assesses surface contact angle and surface energy.

The effects of the nanostructured materials on hMSCs were studied on RGD-modified surfaces with respect to homogeneous RGD-grafted and non-functionalized surfaces. Specifically, immunofluorescence was used to stain hMSCs in order to observe, both qualitatively and quantitatively, changes in cell behavior in terms of cell adhesion and differentiation. We investigate in detail the relationship between chemical nanopatterning and surface functionalization on cell area and spreading, cell morphology, cytoskeletal organization, cell-material contact, focal adhesion conformation and maturation, and hMSC commitment. We deduce through analysis that surface nanostructuration of functionalized biomolecules indeed impacts hMSC fate through increasing integrin-mediated contact between cells and materials. As well, nanodistributions of adhesion peptides induce a clear increase in the occurrence of large focal adhesions, indicative of stable integrin clustering, that form at the onset of cell-material contact. Data obtained through the classification of focal adhesions into

various categories based on area also implicate that focal adhesion maturation and stabilization are main criteria that drive changes in cell dynamics.

In turn, hMSC commitment tests reveal a decrease in STRO-1 (mesenchymal stem cell marker) expression at 4 weeks post-seeding on nanopatterns compared with homogeneous controls, which may be an indication of the loss of "stemness". The results from cell adhesion complement those of commitment studies, as it is hypothesized that degrees of cell-material contact and changes in focal adhesion configuration and organization can trigger mechanotransductive pathways that direct the differentiation of hMSCs into mature cell types.

Finally, we grafted a mimetic BMP-2 peptide (mBMP-2) on our nanopatterns and studied its effect on hMSC adhesion and differentiation. Since growth factors are known to interact intimately with integrins, we hypothesize that the presence of mBMP-2, on top of having an effect on osteospecific differentiation of hMSCs, will also impact the way the cells adhere and exhibit integrin-related behavior. We noticed indeed that hMSCs adhered quite differently on RGD- and mBMP-grafted surfaces, particularly in terms of cytoskeletal organization and the size, distribution, and conformation of the adhesion structures. mBMP-2, unlike RGD, does not induce mature focal adhesions but instead stimulates the formation of sparse, point-like focal complexes. We propose that the nature of hMSC adhesion is inherently different on RGD- and mBMP-grafted surfaces. While RGD is a specific ligand for which integrin is a receptor, adhesion is mediated directly on functionalized surfaces via the ligand-receptor interactions, thus giving rise to the formation of mature focal adhesions. BMP-2, however, is a growth factor that indirectly induces the formation of focal complexes through its communication with integrin. As adhesion is mediated indirectly, the formation of focal complexes on mBMP-grafted surfaces will depend on various factors, including peptide distribution, the availability of BMP-2 receptors, the proximity of BMP-2 receptors to integrin receptors, and the efficiency of BMP-2 receptors in stimulating integrin receptor activity.

To complete the tests of differentiation, we performed alkaline phosphatase and Oil Red O staining on hMSCs grown on RGD-grafted surfaces to assess the presence of osteogenic or adipogenic differentiation, but neither staining gave positive results. Lineage-specific immunofluorescence staining was then performed in an attempt to detect differentiation into unexpected lineages. hMSCs were stained for SOX9 (for

chondrocytes), tubulin β-3 (for neurons), and for osteopontin (for osteoblasts), but no comprehensive conclusion could be drawn from the ambiguous results. Staining of osteospecific proteins, such as osterix and osteopontin, was performed on both RGD- and mBMP-grafted surfaces but the results were not easily interpretable, as there was no clear trend in increased expression with time or in the presence of nanopatterning. Preliminarily, we cannot affirmatively conclude that any differentiation has occurred on the surfaces.

I. Literature Review

1. Overview of current tissue engineering trends

Tissue engineering is a state-of-the-art field in conventional health care that deals with the replacement and regeneration of human cells, tissues, or organs in order to restore their normal function [1]. It is an area of study that has emerged recently as a subset of the much broader and more classic field of biomaterials. The need for development in tissue engineering is prominent as tissue loss and organ failure is a persisting health problem in the world today. Traditionally, organ transplants are performed to treat organ loss and failure. Surgical reconstruction and mechanical devices such as kidney dialyzers are also often used to restore or mimic normal organ function. However, many risks are involved in these conventional approaches. The main restraint in transplantation is the limited number of donors compared to patients, and due to a severe donor shortage, many patients die while waiting for available organs. In terms of surgical reconstruction, long-term post-surgery problems can develop as a result of surgical contamination. Finally, while mechanical devices are able to assist in performing the role of certain organs, it is impossible for a single machine or device to replicate all the intricate functionalities of any organ.

Because of the limit posed by abovementioned routes of organ failure treatment, tissue engineering has emerged as a promising alternative to traditional medicine. Lying at the boundary between biomedical engineering and the life sciences, tissue engineering embodies the design of artificial systems where the principles of tissue growth are exploited for clinical use. Researchers have attempted to engineer many types of mammalian tissues, including bone, cartilage, and liver [2-4] with the aim of one day using these engineered tissues to replace damaged or diseased ones (Figure I.1). Another approach makes use of stem cells as therapeutic tools for tissue regeneration, taking advantage of their multipotent properties that allow them to differentiate into various mature cell types [5, 6]. Because of the regenerative capacities of these techniques, the term “regenerative medicine” is also widely used to describe the current rising trend of organ treatment [7].

There are several cell-based strategies that can be used for the treatment of damaged tissues. Cells and tissues can be directly implanted or injected into the site of injury for regrowth, or they can be grown *in vitro* from a scaffold, and then implanted

[8]. Another strategy is to treat tissues *in situ* by implanting a scaffold into the site of injury in order to stimulate local repair using the body's tissue regeneration mechanisms [8]. The common link between these strategies is the need for a scaffold that can interact biocompatibly with either cells *in vitro* or the patient's body. The purpose of a scaffold used in tissue engineering is to act as a supporting frame for the tissues which will eventually replace it when fully regenerated. A scaffold takes part in a host of interactions with its surrounding environment, including cells, tissues, the extracellular matrix, or other organs. The precise synergy between a scaffold and its biological microenvironment must therefore be fine-tuned to achieve the best effects. Hence, scaffold design remains an ongoing tissue engineering challenge.

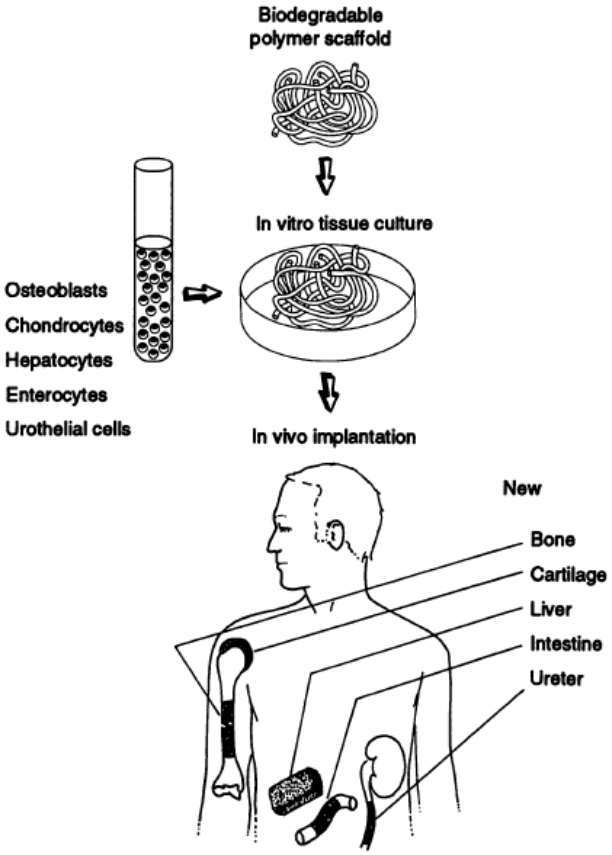

Figure I.1 – General concept of tissue engineering. Various types of matrices are used to create a scaffold for implantation, including natural materials and synthetic polymers. Cells attach to the scaffold *in vitro* and upon implantation, the system is incorporated into the patient's body [1].

Of the types of tissues that have so far been engineered for therapeutic use, there have already been systems that are implanted into the human body, such as artificial skin, blood vessels, and cartilage [9-11]. The case of tissue engineered bone is currently still under the research stage. Bone is a dynamic and highly vascularized tissue that forms the major component in the vertebrate endoskeleton. Composed of mineralized tissue, the three-dimensional internal structure allows bone to act as a rigid support for the human body. Aside from its role as a structural foundation, bone is also responsible for supporting muscular contraction, withstanding load bearing, and protecting internal organs. As a result, bone tissues are subject to many forms of interactions with a variety of objects, and are therefore susceptible to damages and fractures.

One favorable capacity of bone is its high regenerative abilities. Without the need for major intervention, minor bone fractures are generally able to self-heal [12]. However, severe injuries and large bone defects still require complex surgical procedures. One strategy that has been developed to treat bone injuries is autologous bone grafting, whereby bone tissues are harvested from a patient's own body and transplanted to the site of injury [12, 13]. While this strategy has the advantage of lessening the chances of graft rejection, with the donor and recipient of the graft being the same patient, there are many side effects that may complicate the procedure. For example, the supply of suitable bone for transplant is limited, and donor site morbidity may result after the surgery, as well as residual pain and prolonged hospitalization [12-17]. Risk of infection or inflammation is also pertinent, adding to the complications. Another common method for the treatment of bone injuries is allogenic bone grafting, taking bone tissues from another person's body and transplanting it to the patient. Unfortunately, immune rejection and pathogen transmission are introduced with this technique. In addition, the rate of graft incorporation is not as ideal as autologous grafting, neither is the quality of the grafts. Other seriously disadvantages of allogenic bone grafts include poor cellularity (the removal of biological components susceptible to pathogen transmission results in only the mineral structure being left, with few cells), decreased revascularization rate, and limited integration [18-20].

For these reasons, regenerative medicine is being considered as an alternative to bone grafting. Figure I.2 outlines a cell-based procedure that makes use of tissue engineering techniques for the development of a transplantable scaffold. Mesenchymal

stem cells (MSCs) are extracted and expanded in *ex vivo* culture by the addition of growth factors that promote osteogenesis, that is, the formation of bones. The cells are deposited on a scaffold to allow the production of bone extracellular matrix before being implanted in the osseous defect or void in the injured patient [14].

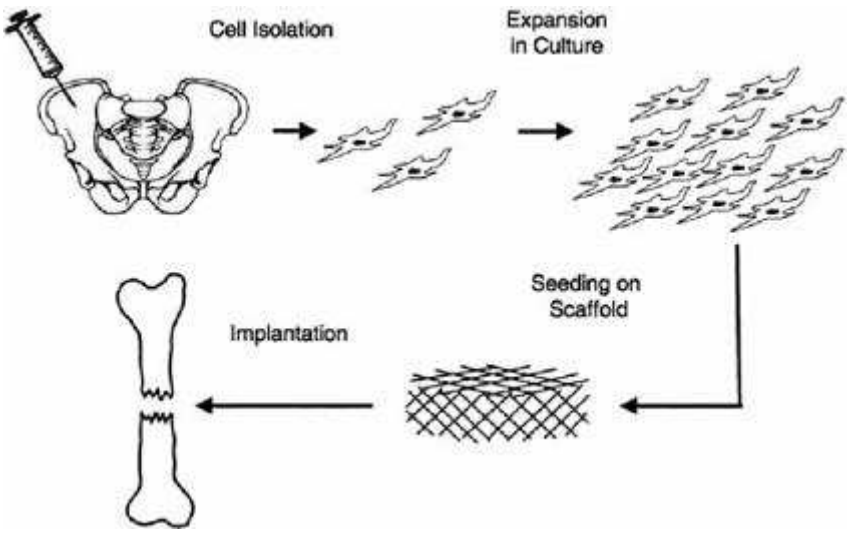

Figure I.2 – *Ex vivo* manipulation of bone cells for scaffold development. In this system, mesenchymal stem cells are expanded in culture. With the addition of specific growth factors, stem cells are directed towards osteogenic differentiation for the formation of bone cells. Seeding of these cells on a scaffold results in the production of bone extracellular matrix, and the scaffold is ultimately implanted into the patient's body at the site of injury [14].

While tissue engineering techniques and biomaterials are being exploited as a solution to treating bone defects, there are still many challenges that must be conquered by scientists and engineers before it can become an effective tool for general use. As tissue engineered products require living components to be in contact with an artificially created environment, the constant aim is to improve systems design by optimizing the various elements therein. To achieve this goal and develop successful products for disease and injury treatment, a comprehensive knowledge of materials science as well as bone biology is required. Ultimately, the combination of advanced materials processing and biological complexity will provide promising routes to gradually move into the potential of clinical applications.

We are currently at a very fundamental stage in understanding the phenomena that occur at the cell-biomaterial interface, and much interest lies in finding out how cell fate can be precisely controlled using biomaterials. Only with this understanding can we begin to advance in tissue engineering applications. The study outlined in this thesis takes a look at activities occurring at the cell-material interface by considering the relationship between a cell and a biomaterial from both the materials science and cell biology points of view. Specifically, we aim to understand the effects of nanoscale surface chemistry on stem cell behavior in order to optimize cell-material interactions and control cell fate. We first present a literature survey that outlines the ongoing works that use biomaterials as a tool to direct cell behavior. We then introduce the fundamentals of stem cell science and basic cell mechanics and we continue with a review of the aspects of biomaterials fabrication. The entirety of this literature review will serve as a general scope for the original work that will be presented in this thesis.

2. Biomaterials design

In the context of tissue engineering, a biomaterial is part of a system that is developed to sustain an artificial environment capable of maintaining favorable cell and tissue growth. An effective biomaterial must be able to interact compatibly in physiological conditions and behave in a controllable manner. In essence, it should possess characteristics that can mimic the structure and function of the extracellular matrix (ECM), with which cells and tissues naturally come in contact. The role of the ECM will be elaborated in Chapter I.4.

As biomaterials are closely integrated with biological systems, the successful production of a robust and practical biomaterial is always a challenge in tissue engineering. From conception to design to fabrication to incorporation, the variability and caveats to consider are numerous. One must carefully contemplate the interaction of the biomaterial with the human body in terms of biocompatibility, durability, and adaptability.

Tissue engineering and biomaterials science encompass the interplay between three basic components: cells, scaffolds, and signaling molecules, with three approaches shown in Figure I.3 [21, 22]. The precise synergy and balance between these components is critical, and so the selection and incorporation of each component becomes a continuing challenge. This section reviews the criteria to be taken into consideration for the design of biomaterials as well as common strategies that have been utilized in their fabrication.

2.1 Scaffolding materials

To ensure efficiency and promote cellular functions, scaffolds used for a biomaterial must possess several characteristics. Biocompatibility is a key feature of a scaffold, as it must be able to exist in harmony while interacting with living systems and performing its desired functions, without causing any serious immune responses or foreign body reactions. Other important features of a scaffold are biodegradability, reproducibility, and porosity [18, 21].

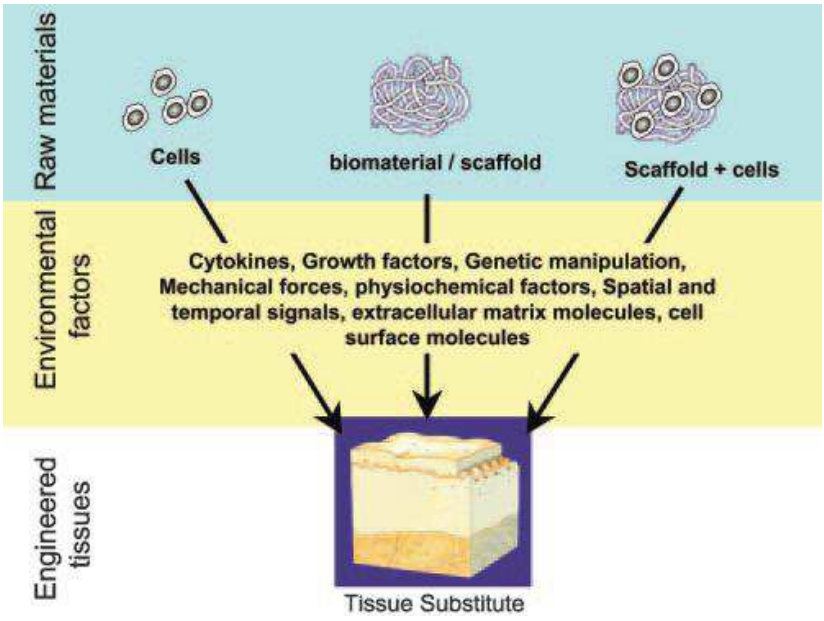

Figure I.3 – Interaction between cells and scaffold in tissue engineering. There are three main approaches: (a) cells alone, (b) scaffold alone, and (c) cells with scaffolds. Whichever approach is selected, external environmental factors and manipulations can be introduced to enhance the system before it is integrated as a tissue substitute [22].

Scaffolds can be grouped into several classes depending on the materials from which they are produced [23], each with its advantages and disadvantages (Table I.1). The most popular choice of materials for fabricating materials is polymers, which themselves are either natural or synthetic. Naturally derived polymers include collagen, chitosan, gelatin, cellulose, among others, and common biodegradable synthetic polymers include poly(lactic acid) (PLA) and poly(glycolic acid) (PGA), among others. For biomedical applications, these polymers have all been approved by the US Food and Drug Administration (FDA), but for use in bone tissue regeneration, there are certain considerations. For example, the biodegradation rate of the polymer scaffold can affect its functionality and must be correlated to the rate of tissue regeneration. If the polymer degrades faster than tissue regeneration, the scaffold will lose its carrier function for cell growth. On the other hand, if the rate of polymer degradation is much slower than that of tissue regeneration, then the process of regeneration will be hindered. Hence, the degradation of the polymer material must be carefully assessed before it could be used as a scaffolding support [21].

As collagen is the protein that primarily forms the structure of native ECM, it has become a popular natural polymer used in scaffolding due to its functional properties. One disadvantage of collagen as a scaffolding material is its high degradation rate and weak mechanical properties. Also, collagen obtained from natural sources has been shown to provoke immunogenic responses [12]. To address these problems, collagen fibers have been cross-linked to decrease the degradation rate, and purified collagen with a low immunogenic response has been developed for commercial use [21].

Table I.1 – Biomaterial classes and their main advantages and disadvantages

Class of biomaterials	**Applications**	**Advantages**	**Disadvantages**	**Refs**
Natural polymers	- Collagen shields - Skin replacement	- Biocompatibility - Functional properties - Abundance - Easily purifiable	- Low strength - Fast degradation - High cost - Immunogenic response	[21, 24]
Synthetic polymers	- Vascular grafts - Heart valve - Sutures	- Manufacturability - Processability	- Lack of cell-recognition signals - Poor wetting	[25, 26]
Metals and alloys	- Joint (hip, knee) replacement - Stents - Dental roots	- High strength - Resistance to fracture	- Corrosion - Lack of biological recognition	[23, 27]
Ceramics and glasses	- Spinal surgery - Orthodontic anchors - Bone plates, screws, wires	- Non-toxic - Non-inflammatory - Osteoinductive	- Brittleness - Slow integration rate - Unpredictable degradation rate	[18, 28-30]

Aside from polymers, metals and alloys are also frequently used as an implant and surgical biomaterial. Metallic biomaterials are primarily used in load-bearing applications, taking advantage of their high strength and resistance to fracture [31]. They are also often used for sensing applications, such as medical tubing, stents, and

catheters [32]. Along with ease of fabrication and widely available fabrication techniques, metallic materials have emerged and evolved substantially in the fields of orthopedics and dentistry. For example, titanium or titanium alloys are regularly used as a material in artificial cardiac pacemakers as well as hip prosthesis due to their high availability, light weight, high strength, and resistance to corrosion [33]. Additionally, Ti-6Al-4V (titanium with 6% aluminum and 4% vanadium) was alloyed to create a material with added strength. This titanium alloy was originally designed for aerospace applications [34], but due to its favorable properties (e.g. biocompatibility), its use in biomedical applications has become more prominent [33]. These alloys can also be coated with hydroxyapatite (which may be classified as a bioceramic material), a naturally occurring form of mineral calcium apatite, to increase osseointegration between the implant and the body tissues [35]. In addition to attractive mechanical properties, metals have chemically reactive surfaces which allow them to be modified in many ways [36]. Surface functionalization, surface coatings, and surface patterning are examples of surface modification techniques that enhance surface properties and will be discussed in Chapters I.4 and I.7 [37].

Another class of functional biomaterials is bioceramics and bioglasses, often used to repair and replace damaged parts of the musculoskeletal system. These materials can be bioinert, bioactive, or bioresorbable [28, 29]. Bioinert ceramics, such as oxide ceramics and silica ceramics, are non-toxic and non-inflammatory [28]. Bioactive ceramics, on the other hand, include hydroxyapatite and bioglass, which can induce intrinsic repair of body tissues, such as bone, by direct chemical bonding [29]. Bioresorbable ceramics are eventually broken down and replaced by the tissues that they are scaffolding, and calcium phosphate (hydroxyapatite, also bioactive) is an example of this type of material. These ceramics have been known to provide efficient scaffolding for bone graft applications, dental implants, and spinal surgery [28].

Researchers in our group have previously studied materials from several of the abovementioned classes of scaffolds, including Ti-6Al-4V, glass, polyethylene terephthalate, and ceramic by surface modification and functionalization [38-54]. The study outlined in this thesis uses silicon as a substrate as we develop methods of fabricating bioactive surfaces to manipulate cell fate for biomedical purposes [55].

2.2 Signaling molecules

In vivo, cells thrive in microenvironments in the presence of a vast variety of signaling molecules, including growth factors and cytokines (Figure I.4). These molecules are responsible for the transmission of information between cells and are indispensible in cell survival. Signaling molecules are incorporated in the design of a biomaterial to play the role of regulating the interaction between cells and a biomaterial at the contact interface.

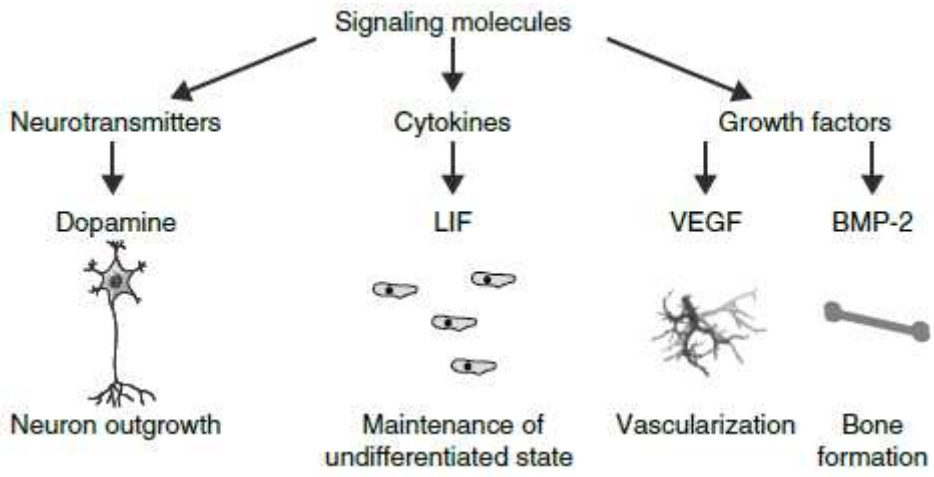

Figure I.4 – Examples of signaling molecules that affect cell behavior. Signaling molecules are present in the cell microenvironment, providing chemical cues to direct cell-specific functions, such as stem cell differentiation and development of specialized tissues [56].

Examples of signaling molecules that are commonly used in tissue engineering include vascular endothelial growth factors (VEGFs), using in vascular engineering to induce vasculogenesis and angiogenesis [57, 58]. Nerve growth factor (NGF) has been covalently immobilized on micropatterned substrates to evaluate neuron response [59], while platelet derived growth factor (PDGF) has been shown to promote periodontal bone regeneration [60]. The two signaling molecules of interest used in this thesis – the cell adhesion-promoting RGD peptide and osteoblastic differentiation-inducing bone morphogenetic protein (BMP) – are discussed in detail in Chapter I.3.4.

During the development of a biomaterial, signaling molecules can be directly immobilized onto the scaffold, added into culture media as a soluble factor, or released

from a device [61] during cell treatment [21]. Each method utilizes signaling molecules as a mediator between cell and material contact. Direct immobilization of a molecule onto a material increases the biofunctionality of the scaffold and allows more precise control over cellular interactions with the material. There is a huge selection of signaling molecules that can be grafted onto a material surface, including proteins, peptides, cell receptors, and growth factors. For example, the covalent grafting of Arginine-Glycine-Aspartic acid (RGD) peptides on material surfaces has been shown to enhance cell adhesion and proliferation [62]. The strategies of immobilizing biomolecules onto a material will be discussed in Chapter I.4.

On the other hand, signaling molecules can be mobilized in cell culture media as soluble factors which can induce specific behaviors of developing cells in culture. Growth factors are often added to cell culture media to direct stem cell differentiation into preferred lineages. For example, stem cells in culture under the influence of dexamethasone, ascorbic acid, and β-glycerophosphate undergo osteoblastic differentiation whereas the combination of dexamethasone, insulin, 1-methyl-3-isobutylxanthine, and indomethacin is known to induce adipogenic differentiation [63-68]. A careful selection of the incorporated soluble factors in the growth environment is therefore crucial for the determination of cell fate, particularly in the case of applications involving stem cells.

The same molecule can affect cells in opposite manners depending on whether it is surface-immobilized or present as a soluble factor. In the case of RGD, when immobilized, it promotes cell adhesion to the material surface, but when in solution, these peptides act as decoys that prevent cell adhesion, causing a form of apoptosis known as “anoikis”, where anchorage-dependent, integrin-mediated cell contact is lost [69-71]. The effects of immobilizing and solubilizing growth factors have been investigated comparatively. In a study by Gao *et al.* involving neural development and induction, dopamine, a neurotransmitter, was immobilized on synthetic polymers as well as solubilized in cell culture medium. The authors showed that immobilized biomolecules more effectively induced neuronal differentiation and enhanced neurite outgrowth compared to dopamine solubilized in culture medium [72]. In another report, Fan *et al.* studied the effects of epidermal growth factor (EGF), whether tethered on a substrate surface or solubilized in media, on mesenchymal stem cell (MSC) proliferation

and survival. The study concluded that surface-tethered EGF, while restricted spatially, was able to better promote cell spreading and survival than soluble EGF due to preferential activation of surface-associated signaling pathways [73]. These findings imply that aside from a correct choice of signaling molecules to use in biomaterials development, local control of the spatial distribution of these molecules is equally important in order to ensure improved cell-implant interactions.

2.3 Cells

In medical procedures such as surgical grafts and bioartifical organ engineering, tissues are put in direct contact with a scaffold to repair damages or fractures. Depending on the type of application and purpose of the biomaterial, different cells may be used. Both somatic cells and stem cells have been utilized in tissue engineering, each with its own benefits but challenges as well.

With various types of cells, specialized tissues or even whole organs would be able to be engineered *in vitro*. For example, functional urinary bladder neo-organs have been successfully generated *in vitro* with autologous urothelial tissues on biodegradable polymers [74]. Another example is tissue engineered heart valve leaflets grown from a mixture of endothelial cells and fibroblasts, either autologous or allogenic, which were shown to be functional when implanted in animal models [75].

Often cells are isolated from a patient's body and expanded *in vitro* [76]. However, it is sometimes difficult to extract sufficient amounts of certain cell types due to their availability, and *in vitro* culture may become tricky [77]. As an alternative to somatic cells, adult stem cells have been used as a tool in tissue engineering owing to their multipotent capacity and ability to self-renew and differentiate into various types of mature cells. In terms of bone tissue engineering, MSCs have gained particular interest, as their ability to differentiate into osseous cells, among other cell types, has been extensively studied. The properties and dynamics of MSCs and their rising potential as a therapeutic tool will be discussed in Chapter I.6.

Previously, our group has carried out studies using human umbilical vein endothelial cells (HUVECs) for applications in vascular tissue engineering. In particular, HUVECs were used to induce angiogenesis and tubulogenesis, ultimately leading to

vascularization [44, 50]. Additionally, human MSCs and other osteoblast precursor cells lines have been used in cell differentiation studies on materials with varying surface properties for bone formation [40, 45, 51-53, 55, 62, 78].

3. Controlling cell behavior with biomaterials

Biomaterials play the role of mimicking the *in vivo* ECM with which cells intimately interact. In this thesis, we are mainly interested in the modification of material surface properties as a strategy of understanding and controlling the fate of mesenchymal stem cells (MSCs). As stem cells are complex and sensitive entities capable of reacting to external stimuli, even the slightest change in environmental growth conditions may be enough to direct their fate. Hence, the precise control of biomaterial properties becomes important in a scaffolding system in order to elicit preferred stem cell responses. In this section, we examine previous works that detail some of the common ways that cell behavior can be controlled with biomaterial characteristics and extrinsic cues.

3.1 Cell morphology

As early as the 1950s, researchers have investigated the changes in cell morphology and cell movement relative to different substrate parameters [79]. Because cells are motile and dynamic, their shapes constantly change as they are subjected to environmental stimuli. The ensemble of cell signaling that determines a cell's fate lies within the conformations of its cytoskeletal structures, which govern the cell's transduction and reception of signals and cues. In turn, changes in cell shape and spreading plays a huge role in directing the various paths of cell behavior.

In a study by Chen *et al.* in 1997, the authors demonstrated that cell shape and morphology affects the conformation of integrin binding, in turn changing the apoptotic behavior of endothelial cells [80]. Fibronectin beads of various sizes were deposited on substrate surfaces, and changes in cell shape and spreading were studied after culture on these surfaces. It was observed that cells attached and spread on larger beads (diameter 25 μm) with a flattened morphology, while cells adopted a more rounded shape as the bead size decreased (diameter 10 μm), resulting in more apparent apoptosis. In the same study, it was shown that by keeping the cell-material contact area constant and solely by inducing a change in cell shape, they can fine-tune projected cell area, cell growth, and cell apoptosis. The correlation between cell shape and focal

adhesions (FAs) was later explored in a paper, with results showing that FA formation was directly proportional to cell spreading [81]. Changes in cell shape and symmetry induce changes in internal cytoskeletal structure, thereby affecting FA assembly which ultimately leads to signal transductions that drive cell function.

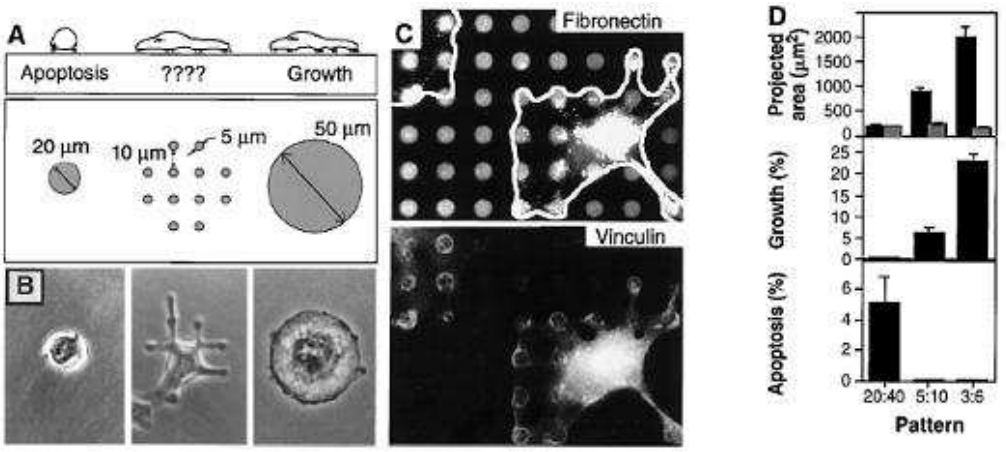

Figure I.5 – Tuning cell shape independent of contact area. The configuration of adhesive islands on the substrate surface profoundly influences the way cells spread and proliferate, in turn affecting their shape and phenotype. Even with a constant cell-material contact, a change in cell shape is enough to determine whether the cell undergoes apoptosis [80].

Another study showing the influence of morphology on cell fate was carried out by McBeath *et al.* using patterned fibronectin islands of varying sizes on PDMS substrate [82]. MSCs were seeded on these protein islands, either 10000 or 1024 μm^2, as single cells per island, and allowed to spread and adhere. MSCs were able to adhere and spread efficiently on large islands, presenting a flattened appearance. Conversely, on small islands, MSCs were observed to be rounded and did not spread due to the limited spacing available for spreading. The degree of osteogenic and adipogenic differentiation was investigated. Consequently, MSCs on large islands differentiated only into osteoblasts while MSCs on small islands differentiated only into adipocytes. These results suggest preliminarily that independent of factors like cell seeding density and cell-cell contact, cell shape alone is a regulator of MSC differentiation.

Kilian *et al.* [83] performed a similar study where microislands of fibronectin were patterned in various shapes with a constant area, only changing the aspect ratio and curvature of the shape. The area of the microislands is optimized as to permit only

one individual cell to adhere and spread, allowing the cell to assume the shape of the underlying island. First, MSCs were cultured on rectangular microislands with a constant area and length-to-width ratios of 1:1, 3:2, and 4:1, and evaluated for osteogenic and adipogenic differentiation. It was noted that osteogenesis increased with length-to-width aspect ratio, while the opposite trend was observed for adipogenesis. That is to say, osteogenesis was more prominent on rectangular microislands at 4:1 aspect ratio while adipogenesis was more apparent for 1:1. Next, MSCs were cultured on constant area microislands with pentagonal symmetry but varying curvature – a flower-shaped island with convex curves, a perfect pentagonal island, and a star-shaped island with concave curves and sharp points at the vertices. With the increase in curve concavity, osteogenesis was more prevalent while adipogenesis showed a decreasing trend. Thus, it was concluded that shape cues can be rationally used to control differentiation-specific signaling in MSCs.

From the combined results of the abovementioned studies, a general link can be drawn between cell morphology and differentiation. It is suggested that stem cell shapes that promote cytoskeletal contractility (flattened shape, high aspect ratio, concavity) lead to increased osteogenesis, while stem cell shapes that limit contractility (rounded shape, low aspect ratio, low concavity) lead to increased adipogenesis. These observations are consistent with the typical appearance of osteoblasts and adipocytes. However, the exact dependency of differentiation on cell shape involves the interplay between complex signaling mechanisms and cannot be easily summarized without taking a look at other factors involved in cell fate determination. Additionally, the abovementioned studies have all made use of fibronectin as a model protein to mediate adhesion between cells and their substrate. As the RGD peptide sequence is the region in fibronectin that is responsible for cell recognition, it has become an important tool for the study of cell adhesion. More details on RGD can be found in Chapter 3.4.

3.2 Substrate properties

Most tissues are anchorage-dependent, meaning that adhesion to a physical solid surface is a requirement for their survival [84-86]. Thus, physical properties of the substrate to which cells adhere, such as its intrinsic elasticity, stiffness, and modulus,

have been shown to alter cell activity. At the cellular level, cells "feel" their surroundings by a process of probing. The actions of anchoring and pulling is dependent on the cell cytoskeletal contractility, which is a central factor that determines the adhesion mechanics through integrins, cadherins, and other signaling molecules [84]. As stem cells sense their surroundings, they are able to respond to physical cues by modifying their differentiation pathways based on substrate properties.

The extreme sensitivity of stem cells to substrate stiffness was demonstrated in a study by Engler *et al.* where MSCs were cultured on substrates with varying matrix elastic modulus E [87]. In this study, substrates with stiffness mimicking primary neurons (E = 0.1 – 1 kPa), myoblasts (E = 8 – 17 kPa), and osteoblasts (E = 25 – 40 kPa) were prepared (cell elastic modulus was measured [87]), and MSC differentiation on the substrates was observed. In terms of cell morphology, matrix-dependent shape variations were observed, where MSCs appeared to take on the shape of the type of cells whose stiffness was replicated by the substrates (Figure I.6). That is to say, MSCs took on branching, spindle, and polygonal shapes corresponding to the appearances of primary neurons, myoblasts, and osteoblasts, respectively [88-90].

A similar study related to substrate modulus was carried out by Saha *et al.* on neural stem cells [91]. A synthetic hydrogel system was developed where the material modulus could be altered from 10 to 10000 Pa. It was noted that on gels with a modulus of ~10 Pa, cell spreading, self-renewal, and differentiation were greatly inhibited. Substrate modulus of ~100 – 500 Pa favored differentiation into neurons, while harder gels with modulus if ~1000 – 10000 Pa favored differentiation into glial cells. In addition, the optimal substrate modulus for neuronal differentiation was observed to be 500 Pa, which is close to the physiological stiffness of brain tissue. This study further supports the consensus that the effective stiffness of the underlying substrate is a crucial regulator of stem cell differentiation.

Substrate rigidity effects on MSC behavior was further investigated by Fu *et al.* who used micromolded elastomeric micropost arrays with different post heights [92]. PDMS microposts were fabricated with the same surface chemistry but varying heights which determine the substrate rigidity. Shorter microposts bend less and are therefore more rigid, while longer microposts bend more easily and are less rigid. The MSCs on rigid microposts were well spread with prominent and highly organized actin stress

fiber and large FA formation, while on soft microposts, the cells presented a rounded morphology, disorganized actin filaments, and small adhesion complexes. In addition, MSCs cultured in a biopotential differentiation medium showed cell lineage commitment, whereby the osteogenic lineage was favored on rigid microposts and the adipogenic lineage was favored on soft microposts. Overall, these observations imply that cell shape, cytoskeletal tension, FA arrangements, and even lineage commitment are coupled to the sensing and response to substrate rigidity.

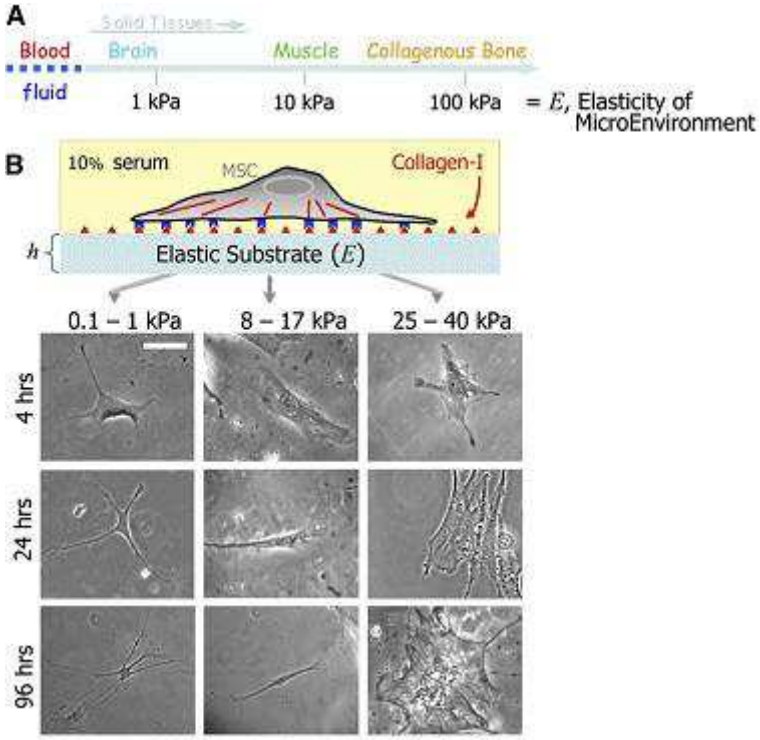

Figure I.6 – Cell response to substrate stiffness, demonstrated by Engler *et al.* MSCs cultured on soft substrates experience low force and tension and tend to differentiate into softer tissues, such as neurons. However, MSCs cultured on stiff substrates are subject to strong intracellular tension, which in turn affect their phenotype, promoting their differentiation into more rigid tissues, such as collagenous bone [87].

In contrast to inducing stem cell differentiation, the multilineage potential of stem cells can be retained by growing them on substrates with an elasticity mimicking that of bone marrows, as reported by Winer *et al.* [93] Results of the investigation suggest that soft substrates are able to mimic the bone marrow niche, where MSCs naturally thrive, hence maintaining the cells in a quiescent, undifferentiated state. The

ability to reproduce these properties in a substrate gives rise to applications where stem cell self-renewal is preferred.

3.3 Mechanical cues

Closely related to substrate properties are the mechanical cues present on the substrate surface. The process of identifying and responding to mechanical cues is vital for cell development and function. Throughout the lifetime of an organism, its body tissues and organs are constantly exposed to various types of mechanical stimuli. These include muscles forces, gravity, blood flow, compression, and shear stress [94]. In turn, cell growth and behavior are inevitably influenced by these mechanical factors. Effectively, presenting mechanical cues on a material can be a way of controlling stem cell fate.

The mechanism by which cells receive mechanical signals and process them into biochemical changes is called mechanotransduction [95]. Early reports have shown that initial mechanoreception events trigger signaling pathways which are activated through changes in the cell cytoskeleton [96]. Further studies also proved that focal contacts, formed during cell adhesion, respond to locally applied mechanical force and behave as individual mechanosensors [97].

To understand the effects of mechanical stimuli on cell behavior, mechanical forces can be broken down at the single cell level by a concept called “force isotropy”, illustrated in Figure I.7 [98]. Force contains two components, magnitude and direction. During cell migration, the cytoskeleton exerts traction forces on the extracellular matrix (ECM) or substrate in contact. If these forces, generated at different directions, vary in magnitude, anisotropic cytoskeletal tension is the result, causing the cell nucleus to deform or elongate. If, however, the traction forces are generated at similar magnitudes in all directions, then the result is isotropic cytoskeletal tension, whereby the cell nucleus takes on a round morphology. Forces that are derived from extracellular sources, like shear stress and hydrostatic pressure, are superimposed on cytoskeletal tension and will have similar effects depending on the force isotropy.

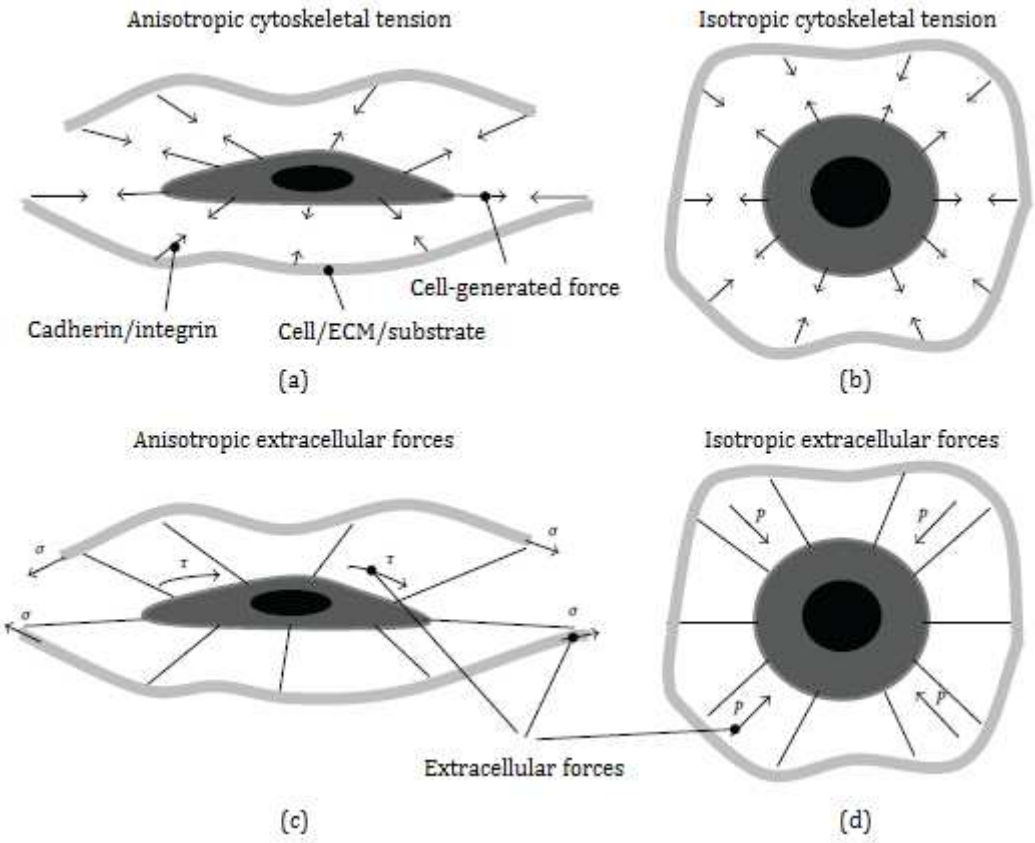

Figure I.7 – Force isotropy described at the single cell level. Force possesses two components, magnitude and direction, and can originate from inside the cell via the cytoskeleton or outside the cell via factors in the extracellular environment. Cells undergoing anisotropic forces (a and c) experience tension from different directions that vary in magnitude, resulting in a flattened nucleus. Cells subjected to isotropic force (b and d), however, experience equal tension from all directions, and the nucleus takes on a rounded shape instead. Cytoskeletal tension is present in the form of cell contractions, whereas extracellular forces are present in the forms of cyclic matrix stress (σ), cyclic fluid-induced shear (τ), and cyclic pressurization (p) [98].

The concept of force isotropy was applied in stem cell mechanosensing by Kurpinski *et al.* [99] PDMS with micropatterned grooves were prepared, and MSCs were cultured on the substrates with the application of a cyclic, uniaxial (anisotropic) strain in a direction parallel or perpendicular to the groove alignment. Cells grown on non-patterned controls showed random morphology when no force was exerted, but aligned perpendicularly when strain was applied. On micropatterned substrates, cell alignment was maintained and observed to be parallel to the microgrooves, whether uniaxial strain was applied or not. Microarray analysis also revealed that uniaxial strain can

cause matrix remodeling in MSCs, with the decrease in expression in several chondrogenic/osteogenic genes when strain is applied. This observation suggests that uniaxial strain promotes the phenotype of tension-bearing tissue types but suppresses compression-bearing tissue types.

MSC differentiation induced by combined effects of substrate alignment and mechanical loading has been demonstrated in a study by Subramony *et al.* [100] Human MSCs were cultured on unaligned and aligned nanofiber scaffolds and a uniaxial tensile strain was applied to the cells in a bioreactor. Evaluation of cell differentiation revealed that without mechanical loading, no differentiation was induced, either on unaligned or aligned fibers. However, with mechanical stimulus, cells on unaligned substrates only modified their morphology without differentiation, while cells on aligned substrates underwent differentiation into ligament fibroblast-like cells. The expressions of various integrin subunits were also upregulated with the application of mechanical loading.

3.4 Chemical cues

In addition to mechanical cues, surface chemical composition can also have a profound effect on cell behavior. The simplest chemical modification that can be applied to a surface is the presence of functional groups. Lee *et al.* performed a study whereby low density polyethylene (PE) surfaces were modified with different chargeable functional groups with similar wettabilities [101]. These functional groups include –COOH, $–CH_2OH$, $–CONH_2$, and $–CH_2NH_2$. Subsequently, cell adhesion and growth were evaluated on these surfaces. The study showed that amine group-grafted PE ($–CH_2NH_2$) promoted cell adhesion most efficiently while the polyacrylic acid-grafted PE (–COOH) resulted in poor adhesion. Since the amine group is positively charged, and a large number of proteins and serums in culture are negatively charged, the electrostatic interaction between the surface and the biomolecules is favorable and directly enhances cell adhesion. Conversely, the polyacrylic acid functional group is negatively charged, and limited cell adhesion is expected. This study showed that simple functionalization that alters surface charge is enough to have an impact on cell behavior.

In the ECM, discussed in Chapter I.4, there are intricate networks of protein complexes that collaborate to ensure proper cell functions. Adhesion is one of the most

basic cell functions required for cell survival (Chapter I.5), and there are many ECM proteins that play roles in promoting cell adhesion. Examples of these adhesion-related proteins are fibronectin, vitronectin, and laminin [70], which can themselves be coated on biomaterial surfaces to improve cell response. One common characteristic of these proteins is the presence of a short peptide region found within their structure that acts as a recognition site for cell adhesion molecules. This amino acid sequence is known as the RGD, or Arginine-Glycine-Aspartic acid peptide sequence [102]. The RGD peptide was discovered in the 1980s by Ruoslahti *et al.* This peptide sequence is found in many ECM proteins, including fibronectin, vitronectin, osteopontin, collagen, and fibrinogen and is responsible for cell attachment via integrin recognition [102].

When RGD is immobilized on a substrate and exposed to cells, integrins on the cell surface recognize the peptide sequence and anchor to it, resulting in adhesion. Because of this property, the peptide is often present on biomaterial surfaces as a chemical cue to enhance cell-material contact through the formation of specific focal contacts [62]. In addition to their major role in molecular anchorage, RGD peptides are also known to affect embryogenesis, cell differentiation, immune response, wound healing, and hemostasis [69]. In a study of RGD-modified titanium, it was demonstrated that osteoblasts showed earlier osteocalcin (marker of differentiated osteoblasts) expression on RGD surfaces, an evidence of earlier differentiation of osteoblasts on these surfaces [103]. In turn, osseointegration can be improved in dental implants with the incorporation of RGD. Another study revealed similar results whereby RGD-coated PMMA surfaces accelerated cancellous bone growth in animal models compared with the uncoated implants [104]. Additionally, RGD peptides can take on many conformations that change their affinity to integrins. For example, the cell attachment activity of cyclic RGD peptides are higher than their linear counterparts, in turn increasing the shear stress cell detachment resistance [69]. A variety of methods have been developed to immobilize RGD peptides onto material surfaces, some of which will be discussed in Chapter I.4.

In addition to RGD, other cell recognition motifs exist and some have been immobilized for cell attachment. One example is KRSR (lysine-arginine-serine-arginine), a sequence found in a number of bone-relative adhesive proteins, including fibronectin and osteopontin. Its use was shown in a study where conventional titanium and

nanophase titanium (material with grain sizes less than 100 nm) surfaces were functionalized with KRSR peptides [105]. Osteoblast adhesion was then evaluated on control and modified surfaces. On both conventional and nanophase titanium, KRSR-modified surfaces showed increased osteoblast adhesion compared with their respective non-functionalized surfaces. However, it is interesting to note that non-functionalized nanophase titanium showed increased cell adhesion compared to peptide-modified conventional titanium, establishing that nanophase materials may be a stronger promoter of cell adhesion than KRSR. Kim *et al.* further note that peptide-based promotion of cell adhesion is specific to cell types. RGD was able to enhance the adhesion and spreading of normal human dermal fibroblasts, while KRSR was more effective on normal human osteoblasts [106]. FHRRIKA (phenylalanine-histidine-arginine-arginine-isoleucine-lysine-alanine) is another adhesion sequence derived from bone sialoprotein. In a study by Schuler *et al.*, it was demonstrated that FHRRIKA-coated titanium surfaces increased rat calvarial osteoblast adhesion when compared with bioinactive surfaces [107]. However, cell numbers did not reach the level found on RGD-coated surfaces, indicating that different adhesion mechanisms may affect efficiency on different cell recognition motifs. Conversely, Sawyer *et al.* showed that on hydroxyapatite surfaces, combinations of RGD with either KRSR or FHRRIKA did not enhance MSC attachment relative to RGD alone [108]. This result was coupled with the observation that hydroxyapatite is a highly adsorptive and reactive material that tends to adsorb pro-adhesive proteins from blood or serum, and hence functionalization on hydroxyapatite surfaces may prove to be of limited value.

In terms of bone development, bone morphogenetic proteins (BMPs) are a class of growth factors in the transforming growth factor beta family (TGF-β) that play strong roles in inducing the formation of bone and cartilage [109-111]. To date, approximately 20 types of BMPs have been identified. The primary role of BMPs is to stimulate bone formation by interacting with specific receptors on the cell surface. There are two types of receptors to which BMPs can bind, known as type I and type II receptors [112]. BMPs bind with weak affinity to type I or type II receptors alone, but with high affinity to type I/type II heteromeric receptor complexes [113, 114]. Activated receptors influence the dynamics of the cell cytoskeleton by activating several signaling pathways that direct cell migration and regulate the expression of differentiation-inducing genes, such as

Runx2 by activating the Smad 1/5/8 pathway [51]. These receptor-ligand interactions promote a series of molecular cascades to be activated through signal transduction mediated by the receptors, resulting in the formation of osteoblasts [111]. As a growth factor, BMP receptors have also been shown to interact dynamically with integrin receptors (Chapter I.5.3), and this observation has important implications in the role of BMPs in cell adhesion and growth [115, 116].

BMPs have been used in combination with synthetic degradable polymers to successfully repair bone defects in the humeri of adult rabbits, inducing the formation of new bone at the site of defect and demonstrating its ability to enhance the regeneration of bone [117]. Mimetic BMP peptides have also been designed by studying the structural composition of the binding interface between BMPs and their receptors and selecting the region responsible for the receptor-ligand interaction [51]. These mimetic peptides, as well as the proteins themselves, have been used to demonstrate functionality.

It was generally accepted that BMPs and their receptors need to be internalized, and so BMPs are delivered as soluble cues [118]. However, recent studies using matrix-bound or surface-immobilized BMPs have brought the issue of internalization to debate, and some researchers believe that non-internalized BMP may actually trigger different, longer lasting signaling events compared with soluble BMPs [115]. In fact, previous studies in our group have shown that surface-immobilized mimetic BMP peptides induce an osteogenic differentiation of stem cells, indicating that BMP internalization is not necessarily required for its function [51, 53].

The work presented in this thesis makes use of RGD and mimetic peptides of BMP-2 as two biomolecules of interest that can be immobilized on material surfaces in a nanoscale spatial distribution, rendering them bioactive. The effects of nanostructured bioactivity are explored with respect to specific stem cell behavior, in particular cell adhesion, proliferation, and differentiation.

3.5 Surface nanotopography

In tissue engineering devices, implant features significantly influence tissue formation and maintenance at the implant surface. An understanding of cell responses to material properties requires an examination of specific surface topography, as it is

becoming increasingly more evident that even minor surface topography is a powerful cue for directing cell behavior. Surface roughness and composition are key factors that determine the properties of adherent cells. As well, cells react to surface features on the micrometric and the nanometric scale, including grooves, ridges, and islands.

To investigate the impact of surface topography on the differentiation of MSCs, a study was performed using two types of titanium surfaces: machined titanium and dual acid-etched titanium. MSCs were allowed to adhere and proliferate on both surfaces, and their protein expression was evaluated. It was observed that on dual acid-etched surfaces, compared with machined titanium, the cells showed increased mRNA expressions of bone morphogenetic protein 2 (BMP-2), Runx2, and osterix, along with specific markers of osteoblastic phenotype, such as bone sialoprotein and osteocalcin [119]. These proteins are all critical players that are interconnected in osteoblastic differentiation, as BMP-2 upregulates the expression of Runx2 and osterix. Runx2 induces MSC differentiation into preosteoblastic cells while osterix ensures that these cells fully develop into mature osteoblasts in the commitment process. Evidently, the increased expression of all of these proteins is a sign that bone formation is favored on dual acid-etched titanium, confirming that surface roughness indeed is a potent modulator of cell fate.

In terms of nanotopography, much work has been done to show that nanoscale variations in dimensions or even changes in order can have a huge impact on cell behavior. Simple topographic features such as cliffs and grooves have been patterned on the microscale and shown to affect the alignment and elongation of cells, as reported by Wilkinson *et al.* [120] Upon interaction with the surface features, cells elongate and align along the grooves (Figure I.8). This change in arrangement causes a reformation of the cell cytoskeleton, whereby the actin microfilaments reconfigure to the shape and dimensions of the surface topography. Similar effects were noted on MSCs in a report by Yim *et al.*, where nanogratings 350 nm in depth were produced on tissue culture plastic and PDMS substrates using the nanoimprinting method. Elongated MSCs were observed to organize in parallel to the nanogratings with an aligned actin cytoskeleton. Since this elongation was seen on two materials with different substrate stiffness, it may indicate that surface topography is a more dominant regulator of cell fate [121]. The same research group looked at MSC differentiation on similar types of gratings but with

changing lateral dimensions ranging from the microscale (1 μm) to the nanoscale (300 nm). A biochemical cue, retinoic acid, was present in culture to upregulate neuronal marker expression, and the aim of the study was to examine whether surface gratings facilitate or enhance MSC differentiation into a neuronal phenotype. As it turns out, an evaluation of microtubule associated protein 2 (MAP2) revealed that gratings with nanosized dimensions were indeed more effective in inducing neuronal differentiation than gratings with microsized dimensions [122].

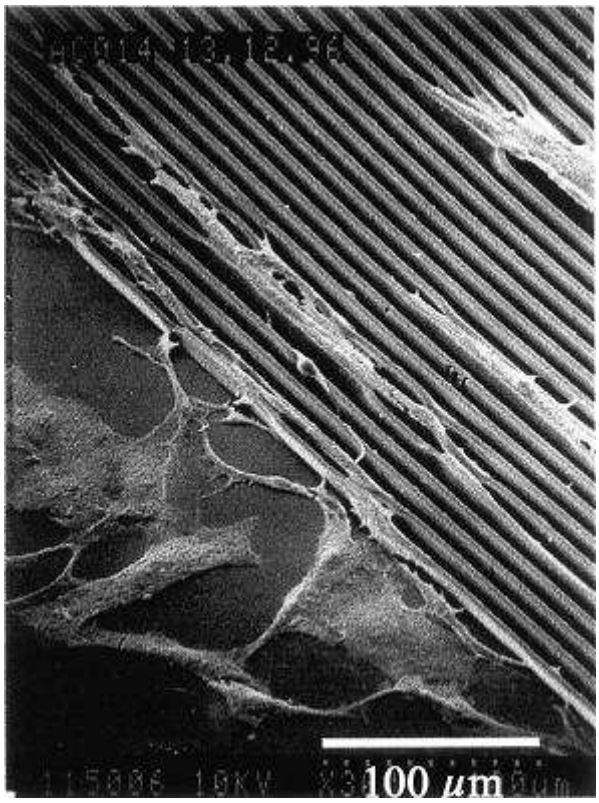

Figure I.8 – Tendon cells elongate and align on topographic features. Cells are able to sense the shape and structure of the substrate onto which they adhere and in turn modulate their own shape and alignment to conform to that of their environment [120].

The order and symmetry of nanofeatures also appear to have a non-negligible impact on stem cell fate. In 2007, Dalby's research group reported on their findings of using nanoscale disorder to stimulate MSC differentiation into bone in the absence of osteogenic factors [123]. Using e-beam lithography, substrates with several types of topographic profiles were prepared. Nanopits with a diameter of 120 nm and a depth of

100 nm, with different arrangements, were fabricated, including a hexagonal array, a square array, square arrays with slight displacements of varying degrees, and a random placement (Figure I.9, top row). Both osteoprogenitors and MSCs were cultured on these surfaces for 21 days and evaluated for the activities of two bone-specific ECM proteins, osteopontin and osteocalcin, with the results for MSCs shown in Figure I.9. In short, osteoblastic expression was noted on substrates where the nanofeatures were displaced at a slight offset from the original square array, with distinct positive immunofluorescent staining for both osteopontin and osteocalcin. Furthermore, bone nodules were seen at 28 days post-culture on the displaced square arrays, indicating the presence of mineralization.

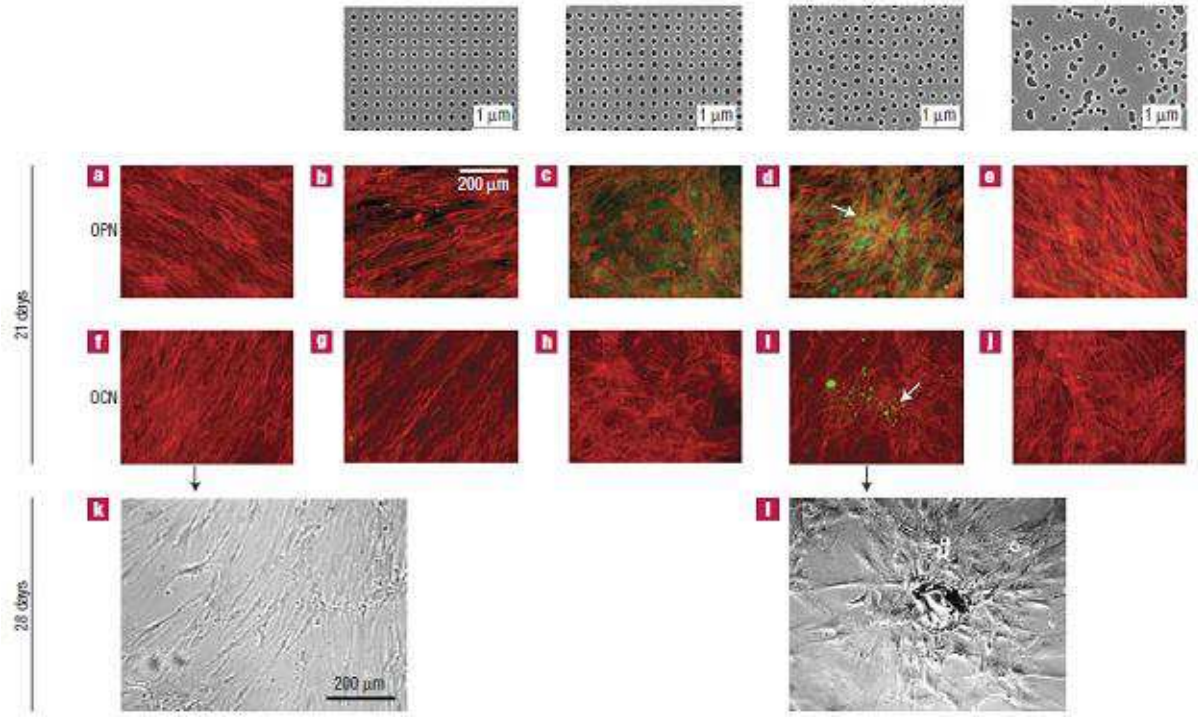

Figure I.9 – The effect of nanofeature order on MSC differentiation, demonstrated by Dalby *et al.* Nanopits with various types of distributions and order were fabricated and MSC were cultured for studies in differentiation – square array (b, g), disordered square array with dots displaced randomly by up to 20 nm (c, h) and 50 nm (d, i) on both aces from their position in a true square, and randomly placed pits (e, j). Square arrays of nanopits displaced with a slight offset induced osteoblastic differentiation indicated by positive staining of osteopontin and osteocalcin, shown in green, after 21 days in culture. Bone nodules also developed after 28 days in culture on these surfaces (k, l) [123].

Another study that addresses the issue of nanopattern order was carried out by Huang *et al.* [124] Nanobeads of RGD peptides were deposited on substrate surfaces via micelle nanolithography, resulting in ordered or random bead distributions with various spacings between the beads. MC3T3-E1 cells were cultured on the substrates and evaluated for integrin-related cell adhesion. The results demonstrated that whether on ordered or disordered beads, cell spreading was better at low bead spacings compared to higher spacings. However, the difference was more evident on ordered beads, which may indicate that although highly spaced disordered beads may inhibit cell spreading, cells can still spread better than on ordered beads with similar spacings. Huang attributed this observation to the mechanism of cell adhesion, noting that efficient adhesion can only occur when integrin spacing is less than 70 nm. To explain adhesion and spreading on disordered beads even at high spacings, it was proposed that integrin clustering must occur at the onset of adhesion. Taking into account global average inter-ligand spacing, it is reasonable to conclude that the polydispersity of the disordered nanopatterns leads to more clustering than an ordered one.

Though nanotopographical effects on MSC differentiation clearly exist, an absolute cause-effect relationship cannot yet be established, as there have been some discrepancies. In a report by Park *et al.*, TiO_2 nanotubes with diameters ranging from 15 to 100 nm were fabricated by anodization on titanium surfaces, and MSC adhesion and osteoblastic differentiation were studied as a function of tube dimension [125]. Using the same materials and similar methods of fabrication, Oh *et al.* performed a similar study [126], but the two experiments presented an interesting inconsistency. While both noted that MSC adhesion is inversely proportional to nanotube diameter (enhanced at smaller diameters and hindered at larger diameters), the observations of cell differentiation yielded opposite results. Park *et al.* showed decreased osteoblastic expression on larger diameters compared with the smaller ones, attributing this effect to the lack of focal contact formation and thus inhibition of differentiation signaling. However, Oh *et al.* demonstrated that osteoblastic was higher on larger diameters compared with the smaller ones, proposing that the cells that do adhere on the large diameters induce cell elongation that leads to cytoskeletal stress and selective differentiation (Figure I.10).

Evidently, it is difficult to draw a comprehensive conclusion that explains these phenomena, and ongoing studies are required to further probe into the detailed mechanisms of cell differentiation and its relationship with nanotopography. However, some explanations for the apparent discrepancies in the works of Oh and Park have been proposed by Zhao *et al.* [127] First, although both studies used MSCs, they were of different origins (human for Oh and rat for Park). The difference in cell type may be one of the reasons that account for the cytocompatibility of TiO_2 nanotubes. Also, different phases of TiO_2 influence cell function in different ways. The conditions of substrate fabrication in these studies may not have been completely identical, adding to the possibility that the substrates play a part in the controversial results. In addition, Park *et al.* used an osteogenic cell culture medium in their study while Oh *et al.* used culture media free of osteogenic growth factors. It would be reasonable to conclude that the composition of the cell culture media would have a substantial effect in cell growth and differentiation.

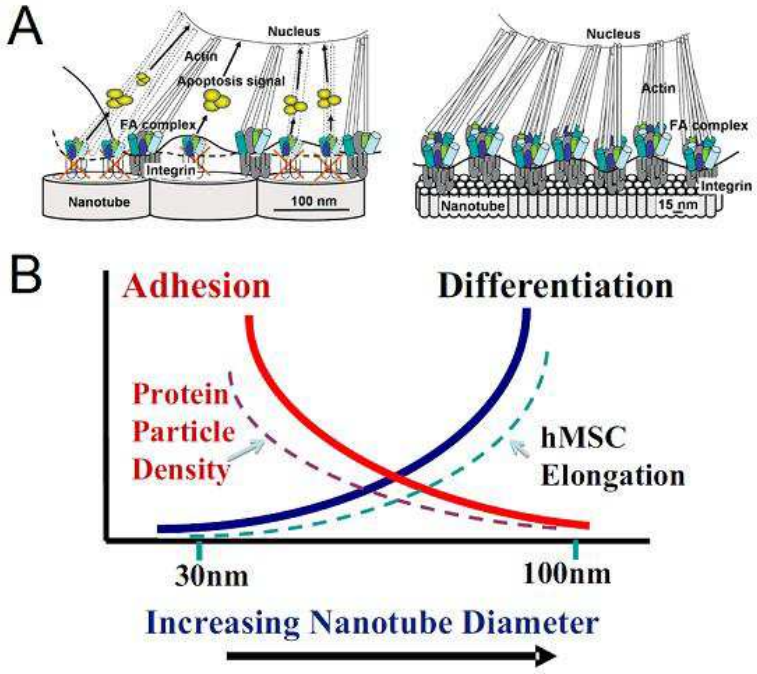

Figure I.10 – Models of MSC differentiation as a function of nanotube diameter, demonstrated by Park *et al.* (A) and Oh *et al.* (B) Park *et al.* postulated that as nanotube diameter increases, cell adhesion is inhibited and thus apoptosis is induced. Oh *et al.*, on the other hand, proposed that differentiation is proportional to nanotube diameter as large diameters result in cell elongation, promoting cell signals that allow differentiation to occur. [125, 126].

Micro- and nanofabrication techniques are often required to prepare materials used to study surface topography and its interaction with cells. A discussion of some of these techniques, including their basic principles and uses in biomedical applications, can be found in Chapter I.7.

4. Biochemical and physical modification of material surfaces

As biomaterials play an integral part in tissue engineering, optimizing their properties is a goal in biomaterials design. Surfaces often need to be modified chemically to be rendered adhesive in order to initiate cell attachment and in turn facilitate cell growth. A common strategy is to modify substrate surfaces with biomolecules that stimulate various effects to take place on cells, for example enhanced adhesion or differentiation towards a particular lineage. Structural miniaturization towards the microscale and eventually the nanoscale is also particularly interesting for applications targeted at the cellular level, and will be elaborated in Chapter I.7. In this section, we review the importance of incorporating surface bioactivity in biomaterials and we introduce some of the conventional methods that are traditionally used for modifying material surfaces.

The extracellular matrix (ECM) is a complex mixture of self-assembled macromolecules, composed predominantly of collagens, non-collagenous glycoproteins, hyaluronan, and proteoglycans (Figure I.11). The ECM is not only a scaffold for the cells, as it also serves as a reservoir for growth factors and cytokines while modulating cell activation status and turnover. The ECM should be considered as a dynamic network of molecules secreted by cells that in turn regulate cell behavior by modulating their proliferation and differentiation, in the case of stem cells. Additionally, the ECM provides structural strength to tissues, maintaining an intricate architecture around the cells and the shape of organs.

Various cell types secrete different matrix molecules and the nature and the amount of these molecules change during developmental age. Consequently, ECM composition, immobilization, and spatial arrangement vary for each tissue type. Bone ECM consists mostly of collagen I mineral and non-collagenous proteins such as osteocalcin, fibronectin, and vitronectin [102, 128]. Growth factors are naturally occurring protein hormones which may act through autocrine or paracrine mechanisms and have potent effects on cell growth, proliferation, and differentiation. Growth factors are often stored and sequestered in the ECM and interact with cells through receptor tyrosine kinases (RTKs). Then, cells evolve *in vivo* (adhesion, migration, differentiation) following biological signals they receive from this local environment in interaction with

the surrounding ECM. Indeed, collagen is a major component of the ECM and connective tissues and consists of a network of fibers that provide the structural integrity and malleability to accommodate both cellular growth and tissue development [129, 130].

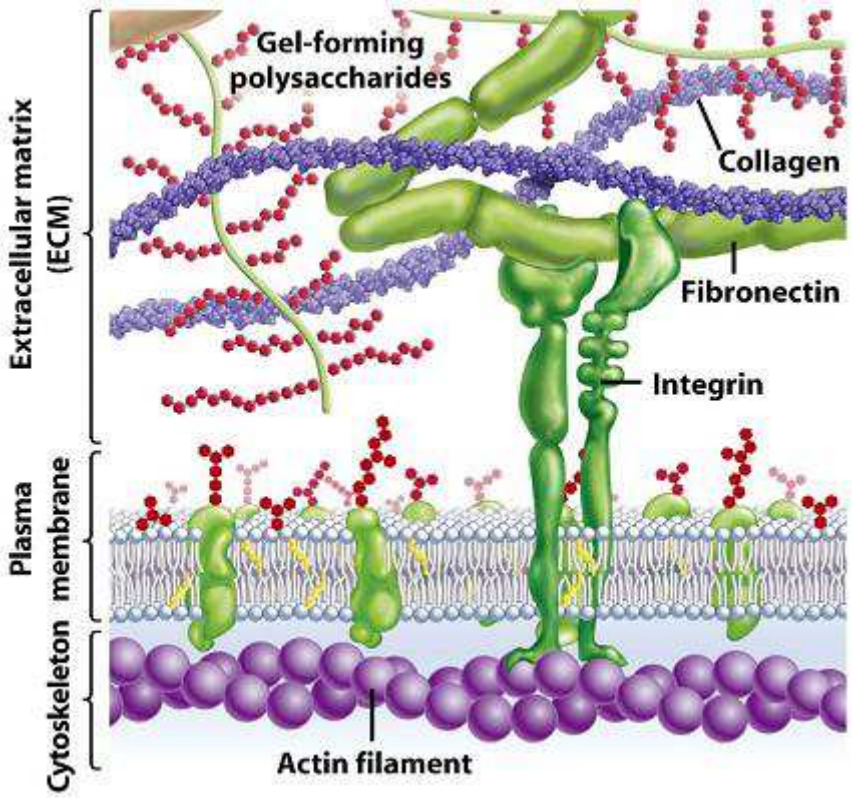

Figure I.11 – Schematic of extracellular matrix and its proteins. The ECM consists of a complex mixture of macromolecules, including various collagens and glycoproteins. Exchange of biological signals occurs through the interaction of cells with the ECM, whereby cell functions, such as adhesion, proliferation, and differentiation, are regulated [131].

To mimic natural ECMs and enhance cell adhesion, biomaterial surfaces have been modified with a great variety of substances ranging from inorganic molecules to short peptides to complex proteins. By simply adding functional groups on the surface of a material, its influence on cell behavior can be tuned [101, 132]. It is undeniable then that the incorporation of bioactive molecules, as well as the method of surface immobilization, will further impact cell-material interactions. For example, as already described in Chapter I.3.4, RGD peptides are commonly used as chemical cues on biomaterial surfaces to promote a specific cell response.

Cells bind to the ECM by interacting with components found therein, including important proteins such as fibronectin, laminin, and vitronectin [69]. Coating the surface of a material before putting it in contact with cells can therefore increase the adhesion between the two components. The use of natural proteins extracted from the ECM provides a platform for biomimetic applications, as the proteins are able to resume their roles even as a coating. However, large proteins present several drawbacks that must be taken into account. First, the isolation and purification of whole proteins is a complicated process that may result in undesired immune responses and risks of infection [69, 133]. As a result, a problem that develops is protein degradation or denaturation. Another disadvantage of using proteins is the issue of molecular orientation and conformation. In the ideal situation, grafted proteins should be able to expose their functional active sites on the material surface so that they are easily accessible to cells. The control of protein conformation, therefore, is of utmost importance [70, 134, 135]. In reality, however, proteins are subject to conformational changes that can be an outcome of surface chemistry or protein folding, in turn altering their functionalities [136-138]. As a result, precise control over protein dynamics can be extremely difficult.

In many cases, a cell recognizes specific regions or motifs on a large protein responsible for the activation of its function. Consequently, the use of small peptides in surface modification has become an alternative for complex proteins, presenting many advantages over their larger counterparts. Among these are the peptides' higher stability, cost-effectiveness, ease of synthesis and characterization, enhanced packing density, defined conformation, and slow enzymatic degradation [69, 104, 139, 140]. Yet, although synthetic peptides seem to be advantageous over proteins in many aspects, it is not possible to reach an absolute conclusion and say that peptides should always be preferred over proteins. The selection of the biomolecule must be tailored specifically to the experimental conditions and applications of each individual study.

To make use of biomolecules as a tool for biomaterial enhancement, such as the ones presented in Chapter I.3.4 (RGD and BMP), they must be properly functionalized on the material surface. Various immobilization techniques are commonly used, with physical adsorption being the weakest and least stable [141]. This simple technique can be achieved by dipping a substrate in a protein solution with the advantages of being

fast and convenient. However, changing the substrate properties can alter the way a protein is adsorbed onto its surface. Studies of fibronectin adsorption on materials with modified surface chemistry revealed that fibronectin adsorbs at different densities and adopts different conformations, in turn significantly affecting its cell-adhesive abilities [142, 143]. Moreover, the relatively weak forces that maintain the biomolecule interaction with the surface are subject to environmental conditions, such as pH, ionic strength, and protein concentration. Changes in these conditions easily cause the adsorbed molecules to desorb, adding to the instability of the system [141].

Covalent immobilization of biomolecules to surfaces is advantageous in that it results in highly stable systems. However, to achieve this stability, the process often involves many steps and requires different types of chemicals and cross-linking agents, so the strategies must be selected carefully. There are many ways to covalently link biomolecules, one being the use of EDC/NHS chemistry, as shown in the scheme in Figure I.12 [144]. In this method, the carboxyl group on the protein heparin reacts with 1-ethyl-3-(3-dimethylaminopropyl)carbodiimide hydrochloride (EDC) to form an unstable intermediate. Upon reacting with N-hydroxysuccinimide (NHS), a more stable, amine-reactive intermediate is formed. Finally, this intermediate is coupled to the amine groups found on the surface of the polymer substrate, completing the immobilization process.

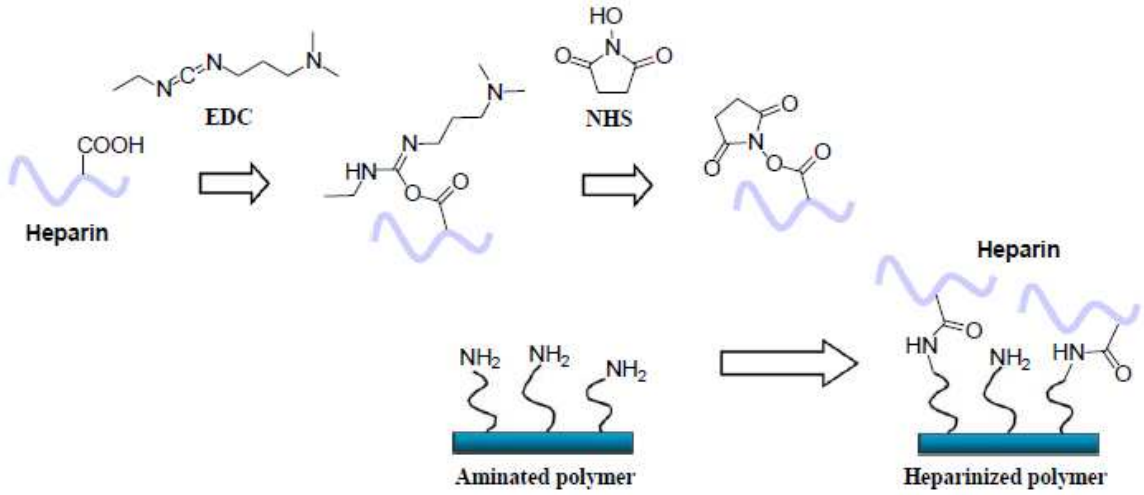

Figure I.12 – Covalent immobilization using EDC/NHS coupling. The EDC/NHS method of surface chemical functionalization is commonly used to graft peptides onto polymer surfaces [144].

Previously in our group, we have employed the EDC/NHS strategy to covalently bind peptides to polyethylene terephthalate (PET) surfaces, but in an approach opposite to the one abovementioned. In our experiments, COOH groups were activated on the PET surface, and the final step involves coupling of the polymer intermediate with the NH_2 groups on our peptides of interest [41-45, 51-54, 62, 78].

Another approach of covalent immobilization used in our group exploits silane chemistry and maleimide-mediated bonding (Figure I.13). This method, usually applied to metallic surfaces, begins with surface hydroxylation, whereby OH groups are activated. Then an amino-silane, 3-aminopropyltriethoxysilane (APTES) in this case, is covalently bound to the substrate, and the system is subjected to a reaction with a hetero-bifunctional molecule, 3-Succinimidyl-3-MaleimidoPropionate (SMP). SMP acts as a cross-linker, which allows thiol linkage to occur through the maleimide group. Thus, a cysteine-containing peptide (cysteine is the only amino acid that contains a thiol group) can be grafted, completing the immobilization process [48, 49, 55].

There are many other methods of immobilizing biomolecules on material surfaces, each with its own advantages and disadvantages. These methods include epoxide-mediated bonding, biotin-(strept)avidin systems, and click chemistry, just to name a few. For a thorough list of biomolecules immobilization methods and their descriptions, refer to the comprehensive review by Wong *et al.* [145]

The study described in this thesis uses the well-established approach of maleimide-mediated functionalization (Figure I.13) to covalently graft GRGDSPC peptides onto silicon surfaces, using 3-aminopropyldimethylethoxysilane (APDMS) in the first step and SMP as a heterolinker.

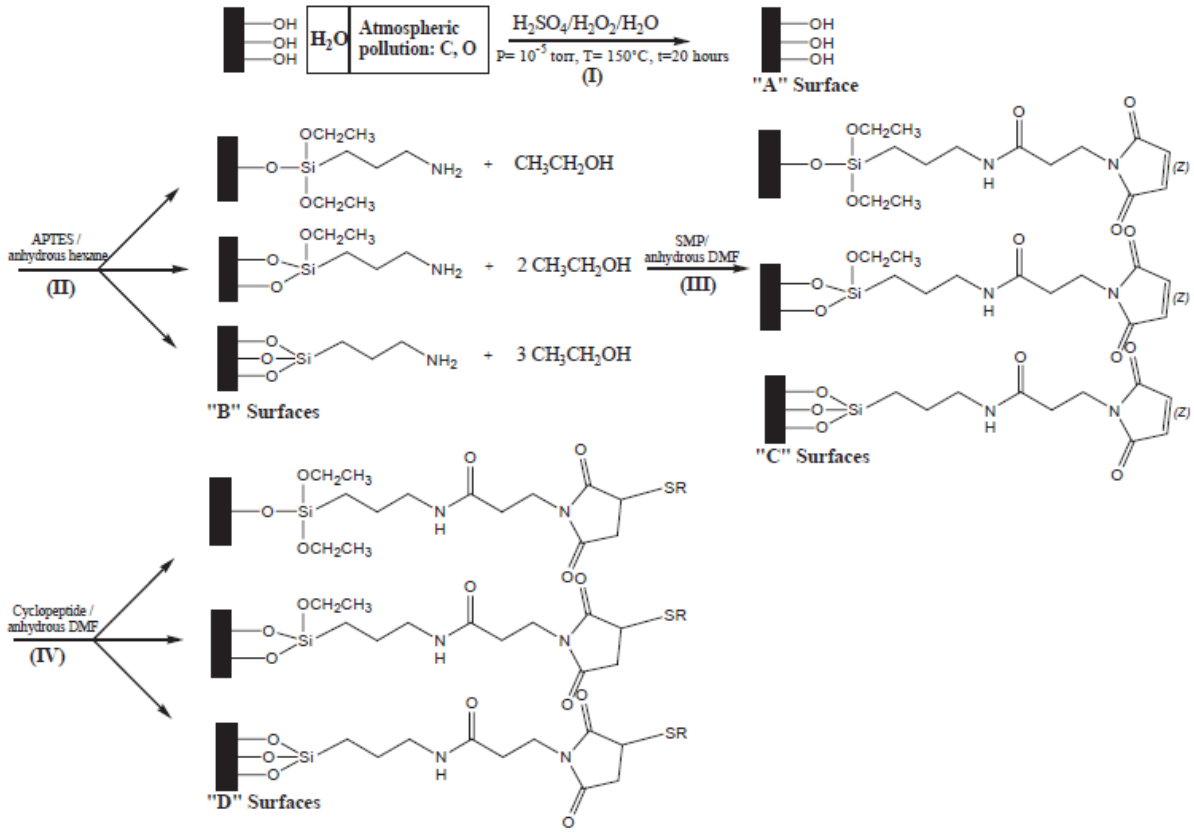

Figure I.13 – Covalent immobilization using silane chemistry. A silane molecule, in this case an amino-silane, is grafted to the substrate via the surface-exposed hydroxyl groups. The amino group then reacts with a hetero-bifunctional cross-linker, whose maleimide group allows grafting of a thiol-containing peptide [48].

5. The dynamics of cell adhesion

Cell adhesion is a critical factor that determines cell survival. The onset of cell signaling occurs upon initial cell contact with its surrounding environment, whether it is the extracellular matrix (ECM), another cell, or a substrate. In short, a cell must be able to anchor efficiently on a surface in order to proliferate and undergo normal cellular functions. There is a myriad of complex reactions that initiate at sites of cell adhesion, involving receptor activation, actin cytoskeletal reorganization, mechanosensing, and responsive signaling, that ultimately determine the outcome of cell fate. This section introduces cell mechanics by looking at a cell's responses upon first contact with its neighboring elements to establish the importance of adhesion to subsequent cell actions.

5.1 Integrins and cell adhesion complexes

Integrins are transmembrane receptors that mediate the connection between a cell and its surroundings. Structurally, they are composed of an α subunit and a β subunit, and each α/β subunit combination gives rise to an integrin with a different configuration and specificity for different binding proteins [146]. The diversity of human integrins and their binding specificities is illustrated in Table I.2 [147].

Adhesion lies at the convergence of integrin clustering, signal transduction, and actin cytoskeleton organization. Cells modify their adhesive behaviors in response to changes in the molecular composition and physical forces present in their ECM environment. Cell-ECM contacts occur through sites where cell adhesion receptors anchor a cell's cytoskeleton to the matrix [148]. When cells interact with the ECM, they recognize the characteristics of the surrounding surface through integrin-based signaling pathways. A specific way through which a cell binds to a surface is via the formation of adhesion complexes. The exact composition of a given adhesion complex will in turn regulate cellular behaviors such as adhesion, migration, proliferation, and differentiation. The stability and further maturation of these adhesion complexes, in turn, is mediated by a variety of factors, such as applied force and spatial and temporal interactions between the actin cytoskeleton and integrin-based molecules [149].

Table I.2 – Ligand-binding specificities of human integrins [147]

Integrins	Ligands
α1β1	Laminin, collagen
α2β1	Laminin, collagen, thrombospondin, E-cadherin, tenascin
α3β1	Laminin, thrombospondin, uPAR
α4β1	Thrombospondin, MAdCAM-1, VCAM-1, fibronectin, osteopontin, ADAM, ICAM-4
α5β1	Fibronectin, osteopontin, fibrillin, thrombospondin, ADAM, COMP, L1
α6β1	Laminin, thrombospondin, ADAM, Cyr61
α7β1	Laminin
α8β1	Tenascin, fibronectin, osteopontin, vitronectin, LAP-TGF-β, nephronectin
α9β1	Tenascin, VCAM-1, osteopontin, uPAR, plasmin, angiostatin, ADAM, VEGF-C, VEGF-D
α10β1	Laminin, collagen
α11β1	Collagen
αVβ1	LAP-TGF-β, fibronectin, osteopontin, L1
αLβ2	ICAM, ICAM-4
αMβ2	ICAM, iC3b, factor X, fibrinogen, ICAM-4, heparin
αXβ2	ICAM, iC3b, fibrinogen, ICAM-4, heparin, collagen
αDβ2	ICAM, VCAM-1, fibrinogen, fibronectin, vitronectin, Cyr61, plasminogen
αIIbβ3	Fibrinogen, thrombospondin, , fibronectin, vitronectin, vWF, Cyr61, ICAM-4, L1, CD40 ligand
αVβ3	Fibrinogen, vitronectin, vWF, thrombospondin, fibrillin, tenascin, PECAM-1, fibronectin, osteopontin, BSP, MFG-E8, ADAM-15, COMP, Cyr61, ICAM-4, MMP, FGF-2, uPA, uPAR, L1, angiostatin, plasmin, cardiotoxin, LAP-TGF-β, Del-1
α6β4	Laminin
αVβ5	Osteopontin, BSP, vitronectin, CCN3, LAP-TGF-β
αVβ6	LAP-TGF-β, fibronectin, osteopontin, ADAM
α4β7	MAdCAM-1, VCAM-1, fibronectin, osteopontin
αEβ7	E-cadherin
αVβ8	LAP-TGF-β

Initial cell attachment occurs upon binding to the ECM, mediated by a host of membrane proteins, including vinculin, paxillin, and talin, leading to integrin clustering [150-153]. Then, the cell body flattens and spreading occurs on the surface, resulting in

the reorganization of actin into microfilament bundles, in turn reconfiguring them into large stress fibers. This reorganization then causes integrins to cluster even more in a positive feedback manner (Figure I.14), further enhancing the adhesion strength and matrix binding between the cell and its surrounding [146]. As a result, sites of adhesion are formed at the actin-ECM interface [69].

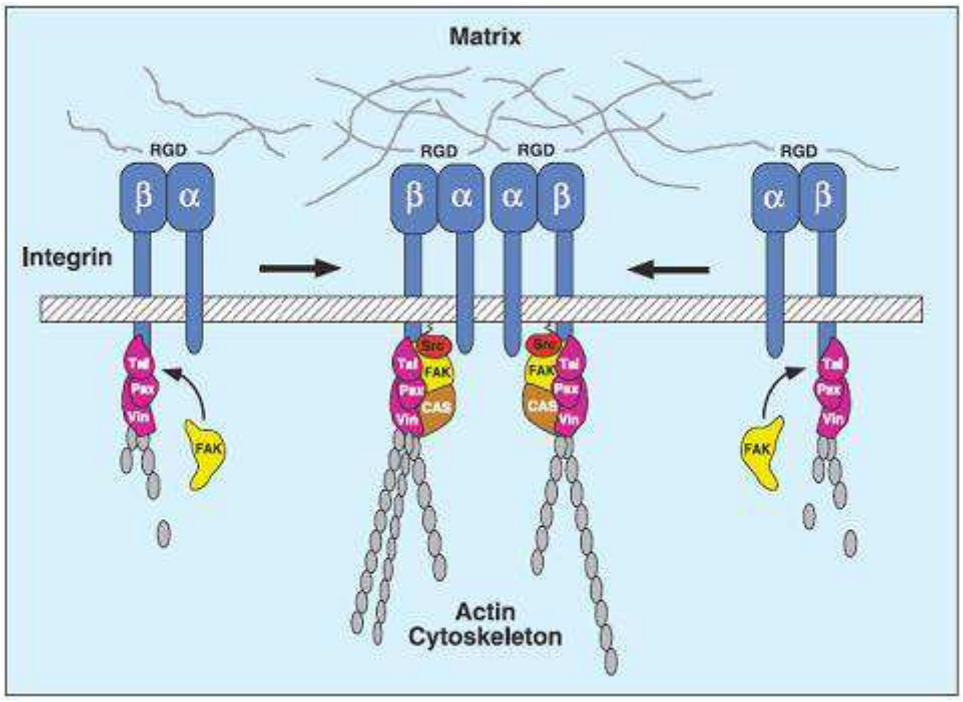

Figure I.14 – Integrin clustering and actin cytoskeleton remodeling. Matrix binding promotes the clustering of integrin ligands, which recognize the adhesion-enhancing RGD motif. Various integrin-related adhesion proteins, such as talin (Tal), paxillin (Pax), and vinculin (Vin), are recruited to the site of clustering. In turn, cytoskeleton reorganization and further clustering is promoted in a positive feedback cycle [146].

The formation of adhesion complexes occurs in several stages, evolving in terms of size, structure, composition, and stability. A summary of different types of cell-matrix adhesions is found in Table I.3 [154]. Integrin assemblies first develop into nascent focal complexes, which are small dot-like compositions that are approximately 1 μm in diameter. Focal complexes are formed under the cell lamellipodia, which are structures found at the periphery of a spreading cell in the shape of flat protrusions, containing branched networks of actin filaments [155-157]. These focal complexes are transient

and unstable, and will therefore either dissolve or develop into more mature structures. Further rearrangement of elementary nanocomplexes and reinforcement of the integrin-cytoskeleton bond will lead to the stabilization of focal complexes, resulting in their development into larger focal contacts, which future mature into focal adhesions (FAs). These FAs are typically elongated structures that are about 2 μm wide and 3-10 μm in length, comprising integrins assembled in a cluster. They essentially serve as the points of contact between the ECM and the contractile actomyosin stress fibers inside the cytoskeleton, transferring chemical signals within and between cells [158]. Another type of adhesions complex is the fibrillar adhesion. These points of adhesion are biochemically and structurally distinct from FAs and located more centrally in cells [159, 160]. Fibrillar adhesions are rich in the protein tensin and are thin, elongated structures formed in alignment with the actin stress fibers, associating with fibronectin matrix deposition [159-161]. As the formation of fibrillar adhesions is driven by an actomyosin-dependent mechanism that affects cell contractility, it is expected that the dynamics of fibrillar adhesions will have a direct impact on stem cell phenotype, which is in part regulated by intracellular tension [160].

Table I.3 – Characteristic features of cell-matrix adhesions [154]

Property/ structure	**Focal complexes**	**Focal adhesions**	**Fibrillar adhesions**
Location	Edge of lamellipodium	Cell periphery	Central region of cells
Morphology	Dot-like	Elongated, oval	Fibrillar or beaded
Size (long axis)	1 μm	2 – 5 μm	Variable: 1 – 10 μm
Typical constituents	• Paxillin • Vinculin • Tyrosine-phosphorylated proteins	• α_v integrin • Paxillin • Vinculin • α-actinin • Talin • Focal adhesion kinase • Tyrosine-phosphorylated proteins	• α_5 integrin • Tensin

5.2 Focal adhesions and cell behavior

The formation of FAs is dependent on many parameters, one of which is the spacing of the integrin ligands present on the contact surface. Arnold *et al.* have famously shown that there is a maximum spacing threshold above which FAs are unable to form [162]. Using a surface patterning technique whereby gold nanodots are functionalized with RGD at well-defined spacings, they were able to ensure that each gold nanodot, with a diameter of 8 nm, provides an anchor point that allows the binding of only one integrin. This technique allows the spacing between the nanodots to be precisely tuned, and the length-scale for integrin spacing can be accurately studied. Results showed that MC3T3 osteoblasts adhered and spread very well on surfaces with nanodot spacings of 28 nm and 58 nm, but very limited cell spreading was observed on nanodots spaced at 73 nm. These tests were repeated with other cell lines (REF52 fibroblasts, 3T3 fibroblasts, B16 melanocytes), yielding the same results, indicating that the effect of spacing is a global phenomenon that characterizes cell adhesion. As cell adhesion was efficient for integrin spacings of ≤ 58 nm but inhibited at length-scales ≥ 73 nm, Arnold *et al.* proposed that restricted integrin clustering is a factor that hinders cell adhesion. In addition, they define the range between 58 – 73 nm as the maximum integrin spacing above which cell adhesion does not occur.

The study of ordered and disordered nanopatterned surfaces functionalized with RGD ligands at various spacings, carried out by Huang *et al.*, confirmed the role of integrin clustering in the formation of FAs (Figure I.15) [124]. The authors proposed a model where a critical ligand spacing of 70 nm was defined, above which cell attachment and spreading are restricted. They divided integrins into two classes, clustering and non-clustering. It was shown that due to the polydispersity of local ligand spacings on disordered nanopatterns, integrin clusters were still able to form despite increasing global average ligand distance, whereas on ordered nanopatterns, the local ligand spacing is fixed and equal to the global ligand spacing. Cell adhesion and spreading are enhanced on disordered nanopatterns as a result of this observation, showing that integrin clustering is indeed an essential criterion for FA development.

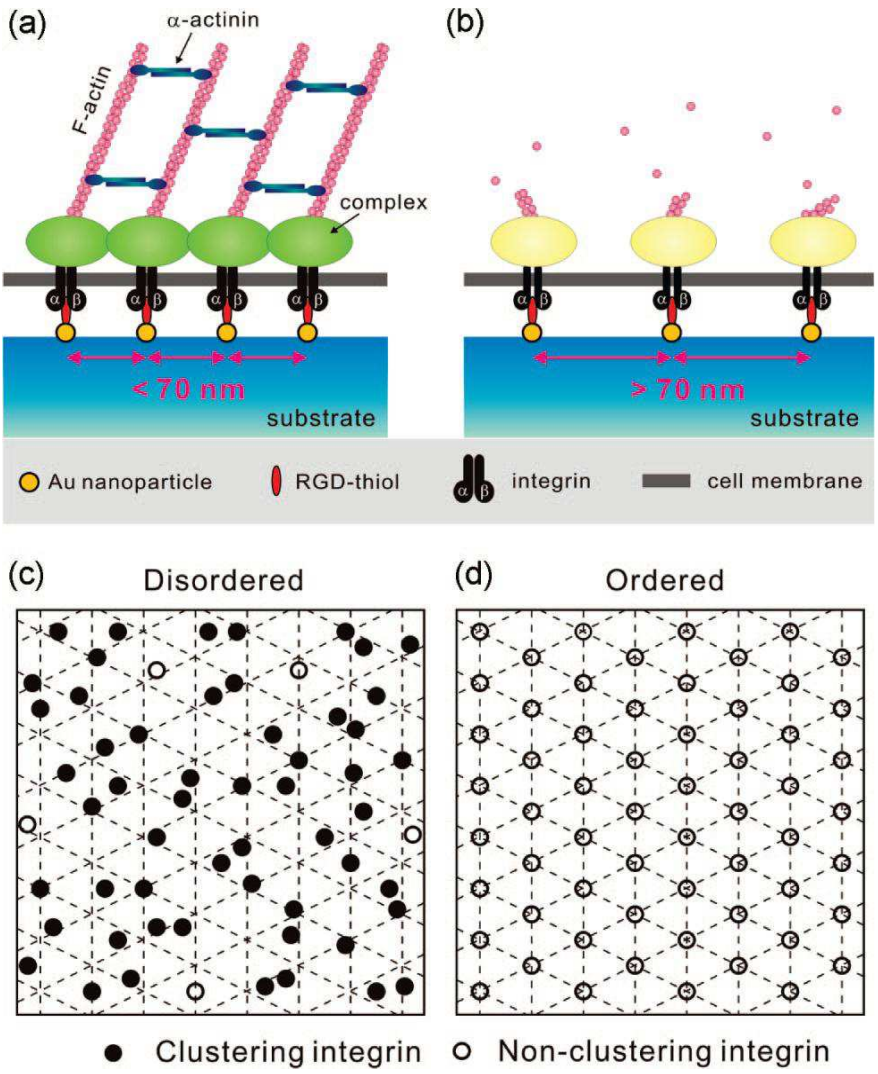

Figure I.15 – Integrin clustering and the formation of focal adhesions. A maximum critical local ligand spacing of 70 nm was defined in (a) and (b), such that above this spacing, focal adhesions fail to form and cell adhesion is restricted. (c) and (d) show two types of integrins on disordered and ordered nanopatterns. Each black circle represents a clustering integrin and each white circle represents a non-clustering integrin. On disordered nanopatterns, even if the global ligand spacing is higher than 70 nm, the local ligand spacing varies, resulting in a polydispersity which still allows a number of integrins to be spaced at less than 70 nm, allowing them to cluster. However, on ordered nanopatterns, global and local ligand spacings stay constant at higher than 70 nm, and at this ligand spacing, integrins remain non-clustered, preventing the formation of focal adhesions [124].

One distinct feature of FAs is their role as mechanosensors. When exposed to force, integrins undergo conformational rearrangements that alter their affinity for adhesion proteins and their association with the cell cytoskeleton. As well, FA and

intracellular tension are closely correlated and work together to regulate cell function. For stable FAs to form, intracellular tension must be well maintained. For example, mesenchymal stem cells (MSCs) in their native bone marrow niche generally form small adhesions. This is due to the low stiffness and elasticity of bone marrow which do not support the formation of large FAs, as the deformation of the matrix absorbs intracellular tension [163]. For osteogenesis to occur, the formation of larger FAs must take place, as osteoblasts express a more contractile phenotype with high levels of intracellular tension that must be supported [159]. This phenomenon suggests that by controlling the intracellular tension exerted by a cell and thus changing the way FAs form, MSC differentiation into specific phenotypes could be controlled and directed.

5.3 Relationship between integrin and growth factor signaling

The cooperation of growth factor signaling and integrin-mediated cell adhesion is an important part of ECM mechanotransduction [116]. Not only do growth factors like bone morphogenetic proteins (BMPs) induce osteoblastic differentiation in MSCs and matrix mineralization, they also stimulate the adhesion and migration of osteoblasts. Apparently, the close relationship between growth factor signaling and the regulation of cell adhesion can affect cell adhesion and subsequently, differentiation.

Many studies have focused on the synergy and interplay between integrins and BMPs and their communication with the ECM. A report by Xiao *et al.* states that BMP production and integrin-mediated cell-collagen interactions are both required for osteoblast differentiation of MC3T3-E1 cells [164]. On top of the BMPs' role in osteoblast-specific gene expression, this study shows that BMPs are only weak inducers of osteoblast-specific gene expression in the absence of ECM synthesis and contrarily, gene expression is enhanced by ECM signals. Moreover, the MAPK (mitogen-activated protein kinase) pathway, a transducer of integrin signals to the cell nucleus, is essential for BMP-induced osteoblast-specific gene expression. As MAPK activity is stimulated by integrins, this draws a connection between the regulations of BMP- and integrin-related signaling pathways.

Lai *et al.* demonstrated in their study an upregulation of integrin expression by BMP-2, which in turn upregulates osteoblast functions. It was shown that human

osteoblasts express various types of integrins at sites of focal adhesion, and the level of integrin expression is enhanced by BMP-2, which promoted also osteoblast adhesion on osteopontin and vitronectin. To show that integrin activity is necessary for osteoblast differentiation, integrin function was blocked in human osteoblasts and the osteoinductive effects of BMP-2 were severely reduced. Normally, BMP-2 inhibits the proliferation of human osteoblasts [165], but when integrin was blocked, this anti-proliferative effect was eliminated. Additionally, alkaline phosphatase activity, stimulated by BMP-2, was severely reduced while expression of osteocalcin, osteopontin, and bone sialoprotein was downregulated. Matrix mineralization was also hindered. Furthermore, BMP-2 receptors were found to colocalize with integrin-mediated sites of adhesion, and it was hypothesized that integrins may serve as anchors for BMP-2 receptors at FA sites where they will make contact with matrix-bound BMP-2 [166]. The ensemble of these results firmly suggests that integrins play a central role in BMP-2 function in osteoblasts.

Further revelation about the intimate relationship between cell adhesion receptor signaling and growth factor signaling has been made possible by studying the influence of BMP-2 on stem cell differentiation on matrices of different stiffnesses [53], the impact of matrix-bound BMP-2 on cell adhesion and migration [115], and the effects of integrin internalization on stem cell activity [167]. Crouzier *et al.* developed a type of biomimetic film that was tunable in terms of stiffness and bioactivity. A soft polymeric film composed of layer-by-layer assemblies of poly($_L$-lysine) and hyaluronan was designed and deposited on a supporting substrate. The stiffness of this film can be controlled by tuning the crosslinking chemistry. Additionally, BMP-2 was loaded into and trapped inside the polymeric film, rendering it “matrix-bound”. The combined effects of film stiffness and bioactivity were evaluated by culturing C2C12 myoblasts on soft and stiff films, and BMP-2 was either loaded (matrix-bound) or delivered in solution. The results revealed that matrix-bound BMP-2 was more efficient in promoting cell adhesion, spreading, and migration on soft substrate when compared with soluble BMP-2. Several hypotheses were drawn to explain these results. First, the spatial confinement of matrix-bound BMP-2 modifies the kinetics of BMP-2 receptor/ligand interactions. This confinement allows BMP-2 receptors to be in close proximity with adhesion receptors, inducing a possible interplay between the two

(Figure I.16). This phenomenon was not observed when BMP-2 was present in its soluble form as it was able to freely diffuse, limiting the availability between receptor and ligands. Moreover, since soluble growth factors are present in solution rather than constrained to the substrate surface, they are not able to interact with adhesion receptors, which are found at sites of cell-material contact. It is possible also that BMP-2 receptor signaling is concomitantly associated with integrin signaling, thus the two types of receptors may facilitate cell behavior (adhesion and differentiation) collaboratively. The limitation of BMP-2 internalization was also proposed in the case of matrix-bound BMP-2, which may lead to different signaling events compared with soluble BMP-2 [115].

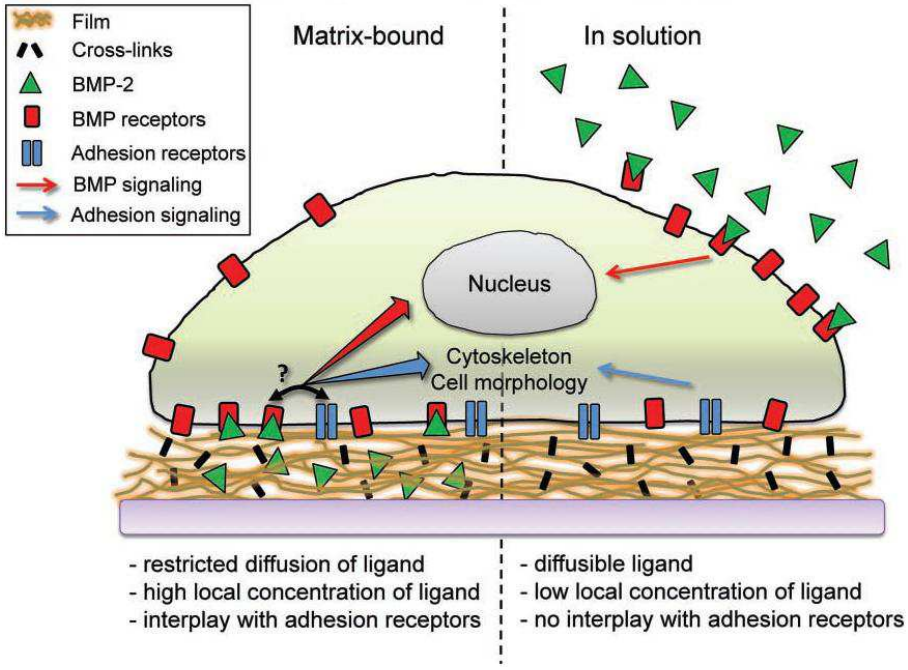

Figure I.16 – Receptor interactions in the presence of differently conformed BMP-2. When BMP-2 is matrix-bound (left), its diffusive abilities are limited due to spatial confinement within the polymeric film. As a result, cell receptors responsible for sensing BMP-2 are allowed to come in close contact with integrin receptors which, upon cell adhesion, are present on the film surface. This proximity induces interplay between the BMP-2 and integrin receptors via a pathway whose mechanism is still unknown, in turn causing cytoskeletal remodeling. When BMP-2 is present in its soluble form (right), the cooperative effects of BMP-2 and integrins are lost as diffusing BMP-2 causes BMP-2 receptors to relocalize on the cell plasma membrane and cannot come in close contact with integrin receptors [115].

6. Mesenchymal stem cells

The human mesenchymal stem cell (MSC) is a progenitor cell which has the potential of giving rise to various types of skeletal tissues, including cartilage, bone, tendon, ligament, and marrow stroma [168]. Isolated from the bone marrow, MSCs have been widely used in tissue engineering as they have shown promise in the regeneration of damaged tissues due to their multipotent capacities. To make efficient use of MSCs as a therapeutic tool, a general understanding of stem cell characteristics and dynamics must be grasped. This section addresses main concepts in stem cell biology, including the stem cell niche, self-renewal, and cell differentiation.

6.1 The stem cell niche

The defined microenvironments in which stem cells dwell are called niches. Different types of stem cells dwell in different natural habitats where they undergo growth and transition (Table I.4) [169-171].

Table I.4 – Types of human stem cells [170]

Stem cell	Location (source)	Cells produced	Refs
Hematopoietic	Bone marrow	Blood, endothelial, hepatic (oval), muscle cells	[172, 173]
Neural	Brain	Neurons, astrocytes, oligodendrocytes, blood cells	[174, 175]
Epithelial	Gut, epidermis	All cells in epithelium crypts; all cells in epidermal layers	[176, 177]
Mesenchymal	Bone marrow	Bone, cartilage, tendon, adipose, muscle, marrow stroma, neural cells	[5, 6]
Embryonic	Blastocyst inner cell; mass primordial germ cells	All cells	[178-180]

Within the bone marrow, both hematopoietic stem cells (HSCs) and mesenchymal stem cells (MSCs) exist in a reciprocal relationship [181]. HSCs are

responsible for the development of all types of blood cells (including macrophages, neutrophils, and platelets) while MSCs give rise to osteocytes, chondrocytes, adipocytes, and myocytes, among other cell types.

Various niche factors play a role in determining stem cell gene expression and ultimately directing their proliferation and differentiation. Within the niche, elements that affect the regulation of stem cell characteristics include interactions between stem cells and objects such as other stem cells, differentiated cells, and extracellular matrix (ECM) components (adhesion molecules, growth factors, cytokines). The ensemble of elements maintains the stem cells in their undifferentiated state while external signals eventually enter the niche to activate the cells' differentiation potential (Figure I.17) [182-184]. The physical-chemical nature of the stem cell niche also contains decisive factors for directing stem cell activity, such as metabolite concentration and pH [185].

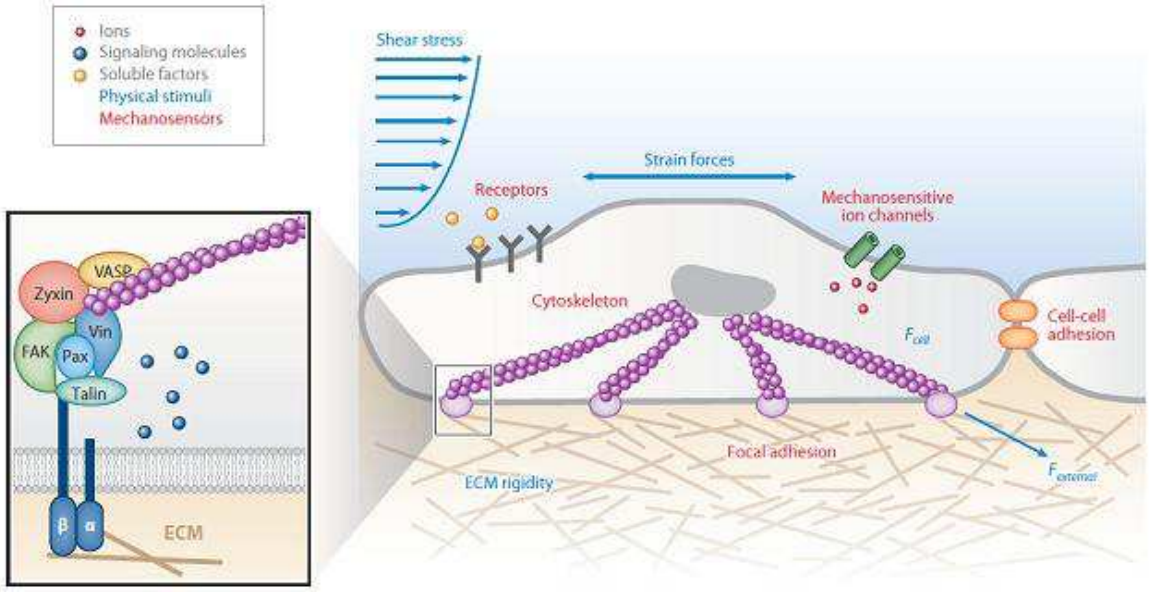

Figure I.17 – Biophysical signals in the stem cell niche. The extracellular environment surrounding the stem cell niche is composed of a complex hydrated protein and proteoglycan-based gel network which elicits biophysical cues such as matrix rigidity, topography, flow shear stress, and strain forces. Stem cells sense these stimuli through ion channels, focal adhesions, and cell surface receptors, among other sensing media, which all act as mechanosensors [184].

6.2 Self-renewal

Self-renewal is the process through which stem cells proliferate and divide while retaining their undifferentiated stem state. At the same time, adult stem cells are able to differentiate into various lineages. For example, MSCs give rise to chondrocytes, osteoblasts, fibroblasts, adipocytes, endothelium, and myocytes [181]. Due to the unique ability of adult stem cells to both self-renew and differentiate, a well-balanced tissue homeostasis must be maintained in order to regulate these two processes. If self-renewal overwhelmed differentiation, an unnecessarily large stem cell population may be present, but if differentiation is uncontrolled, the stem cell population will exhaust quickly.

Of course, the stem cell niche plays an important role in keeping the balance between self-renewal and differentiation through several mechanisms. Stem cells divide through a process known as asymmetric division [181]. The two established asymmetrical models of stem cell division are known as invariant asymmetry and populational asymmetry [186], as depicted in Figure I.18. In invariant asymmetric cell division, an adult stem cell gives rise to two daughter cells, one of which stays a stem cell while the other undergoes differentiation. This route of stem cell division is most prevalent in unicellular organisms and invertebrates. Mammalian stem cells, on the other hand, generally follow the route of populational asymmetric division, which is highly regulated. In this mechanism, each adult stem cell divides to give rise to daughter cells that each has a finite probability of staying as a stem cell or becoming a committed progenitor that will undergo differentiation. Statistically, one stem cell results in one stem daughter and one committed progenitor. However, it is also possible for both daughter cells to be stem or committed progenitors. The fate of the daughter cells is dependent on a variety of extrinsic cues that are exposed in the ECM. Thus, a complex combination of niche factors works together to dictate the outcome of each cell division, thereby upholding a precise balance between stem cell self-renewal and differentiation [186].

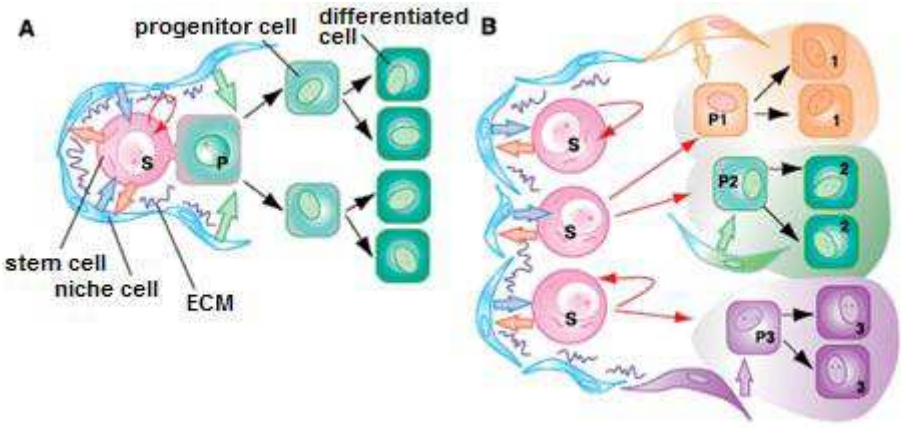

Figure I.18 – Cell division by invariant and populational asymmetry. S denotes stem cell and P denotes progenitor cell. (A) In invariant asymmetric cell division, a mother cell gives rise to two daughter cells, one of which stays stem (curved arrow) while the other becomes a progenitor cell that goes on to become a fully differentiated cell. (B) In populational asymmetric cell division, each daughter cell has a finite probability of staying as a stem cell or becoming a progenitor cell. Depending on various environmental factors, the daughter cells can go down different routes and become different types of progenitor cells (P1, P2, P3) and ultimate become fully differentiated cells. Some unicellular organisms and invertebrates tend to undergo invariant asymmetric cell division while most mammalian self-renewing tissues go through populational asymmetric cell division [186].

6.3 MSC differentiation

MSCs are a unique type of stem cells derived from the bone marrow capable of differentiating into distinctive end-stage cell types (Figure I.19) [187, 188]. These cells include but are not limited to osteoblasts (bone), chondrocytes (cartilage), adipocytes (fat), myoblasts (muscle), and fibroblasts (tendon). The differentiation process follows a strict route whereby the MSC first undergoes a highly proliferative stage, then enters commitment and gradually becomes a differentiated cell type through lineage progression.

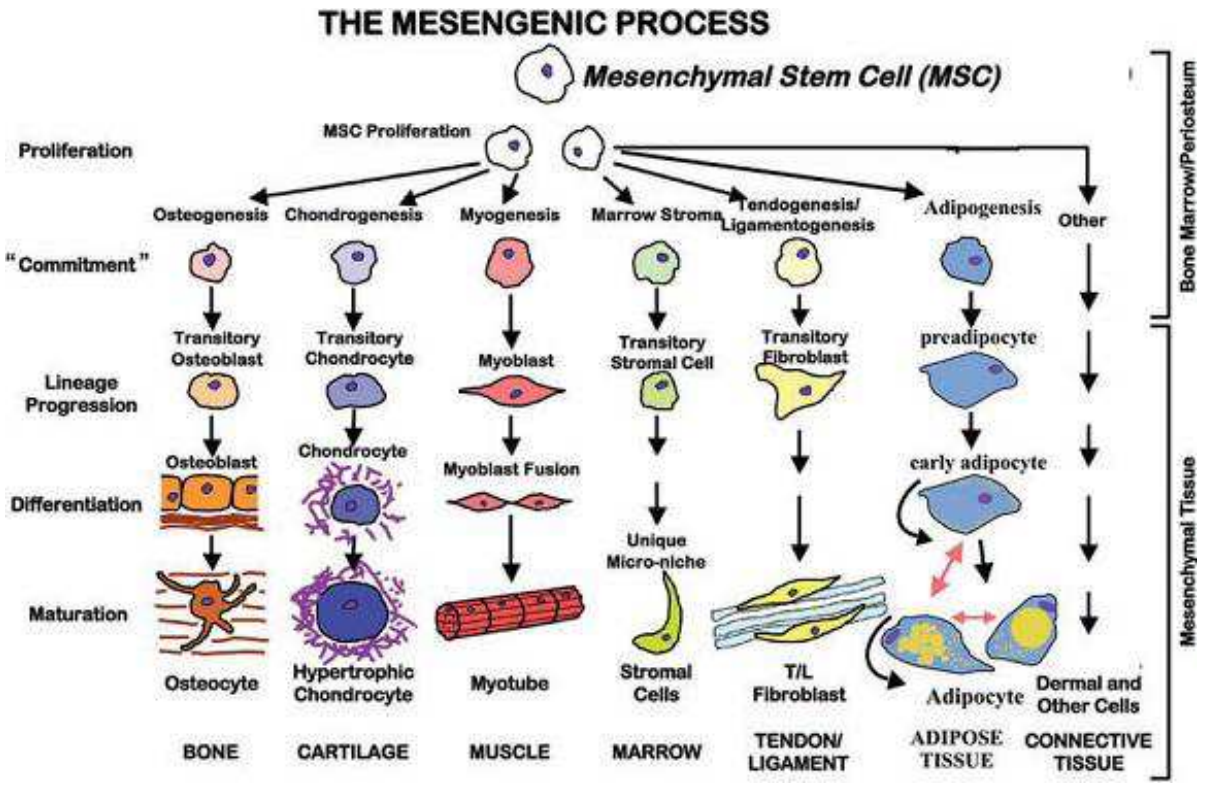

Figure I.19 – The MSC differentiation process. MSCs are able to differentiate into many different types of mature, end-stage cells. Throughout the differentiation process, MSCs are capable of producing cells with distinct phenotypes at intermediate stages [188].

As mentioned in Chapter I.2.2, chemical signals are directly implicated in the differentiation of stem cells. The differentiation of MSCs into a particular lineage can be stimulated by the presence of growth factors and specific chemicals that activate the differentiation pathway. It has been well established that the combination of dexamethasone, ascorbic acid, and β-glycerophosphate will induce MSC differentiation into osteoblasts. In the case of adipocytes, the combination of dexamethasone, insulin, 1-methyl-3-isobutylxanthine, and indomethacin is used. A comprehensive list of potential MSC lineage-specific differentiations and their chemical stimuli can be found in a review by Minguell *et al.* [170]

The phenotype of terminally differentiated cells can be distinguished by their morphology and chemical properties. The shape of cells and their specific interaction with their surroundings may provide clues that define their identity. For instance, mature cells with high tension morphologies, such as osteoblasts, will present a distinct appearance characterized by a well-spread cytoplasm, highly organized actin stress

fibers, and stable, mature focal adhesions to support intracellular tension. In contrast, low tension morphologies are present in adipocytes which tend to take on a rounded shape with sparse, undeveloped focal complexes. The detection of molecular and cellular markers at various stages of MSC differentiation will also characterize the lineage development of the cell. The expression of specific transcription factors and extracellular matrix proteins identifies the mature cell, and a detailed summary of these chemical markers can be found in the review by Minguell *et al.* [170]

Because of their strong differentiation potential, we use human MSCs in our work to study the effects of chemical cues present on a material surface on lineage-specific differentiation. Herein, we do not involve soluble factors in culture environments, but we introduce a spatially distributed bioactivity on our substrate surfaces. We aim to explore whether the differentiation of MSCs can be influenced solely by the presence of these surface cues, and we also aim to establish a link between the dynamics and mechanisms of cell adhesion and differentiation.

7. Surface patterning

In addition to modifying surfaces with biomolecules, the spatial organization and distribution of surface motifs also affect the way in which cells interact with a material. As *in vivo* cellular interactions occur on the nanoscale, surface patterning has gained interest and attention in recent years for tissue engineering applications due to its unique potential of mimicking micro and nanoenvironments in which cells and tissues thrive. Many well-developed microfabrication techniques that are commonly used in the microelectronics industry have, within the past few decades, gained attention in the biomedical field and are gradually being introduced as tools for biomaterial fabrication and tissue engineering. This subsection briefly describes some of these approaches.

7.1 Soft lithography

Soft lithography is a set of microfabrication techniques that uses elastomeric stamps as a pattern transfer template [189, 190]. Some soft lithographic techniques commonly used for the patterning of proteins and cells include microcontact printing and microfluidic channel patterning. The process of stamp fabrication using replica molding and its application for microcontact printing is outlined in Figure I.20 [189]. Briefly, a patterned "master" with features at defined dimensions is created by photolithography, with photoresist remaining on the substrate. Polydimethylsiloxane (PDMS) is casted onto the master and allowed to cure before being peeled off the master, resulting in a PDMS stamp. The stamp can then be used in microcontact printing to pattern proteins and cells, often in combination with the self-assembly process. In Figure I.20b, a PDMS stamp is dipped into a solution of alkanethiol and applied onto a metal surface, generally gold or silver, to allow a pattern of the alkanethiol to undergo self-assembly with the substrate. The non-patterned areas of the substrate can subsequently be functionalized with a different alkanethiol.

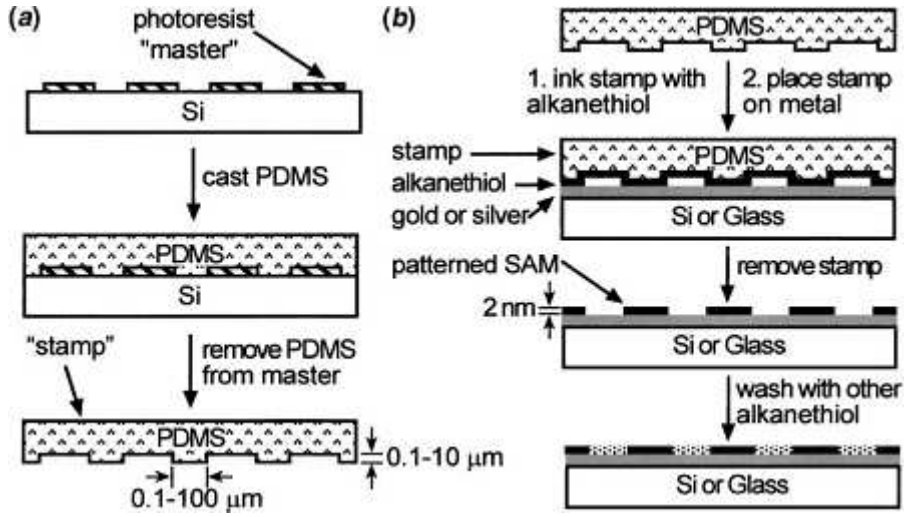

Figure I.20 – Stamp fabrication in soft lithography and microcontact printing application. (a) A photoresist master is patterned by photolithography, and PDMS is casted around the pattern on the substrate. After curing, the PDMS is removed and can act as a mold for printing. (b) A PDMS stamp is dipped into a solution containing alkanethiol and placed in contact with gold or silver on the substrate surface. The alkanethiol that has adsorbed to the stamp is allowed to react, resulting in a patterned self-assembled monolayer. The non-patterned areas can later be filled with a different alkanethiol [189].

Microcontact printing is often used to pattern adhesive proteins on substrates. To effectively take advantage of this ability, Tan *et al.* looked at the properties of the various parts of the microcontact printing system and examined their roles on protein adsorption, concluding that the wettability of the stamp and the substrate are crucial parameters that determine the success of protein patterning [191]. Chen *et al.* made extensively use of this technique in the fabrication of fibronectin-coated nanoislands for the assessment of cell survival, cell shape and function, and focal adhesion (FA) assembly in relations to surface microstructures [80, 81, 192]. The flexibility of microcontact printing has also been demonstrated by Kilian *et al.* who deposited fibronectin patches in a variety of shapes, including rectangles and stars with different aspect ratios and curvatures [83].

Instead of using the PDMS stamp to directly print a pattern onto a substrate, it can be used as a device to restrict fluid flow to certain regions of a substrate. The procedure, developed by Kim *et al.*, is known as "micromolding in capillaries", or MIMIC, and is used to create polymeric patterns on the micrometric scale (Figure I.21) [193].

Using a PDMS stamp and putting it in close contact with the substrate, microchannels are formed on the surface. A low viscosity polymer precursor is allowed to come into contact with the stamp, and through capillary action, the precursor fills the microchannels. The polymer is then cured and the PDMS stamp, which can be reused, is removed from the system, resulting in freestanding polymer microfeatures to be structured on the surface.

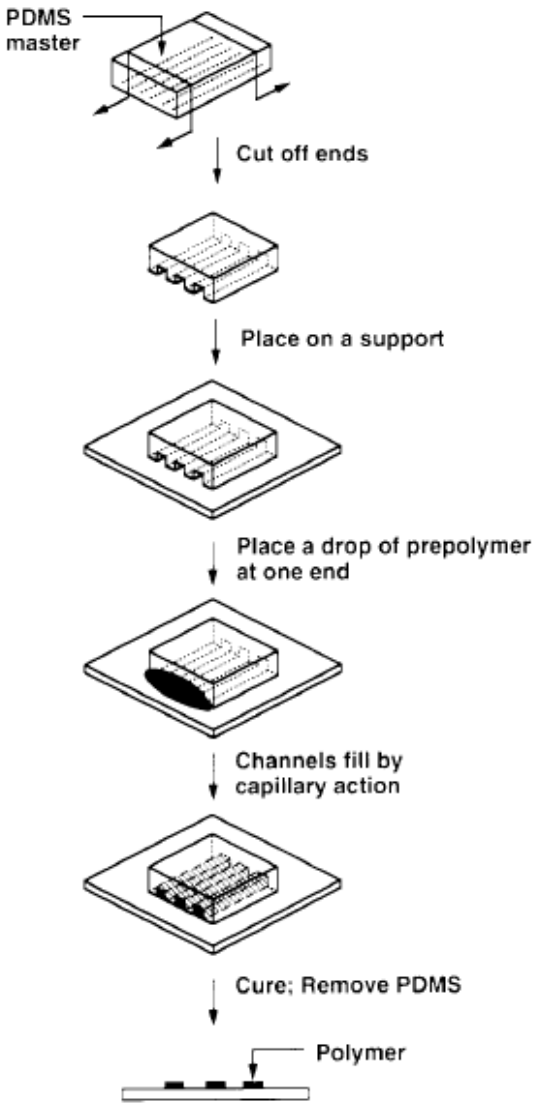

Figure I.21 – The "micromolding in capillaries" process. A PDMS stamp is placed in contact with a substrate, effectively creating microchannels in which a polymer precursor can move by capillary action. The polymer is then cured, and removal of the PDMS stamp results in surface polymeric structures in the shape of the microchannels [193].

Since the development of microfluidic channel patterning, the technique has evolved and been extended to biological applications. Using microfluidic networks, Delamarche *et al.* successfully generated patterns of immunoglobulins to gold, glass, and polystyrene substrates. In this report, due to the highly localized interaction between the protein and the substrate surface, only microliters of reagents were required to cover millimeter-sized areas. In addition, the proteins remained confined to the micropatterned areas and were viable for use in assays [194]. Cell patterning can also be achieved with the same approach, as shown by Chiu *et al.* in a study of three-dimensional microfluidic systems. Two types of cells, human bladder cancer cells and bovine adrenal capillary endothelial cells, were patterned in concentric squares on the same substrate using a 3D PDMS stamp, as depicted in Figure I.22 [195].

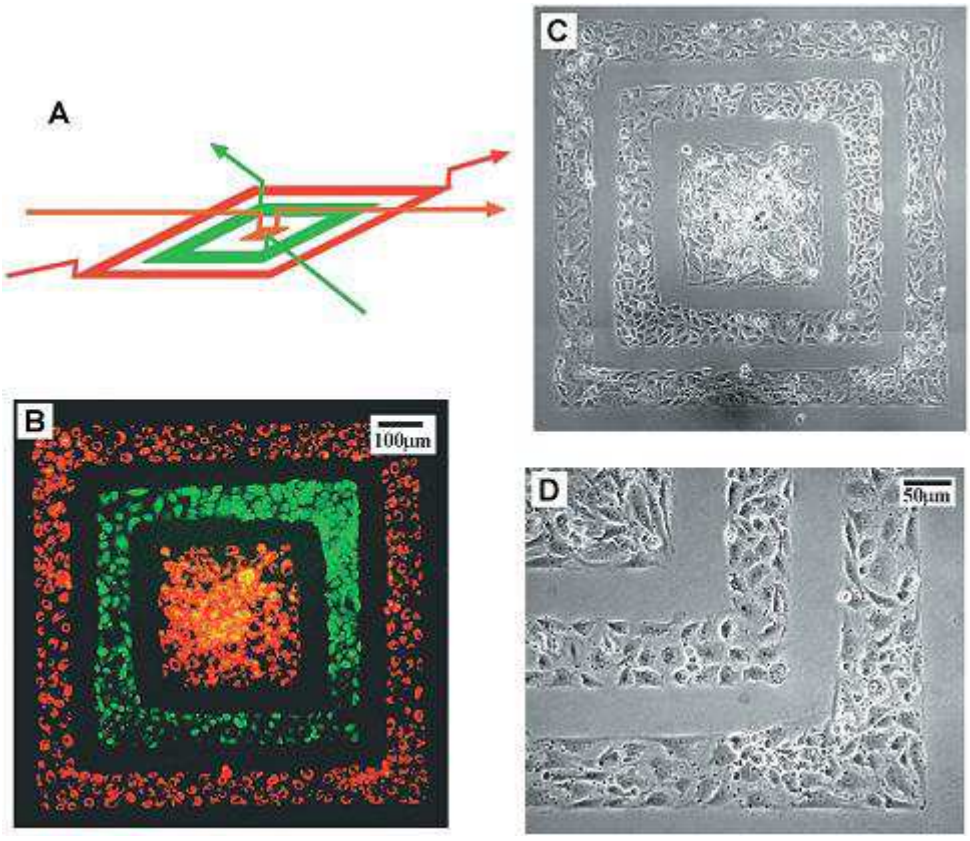

Figure I.22 – Patterning cells using a 3D microfluidic system. The 3D system in (A) allows different cell types to be concentrically patterned on the substrate, with human bladder cancer cells in green and bovine adrenal capillary endothelial cells in red (B). (C) and (D) are phase contrast images of the patterned cells [195].

Similarly using microfluidic patterning, microchannels were fabricated in a 3D fibrin hydrogel for the co-culture of endothelial cells and mesenchymal stem cells (MSCs). The vasculogenic potentials of MSCs derived from different sources were evaluated through the formation of capillary-like vascular structures [196]. These studies demonstrate that 3D microfluidic systems tailored for cell culture allow the assessment of interactions between different cell types with a topographical relationship, which will enable the further investigation of tissue architecture and its functional significance.

7.2 Photolithography

Photolithography is a common microfabrication method that is primarily used in the microelectronics industry for applications such as semiconductors or integrated circuits. The principle of photolithography involves the use of a mask as a template for pattern transfer, and is illustrated in Figure I.23 [197]. A light-sensitive photoresist is first deposited onto the substrate surface, generally by spin coating. A mask with pre-defined patterns is then placed over the resist-covered substrate, and UV light is allowed to penetrate through the exposed regions of the mask. The substrate is then immersed in a developer solution, where the outcome depends on whether positive or negative photoresist is used. In both cases, exposure to light changes the chemical structure of the resist. If positive photoresist is used, the light renders the resist soluble to the developer solution, and thus the regions exposed by the mask dissolve and are washed away. Contrarily, negative photoresist becomes polymerized and reinforced by light, and exposure makes it difficult to dissolve. As a result, only the parts that were initially covered by the mask would be washed away. In any case, the process results in a pattern transfer where specific regions of bare substrate are exposed for processing. In conventional microfabrication for semiconductors, this may involve a further etching step, but in bioengineering, the surface is subjected to surface modification with biomolecules. The final step is residual photoresist removal, which takes place after the functionalization steps and involves washing with an organic solvent.

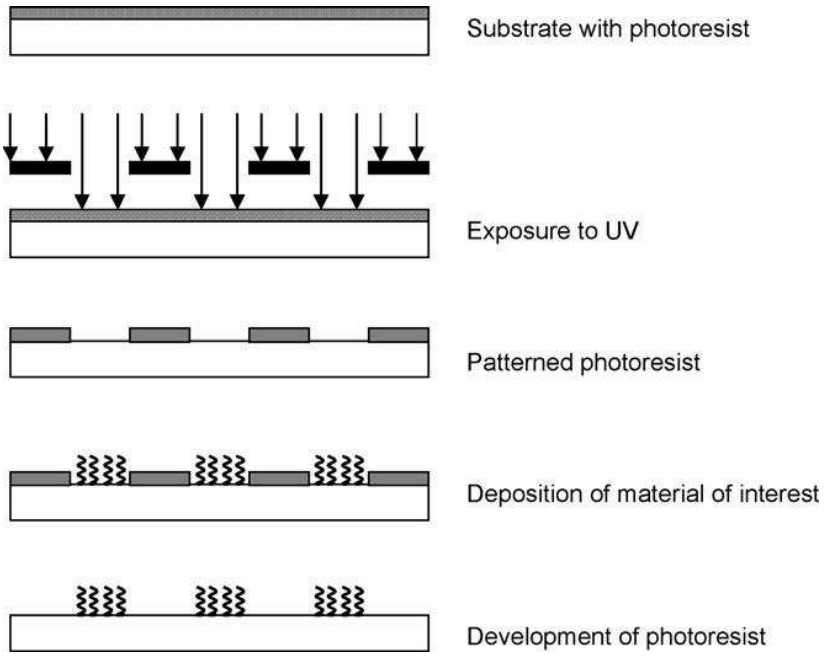

Figure I.23 – Overview of the photolithography process with a positive photoresist. A substrate is coated with a photo-sensitive resist and subjected to light under a patterned mask. The patterned regions are developed to expose the underlying substrate to surface treatment, which may involve biofunctionalization. The final step is the removal of the residual photoresist, usually by an organic solvent [197].

As photolithography is a well-developed microfabrication technique, it has gained popularity in biomedical applications such as protein or cell patterning. One study used photolithography to pattern microscale structures that were mineralized with calcium phosphate to examine effects on cell adhesion and bone regeneration [198]. Similarly, Yan *et al.* prepared micropatterned RGD surfaces on glass, using photolithography, to study the adhesive behavior of various cell lines [199]. Aside from altering surface chemistry, photolithography allows the physical modification of surfaces, as demonstrated by Chen *et al.* who fabricated structures with nanoroughness on glass using a combination of photolithography and reactive ion etching to study the adhesion, spreading, and self-renewal of embryonic stem cells [200].

In previous works done in our group, photolithography has been applied to prepare micropatterns that were used to study cell adhesion and vascularization. By culturing MC3T3-E1 osteoblast-like cells on RGD-grafted micropatterns on polyethylene terephthalate prepared by photolithography, it was demonstrated that cells selectively

aligned only to the RGD lines [78]. In a later study, stripes of angiogenic SVVYGLR peptides were patterned on PET with varying widths. Growth of endothelial cells on these micropatterned substrates induced the formation of vascular networks (Figure I.24), as mimicked by the shape and morphology of the peptide stripes [43-45].

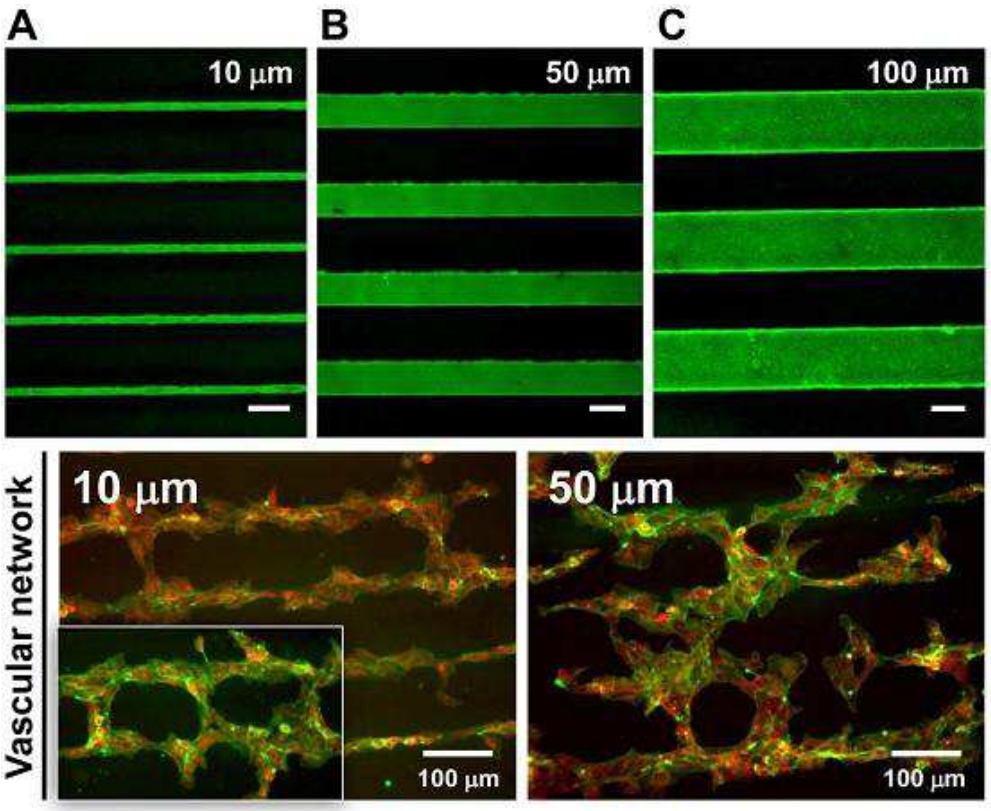

Figure I.24 – Vascular network formation on micropatterned SVVYGLR peptides. (A) to (C) – Fluorescent SVVYGLR peptides grafted on lines of various widths micropatterned by photolithography, scale bar = 50 μm. Endothelial cells were cultured on SVVYGLR peptide stripes 10 μm and 50 μm in diameter, and tube formation mimicking vascular networks was observed. Cells were immunofluoresecently stained with phalloidin (actin cytoskeleton), vinculin, and nuclei in green, red, and blue, respectively [44].

Though a widely used technique, photolithography does have its drawbacks. Due to the diffraction limits of light, photolithography is restricted to a certain resolution, generally close to the wavelength of light, and it is difficult to produce patterns with dimensions exceeding the lower resolution limits using this technique [201]. Additionally, photolithography is unsuitable for patterning on non-planar surfaces. The exposure of the substrate to toxic chemicals during the photolithography process may

also be an issue when patterning biomolecules, which may introduce problems for certain applications requiring specific biological functionalization [190, 202].

7.3 E-beam lithography

To overcome the resolution limit posed by the diffraction of light, electron beam lithography (EBL) has been developed to reach the nanometer scale not achievable by photolithography. The principle of EBL is similar to that of photolithography, except the resist is exposed to a beam of electrons instead of light, and instead of using a mask, the pattern is transferred by direct-writing in EBL (Figure I.25). The ability of direct-writing makes EBL a flexible tool as patterns of arbitrary shapes and sizes can be fabricated. The resist used in EBL is electron-sensitive and is either positive or negative, but negative resists tend to yield a lower resolution [203]. A significant advantage of EBL over photolithography is its resolution, which is dependent on electron scattering on the resist and substrate and can reach 3-5 nm, allowing the nanoregime to be reached [204]. The drawbacks of this patterning method are its high cost, the time-consuming process, and the small available area for patterning [203, 205].

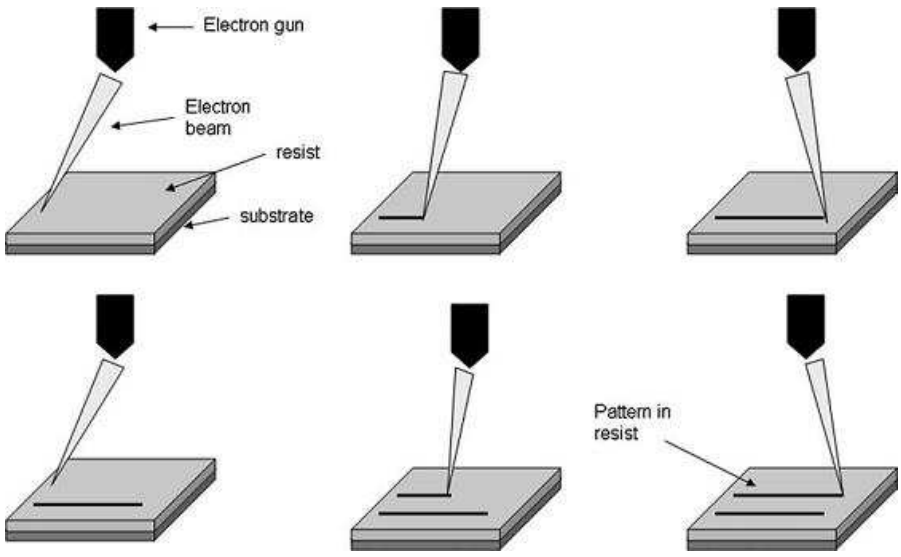

Figure I.25 – General schematic of the electron beam lithography process. An electron-sensitive resist is deposited on the material surface, and a beam of electron traverses the resist to create the desired pattern. The substrate is subsequently subjected to a development process to remove the electron-patterned regions of the resist [203].

EBL is widely applicable in tissue engineering, as shown by the works of many research groups that take advantage of its resolution to study cell-material interaction on the nanoscale. In combination with micellar lithography, Arnold *et al.* used EBL to fabricate surface structures spaced at 58 nm and functionalized with RGD peptides at varying densities to study FA formation in embryonic rat cells [206]. Dalby *et al.* reported, in several studies, the effects of EBL-fabricated nanotopography on cell behavior, demonstrating that nanostructures with different spatial organization and symmetry can be produced to direct cell fate (Figure I.26) [123, 207]. Kulangara *et al.* prepared nanogratings on polydimethylsiloxane (PDMS) with EBL to study MSC FA remodeling, further establishing nanotopography as a modulator of cell function [208].

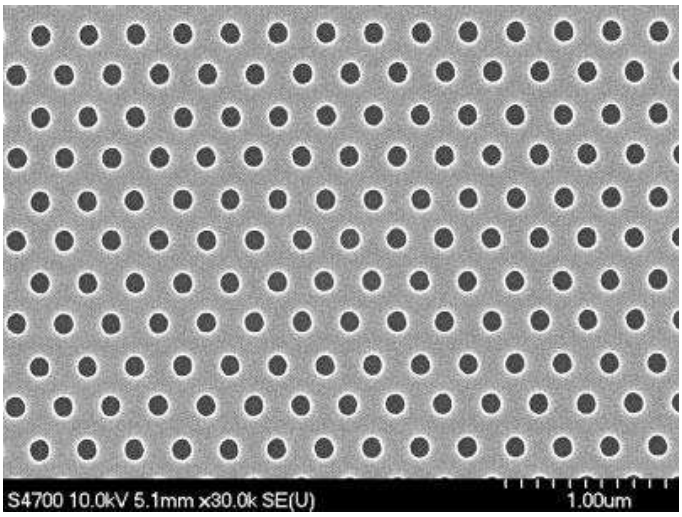

Figure I.26 – Hexagonal arrays of nanopits produced by electron beam lithography, with 120 nm diameter, 100 nm depth, and 300 nm center-to-center spacing [207].

7.4 Nanoimprint lithography

Nanoimprint lithography (NIL) was first developed by Stephen Y. Chou in 1996 as a high-throughput, low-cost technique of fabricating surface patterns with feature sizes down to the 25 nm regime [209]. As its name implies, the NIL method is based on compression molding and pattern transfer. A simple yet representative schematic of the NIL process is shown in Figure I.27. Briefly, a polymer resist, preferably a thermoplastic,

is first deposited onto the substrate surface. A solid mold with pre-defined nanometer-scale features is then pressed onto the resist as the system is heated to above the polymer's glass transition temperature. At this state, the polymer behaves as a liquid and can therefore conform to the shape of the mold. After the mold is removed following the imprint process, a reactive ion etching (RIE) step is performed to remove the resist remaining on the patterned regions, exposing the underlying substrate and completing the pattern transfer process [209].

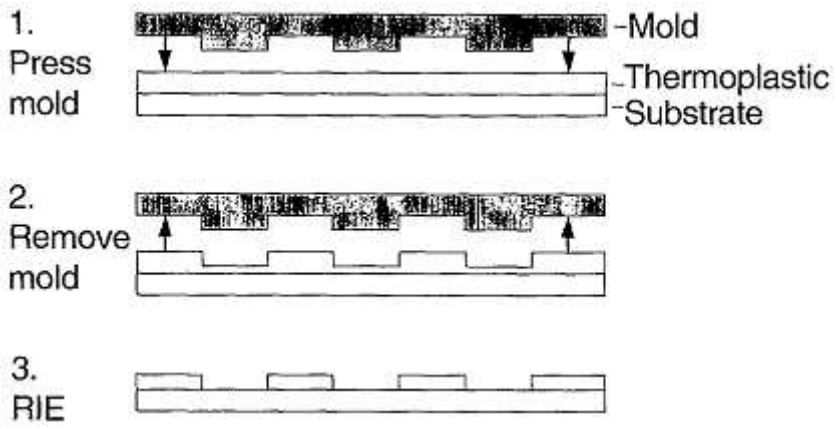

Figure I.27 – Thermo-based nanoimprint lithography process, as described by Chou *et al.* A thermoplastic resist is spin-coated on the substrate to act as a mask, and a mold is pressed onto the mask to transfer the pattern. The mold is then removed, and a reactive-ion-etching (RIE) step is added to remove residual resist to expose bare substrate in the patterned regions [209].

In the development of NIL, Chou *et al.* demonstrated the feasibility of the technique using silicon as a substrate, silicon dioxide molds, and polymethylmethacrylate (PMMA) as a model polymer. Holes of 25 nm in diameter with a period of 120 nm were imprinted on PMMA resist, as well as trenches 100 nm wide with a period of 250 nm [209].

Aside from thermo-based NIL, other variations of NIL exist. Among these are UV-assisted NIL and step-and-flash imprint lithography (SFIL), which both use UV light instead of heat in the system. In UV-based NIL, the resist is a low viscosity UV-curable precursor material. Photo-initiators are added so that the resist can be polymerized and hardened when exposed to UV light, conforming to the shape of the mold. In such case, a transparent material, such as quartz, is used to create the mold as UV light must be

allowed to penetrate through the mold to interact with the resist [210, 211]. An advantage of UV-based NIL over thermo-based systems is that it can be performed in room temperature. As a result, it avoids repeated heating and cooling cycles imposed by the thermo process, which can decrease throughput and cause improper overlay of device layers and features in multi-layer fabrication [211].

Because NIL functions by direct mechanical deformation of the resist material, it can overcome the limits of resolution posed by light diffraction and beam scattering in photolithography and electron beam lithography, respectively. However, to successfully construct reliable surface nanostructures, one must carefully consider the variable criteria in NIL. These criteria include material selection for the imprinting mold, surface properties of the mold and substrate, and the characteristics of the polymer resist [212]. As the technique allows sub-50-nm resolution to be achieved, NIL has become increasingly popular in the microelectronics industry, particularly in the manufacturing of semiconductors, magnetic nanodevices, and optoelectronic systems [213-215]. Recently, NIL has gained interest as a surface patterning tool for biological studies. In a 2004 report by Falconnet *et al.*, protein patterns with nanoscale resolution (Figure I.28) were produced by combining NIL and molecular assembly patterning by lift-off (MAPL) [216]. In terms of cell studies, Engel *et al.* utilized NIL as a method of physically modifying PMMA with microstructured surface features, which were then used to study stem cell morphology, proliferation, and differentiation [217]. Franco *et al.* created gratings of varying widths and depths on cyclic olefin copolymer foils using NIL to evaluate endothelial cell spreading and integrin signaling [218]. These studies show the potential of NIL as a unique tool whose application can be extended into tissue engineering.

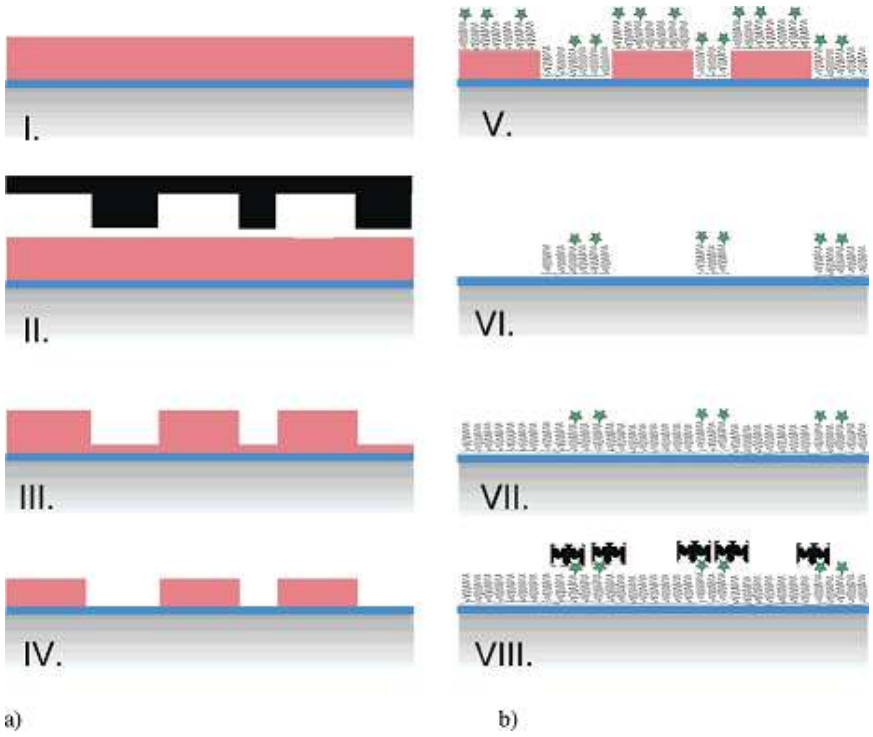

Figure I.28 – Protein patterning using NIL and MAPL. Nanoimprint lithography is used to create prepatterned samples (I-IV) and functionalized with PEG-biotin (V). The residual PMMA mask is washed off, leaving PEG-biotin in the patterned areas (VI). A non-fouling PEG is used to fill the background (VII) and finally, streptavidin specifically binds to the biotin-functionalized areas of the substrate (VIII) [216].

7.5 Other patterning techniques

Many other types of surface preparation techniques, whether or not based on lithographic principles, have been used to pattern and functionalize materials for cells studies. Among these are anodization [125, 126, 219], micelle nanolithography [124], colloidal lithography [220], dip pen lithography [221], nanostencil lithography [222], block copolymer self-assembly [223, 224], and robotic deposition [225]. In short, the selection of an appropriate patterning method for any particular application depends not only on technicality, but as well material compatibility, reproducibility, throughput, and overall efficiency contributed to the system.

II. Problems and Objectives

While tissue engineering has emerged as a promising tool for therapeutic usage, scientists and engineers still face a host of problems associated with its application, especially with regards to the integration of biomaterials into a clinical system. The successful integration of a biomaterial involves precisely tuned interactions between the material surface and its surrounding environments, especially the cells with which they come in contact. At present, we are at a very elementary stage in understanding the phenomena that occur at the cell-biomaterial interface, and fundamental research involves finding out how cell fate can be precisely controlled using biomaterials. The interest lies in understanding these phenomena more thoroughly in order to utilize available tools to advance in tissue engineering applications.

Current research focuses on surface modification techniques that aim towards controlling and manipulating stem cell behavior in terms of adhesion, migration, and differentiation. The goal is to direct stem cell fate into a preferred phenotype for clinical applications, for example neurons for nerve regeneration, and osteoblasts for bone scaffolding [20, 226]. Biomaterials have been modified with biomolecules to increase surface bioactivity and induce upregulated interaction with cells [69]. The effects of physical surface properties, such as roughness, elasticity, and topography on cell behavior have also been studied [87, 119, 123]. Nevertheless, the effects of nanostructuration and nanodistribution of bioactive molecules, such as peptides and growth factors, on stem cell behavior and fate are largely unknown, and remain a topic of interest that involves in-depth design of experiments, both with regards to the materials and biological aspects.

The study detailed in this thesis aims to understand the interaction between human mesenchymal stem cells (hMSCs) and nanostructured bioactive material surfaces. Specifically, we want to study the effects of nanoscaled distributions of peptides on hMSC adhesion and differentiation, and ultimately draw a correlation between the two. Does a nanopatterned peptide surface change the way stem cells attach to a material through spreading and maturation of their focal adhesions (FAs)? If so, in what way and through which mechanisms do the interactions occur? Does the way stem cells adhere to their surrounding environment eventually relate to their commitment and differentiation into a specific lineage? These are the questions that we aim to answer through our study. We hypothesize that since cells naturally interact with

their surrounding environments through nanoscale components, a biomaterial surface that mimics such environment through nanostructuration will facilitate cell behavior in interesting ways. Our objectives are detailed as follows.

Objective #1 – Surface modification

The primary objective of this study is to develop a system of fabricating nanopatterned, bioactive silicon surfaces for cellular assays. Silicon is chosen as the substrate used in this study because of its very flat surface that presents minimal roughness. Silicon surfaces can be activated for functionalization purposes, and it is also compatible with a number of common micro- and nanofabrication techniques.

This objective incorporates two parts. First, a nanofabrication technique must be chosen for the construction of nanopatterns on a large-area material surface. From the list of available nanofabrication techniques, we chose nanoimprint lithography, a template-based fabrication method, due to its versatility, high throughput, and ease of process. Using nanoimprint lithography, a wide range of motifs and dimensions, down to the nanoscale, can be replicated on a material surface using a pre-fabricated mold.

The second part of this objective is the surface functionalization of bioactive molecules. We chose an Arginine-Glycine-Aspartic acid (RGD) peptide for our preliminary studies, as it is a peptide sequence found on many extracellular matrix proteins, such as fibronectin, vitronectin, and osteopontin, which facilitate cell-material nanointeraction. Mimetic peptides of the osteogenic bone morphogenetic protein 2 (mBMP-2) were also used in our studies to evaluate osteogenic potential of hMSCs. In order to make use of these peptides, they must be immobilized onto our silicon surface. Our strategy involves the use of silane chemistry, whereby silicon is surface-activated and modified with a silane molecule. A cross-linker is required to anchor the peptide to the silane, rendering the silicon surface bioactive. Both homogeneous and nanopatterned surfaces (two different motifs) were prepared for our study.

When both the nanopatterning and surface functionalization steps are fully optimized to obtain the preferred surface characteristics, they are combined to yield substrates where nanopatterned regions of interest are grafted with the RGD or mBMP-2 peptide. Surface characterization is performed at every step to monitor the process of modification. The material characterization techniques used in our study include

fluorescence microscopy, X-ray reflectivity, X-ray photoelectron spectroscopy, confocal microscopy, atomic force microscopy, and surface energy analysis.

Objective #2 – Human mesenchymal stem cell studies on RGD-grafted surfaces

Once Objective #1 has been achieved, substrates for cellular testing can be readily prepared. We observe initial hMSC adhesive behavior on nanopatterned RGD-grafted surfaces after 24 hours in culture, comparing it to homogeneous peptide-grafted surfaces and non-bioactive silicon controls. Through quantitative fluorescent analysis, we study the post-adhesion morphologic changes, evaluating cell properties such as cell shape, projected cell area, and actin cytoskeleton organization. We are particularly interested in the FA dynamics in stem cell adhesion, and we attempt to relate FA conformation and maturation to nanostructuration by evaluating FA area, orientation, and cell-material contact area mediated by FAs.

We are also interested in the commitment and differentiation behaviors of hMSCs with respect to the nanopatterned RGD-grafted surfaces that have been fabricated in Objective #1. Through long-term cell culture (3 to 4 weeks), we aim to study whether RGD nanopatterns induce a commitment state that is different from non-patterned or non-functionalized surfaces. Specifically, we look at STRO-1, a mesenchymal stem cell-specific marker, to evaluate cell stemness after long-term culture. We also aim to see whether nanopatterns direct cell fate preferentially into a specific lineage by staining for various types of mature cells, including osteoblasts, adipocytes, chondrocytes, and neurons. Ultimately, we are aiming to establish a link between FA dynamics and the commitment behavior of hMSCs.

A sub-objective is to develop a way of visualizing cultured cells and the underlying nanopatterned surface simultaneously. Various potential imaging techniques can be trialed to achieve this goal, including stimulated emission depletion microscopy (STED) and confocal laser scanning microscopy (CLSM). Herein, we aim to use CLSM to perform preliminary tests using fluorescently-tagged peptides and immunofluorescent staining of adherent cells.

Objective #3 – Human mesenchymal stem cell studies on mBMP-grafted surfaces

We then observe the behavior of hMSCs on surfaces grafted with a mimetic peptide of the bone morphogenetic protein 2 (mBMP-2), which is known to upregulate osteospecific differentiation. The process of functionalization follows the same step as in the case of RGD, and we study cell behavior on peptide-grafted nanopatterns in controls with homogeneous peptide-grafted surfaces and non-bioactive silicon surfaces. In a fashion parallel to RGD, we study the post-adhesion morphologic changes of hMSCs on mBMP-grafted surfaces using quantitative fluorescent analysis, evaluating cell properties such as cell shape, projected cell area, actin cytoskeleton organization, and the formation of adhesion structures. Here we are interested in the different ways hMSCs respond to chemical signals by comparing the effects of RGD and mBMP-2, specifically in terms of the maturation of adhesion structures. We will attempt to shed light on the specific interactions between mBMP-2 and integrin receptors.

Finally we will take a brief look at the effects of mBMP-2 surface grafting on the commitment behavior of hMSCs. We look at the expression of some osteospecific markers (osterix and osteopontin) to see whether any changes in hMSC commitment has occurred after 4 days in culture on mBMP-grafted surfaces. Theoretically, the presence of mBMP-2 should direct hMSC commitment into an osteospecific lineage. This prediction remains to be validated with immunofluorescence studies.

Strategy and approach

To achieve our objectives, we developed our strategy by choosing among the techniques and molecules that are potentially suitable for our system. We started off by selecting an appropriate method of creating nanosized motifs on our substrate surfaces via nanofabrication techniques. The motifs must be sufficiently small to facilitate the observation of nanoscale interactions that occur between cells and biomolecules, in particular the formation of FAs. Also, these motifs should be uniformly nanopatterned on a large-area surface without consuming a significant amount of time. For these purposes, several methods of nanopatterning are available in the laboratory. These methods and their operating parameters are listed in Table II.1.

Table II.1 – List of available nanofabrication techniques and their parameters

	Optical lithography	**Electron beam lithography**	**Nanoimprint lithography**	**SPM-based lithography**
Minimum feature size	~0.5 µm	~10 nm	~50 nm	~30 nm
Patternable surface area	In the range of cm^2	In the range of μm^2	In the range of cm^2	In the range of μm^2
Throughput	High	Very low	Moderate	Very low

Taking into account the desired feature size, patternable area, and the overall throughput of the available systems, we chose to proceed with nanoimprint lithography as it provides us with parameters that satisfy the requirements of our application. Mainly, large-area surfaces can be fabricated easily with individual feature dimensions in the nanoscale, which is suitable for our cellular investigations.

In terms of the technique of peptide grafting, we chose to use an already established protocol that has been routinely used in the laboratory on metal surfaces [48, 49]. The protocol utilizes silane chemistry during its first step to act as a linker between the substrate surface and the biomolecules to be grafted. We tested two different silanes: 3-aminopropyldimethylethoxysilane (APDMS), ending with an amino functional group (-NH_2), and 3-mercaptopropyltriethoxysilane (MPTES), ending with a

thiol functional group (-SH). We found that the usage of MPTES results in thiol oxidation, which reduced the reproducibility of our system. In turn, our trials using APDMS were successful in that it yielded stable, reproducible surfaces with controllable monolayer thickness. APDMS was used instead of 3-aminopropyltriethoxysilane (APTES) as it only has one reactive functional group, allowing a single linkage with the silicon surface, whereas the three reactive functional groups on APTES introduce uncertainty and decreases the reproducibility of the surface.

As per the standard protocol, we used 3-succinimidyl-3-maleimidopropionate (SMP) as a hetero-bifunctional cross-linker to graft a thiol-containing (cysteine-containing) peptide. The Arginine-Glycine-Aspartic acid (RGD) peptide sequence was chosen for our preliminary studies, as it is a peptide sequence found on many extracellular matrix proteins, such as fibronectin, vitronectin, and osteopontin. RGD is the specific region on these proteins that is recognized by integrins to facilitate cell-material nanointeraction. In our experiments, we use the 7-amino acid sequence, GRGDSPC, as it has been shown to be more active than the RGD tripeptide and RGD-derived tetrapeptides (RGDS and RGDC, for example) [69]. Additionally, mimetic peptides of the osteogenic bone morphogenetic protein 2 (mBMP-2) were used in our studies to evaluate the osteogenic potential of hMSCs.

For the study of cell behavior on nanopatterns, we use hMSCs due to their multipotent capacities that allow efficient regeneration of damaged tissues. Previous studies in our lab have already shown the effects of surface-immobilized peptides on other cell types, such as pre-osteoblasts and osteoblasts. The commitment of hMSCs can be modulated by chemical and physical forces present within the microenvironment, and their self-renewal and differentiation can be precisely tuned depending on various conditions. In our work, we try to determine the specific impact of nanodistributed surface chemical cues on the adhesion and differentiation of hMSCs. For this reason, we chose to use culture media without any addition of growth factors that would stimulate lineage-specific differentiation, in order to ensure that any changes in hMSC behavior are solely the result of surface bioactivity.

Finally, the strategy for carrying out cell culture is described in the following flow chart. Various time points are chosen such that representative data can be extracted related to adhesion and differentiation of hMSCs. Cells are allowed to adhere

for 24 hours upon initial seeding on material surfaces in order for stable adhesions to form. The evolution of FA formation could be tracked by looking at FA proteins at earlier time points (4 hours and 16 hours, for example), but due to constraints in time and available number of samples, these time points were excluded from our study. In terms of hMSC differentiation, sufficient time is allowed to pass before fixing cells for immunofluorescence such that transcription factors and proteins related to lineage-specific differentiation can fully be expressed. For studies on RGD-grafted surfaces, this involves two time points – 2 weeks and 4 weeks – in order to compare the difference in the degree of protein expression, if any is present. For studies on mBMP-grafted surfaces, differentiation is only investigated at 4 days due to time constraints as well as cell culture issues related to contamination, which hindered the evaluation at longer time points.

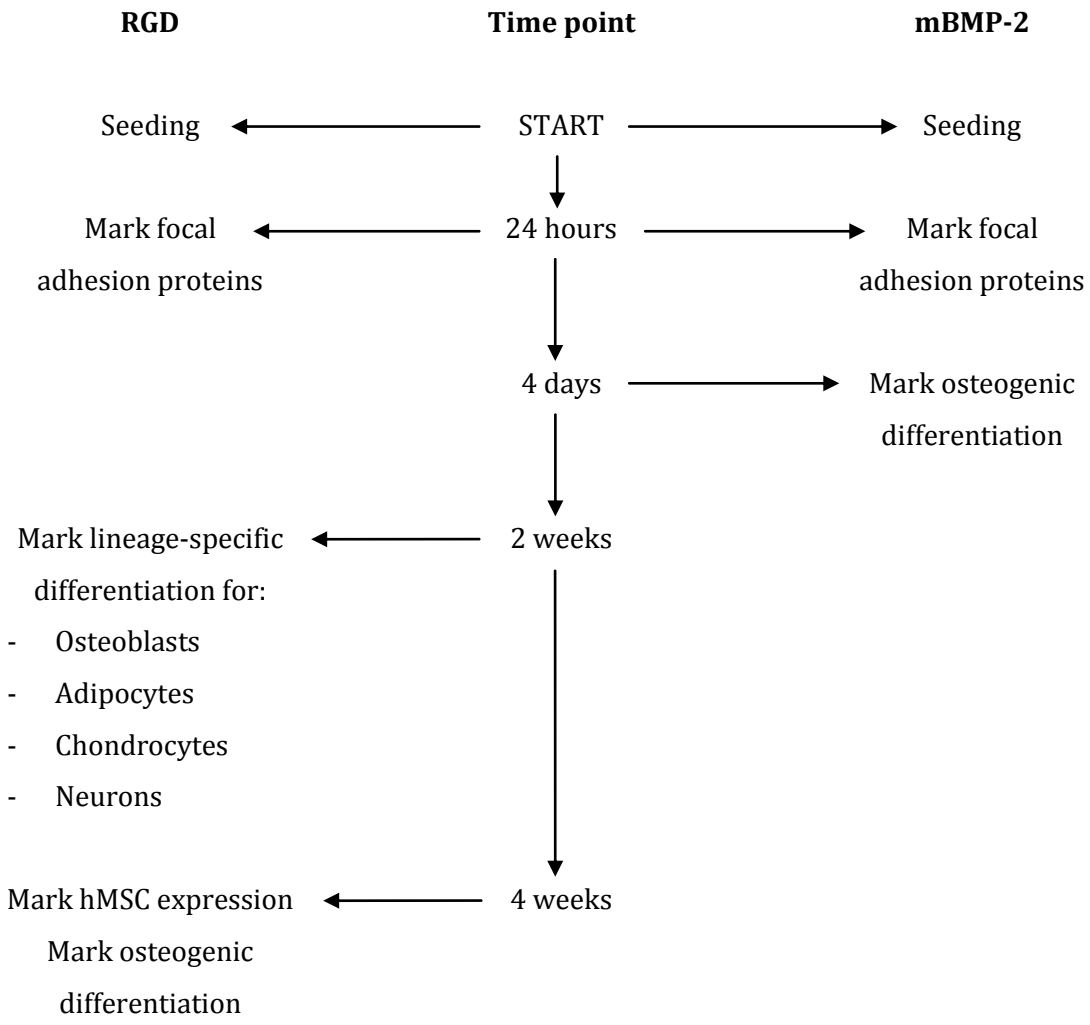

III. Materials and Methods

1. Materials

Silicon wafers with a diameter of 4 inches and a thickness of 525 µm, polished on one side, were purchased from Active Business Company GmbH, Germany, or from Applications Couches Minces, France. Poly(methyl methacrylate) (PMMA), molar mass by weight 120000 g/mol, was purchased from Agilent Technologies, Belgium. 3-aminopropyldimethylethoxysilane (APDMS; 97%) and 2-[methoxypoly(ethyleneoxy)$_{6-9}$propyl]trimethoxysilane (PEO silane; 90%) were purchased from ABCR GmbH, Germany. Dry dimethylformamide (DMF) and 3-succinimidyl-3-maleimidopropionate (SMP; 99%) were purchased from Sigma-Aldrich, France. Dry toluene was purchased from Fisher Scientific, Belgium. Customized GRGDSPC peptides and mBMP-2 peptides (CKLPKLSTAPSELSGISTLYL) were synthesized by Genecust, Luxembourg.

1.1 Molecular structures

3-aminopropyldimethylethoxysilane (APDMS)

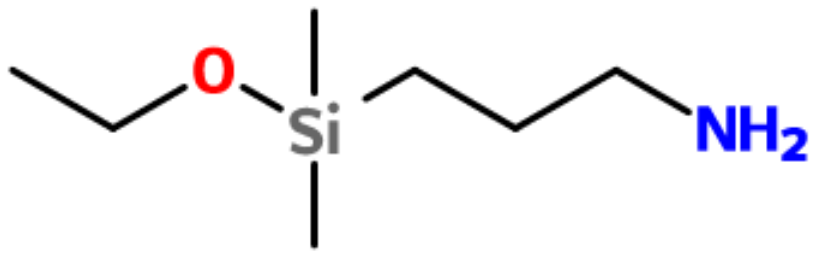

3-succinimidyl-3-maleimidopropionate (SMP)

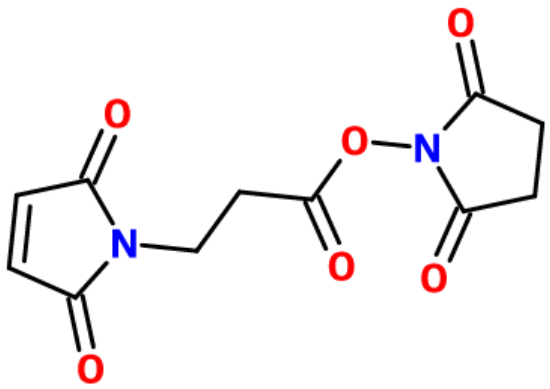

GRGDSPC peptide

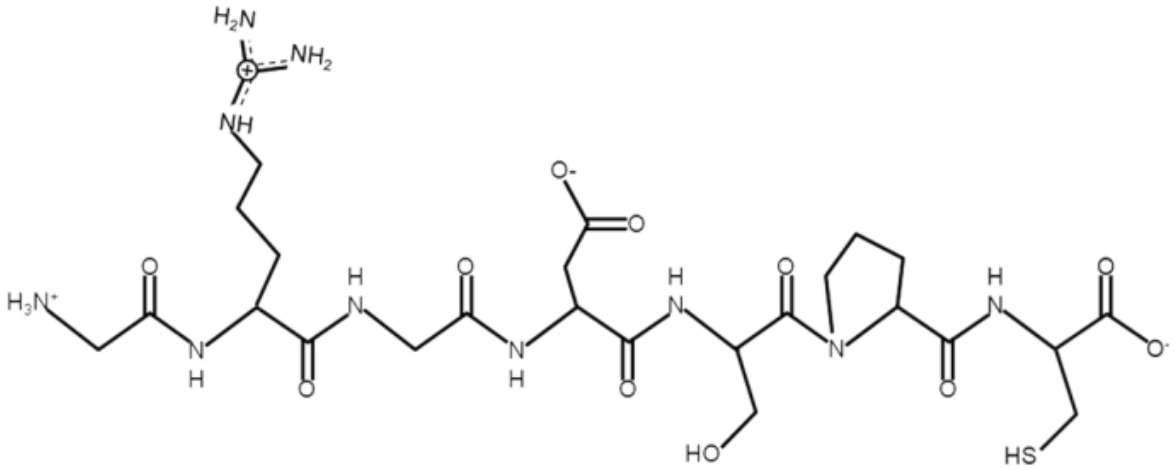

CKLPKLSTAPSELSGISTLYL peptide

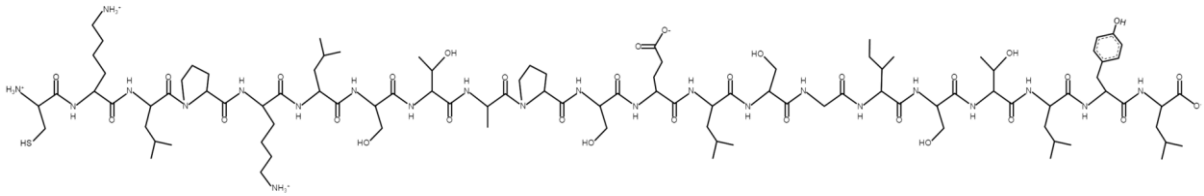

2-[methoxypropyl(ethyleneoxy)$_{6-9}$propyl]trimethoxysilane

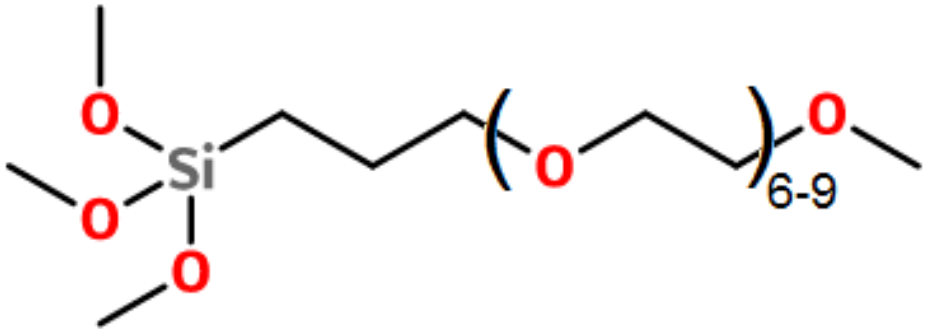

TAMRA fluorophore (5-Carboxytetramethylrhodamine)

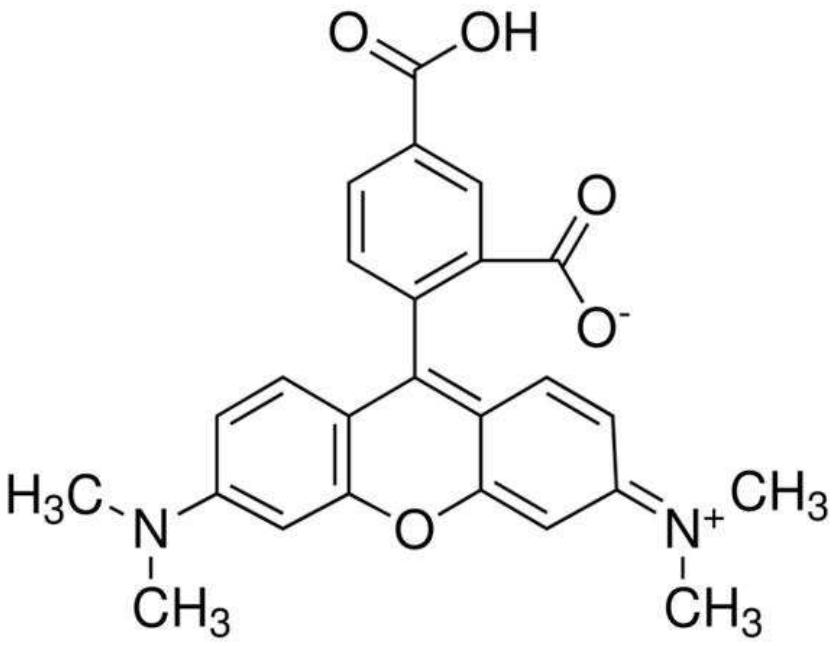

2. Surface preparation

2.1 Nanoimprint lithography (NIL)

The nanoimprint lithography process was entirely performed in the WinFab laboratories at Université catholique de Louvain (UCL) in Belgium. Silicon substrates were first cleaned in a piranha solution made up of a 3:1 mix of H_2O_2 (30%) and H_2O_4 (98%) to remove organic residues. The clean substrates were then subjected to a nanoimprint lithography procedure (Figure III.1). The operation of nanoimprinting follows a template-based model. A 4% w/w poly(methyl methacrylate) (PMMA) solution was prepared in toluene and filtered through a 0.45 µm membrane. PMMA was spin-coated onto the silicon (Si) samples using a Laurell WS-650MZ-23NPP/LITE spin-coater at a speed of 5000 rpm with an acceleration of 7000 rpm/s for 60 seconds to create a uniform polymer mask. The thickness of the mask was measured by ellipsometry to be approximately 120 ± 10 nm. A silicon mold with an area of 1 x 1 cm^2 (purchased from AMO, GmbH) presenting a circular motif and a height of protrusion of 100 nm was first coated with a 1H,1H,2H,2H-perfluorodecyl-trichlorosilane in the gas phase to reduce post-imprint sticking [212]. To perform the imprint, the mold was pressed onto the polymer mask using an Obducat nanoimprinter. The sample was pre-heated at 170 °C for 3 minutes, then the pressure was increased from 5 bars to 60 bars and left for 3 minutes to perform the imprint. The system was then cooled down to 70 °C and the mold was detached from the sample. Samples were subjected to a descum process for 210 seconds using an Electrotech Plasmafab 310/340 reactive ion etcher, in oxygen plasma at an etching rate of 14 nm/min, to remove the residual polymer mask left on the patterned regions of the sample, leaving bare silicon with exposed silanol groups for the subsequent functionalization steps. Samples were immediately subjected to the next step to avoid surface contamination.

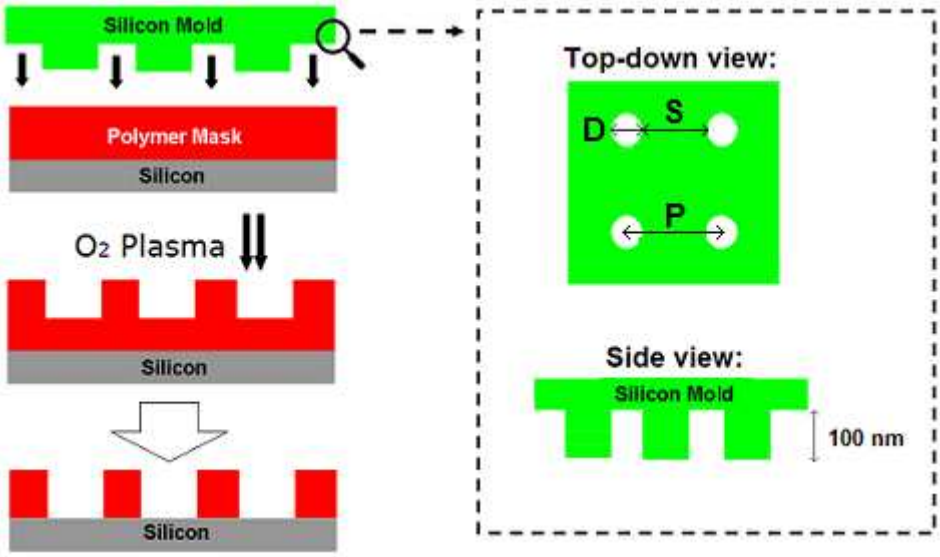

Figure III.1 – Nanoimprint lithography outline. PMMA mask is spin-coated on silicon substrates that have been cleaned with piranha solution (3:1 mix of 30% H_2O_2 and 98% H_2SO_4) to remove organic contaminants. A silicon mold with an array of nanodots of diameter D, center-to-center spacing P, and interdot gap width S = D – P is pressed onto the PMMA mask at 170°C and 60 bar to transfer the pattern. The mold is then removed and an oxygen plasma descum treatment is applied to the substrate to etch the residual PMMA on the nanopatterned regions, in order to expose these regions to the subsequent surface functionalization steps. Samples are named D_mS_n where m = diameter and n = interdot gap width in nanometers. The templating approach allows surface features of varying geometries and dimensions to be readily fabricated.

2.2 Surface functionalization

Surface functionalization was performed at UCL and the process took place in three steps, as outlined in Figure III.2. Descummed samples were placed on a Teflon sample holder in a Schlenk reactor heated in a silicone oil bath at 80 °C. The reactor was filled with argon for 30 minutes, then vacuum-pumped for 90 minutes and again filled with argon. 0.1 mL of APDMS was injected into the reactor and the reaction was run overnight at 80 °C. To stop the reaction, the samples were removed from the Schlenk reactor and immediately immersed in acetone. The samples were then washed in acetone using a Soxhlet apparatus set-up for 2 hours to completely remove the remaining traces of PMMA mask and silane.

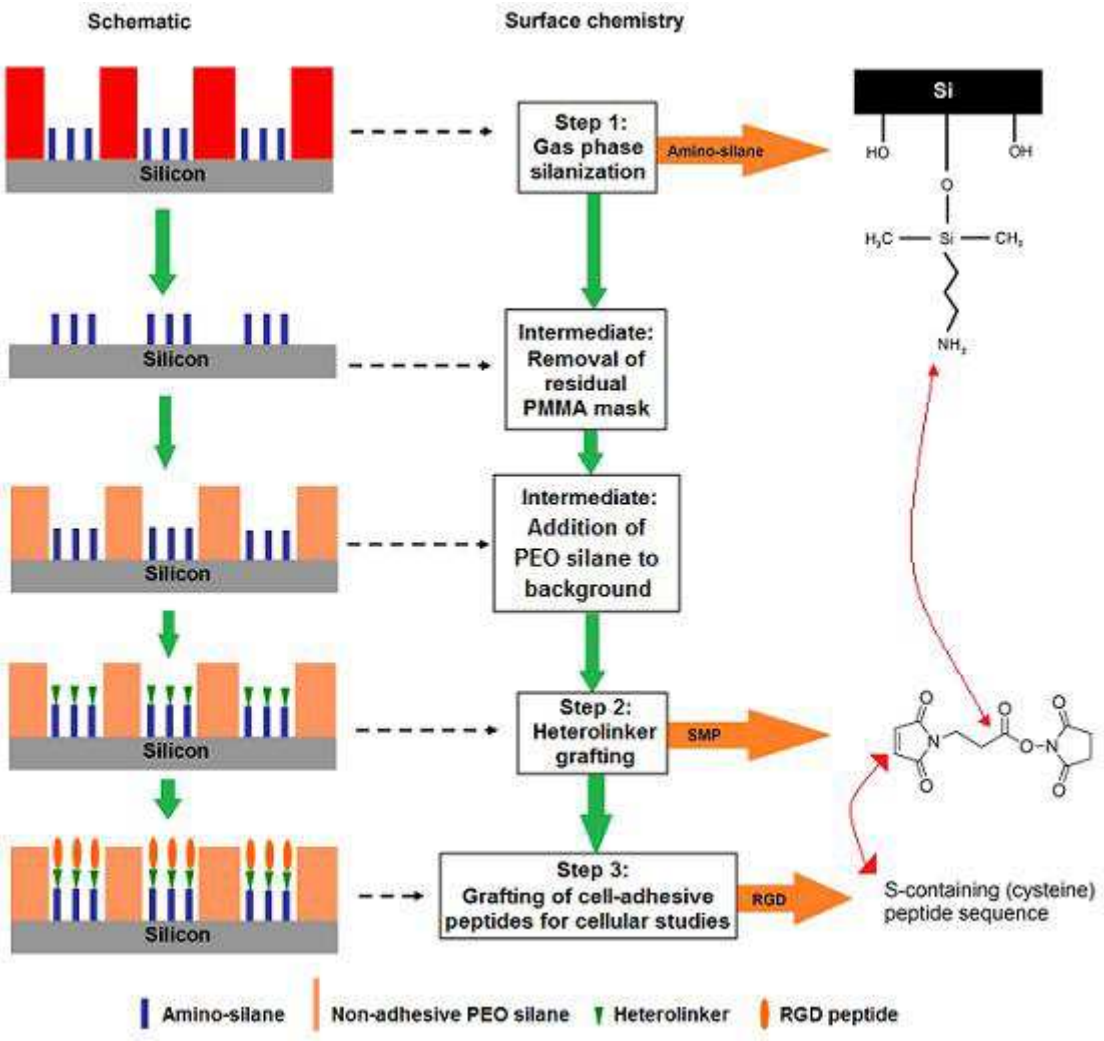

Figure III.2 – Surface functionalization schematic. After oxygen descum, the substrates are immediately subjected to a three-step surface functionalization process. In the exposed, nanopatterned regions, an amino-silane (APDMS) is grafted to the silicon substrate via reaction with the surface silanol groups. An acetone washing is then performed using a Soxhlet apparatus set-up for 2 hours to remove the remaining PMMA mask, as well as any excess amino-silane. A PEO silane is then grafted to the non-patterned regions of the substrates as a passivation step to render the background non-adhesive to cells and proteins. The second functionalization step is the grafting of a hetero-bifunctional cross-linker. In this case, 3-succinimidyl-3-maleimidopropionate (SMP) reacts with the amino-silane layer to form an amide bond. In the last step, a cell-adhesive RGD peptide, containing a cysteine in its sequence, is grafted to the SMP via thiol linkage with the maleimide group. This last operation is performed at a later stage, just before using the substrates for cell culture.

After Soxhlet washing, the samples were immediately immersed in a solution of non-adhesive PEO silane in dry toluene (0.05 mL PEO silane per mL of toluene). The reaction was run overnight in a glove box with a controlled argon atmosphere to ensure the reaction environment was completely free of water and oxygen. Samples were then rinsed with toluene and dried. The purpose of this PEO passivation step was to create a chemically inert and cell non-adhesive environment that serves as a background for the nanopatterned surfaces, allowing specific adhesive interactions to occur solely on the functionalized nanopatterns.

Passivated samples were immersed in an 3-succinimidyl-3-maleimidopropionate (hetero-bifunctional cross-linker) solution in dry DMF at a concentration of 2×10^{-3} M [49]. The reaction was run for 2 hours at room temperature in a glove box with a controlled argon atmosphere. Samples were then rinsed with DMF for 15 minutes and further rinsed with Milli-Q water. Samples were immersed in a peptide solution in Milli-Q water at a concentration of 5×10^{-4} M. For cell adhesion studies, GRGDSPC peptides, fluorescently tagged with a TAMRA fluorophore on the cysteine end, were used. For cell differentiation studies, a mimetic BMP-2 peptide, CKLPKLSTAPSELSGISTLYL, was used. The peptide solution was filtered through a 0.45 μm membrane and briefly sonicated to improve dissolution. The reaction was run for 4 hours at room temperature under gentle agitation. The samples were then rinsed in Milli-Q water for one week to remove peptide aggregates and attachment due to adsorption and replaced with new Milli-Q water 4 to 5 times a day. The final peptide grafting step was performed in Université de Bordeaux 1 (UB1) in France.

3. Surface characterization

3.1 Epifluorescence microscopy

Fluorescent peptide-grafted substrate surfaces were imaged using a Leica DM5500B epifluorescence microscope with a motorized, programmable stage using a CoolSnap HQ camera controlled by Metamorph 7.6 (UB1). A TX2 filter cube from Leica Microsystems was used to visualize the TAMRA fluorochrome. Images were taken using a 2.5X dry objective with a numerical aperture of 0.07 to observe fluorescent signal indicative of peptide grafting. Leica MMFA software was used for image acquisition and ImageJ was used for image treatment and analysis.

3.2 X-ray reflectivity (XRR)

The measurements were carried out with a modified Siemens D5000 2-circle goniometer (0.002° positioning accuracy), available at UCL. X-rays of 0.15418 nm wavelength (Cu Kα) were obtained from a Rigaku rotating anode operated at 40 kV and 300 mA, fitted with a collimating mirror (Osmic, Japan) delivering a close-to-parallel beam of ~0.0085° vertical angular divergence. The beam size was defined by a 40 μm-wide slit placed 17.5 cm away from the focal spot. The sample was placed within 2 μm of the center of the goniometer and the reflected beam was collected through a 200 μm-wide detector slit. Soller slits in the incident and reflected beam limited axial divergence to 0.02°. The data were corrected for spillover and normalized to unit incident intensity; they are reported as a function of k_{z0}, the vertical component of the photon wavevector in a vacuum ($k_{z0} = (2\pi/\lambda)\sin\theta$, where θ is the angle between the incident ray and the sample surface, and λ is the wavelength).

The XRR data were analyzed in the following way. First, an estimation for the average thickness of the monolayer, d_X, was obtained from the value of $k_{z0,min}$ in the reflectogram, according to $d_X = \pi/(2k_{z0,min})$. Here, $k_{z0,min}$ is the k_{z0} value corresponding to the first minimum in the reflectivity curve, arising from destructive interference. Alternatively, a Patterson function was computed from the data as described elsewhere [227, 228], from which a second estimatate for the average thickness d of the layers was

obtained by taking the location of the last maximum in the Patterson function. In addition, the maximal thickness of the layer (including the protrusions arising from roughness), d_{max}, was taken as the value for which the last peak in the Patterson function goes back to the baseline. Secondly, the film was modeled as a succession of thin virtual homogeneous layers of zero interfacial roughness, stacked over the Si substrate of electron density held a 700 electron/nm^3. The electron density ρ_i of the virtual layers were fittable parameters, whereas their widths w_i were held constant at a single value corresponding to the information content of the XRR curves, $w_i=\pi/(2k_{z0,max})$ with $k_{z0,max}$ the maximal experimental value of k_{z0}. For the experiments reported here, w_i = 0.35 nm. The absorbance of the virtual layers was set to $5\text{x}10^{-7}$ nm^{-1}, and the absorbance of the Si substrate to $1.5\text{x}10^{-5}$ nm^{-1}. The initial number of virtual layers was set to d_{max}/w_i; if required - which happened rarely -, supplementary slabs were added in the course of the fit. From this model of electron density, the film reflectivity was computed using dynamical theory [229, 230], and the chi-square function was minimized with a Marquardt-Levenberg algorithm. In order to avoid numerical problems and unphysical solutions due to the large number of parameters in the final model of the electron density, a regularization technique was applied by adding a smoothing constraint to the chi-square function, as fully described elsewhere [227, 231, 232].

The grafting densities were obtained from the electron density profiles $\rho(z)$ in the following way. For silane monolayers, the electron density profile of a clean silicon wafer, $\rho_{Si}(z)$, was subtracted from $\rho(z)$, after horizontal displacement to bring the Si interfaces in coincidence. Then, the area below the resulting difference profile was computed, giving access to ζ_g, the total number of electrons belonging to grafted molecules, per unit surface. The grafting density of the silanes was then obtained as $\sigma_g = \zeta_g/Z$, where Z is the number of electrons of the silane molecule, excluding the reactive alkoxy or chlorine groups. Due to experimental errors, to the small thickness of the silane layer, and to the uncertainty of the lateral shift of one profile versus another, errors of about 20% are to be expected on the values of the grafting density obtained from the density profiles of the silane monolayers. A similar procedure was applied for activated or protein-grafted layers; in this case, however, the grafting density was obtained as $\sigma_g = (\zeta_g - \zeta_g')/Z$, where ζ_g' is the number of electrons belonging to the

underlying layer, and Z is the number of electrons of the grafted moiety. Because the thickness of these monolayers is usually larger, the estimated error on the grafting density is lower, in the 10% range.

3.3 X-ray photoelectron microscopy (XPS)

For the characterization of silicon cleaning methods, a VG Scientific ESCALAB photoelectron spectrometer (UB1) was used with an MgK X-ray source (1253.6 eV photons, 100 W). Spectra fitting and determination of atomic composition were realized with software provided by VG Scientific, with each spectrum being referenced by setting carbon pollution at 284.8 eV. For the functionalized surfaces, the analyses were performed on a SSX 100/206 photoelectron spectrometer (UCL) from Surface Science Instruments (USA) equipped with a monochromatized micro focused Al X-ray source (powered at 20 mA and 10 kV), a 30° solid angle acceptance lens, a hemispherical analyzer and a position sensitive detector. The samples powder pressed in small stainless steel troughs of 4 mm diameter were placed on an aluminum conductive carousel. Due to their semi-conductor character some samples undergo a differential charging effect when they are deposited on a conductive carousel. This provokes broadening, distortion, or even splitting of peaks which can be confused with a chemical shift effect. The differential charging effect can be avoided by mounting the sample on an insulating homemade ceramic carousel (Macor ® Switzerland), with the nickel grid, mentioned below, still grounded to the carousel support. The pressure in the analysis chamber was around 10-6 Pa. The angle between the surface normal and the axis of the analyzer lens was 55°. The analyzed area was approximately 1.4 mm^2 and the pass energy was set at 150 eV. In these conditions, the full width at half maximum (FWHM) of the Au $4f_{7/2}$ peak of a clean gold standard sample was about 1.6 eV. A flood gun set at 8 eV and a Ni grid placed 3 mm above the sample surface were used for charge stabilization. The following sequence of spectra was recorded: survey spectrum, C 1s, O 1s+Pd $3d_{5/2}$, Pd 3p, Mn 3d…and C 1s again to check the stability of charge compensation with time (and the absence of sample degradation). The C-(C,H) component of the C1s peak of carbon has been fixed to 284.8 eV to set the binding energy scale. Data treatment was performed with the CasaXPS program (Casa Software Ltd, UK), some

spectra were decomposed with the least squares fitting routine provided by the software with a Gaussian/Lorentzian (85/15) product function and after subtraction of a non linear baseline. Molar fractions were calculated using peak areas normalized on the basis of acquisition parameters and sensitivity factors provided by the manufacturer (mean free path varying according to the 0.7^{th} power of the photoelectron kinetic energy; Scofield cross sections; transmission function assumed to be constant).

3.4 Atomic force microscopy (AFM)

Atomic force microscopy (AFM) was performed in air using a Veeco Nanoscope V system (UCL) in contact mode on imprinted samples and functionalized nanopatterned samples to characterize surface topography and chemical contrast. Bruker Silicon Nitride Lever (SNL-10) cantilevers were used, with a spring constant of about 0.12 N/m and a tip radius of 2 nm. The scan rate was 2 lines per second with a deflection setpoint of 2V. Integral and proportional gains were empirically set for each scan. Images were scanned at a resolution of 512 pixels by 512 pixels. Gwyddion software was used for AFM image analysis.

3.5 Contact angle and surface energy analysis

Contact angle and surface energy experiments were performed by the industry partner Rescoll in France. Contact angle measurements were taken at ambient temperature using a DataPhysics OCA40 goniometry device from Rescoll. The contact angles of three different liquids (water, diiodomethane, and ethylene glycol) were measured on the different types of surfaces that were fabricated. Three drops of each liquid were placed on different regions of each sample and the contact angle was measured. Using these data, the surface energy of each liquid on different surfaces was calculated and broken down into their polar and dispersive components.

4. Cell culture

All cell culture experiments were performed at UB1. Human mesenchymal stem cells (hMSCs) are commercially available and were purchased from Lonza. The hMSCs were cultured in Alpha Minimum Essential Medium (αMEM) supplemented with 10% (v/v) Fetal Bovine Serum (FBS) and 1% penicillin-streptomycin, and incubated in a humidified atmosphere at 37 °C, containing 5% (v/v) CO_2. Before cell seeding, material surfaces were sterilized in 70% ethanol for 10 minutes and washed twice with PBS. For all experiments, cells at passage 4 were seeded at a density of 10^4 cells/cm^2 in serum-free αMEM supplemented with 1% penicillin-streptomycin. All experiments were performed in duplicates (two samples per condition) and data sets were extracted from at least two separate experiments.

For adhesion studies, hMSCs were cultured in serum-free αMEM for the first 6 hours post-seeding on material surfaces. Then, the medium was changed to αMEM supplemented with 10% (v/v) FBS and 1% penicillin-streptomycin with no additional growth factors. hMSCs were cultured for a further 16 hours to allow cell attachment to the material surface before being fixed for immunofluorescent staining.

For differentiation studies, hMSCs were cultured in serum-free αMEM for the first 6 hours post-seeding on material surfaces. Then, the medium was changed to αMEM supplemented with 10% (v/v) FBS and 1% penicillin-streptomycin with no additional growth factors. hMSCs were cultured for a further 4 days, 2 weeks, or 4 weeks depending on the study being performed. The time points were chosen to allow sufficient time for hMSCs to undergo commitment and differentiation before being fixed for immunofluorescent staining.

5. Biological characterization

5.1 Immunofluorescence

After various times of cell culture (24 hours for adhesion studies, 4 days, 2 weeks, or 4 weeks for differentiation studies), samples with hMSCs were removed from the incubator. Culture medium was discarded and cells were fixed with a 4% (w/v) solution of paraformaldehyde for 15 minutes at 4 °C. Fixed cells were permeabilized with 0.5% Triton-X 100 in PBS for 15 minutes at 4 °C, and blocked with 1% bovine serum albumin (BSA) in PBS for 30 minutes at 37 °C. Cells were then incubated with primary antibody (Table III.1) for 1 hour at 37 °C. After washing, cells were stained with either Alexa Fluor® 568 or Alexa Fluor® 647 secondary antibody for 30 minutes at room temperature, then stained for F-actin using Alexa Fluor® 488 phalloidin for 1 hour at 37 °C. All antibodies were diluted in 1% BSA in PBS. Cell nuclei were counterstained with DAPI in water for 10 minutes at room temperature. Samples were washed twice with 0.05% Tween 20 in PBS between each staining step. After DAPI staining, samples were washed twice with water and mounted with coverslips in Vectashield mounting media on microscope slides. Cells were observed using fluorescent microscopy.

Table III.1 – List of primary antibodies used for immunofluorescence

Antibody	Purchased from	Type of study	What it detects
Alexa Fluor® 488 phalloidin	Invitrogen	Adhesion	Cytoskeleton, actin stress fibers
DAPI	Invitrogen	All	Cell nucleus
Vinculin	Sigma-Aldrich	Adhesion	Focal adhesions
STRO-1	R&D Systems	Differentiation	Mesenchymal stem cells
Osterix	Tebu-bio	Differentiation	Osteoblastic differentiation
Osteopontin	Tebu-bio	Differentiation	Osteoblastic differentiation
SOX9	Santa Cruz	Differentiation	Chondrogenic differentiation
Tubulin β-3	Sigma-Aldrich	Differentiation	Neuronal differentiation

5.2 Epifluorescence microscopy

Samples were fluorescently labeled following cell culture and were imaged using a Leica DM5500B epifluorescence microscope with a motorized, programmable stage using a CoolSnap HQ camera controlled by Metamorph 7.6 (UB1). The following filter cubes from Leica Microsystems were used: A4 for the visualization of DAPI, L5 for Alexa Fluor® 488, TX2 for Alexa Fluor® 568, and CY5 for Alexa Fluor® 647. Images were taken using a 40X oil objective with a numerical aperture of 1.30 to observe fluorescent signal indicative of cell adhesion. Leica MMFA software was used for image acquisition and ImageJ was used for image treatment and analysis.

Cells were imaged for general adhesive activity after 24 hours in culture, as well as STRO-1, osterix, osteopontin, SOX9, and tubulin β-3 expression after 4 days, 2 weeks, or 4 weeks. Images were taken at 40X magnification for the quantification of cell area, focal adhesion (FA) count, FA size, and lineage-specific protein expression. Absorption and emission spectra of the fluorescent dyes used are presented in Figure III.3.

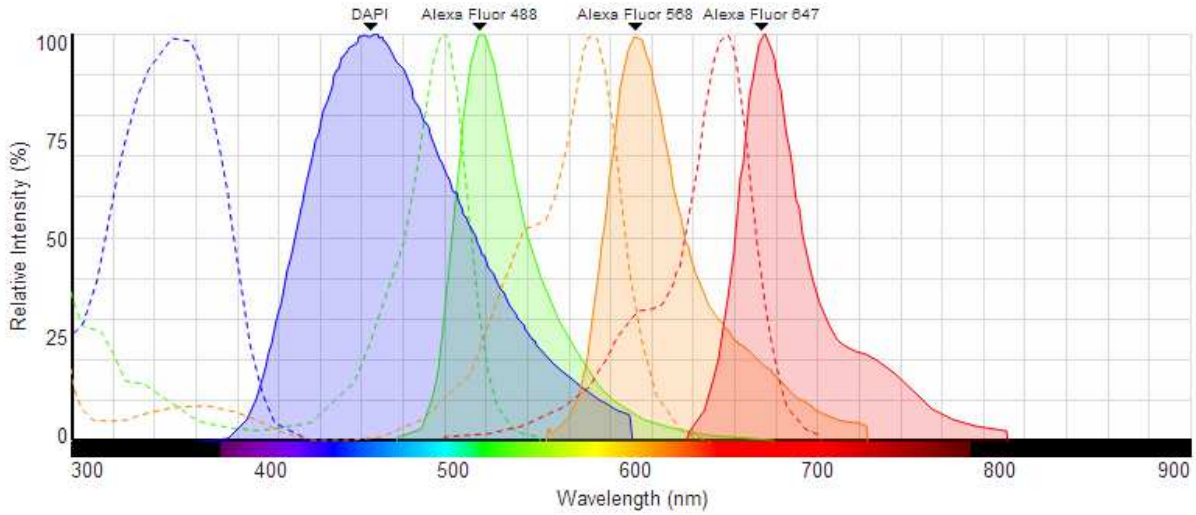

Figure III.3 – Absorption and emission spectra of fluorophores used for immunofluorescence. DAPI was used to mark the cell nucleus, Alexa Fluor® 488 was used to mark the actin cytoskeleton, and Alexa Fluor® 568 and 647 were used to mark various proteins of interest (e.g. vinculin and STRO-1). Dotted lines represent the absorption spectra while the solid lines represent the emission spectra of the fluorescent dyes.

5.3 Confocal microscopy

A Leica SP5 confocal microscope (Bordeaux Imaging Center, Bordeaux, France) was used to image nanopatterned surfaces with a fluorescently-tagged peptide grafted on the nanosized features. This allows the visualization of homogeneous arrays of large-area nanopatterned peptide dots. Moreover, confocal microscopy enables the visualization of cells, in particular the cytoskeletal structure and the points of FA, on the same field of view as the fluorescent nanopatterns. Confocal microscopy was also used to perform imaging of cells for adhesion studies, after 24 hours in culture, at a magnification of 63X (oil immersion) and at different z-depths. Cells with morphologies representative of each condition were imaged.

5.4 Image quantification and analysis

Fluorescent images of at least 50 cells at each surface condition were taken for quantitative analysis, both for adhesion and differentiation studies. Quantification of FA count, FA area, projected cell area, STRO-1 expression, and lineage-specific protein expression (osterix, osteopontin, SOX9, and tubulin β-3) was carried out using ImageJ software on images taken at 40X magnification. For analysis of FAs, fluorescent images of vinculin staining were analyzed. The raw images were opened and converted into an 8-bit file. The region surrounding the cell was selected, and the background was removed using a rolling ball radius of 10. A threshold was empirically set and retained for all images of the same surface condition. Regions corresponding to noise and artifacts were selected and removed. The “Analyze Particles” tool in ImageJ was used to calculate the number of FAs per cell and the area of each FA. Objects that are less than 50 pixels were not taken into account. For analysis of cell area, fluorescent images of actin staining were analyzed. The outline of the cell was precisely defined, and the “Measure” tool on ImageJ was used to calculate the area of the drawn outline of the cell. For analysis of protein expression (STRO-1, osterix, osteopontin, SOX9, and tubulin β-3), images of immunofluorescence staining were analyzed. The “Measure” tool on ImageJ was used to calculate the mean and integrated fluorescent density as well as corrected total cell fluorescence of protein signals on each image.

5.5 ALP and Oil Red O staining

Alkaline phosphatase activity was evaluated using the Sigma-Aldrich® Alkaline Phosphatase kit (Procedure No. 85). Briefly, a pre-formulated Fast Violet B capsule was dissolved in distilled water and solubilized. Naphthol AS-MX Phosphate Alkaline Solution (from kit) was added to the diluted diazonium salt solution. Samples were fixed by immersion in citrate buffered acetone for 30 seconds and rinsed gently for 45 seconds in deionized water. Samples were then added to the alkaline-dye mixture and incubated for 30 minutes away from direct light. After incubation, samples were rinsed thoroughly in deionized water for 2 minutes. Place the samples in Mayer's Hematoxylin Solution for 10 minutes and rinse counterstained slides in tap water for 2 minutes. On the same samples, Oil Red O staining for fat and lipid deposits was carried out. Briefly, a stock Oil Red O solution was prepared by adding 300 mg of Oil Red O powder to 100 mL of 99% isopropanol. An Oil Red O working solution was prepared by diluting the stock solution with deionized water at a stock to water ratio of 3:2. The working solution was filtered using filter paper. Samples were incubated in the Oil Red O working solution for 15 minutes, then washed with deionized water 5 times. Samples can be viewed under a microscope for osteogenic and adipogenic differentiation. Osteogenic cells stain blue-purple and adipogenic cells stain red.

5.6 Statistical analysis

Numerical data are presented as mean values ± standard deviation (SD). Statistical analysis was performed using one-way analysis of variance (ANOVA) (OriginPro 8, OriginLab Corporation, USA), followed by LSD or Dunnett post-hoc test for multiple comparisons, where appropriate. For FA area analysis, two-sample t-test was used to compare significant difference between the percentages. A p-value of less than 0.05 is considered statistically significant.

IV. Results and Discussions

Zhe A. Cheng, Omar F. Zouani, Karine Glinel, Alain M. Jonas, Marie-Christine Durrieu. *Bioactive chemical nanopatterns impact mesenchymal stem cell fate*. **Nano Letters**, 2013. **13**(8): p. 3923-9.

The studies outlined in this thesis aim at achieving a clear understanding of the nanoscale interactions between cells and biomaterials for tissue engineering applications. Herein, we designed nanostructured material surfaces presenting various forms of bioactivity to mimic the extracellular matrix, whereby cells interact with their microenvironment on the nanoscale. The combination of various surface properties will influence cell response in many ways. These properties include but are not limited to substrate rigidity and stiffness, nanotopography, surface energy, and bioactivity.

In the first part of our results, we carry out surface characterization in order to fully comprehend the nature and attributes of our fabricated surfaces. We successfully fabricated two types of nanodots which were subsequently functionalized with either a cell adhesion-promoting RGD peptide or a mimetic peptide of bone morphogenetic protein 2 (mBMP-2) through a three-step grafting procedure. Each step of the surface modification process was monitored through a variety of surface characterization techniques to ensure the validity of the protocol. These techniques include fluorescence microscopy, which confirms successful peptide grafting; X-ray reflectivity, which verifies monolayer thickness and molecular density; X-ray photoelectron spectroscopy, which examines elemental composition; confocal microscopy, which allows visual inspection of nanopatterned peptides; atomic force microscopy, which demonstrates chemical topography and compositional contrast; and goniometry, which assesses surface contact angle and surface energy.

In latter parts of the results, we evaluate human mesenchymal stem cell behavior on RGD-grafted and mBMP-grafted surfaces that have been fully characterized. We assess cell adhesion based on cytoskeletal arrangements and the dynamics of focal adhesions, including their conformation, distribution, stabilization, and maturation. We also evaluate the relationship between integrins and growth factors by observing induced adhesions on mBMP-grafted surfaces. Finally, we attempt to detect whether any specific differentiation had occurred on our surfaces by performing a series of immunofluorescence staining using lineage-specific markers, as well as the mesenchymal stem cell marker STRO-1. The ensemble of these results will give us a reasonable overview of the effects of nanostructured surface bioactivity on the fate of human mesenchymal stem cells.

1. Bioactive surface characterization

1.1 Surface preparation

In this study, we combined nanoimprint lithography with surface modification techniques to prepare material surfaces that are chemically patterned with nanosized bioactive features, over a total area of about 1 cm^2. In literature, various nanofabrication techniques such as electron beam lithography [123], colloidal lithography [220], and nanoimprint lithography (NIL) [217] were explored to produce nanopatterned surfaces. Among them, NIL offers a series of advantages related to its ease of processing, rapidity, and versatility. As a template-based system, NIL operates by transferring a pre-defined pattern from a master mold to a material surface. Thus, surface features ranging from the microscale down to the nanoscale can be constructed with no limit on geometry. Motifs with varying shapes (circles, squares, lines), sizes, and interspacing can be fabricated, contributing to the versatility of the system. Furthermore, the imprinting method allows large areas to be patterned on the nanoscale without the need of a time-consuming process. These platforms allow cellular assays to be carried out for the investigation of cell-material nanointeraction.

In the preparation of surfaces for biological assays, three types of control surfaces were used: polished silicon without modification (Si poli), silicon modified with an anti-fouling oligoethylene oxide layer (Si PEO), and silicon homogeneously grafted with peptide (RGD H or BMP H, H = homogeneous). For the patterned surfaces, square arrays of nanodots of unit cell parameter P were transferred from a silicon mold onto silicon substrates via a polymer mask (see Materials and Methods, Chapter III.2.1). Two types of peptide-grafted arrays (RGD or mBMP-2) were realized, hereafter noted as $D_{150}S_{350}$ and $D_{80}S_{110}$, where D and S = P – D denote the nanodot diameter and interdot gap width in nanometers, respectively. A visual representation of the nanodot arrays is shown in Figure IV.1. Note that the percent coverage of the peptides are 7% and 14% for $D_{150}S_{350}$ and $D_{80}S_{110}$, respectively. The nanopattern fabrication and peptide grafting procedures were outlined in the Materials and Methods, Chapter III.2.2.

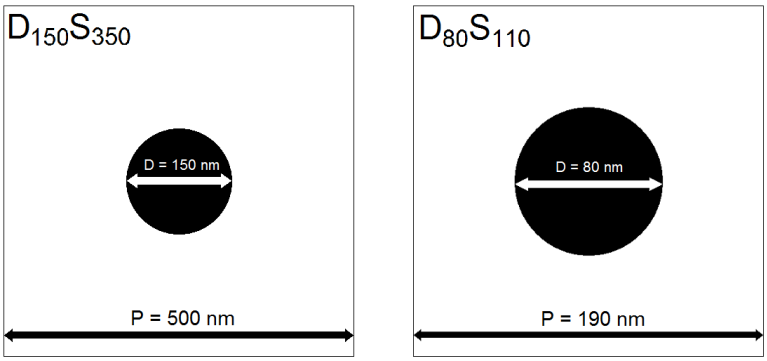

Figure IV.1 – Peptide nanodot dimensions for the two nanopatterned surfaces, $D_{150}S_{350}$ and $D_{80}S_{110}$. Peptides are grafted on nanodots (black circle) which are geometrically distributed within a PEO background (white background) in square arrays. On $D_{150}S_{350}$, peptides cover approximately 7% of the surface while on $D_{80}S_{110}$, peptides cover approximately 14% of the surface.

A scanning electron microscopy (SEM) characterization is shown in Figure IV.2 of the master mold used for nanoimprint lithography (A) and an imprinted PMMA mask (B) before the functionalization process. In (A), a master mold with a square array of pillars with diameter D = 150 nm, pitch spacing P = 500 nm, and height or protrusion of 100 nm was used to fabricate samples denoted as $D_{150}S_{350}$. In (B), nanoimprinted PMMA mask is imaged with SEM before functionalization. Very few defects were seen on the mold, resulting in a well-patterned mask.

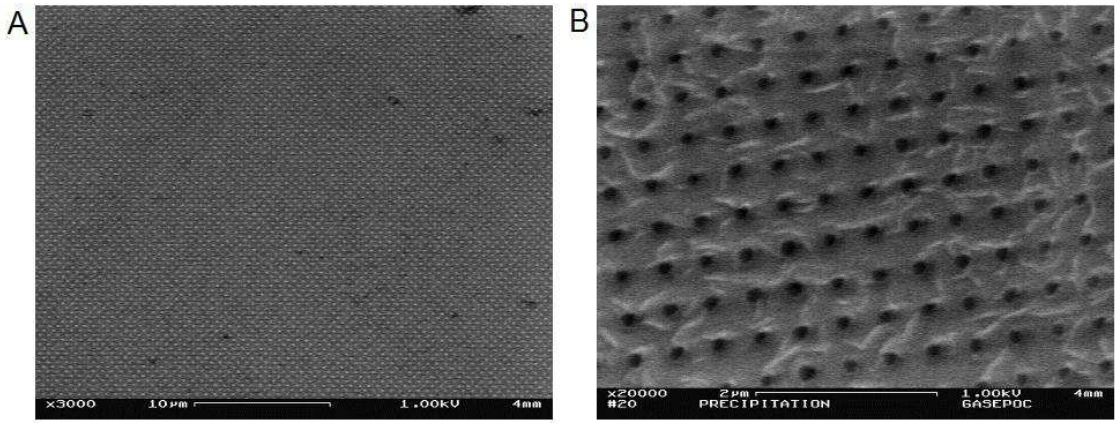

Figure IV.2 – Scanning electron microscopy characterization of (A) the master mold used for nanoimprint lithography to produce $D_{150}S_{350}$ surfaces, imaged at 3000X magnification with scale bar = 10 µm, and (B) nanoimprinted PMMA mask using the mold in (A), imaged at 20000X magnification with scale bar = 2 µm.

1.2 Fluorescent visualization of peptide-grafted surface

To validate the process of functionalization visually, fluorescent GRGDSPC peptides tagged with a TAMRA fluorophore (absorption and emission spectra shown in Figure IV.3, from Biosearch Technologies) were homogeneously grafted following the previously described functionalization procedure, without the initial nanoimprint steps and the passivation step. TAMRA was chosen as a fluorophore because of its bright fluorescence and resistance to photobleaching compared to other dyes (like FITC) [233]. The surfaces were then viewed with epifluorescence microscopy. An image of a surface expressing fluorescence is shown in Figure IV.4. As described in the Materials and Methods (Chapter III.2.2), the materials were rinsed in Milli-Q water for one week after functionalization to remove peptide aggregates. After rinsing, a layer of red is homogeneously distributed about the surface (with few peptide aggregates, Figure IV.4), which confirms that the successful grafting of the fluorescent RGD peptide is due to covalent interactions and not adsorption of peptides.

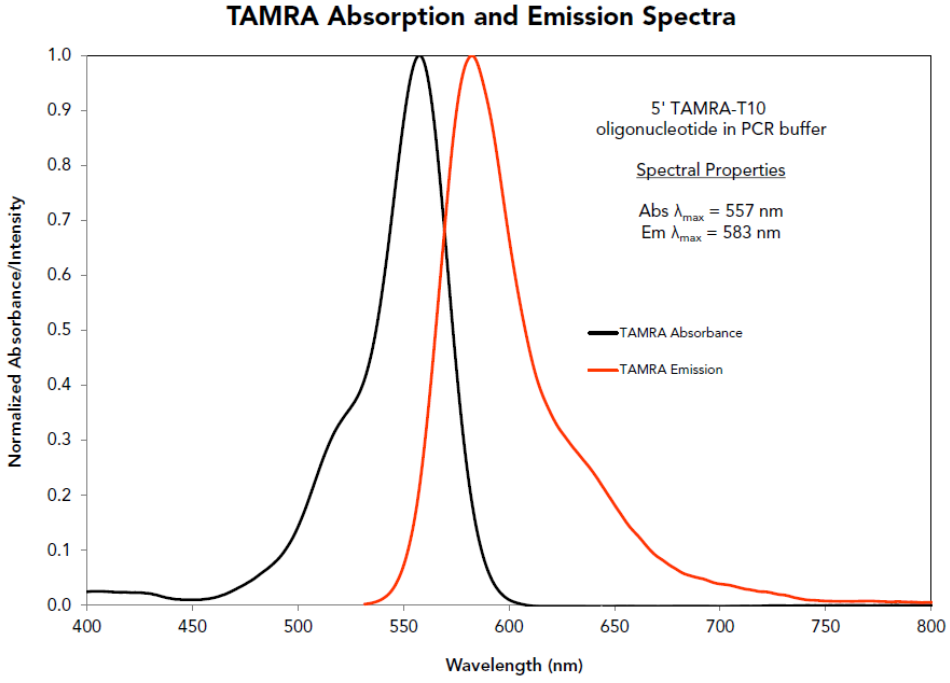

Figure IV.3 – Absorption and emission spectra of TAMRA, or 5-carboxytetramethylrhodamine. This fluorophore is readily excited at 557 nm and has an emission maximum at 583 nm.

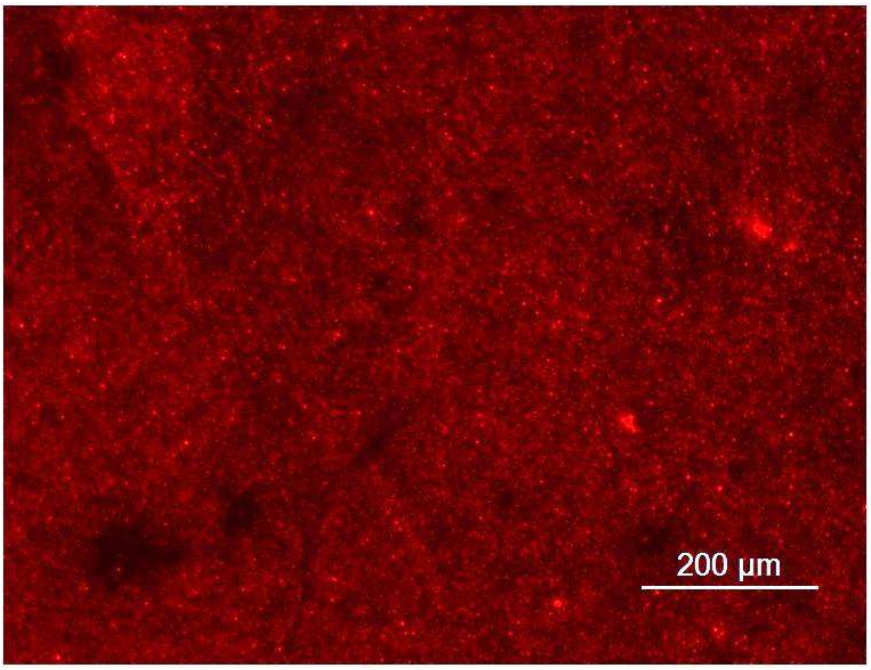

Figure IV.4 – Fluorescent visualization of silicon surface grafted with TAMRA-modified GRGDSPC peptide, after one week of rinsing.

1.3 X-ray reflectivity analysis of electron density and monolayer thickness

At each step of the functionalization process, homogeneous surface controls were included in simultaneous runs and subjected to X-ray reflectivity (XRR) analysis, which measures the surface electron density associated with surface monolayer thickness. Figure IV.5 shows the reflectivity profiles of monolayer deposition at each grafting step, as well as the electron density plotted against the layer thickness at which the density was detected.

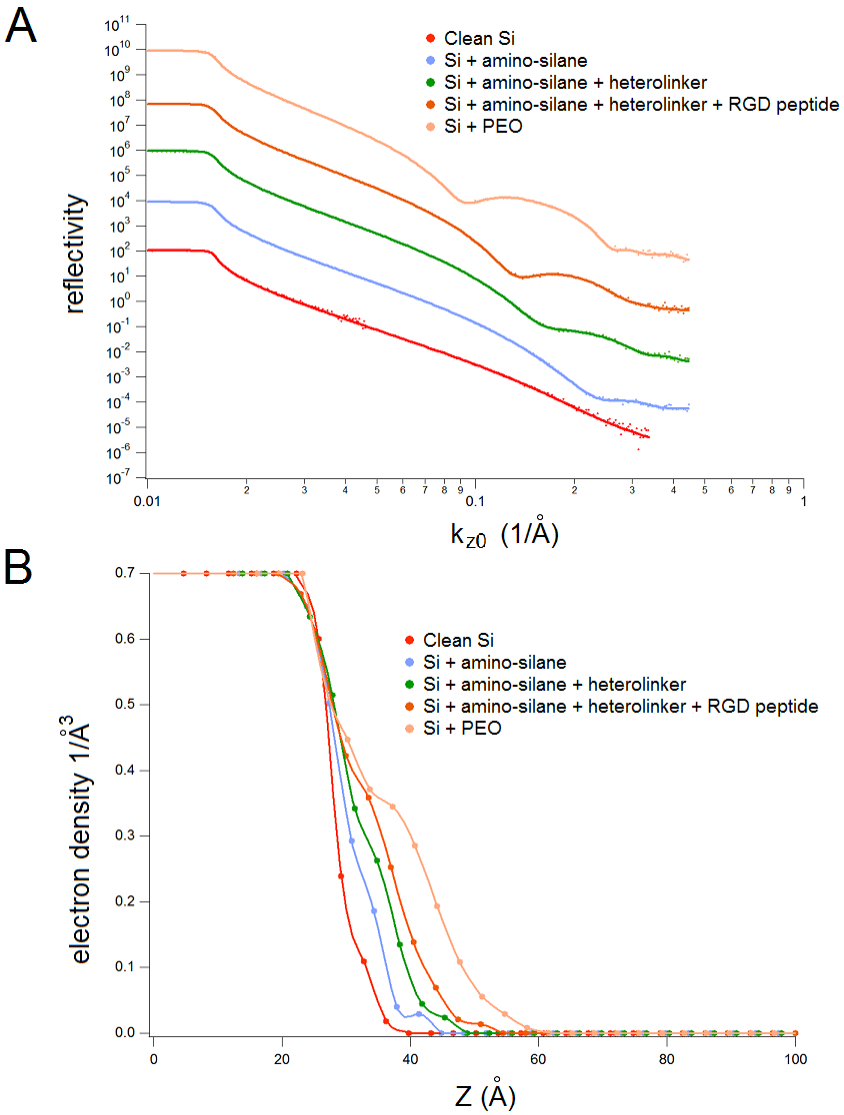

Figure IV.5 – XRR profiles during peptide grafting process. At each functionalization step, X-ray reflectivity (A) was measured and the electron density of the systems (B) was computed using procedures described elsewhere [234]. Evidently in (B), the thickness of the organic film increases with each grafting step, indicating that the successive deposition of molecules was achieved.

The grafting of each intermediate molecule during the functionalization process is further broken down into separate XRR profiles. As many measurements of layer thickness were made for each step, the average value of the measurements was calculated. Figure IV.6 and Figure IV.7 show the electron density versus monolayer thickness for the amino-silanization and the cross-linking steps, respectively. Figure IV.8 shows the increase in layer thickness following different types of peptides that have been grafted.

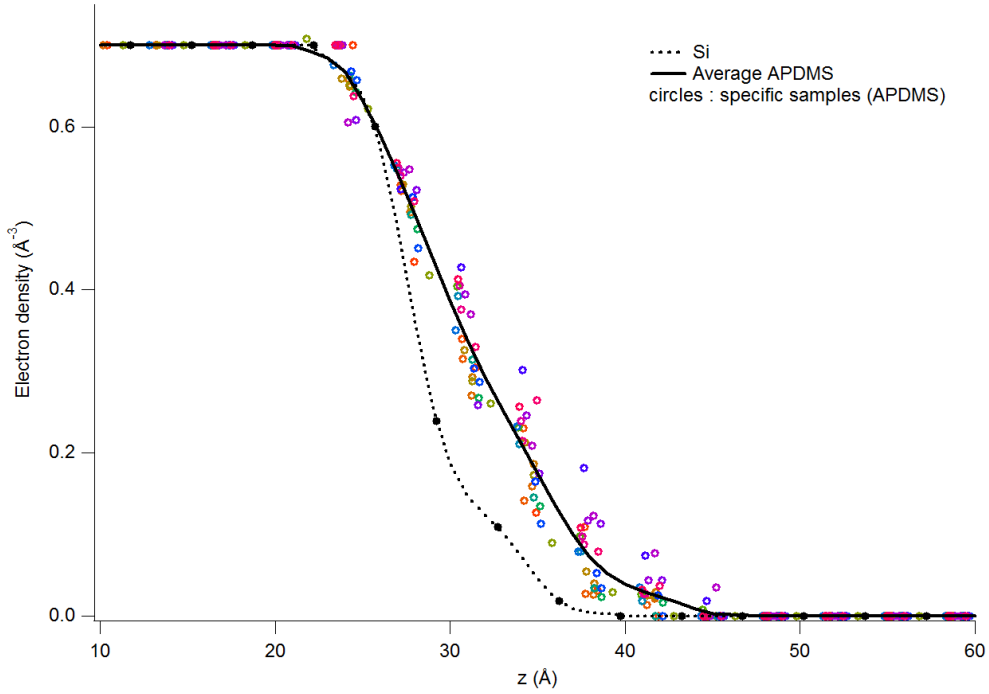

Figure IV.6 – XRR electron density profile of APDMS grafting. The circles represent data obtained from individual measurements after APDMS grafting, fitted with the black solid curve.

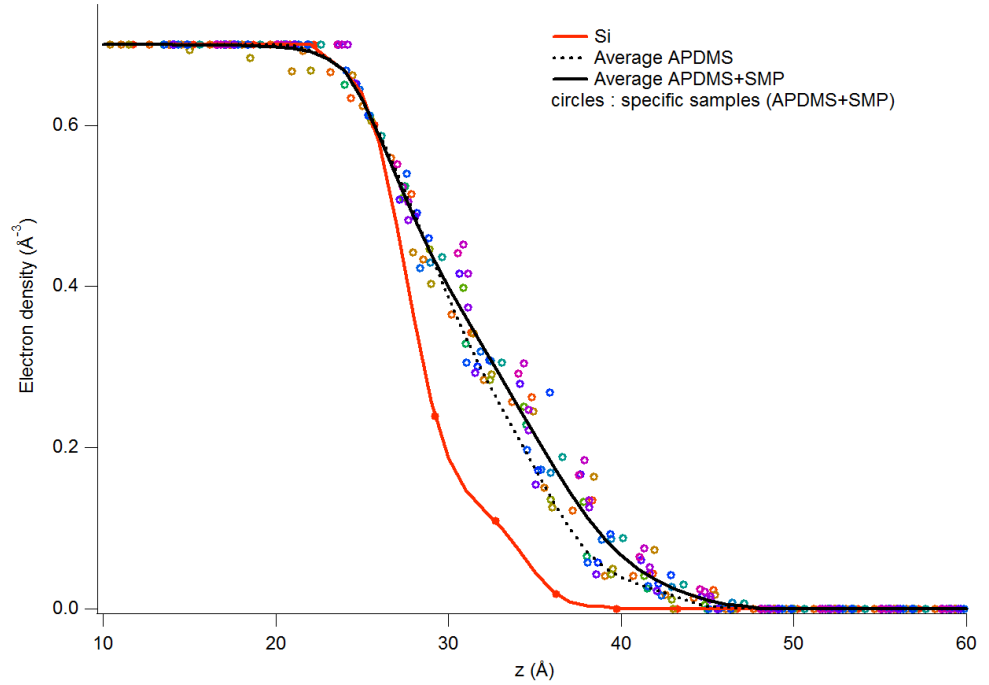

Figure IV.7 – XRR electron density profiles of APDMS and SMP grafting. The circles represent data obtained from individual measurements after SMP grafting, fitted with the black solid curve.

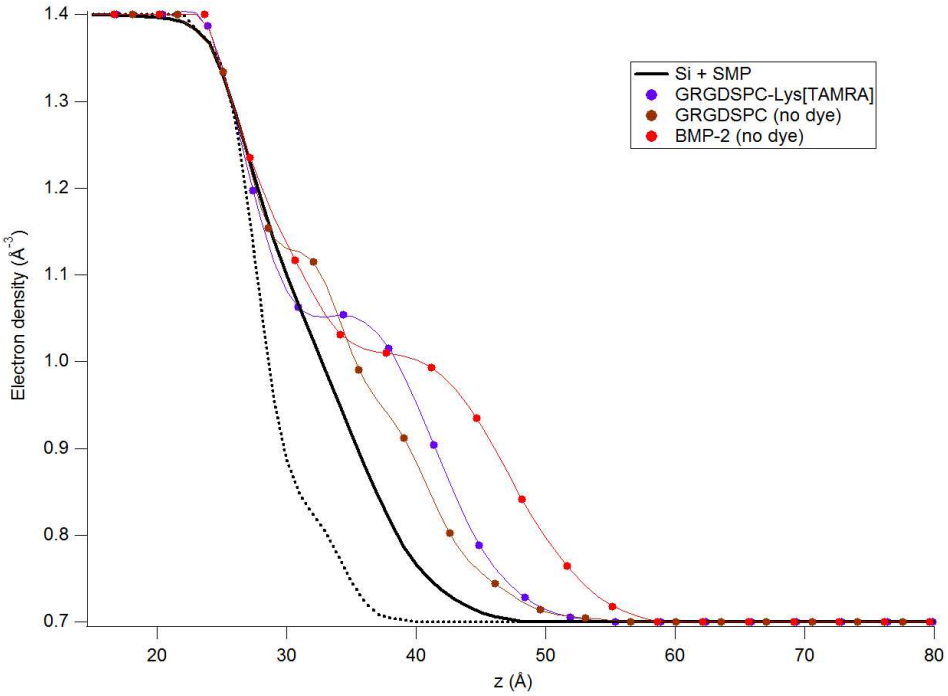

Figure IV.8 – XRR electron density profiles of peptide grafting. Three different types of peptides were measured: non-fluorescent GRGDSPC, fluorescent GRGDSPC-Lys(TAMRA), and non-fluorescent mBMP-2, each increasing the thickness at which electron density is detected.

Using the reflectivity profiles, monolayer thicknesses and molecular density (molecules per nm^2) are calculated for each grafting step, as described previously [232, 234], and shown in Table IV.1.

Table IV.1 – XRR measurements of monolayer thickness and molecular density

	Overall layer thickness ± standard error (nm)	**# molecules per nm² (± standard error)**	**Number of samples measured**
Si + amino-silane APDMS	0.71 ± 0.02	2.80 ± 0.15	23
Si + APDMS + heterolinker SMP	0.84 ± 0.03	0.6 ± 0.04	20
Si + APDMS + SMP + peptide GRGDSPC	1.19	0.42	1
Si + APDMS + SMP + peptide GRGDSPC-Lys(TAMRA)	1.48	0.33	1
Si + APDMS + SMP + peptide mBMP-2 (CKLPKLSTAPSELSGISTLYL)	1.86	0.29	1
Si + PEO (n=6-9) trimethoxysilane	1.64 ± 0.09	2.6 ± 0.2	5

As seen in the XRR analysis, the thickness of the APDMS is on average 0.71 nm, which is in agreement with previously published work [234]. The deposition of the APDMS, the heterolinker, and the peptide yielded successively increasing thicknesses, confirming successful grafting. The decreasing molecular density is attributed to the difference in the size of each molecule, steric effects, and incomplete reactions (i.e. not every single silane molecule reacts with an SMP molecule and not every SMP molecule reacts with a peptide molecule, resulting in a < 100% yield). We also noted that the PEO layer showed the highest thickness, indicating that the PEO silane is longer than the combination of amino-silane, heterolinker, and peptide, except for mBMP-2.

The grafting of APDMS is very reproducible. Since the silane has only one reactive functional group, there is generally no variation between samples in terms of layer thickness and molecular density because the silane only interacts with the substrate surface in one way. However, the results of SMP grafting show a moderate degree of variability. The molecular density of SMP is calculated to be 0.60 per nm², and compared to 2.80 per nm² for APDMS, we can assume that for every nm², approximately three amine groups are unreacted following SMP grafting. The calculation of SMP layer thickness is performed by the subtraction of the previous calculated thickness of Si +

APDMS from the overall thickness of Si + APDMS + SMP. Since SMP is a small molecule, the difference between these layers is very small, and the subtraction of two large layer thicknesses (close to the resolution limit of XRR) may be the source of the error present within the calculations. While the grafting works, the precision of the thickness measurements is weak. Nonetheless, the low SMP grafting density is not a big problem for the grafting of large peptides.

Taking a look at the grafting of peptides, we get 0.2 to 0.4 peptide molecules per nm^2 on average. Due to the size of the peptides, this small grafting density is to be expected and overcomes the problem of low SMP grafting density. The electron density profile (Figure IV.8) correctly indicates an increase in layer thickness when an RGD peptide is labeled with a fluorescent TAMRA dye. Additionally, the 21 amino acid sequence of mBMP-2 is shown with a much higher layer thickness than the RGD peptides when grafted (1.86 nm and 1.19 nm for mBMP-2 and RGD, respectively). In parallel, the molecular density of mBMP-2 is lower than that of fluorescently-tagged RGD, which in turn is lower than that of normal RGD with no dye.

1.4 X-ray photoelectron spectroscopy analysis of elemental composition

To measure the surface elemental composition at each step of the grafting process, X-ray photoelectron spectroscopy (XPS) was performed during the functionalization of RGD peptide. Four surfaces (1, 2 3, 4) were analyzed and represented in Figure IV.9, Figure IV.10, Figure IV.11, and Figure IV.12, corresponding to each step of functionalization.

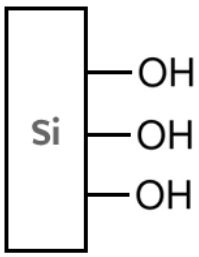

Figure IV.9 – Surface 1, silicon after piranha solution wash. OH groups are exposed after cleaning.

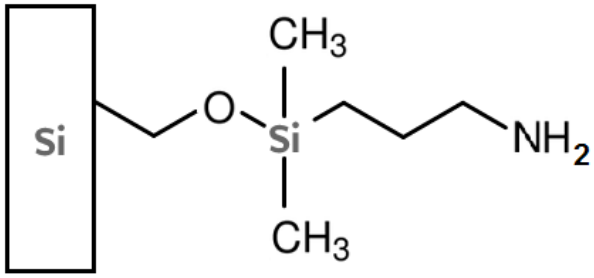

Figure IV.10 – Surface 2, silicon grafted with APDMS.

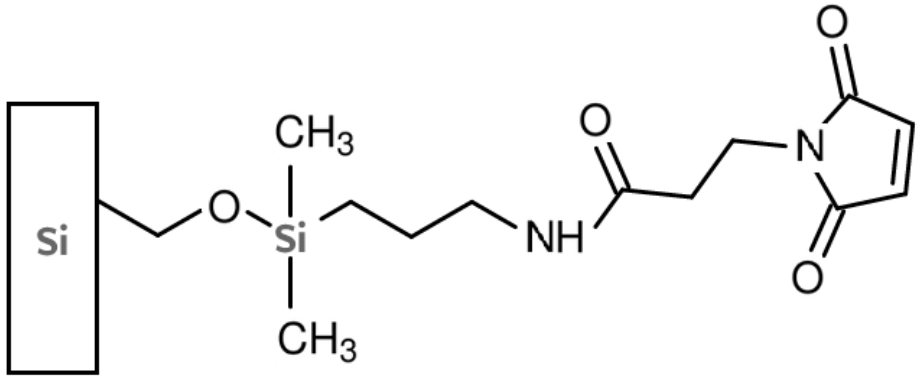

Figure IV.11 – Surface 3, silicon grafted with APDMS and SMP.

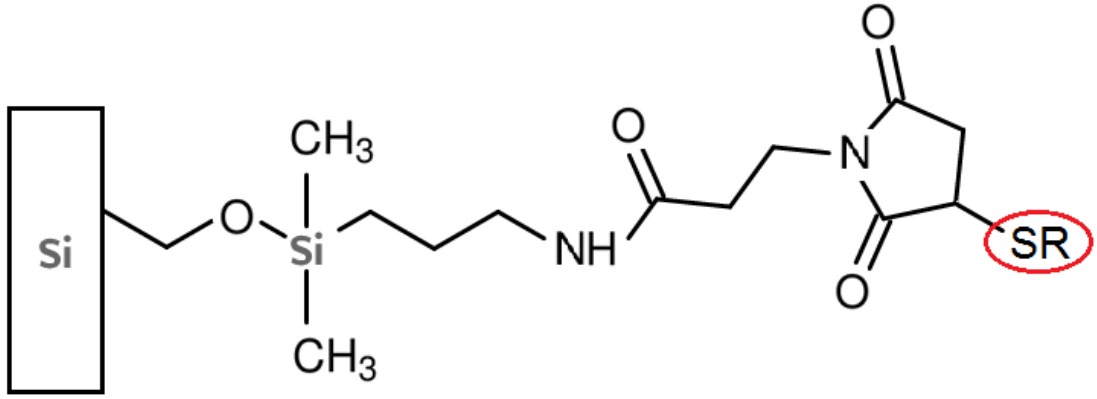

Figure IV.12 – Surface 4, silicon grafted with APDMS, SMP, and cysteine-containing peptide. The maleimide in SMP reacts with a thiol group, present on the amino acid cysteine in the peptide GRGDSPC (C = cysteine). The molecular structure of the grafted peptide is shown in Figure IV.13.

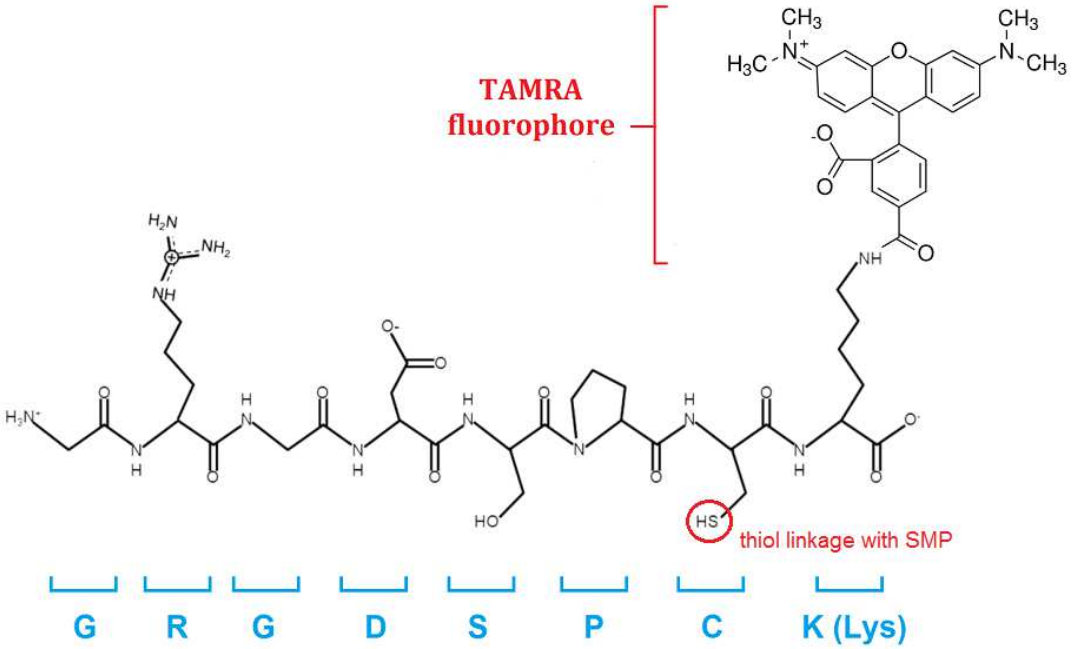

Figure IV.13 – GRGDSPC-Lys(TAMRA), fluorescent peptide grafted to Surface 4 via thiol linkage with SMP. A lysine (Lys) is added to the end of the peptide sequence to allow the TAMRA fluorophore to be linked via an amide bond.

Before functionalization, several methods of cleaning the substrate surface (Figure IV.9) were tested: sonication with ethanol followed by sonication with acetone; rinsing with dichloromethane, ethanol, and acetone successively; and cleaning with a 3:1 mix of H_2SO_4:H_2O_2 piranha solution. Substrates were then analyzed by XPS (Figure IV.14) for surface composition and specifically evaluated for possible contamination. As seen in Figure IV.14, the XPS spectra show clear peaks for the silicon substrate and oxygen species present as OH groups on the surface. There is also some adventitious carbon present on the surface. In turn, no other elements were detected on the surfaces, meaning that each method of surface cleaning effectively removes surface contaminants before subjecting the samples to functionalization.

The elemental compositions of carbon, oxygen, and silicon on each cleaned surface are shown in Table IV.2. To select the most appropriate method of cleaning, we compared the amount of carbon pollution and the oxygen that is exposed on the surface, as it is crucial to have an abundance of surface OH groups for silanization. We concluded that piranha solution is the most suitable method of cleaning our silicon surfaces as it yields low carbon contamination while activating the surface and being fully compatible

with standard cleanroom processes (for nanoimprinting). (It should also be noted that stockage time between sample cleaning and XPS measurements contributes to carbon contamination on the surface, and the values obtained for piranha solution rinse is not fully representative of experimental conditions, where samples are subjected to silanization immediately following cleaning.)

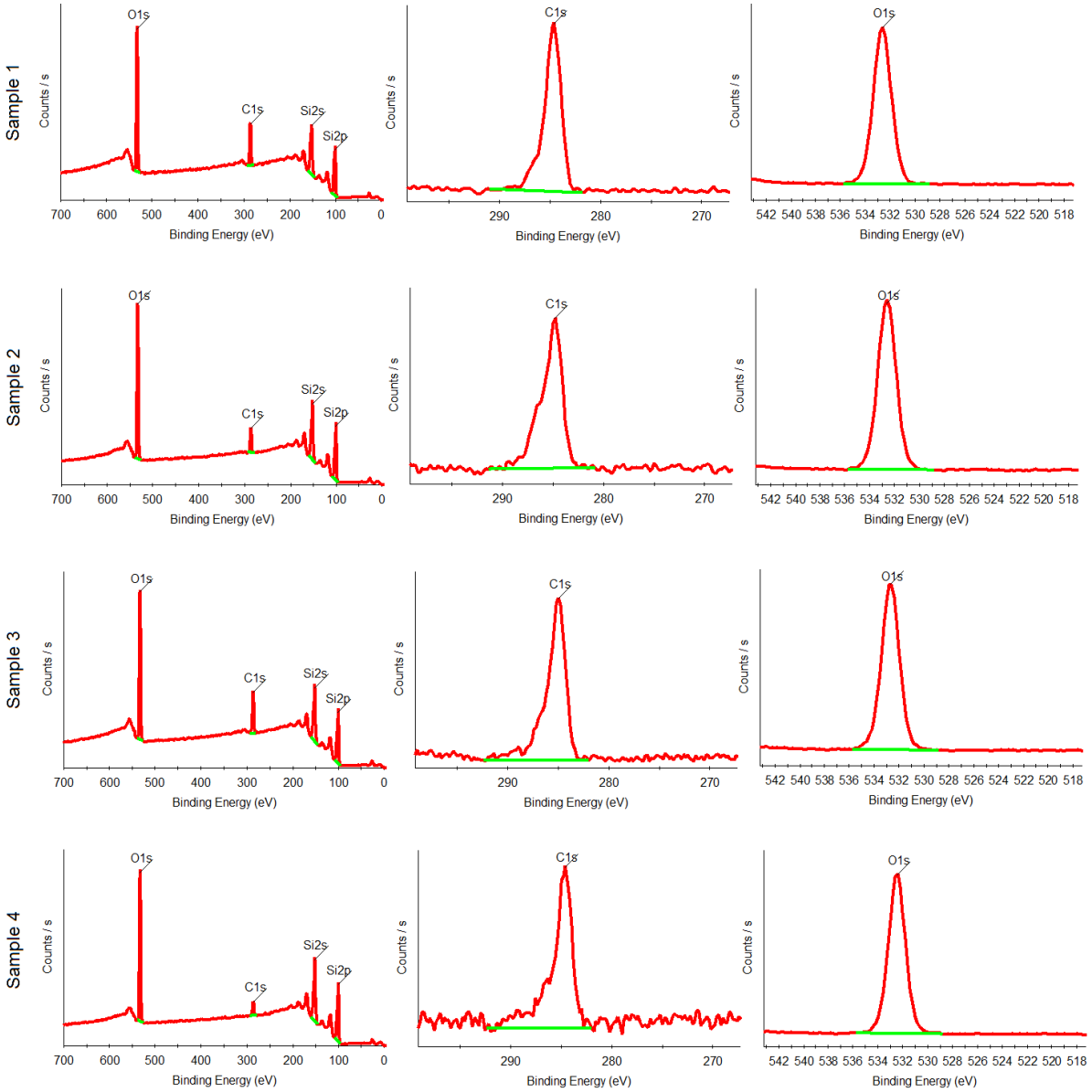

Figure IV.14 – XPS spectra for Surface 1, bare silicon substrates cleaned using various methods. Sample 1: no cleaning; sample 2: sonication in ethanol (30 minutes) + acetone (30 minutes); sample 3: rinsing in dichloromethane (2 minutes), acetone (2 minutes), and ethanol (10 minutes); sample 4: immersion in piranha solution with 3:1 H_2SO_4:H_2O_2 ratio (30 minutes).

Table IV.2 – Atomic concentration for silicon surface cleaned using various methods, data presented with a relative uncertainty of 5%

Sample	Cleaning method	% C	% O	% Si
1	No cleaning	26.2 ± 1.3	31.0 ± 1.6	42.8 ± 2.1
2	Sonication in ethanol (30 mins) + acetone (30 mins)	15.6 ± 0.8	35.6 ± 1.8	48.8 ± 2.4
3	Rinsing in dichloromethane (2 mins), acetone (2 mins), and ethanol (10 mins)	10.1 ± 0.5	34.9 ± 1.7	54.9 ± 2.7
4	Immersion in 3:1 ratio of H_2SO_4:H_2O_2 piranha solution (30 mins)	12.8 ± 0.6	36.1 ± 1.8	49.6 ± 2.5

The XPS spectra for Si-APDMS, Si-APDMS-SMP, and Si-APDMS-SMP-[GRGDSPC-Lys(TAMRA)] are shown in Figure IV.15, Figure IV.16, and Figure IV.17, respectively. In each figure, the top diagram represents the full XPS spectrum while the middle and bottom diagrams show highly resolved and fitted C1s and N1s spectra, respectively. As the GRGDSPC-Lys(TAMRA) should exhibit detection of a sulfur atom, the highly resolved S2s spectrum is shown in Figure IV.18 for this substrate.

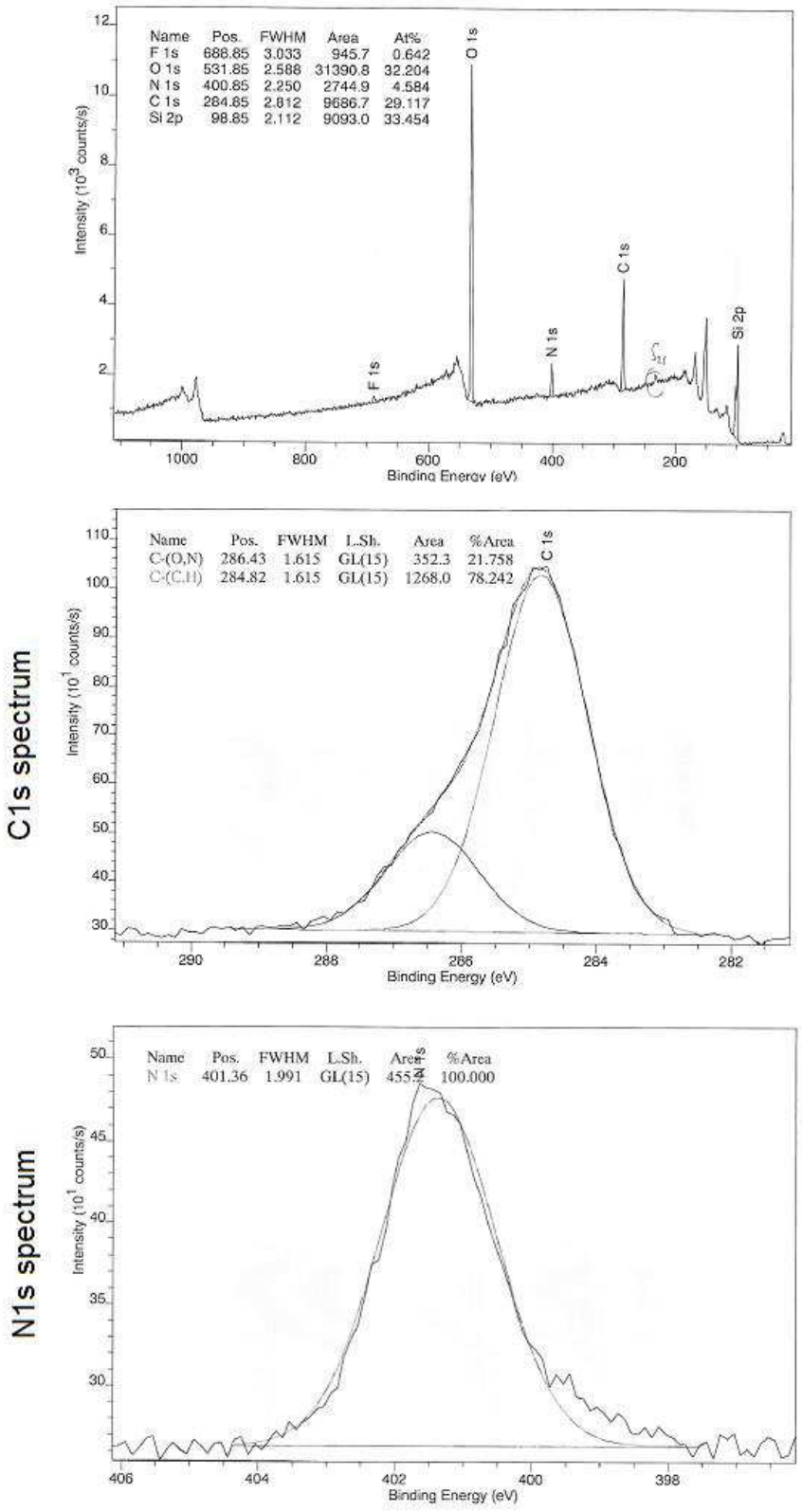

Figure IV.15 – XPS spectra for Surface 2, Si-APDMS. Top: full spectrum; middle: C1s spectrum; bottom: N1s spectrum. 3 different zones were scanned on the sample.

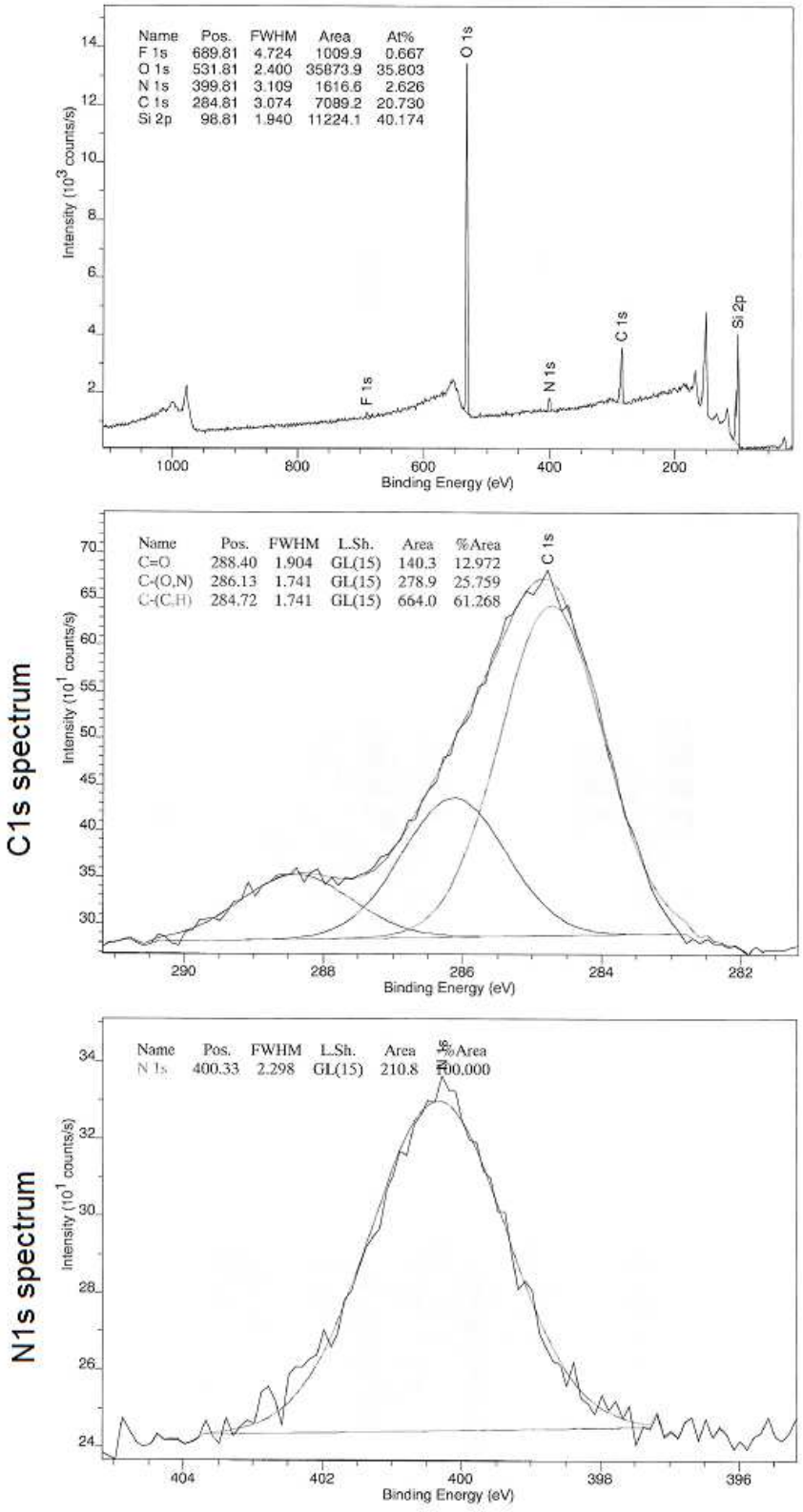

Figure IV.16 – XPS spectra for Surface 3, Si-APDMS-SMP. Top: full spectrum; middle: C1s spectrum; bottom: N1s spectrum. 3 different zones were scanned on the sample.

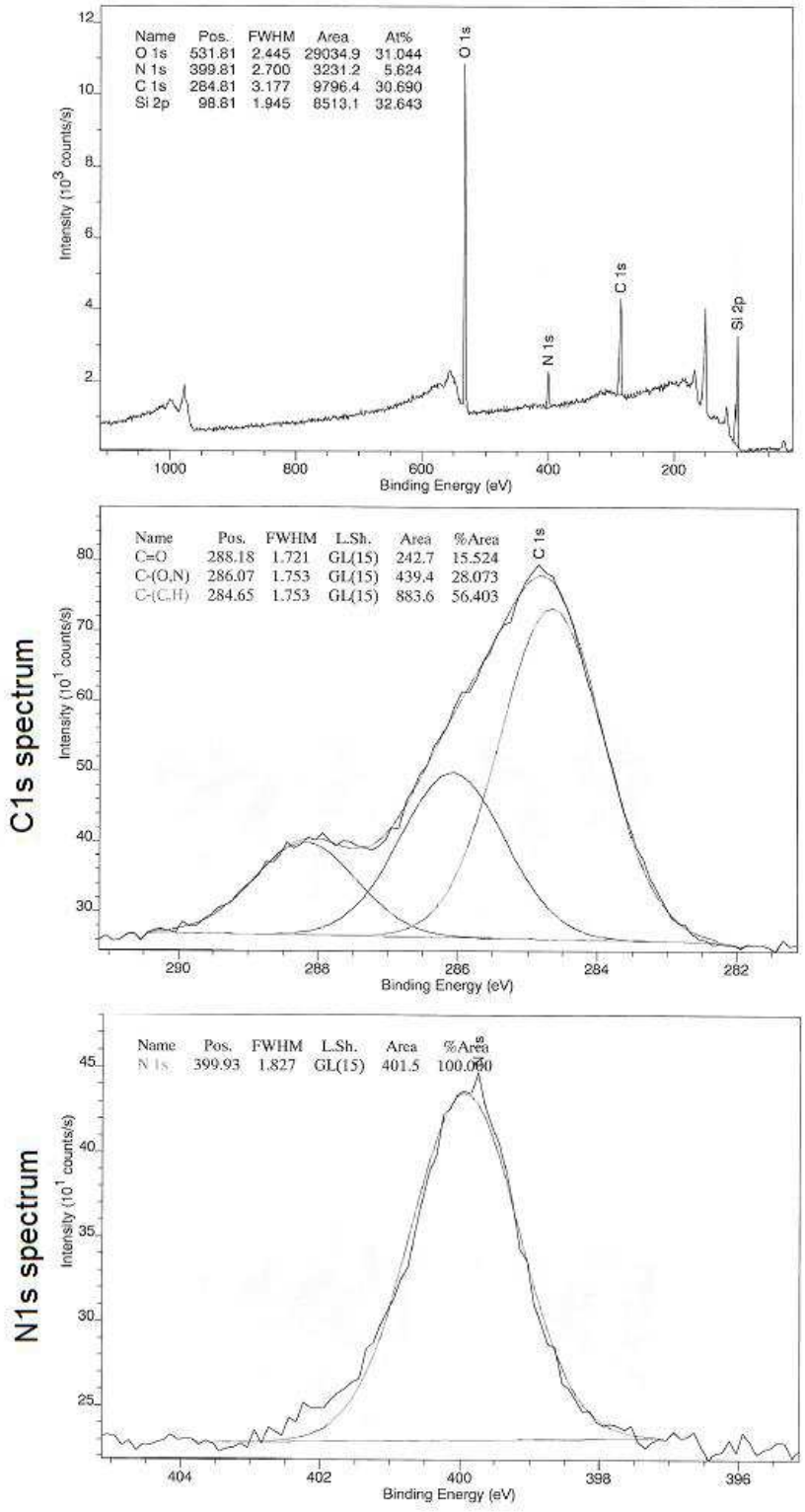

Figure IV.17 – XPS spectra for Surface 4, Si-APDMS-SMP-[GRGDSPC-Lys(TAMRA)]. Top: full spectrum; middle: C1s spectrum; bottom: N1s spectrum. 3 different zones were scanned on the sample.

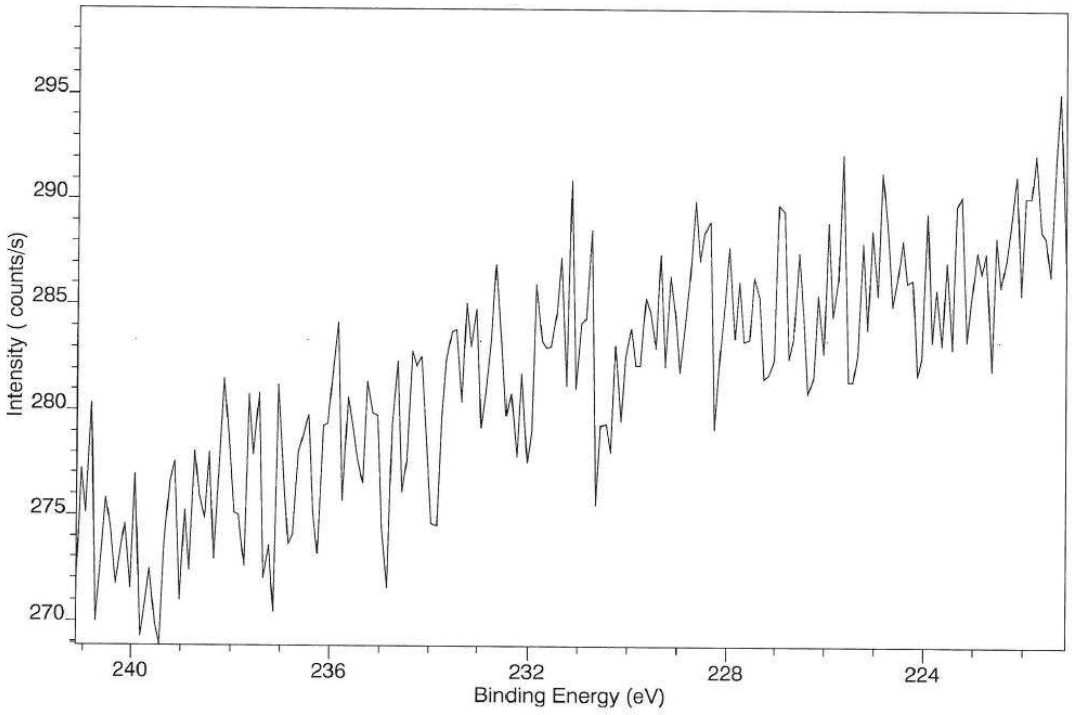

Figure IV.18 – Highly resolved S2s fit for Surface 4, Si-APDMS-SMP-[GRGDSPC-Lys(TAMRA)].

An analysis of atomic concentrations for the four surfaces was carried out based on elemental composition analysis and molecular density from XRR results presented previously. These results are outlined in Table IV.3. The ratios of atomic concentration are shown in Table IV.4.

Table IV.3 – XPS analysis of atomic concentration for the four surfaces, T = theoretical value, E = experimental value

	Atomic concentration %							
	C		**N**		**O**		**S**	
	T	**E**	**T**	**E**	**T**	**E**	**T**	**E**
Surface 1 – Silicon	---	12.8	---	0	---	36.1	---	---
Surface 2 – Previous + amino-silane APDMS	22.7	29.1	4.5	4.6	4.5	33.5	---	---
Surface 3 – Previous + heterolinker SMP	26.8	20.7	4.9	2.6	10.5	35.8	---	---
Surface 4 – Previous + peptide GRGDSPC-Lys(TAMRA)	31.8	30.7	7.3	5.6	10.4	31.0	0.4	---

Table IV.4 – Atomic concentration ratio for the four surfaces, T = theoretical value, E = experimental value

	Ratio of atomic concentrations			
	N/C		**O/C**	**N/Si**
	T	**E**	**E**	**E**
Surface 1 – Silicon	0	0	2.86	0
Surface 2 – Previous + amino-silane APDMS	0.20	0.16	1.11	0.14
Surface 3 – Previous + heterolinker SMP	0.18	0.13	1.72	0.06
Surface 4 – Previous + peptide GRGDSPC-Lys(TAMRA)	0.23	0.18	1.01	0.17

All experimental ratios of surface nitrogen to carbon are slightly lower than the theoretical values. A small amount of adventitious carbon on the surface contributed to this result, and is expected [235]. Oxygen atoms continue to be abundantly detected on at every step due to the existence of a layer of native Si oxide on the substrate surface. Surface 2, which represents the first step of functionalization with an amino-silane, shows a contribution of N1s spectrum, indicative of the C-N(H_2) bonds on the ADPMS. Additionally, the appearance of a peak at 401.36 eV shows that nitrogen is involved in oxidized environments (for example C-N-O bondings combined with oxygen pollution or due to some interactions between terminal amino group and oxygen groups near the substrate [49, 236]). This contribution of nitrogen has been observed previously [48, 49]. The appearance of a C=O peak at 288.40 eV on the C1s spectrum of Surface 3 (Figure IV.16) upon the addition of the heterolinker is expected due to the C=O bonds that are present on the SMP molecule. At the peptide grafting step, the atomic concentration of N increases from the previous step (Figure IV.17), which is reasonable due to the amide bonds present within the peptide and the nitrogen atoms on the arginine. Moreover, the presence of C=O bonds in the peptide on Surface 4 increases the C=O ratio, apparent at 288.14 eV, in the C1s spectrum of the last step (Figure IV.17). In terms of sulfur (S), there is only one S that appears throughout the entire functionalization process, on the peptide that is grafted in the final step. The molecular

density of the peptide on the surface is very low, as detected by XRR, which in turn corresponds to a relatively small amount of S present on the surface. In addition, since the S is directly linked to the heterolinker SMP, it is well nested under the peptide chain. XPS was unable to detect this S due to this low surface density of S atoms and the depth at which the S is found. The instrument may not have been sensitive enough to detect the strongly attenuated electrons from deeper into the sample, giving a poor sensitivity in the final spectrum.

We can compare the values of atomic concentration ratio to published results where similar functionalization protocols were employed. In our group, we have previously grafted RGDC peptides using the same three-step procedure, first on silica [49] and then on Ti-6Al-4V alloy surfaces [48]. APTES, an amino-silane with three reactive ethoxy groups, was used in these studies instead of APDMS, a monofunctional amino-silane. We also compare our results with a study done using silicon as a base substrate and APTES in the silanization step [237]. SMP was used as a heterolinker in all of these studies and a cysteine-containing RGD peptide was grafted onto the surfaces. We find that on all surfaces, the N/C ratio is relatively consistent across every study. However, there is substantial variation in the ratios of O/C and N/Si. Our results generally show a much higher O/C ratio and much lower N/Si ratio compared to the three studies that were cited. For example, on the silane functionalized silicon surfaces, our results for the O/C and N/Si ratios are 1.11 and 0.14, respectively, while Davis *et al.* reported values of 0.43 and 0.55. It is nearly impossible to calculate the expected atomic concentrations of Si and O due to the underlying Si substrate and the activated OH groups that are present, but several possibilities could account for these differences in atomic ratios. To clean our surfaces, we used a 3:1 mix of H_2SO_4:H_2O_2 in our piranha solution, while mixtures of 1:1 and 9:1 were used in previous reports of our lab. Also, Davis *et al.* treated samples using a mixture of H_2O_2 and ammonia (instead of H_2SO_4). The initial surface cleaning method may have resulted in different surface compositions at the beginning of the functionalization, thus affecting grafting density in subsequent steps. In addition, our silanization step was performed in the gas phase obligatorily to avoid problems related to capillarity and resist swelling (in nanopatterned samples, as they were functionalized in parallel with homogeneous controls). In the other studies, this step was performed in the liquid phase. The difference in experimental conditions,

in combination with reaction time and temperature, may account for a different density of grafted silane. Finally, as analyzed in Chapter IV.1.3 with XRR, SMP resulted in very low grafting density, which may have contributed to the high O/C and low N/Si ratios on Surface 3 (Table IV.4).

1.5 Atomic force microscopy characterization of nanopatterned surfaces

AFM was performed in contact mode on both $D_{150}S_{350}$ and $D_{80}S_{110}$ nanopatterned surfaces to show the topographical contrast between the PEO silane background and the nanopatterned regions (Figures IV.12A and IV.12B for $D_{150}S_{350}$ and $D_{80}S_{110}$, respectively). Data was acquired in height mode to obtain a topographical representation of the surface, with 3D rendering showing well-defined nanopatterned features in Figure IV.19C and Figure IV.19D. The inspection of the linear profiles extracted from these images showed that a feature diameter of 150 nm and a interdot gap width of 350 nm were obtained for $D_{150}S_{350}$ (Figure IV.19E) and a feature diameter of 80 nm and a interdot gap width of 110 nm were obtained for $D_{80}S_{110}$ (Figure IV.19F). These values are in perfect agreement with the master mold specifications, testifying for the accuracy of the implemented nanofabrication process.

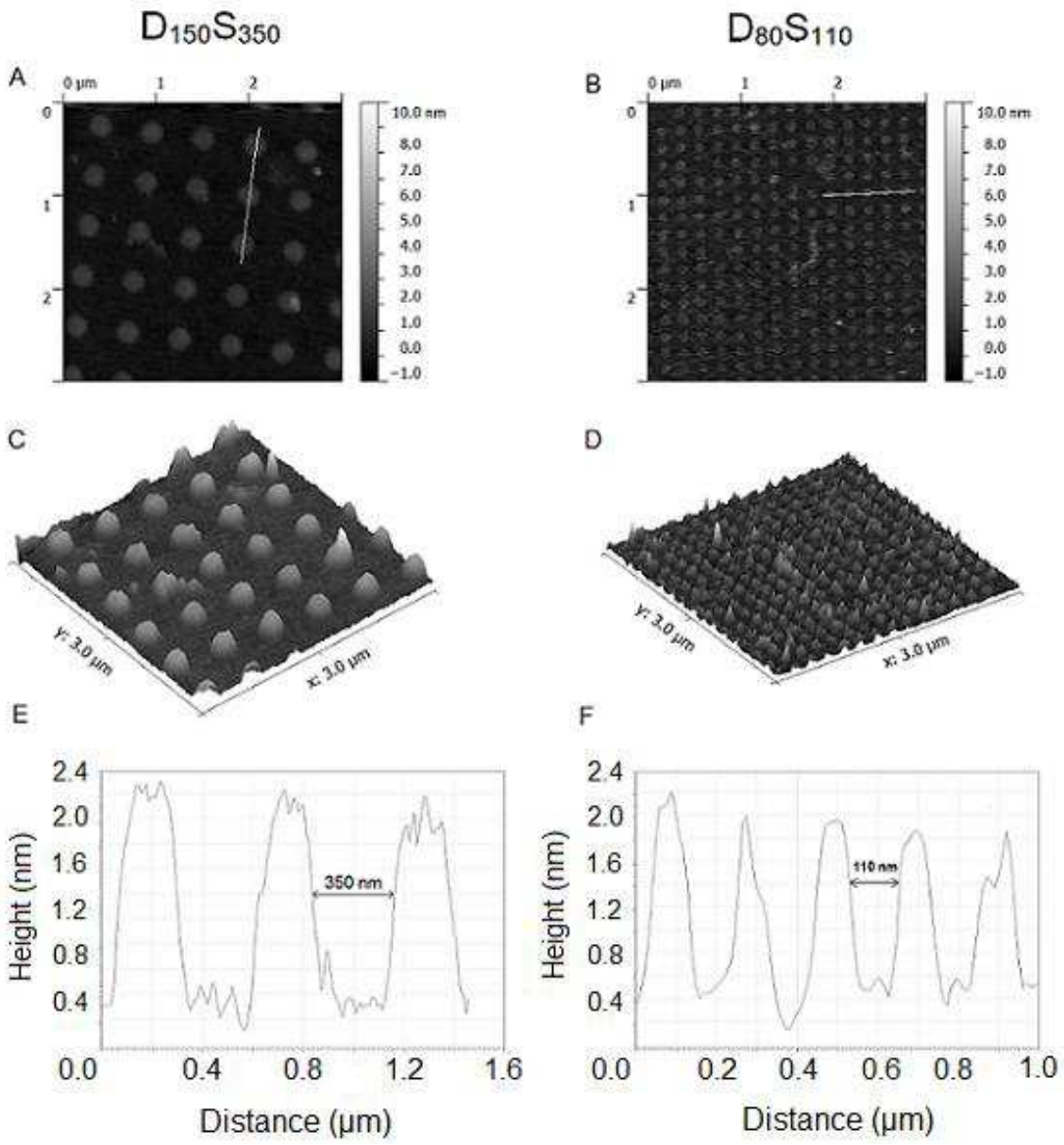

Figure IV.19 – AFM characterization of nanopatterned surfaces. Contact mode measurements performed on (A) $D_{150}S_{350}$ and (B) $D_{80}S_{110}$ surfaces. The nanosized features are grafted by SMP (hetero-bifunctional cross-linker). The difference in height between the background and the nanodots is indicative of topographical contrast between the SMP and the PEO layers. 3D reconstruction of the (C) $D_{150}S_{350}$ and (D) $D_{80}S_{110}$ surfaces was performed on an area of 3 x 3 µm² to illustrate topography. Height profiles of the lines drawn in (A) and (B) are shown respectively in (E) and (F).

AFM is a popular surface characterization technique often used to probe biomolecules and biomaterial surfaces and interfaces [238, 239]. Aside from revealing the topographical and chemical nature of a surface, AFM has also been used as a tool to

measure mechanical properties and surface interactions using force spectroscopy [240]. Because of its high resolution, AFM imaging allows surfaces involving nanostructures to be validated by showing individual nanofeatures present on the surface. For instance, nanoscale topographical features, whether through the creation of physical nanotopography [121, 241] or chemical nanotopography [124, 224], have been visualized using AFM. The technique has also been used in our group to assess surface roughness and morphology [43].

Herein, we use AFM to get a more precise idea of the type of topographical features that we are working with. In developing the technique of functionalizing our surfaces using a silanization method, our group in Belgium has previously validated the approach by preparing nanopatterned surfaces that were modified with different silanes that contain a wide-range of functional groups [234]. Different types of nanopatterns have been produced using electron beam lithography, including lines with nanoscale width and periodicity and dots with varying diameters and pitch spacing. These surfaces have been successfully characterized using AFM, with clear topographical contrast and height profiles, showing the very high accuracy and resolution that can be attained.

Our results of AFM analysis can be coupled to homogeneous surface characterization by XRR to yield additional implications. Surprisingly, in the AFM images, the SMP-grafted features are seen higher than PEO background which contrasts with XRR data (Table IV.1). This phenomenon could be due to the softer nature of the PEO silane monolayer, which permits the tip to penetrate the layer, and to the coupling of friction and topography in the images [242, 243]. In contact mode, since the background component of the surface (PEO silane) is soft, it is indented by the AFM tip and thus a topography image of apparently lower height is generated [244]. The difference of height between the different regions is lower than 2 nm, showing that the topographical variation can be neglected. Importantly, it should be realized that the observed difference of topography may be smaller than measured, due to possible AFM artifacts for chemically-patterned close-to-flat surfaces.

As a perspective, we propose several modifications in our use of AFM in order to further improve accuracy and resolution. First, instead of using either contact mode or tapping mode during the acquisition, we can attempt to image using force mapping

mode. This mode offers several working advantages over contact or tapping mode, including the decrease in lateral forces and the independence of zero-force height and zero-force volume on trigger force. In turn, force mapping mode allows a more accurate measurement of height and volume on soft samples [244]. Second, the AFM tip can be functionalized to enhance its efficiency. Tip functionalization minimizes tip-sample adhesion and allows molecular recognition to be more specific [245]. Finally, image acquisition could be done in liquid instead of in air. In this way, soft samples, such as the PEO silane, are less susceptible to disruption in liquid and so can be imaged with minimal damage [246].

1.6 Fluorescent visualization of nanopatterned surface

With confocal microscopy and the use of a fluorescent peptide, functionalized nanopatterns can be visualized. A nanopatterned ($D_{150}S_{350}$) surface functionalized with a TAMRA-tagged GRGDSPC peptide was imaged and shown in Figure IV.20. Herein, our results complement those obtained with AFM, confirming the successful transfer of the nanopatterns via nanoimprint lithography and the grafting of peptides on the nanopatterned regions. While AFM is able to detect chemical contrast locally, its scan size is usually limited within a few micrometers. Confocal microscopy, on the other hand, enables imaging of a much larger field of view, and the nanopatterns in Figure IV.20 indeed affirm that large areas can be patterned and functionalized on the nanoscale using the nanoimprint method. Furthermore, while we note the presence of peptide aggregates on the surface, it is also clear that on the grand scheme, the nanopatterned peptide nanodot arrays are very ordered and regularly distributed.

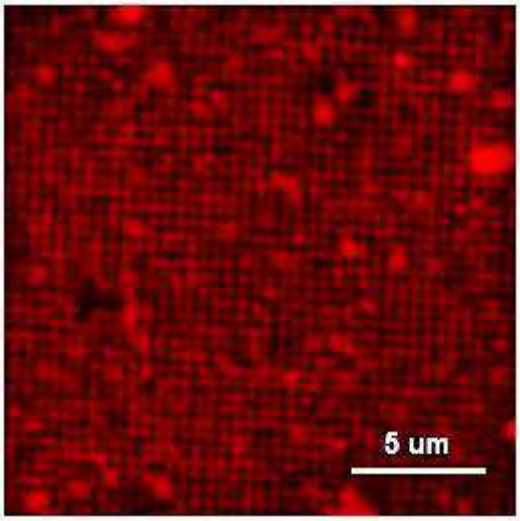

Figure IV.20 – Confocal microscopy visualization of nanopatterns, with $D_{150}S_{350}$ surface functionalized with fluorescent TAMRA-grafted GRGDSPC peptide.

1.7 Evaluation of substrate stiffness and elasticity

In the surface characterization part of our studies, we planned to evaluate the mechanical properties of our materials before and after the grafting of peptides. We wanted to find out whether surface functionalization using peptides can modify the surface in terms of hardness and elastic modulus. We intended to carry out this part of the study in collaboration with our industry partner in Bordeaux, Rescoll. For the analysis of very thin films and coatings, an available technique at Rescoll is ultra nanoindentation. We attempted to extract some useful information about substrate rigidity and stiffness using this technique but the trials were unsuccessful due to the extremely small thickness of our peptide layers, far below the range measurable by ultra nanoindentation. Thus, no conclusions were drawn from these tests.

Substrate stiffness is a macroscopically observable property whereas the modification of a substrate surface with peptides is a nanometric phenomenon. When referring to stiffness, one alludes to a cell's sensing of its environment in terms of substrate rigidity and deformability. In such case, peptide grafting has negligible influence on mechanical properties such as hardness and surface elastic modulus. However, the mechanical interactions between cells and surface-immobilized peptide chains are interesting, in particular with regards to the force that is exerted on the cell

by the elasticity and flexibility of the peptide chains. These chains are present in different states or conformations depending on the environmental conditions, such as the addition of a solvent that causes the peptide to swell or stretch. In turn, the swelling and stretching motions of the peptide chains may introduce forces on cells that would not be observed on non-functionalized surfaces.

We propose the use of more sensitive techniques to measure the interactions between cells and molecules present on the substrate surface. AFM-based methods such as AFM indentation and single molecule force spectroscopy can be employed to measure force-related phenomena at the single-molecule level [240, 247-249]. Since AFM measurements can be done at the nN range (compared to μN for ultra nanoindentation), it is possible for information related to cell-peptide interactions to be extracted. The proposal of these techniques forms the basis of our future works and perspectives. (The work that was done at Rescoll using ultra nanoindentation is summarized in the Appendix A.2.)

1.8 Contact angle and surface energy analysis

The surface energy of a material has been known to be related to cell adhesion [250-254]. It is of interest for us to study the surface energy of the different substrates used in our experiments and see whether surface energy may be a parameter that impacts cell behavior. To measure surface energy, the sessile drop technique was applied using a goniometer, where the surface contact angles of various test liquids were observed on different surfaces. The test liquids have different degrees of polarity with known values of surface tension (γ_L), which is further split into dispersive and polar components, γ_L^d and γ_L^p, respectively. The measured values of contact angle can then be used to calculate surface energy, specifically the components that correspond to non-polar and polar interactions. This method directly relates surface wettability to surface energy. For our study, three test liquids (water, diiodomethane, ethylene glycol) were used to measure contact angle on different modified substrates. The values of surface tension for these liquids are broken down into dispersive and polar components, and shown in Table IV.5.

Table IV.5 – Literature values of surface tension components of common test liquids [255]

Liquids	γ_L (mN/m)	γ_L^d (mN/m)	γ_L^p (mN/m)
Water (H_2O)	72.8	21.8	51.0
Diiodomethane (CH_2I_2)	50.8	50.8	0
Ethylene glycol ($C_2H_6O_2$)	48.0	29.0	19.0

Dispersion forces are universal forces that act between any atoms or molecules, both polar and non-polar. However, when polar or chemically-interacting substances are involved, additional forces may come into play. For example, considering the case of wetting a surface with water or alcohol, not only dispersive but also dipole-dipole and hydrogen bonding interactions are to be taken into account. These specific interactions result in stronger adhesion between the liquid and substrate due to the contribution of the polar components [256].

Evidently, the polarity of the three test liquids varies, resulting in differences in specific surface interactions with the substrates. Diiodomethane is a non-polar molecule and thus its polar component of surface tension is zero. Contrarily, water is a highly polar molecule, as demonstrated by its high polar component of surface tension. To calculate surface tension of a substrate, several equations of state have been developed. One commonly used formula is the Fowkes equation [251, 255, 257], which states that:

$$\gamma_L(1+\cos\theta) = 2[\sqrt{\gamma_L^d \gamma_S^d} + \sqrt{\gamma_L^p \gamma_S^p}]$$

where the parameters are defined as follows:

Υ_L = total surface tension of test liquid
Υ_L^d = dispersive component of test liquid surface tension
Υ_L^p = polar component of test liquid surface tension
Υ_S^d = dispersive component of substrate surface energy
Υ_S^p = polar component of substrate surface energy
θ = contact angle of test liquid on substrate

Using the Fowkes equation and the measured contact angles of each test liquid on the various surfaces, surface energy can be calculated by adding the dispersive and polar components. We performed contact angle measurements on different material surfaces with three drops of each test liquid on different regions of each sample. The average values of the measured contact angles and calculated surface energies are shown in Table IV.6 and Table IV.7, respectively.

Contact angle measurement is a quick and simple tool of determining whether a surface has been modified properly. As seen in Table IV.6, the contact angle of water shows a slight decrease when silicon is modified with the PEO silane. In the case of APDMS, a sharp increase in contact angle was observed, indicating that modifying the surface with an amino-silane increases its hydrophobicity [258, 259]. The grafting of RGD again lowers the contact angle in both homogeneous and patterned cases, demonstrating that the surface has been further modified.

Table IV.6 – Contact angle measurements in different test liquids ± standard deviation

	Water (°) ± SD	**Diiodomethane (°) ± SD**	**Ethylene glycol (°) ± SD**
Si poli	43.3 ± 0.1	48.3 ± 1.0	28.4 ± 2.4
Si PEO	38.3 ± 0.4	30.5 ± 1.3	26.5 ± 0.3
Si APDMS	82.0 ± 1.5	52.6 ± 2.0	58.2 ± 4.3
RGD H	66.6 ± 0.8	39.3 ± 1.1	55.5 ± 3.5
$D_{150}S_{350}$	59.0 ± 0.5	39.9 ± 1.9	44.1 ± 1.6

Table IV.7 – Surface energy analysis using goniometry

	γ_L **(mN/m)**	γ_L^d **(mN/m)**	γ_L^p **(mN/m)**
Si poli	54	29	25
Si PEO	58	35	23
Si APDMS	34	30	4
RGD H	42	32	9
$D_{150}S_{350}$	46	33	13

The contact angle on each substrate is used to calculate the surface energy and as expected, there is an inverse correlation between the two parameters. The substrate with the highest contact angle, APDMS, has the lowest surface energy, while the substrate with the lowest contact angle, Si PEO, has the highest surface energy. The value of surface energy for the nanopatterned, peptide-modified substrate $D_{150}S_{350}$ lies between the values for Si PEO and RGD H. This result is logical as the $D_{150}S_{350}$ surface essentially contains large square arrays of RGD-grafted nanodots distributed within a PEO background (refer to Figure III.1 and Figure IV.1). Even though the peptides only occupy approximately 7% of the entire substrate surface (Figure IV.1), the presence of peptide on nanodomains and their specific interactions with the test liquids exert enough impact to cause a change in surface energy on a substrate which is mostly grafted with PEO.

Because surface tension is a surface free energy, the surface tension of the composite surfaces should be a linear combination of the surface tensions of the homogeneous surfaces, with the relative surface fractions being the multiplicative factors. However, this is not the case, since the surface tension of $D_{150}S_{350}$ is much closer to the one of the RGD H surface than expected based on its composition. This suggests that the measurement of contact angle might have been affected by effects such as droplet pinning, which should tend to increase the contact angle and therefore translate into lower apparent surface tensions.

In terms of the relationship between surface energy and cell adhesion, different conclusions have been drawn in the literature. Some studies conclude that cell adhesion is enhanced as surface energy increases [250-252]. Others, however, point out an inverse relationship between cell adhesion and surface energy, arguing that hydrophobic surfaces (high contact angle, low surface energy) enhances protein adsorption and in turn promotes cell adhesion [253, 254]. These discrepancies can be explained by the differences in experimental conditions, such as material selection, fabrication methods and parameters, cell type, and cell culture environment. In light of these different conclusions, our results are in agreement with the set of studies that propose an enhancement of cell adhesion as a result of lowered surface energy (however, we must keep in mind that this is the case on non-bioactive surfaces, and the presentation of an adhesion motif will change the dynamics of interaction). Our surfaces

with the lowest surface energies (Si APDMS, RGD H, and $D_{150}S_{350}$) indeed do show better cell adhesion, as will be shown in Chapter IV.2. This phenomenon is to be expected, as cells are known to adhere well on amine-modified surfaces (Chapter I.3.4), and RGD, being an adhesion-promoting ligand, definitely enhances cell adhesion as well. It is also the case that while increasing surface energy is correlated with increasing cell adhesion in the absence of surface modification, the sequence-specific recognition of the RGD motif is a stronger factor in determining cell adhesion than surface energy. Thus, the changes in surface energy observed with surface modification do little to alter the adhesion behavior that is elicited by the RGD peptide.

2. Influence of RGD on hMSC adhesion and differentiation

2.1 Human mesenchymal stem cell adhesion

Human mesenchymal stem cells (hMSCs) were cultured on different types of silicon surfaces, including homogeneous controls (Si poli – bare, polished silicon; Si PEO – silicon modified with cell-repellent PEO silane; Si APDMS – silicon modified with APDMS; and RGD H – silicon homogeneously functionalized with GRGDSPC peptide) and two types of GRGDSPC peptide-functionalized nanopatterns, $D_{150}S_{350}$ and $D_{80}S_{110}$ (as described in Materials and Methods, Chapter III.2.1). hMSCs were immunofluorescently stained after 24 hours in culture to visualize and compare their adhesive behaviors on silicon substrates, whether homogeneous or nanopatterned (Figure IV.21). See culture conditions and immunofluorescence procedure in Materials and Methods, Chapters III.4 and III.5.1, respectively.

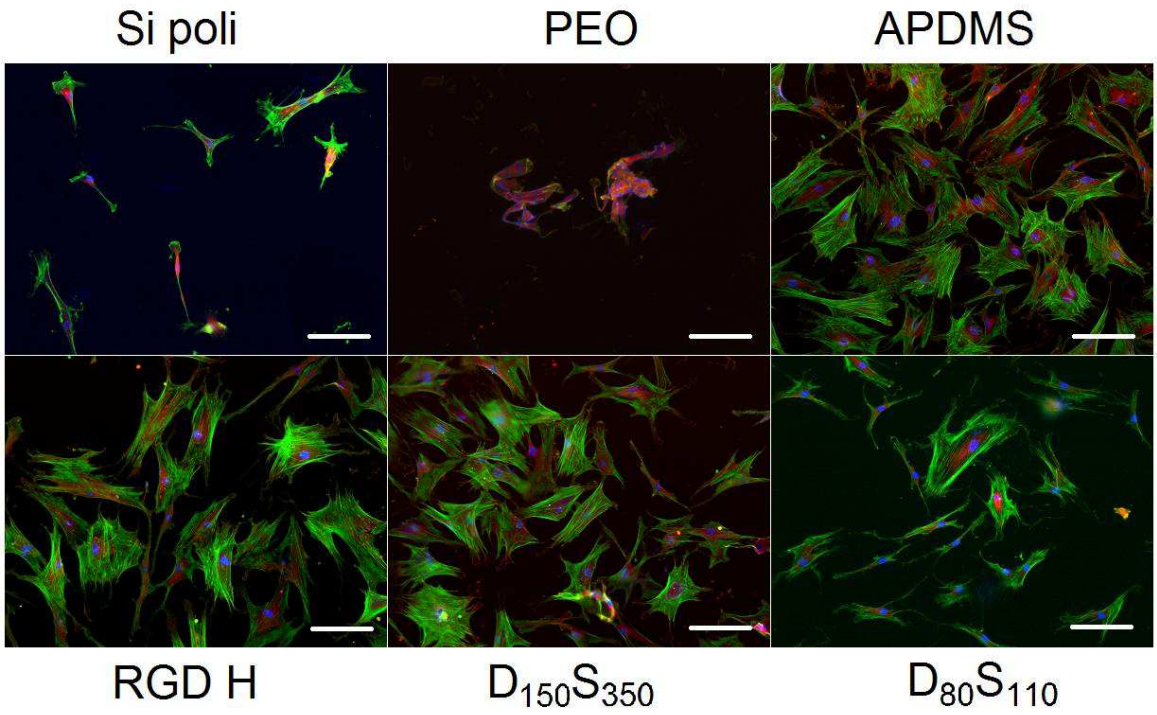

Figure IV.21 – hMSC adhesion at 24 hours and 4 weeks post-seeding on RGD-grafted surfaces and non-functionalized controls, low magnification fluorescent images; scale bar = 100 µm. Experiments were performed in duplicates (n = 2 samples per condition).

As expected, cells failed to adhere on Si PEO surfaces due to the cell-repellent nature of the PEO silane, confirming that cell interactions with the nanopatterned materials is strictly mediated by RGD. Few cells adhered on Si poli, and limited spreading is observed for the cells that did adhere. Additionally, an APDMS surface, where Si is functionalized with APDMS, is included in the analysis, as amine functional groups have been shown to promote cell adhesion [101]. Indeed, this is the case as more hMSCs adhered on APDMS surfaces than Si poli. In terms of the three RGD-grafted surfaces (RGD H, $D_{150}S_{350}$, and $D_{80}S_{110}$), all show relatively higher numbers of adhering cells compared to non-modified Si poli.

Confocal microscopy enables fluorescent, nanopatterned peptide dots to be visualized at the same time as hMSCs that have been immunofluorescently stained, as shown in Figure IV.22. Ideally, the correlation between nanopatterns and cell properties, such as size and orientation, can be extracted with this method. An image of a nanopatterned ($D_{150}S_{350}$) peptide grafted surface is taken after cell culture (Figure IV.22B). The image shows the grid-like backdrop which represents the nanopatterns that have been functionalized with the fluorescent peptide (see Chapter IV.1.6). After cell culture, the image shows focal adhesions (FAs) in the form of red clusters in the foreground, on top of the grid lines. Individual filaments extending from the cell body were also observed to interact with the nanopatterns in Figure IV.22B.

The number of adherent cells per cm^2 was characterized at 24 hours and 4 weeks post-seeding and the 4-week proliferation rate was calculated (Figure IV.23 and Figure IV.24). RGD samples clearly showed higher cell counts than Si poli at both time points, while nanopatterned samples have fewer adherent cells than the homogeneous RGD control at 4 weeks. Cell proliferation is expressed as percentage change from 0 to 4 weeks. Si poli showed almost no proliferation while cells on RGD H proliferated significantly better than on both $D_{150}S_{350}$ and $D_{80}S_{110}$.

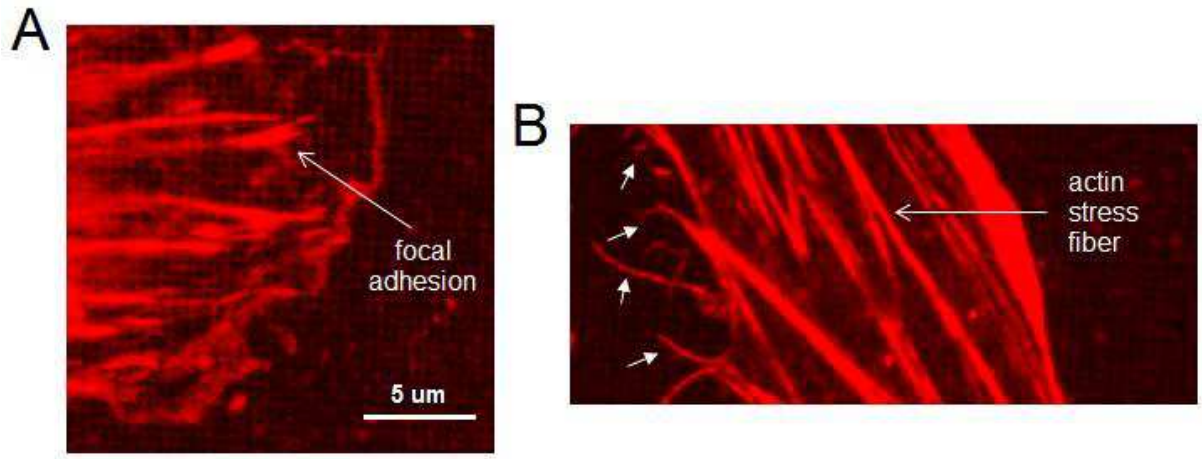

Figure IV.22 – Confocal microscopy visualization of nanopatterns after cell culture, with $D_{150}S_{350}$ surface functionalized with fluorescent TAMRA-grafted GRGDSPC peptide in the background. hMSCs were cultured on nanopatterns and images were taken 24 hours after seeding (A). Focal adhesions are labeled as red clusters in the foreground. Individual cell interactions with the nanopatterns are seen in (B), indicated by small white arrows.

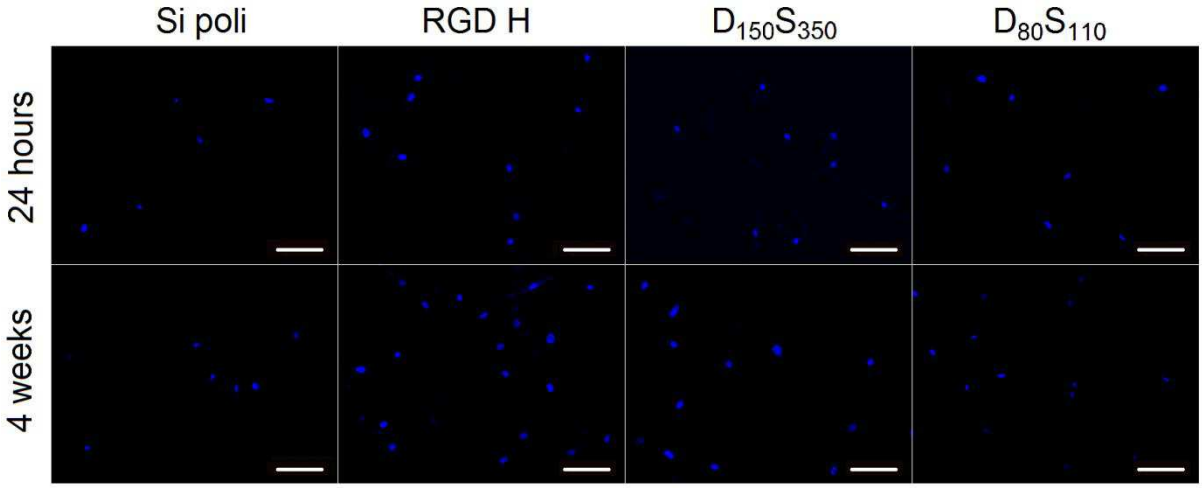

Figure IV.23 – Nuclear staining of hMSCs 24 hours and 4 weeks post-seeding on RGD-grafted surfaces and non-functionalized control. The number of adherent cells on each sample was obtained by counting the number of nuclei present on each surface and calibrating with a magnification factor; scale bar = 100 µm. Experiments were performed in duplicates (n = 2 samples per condition).

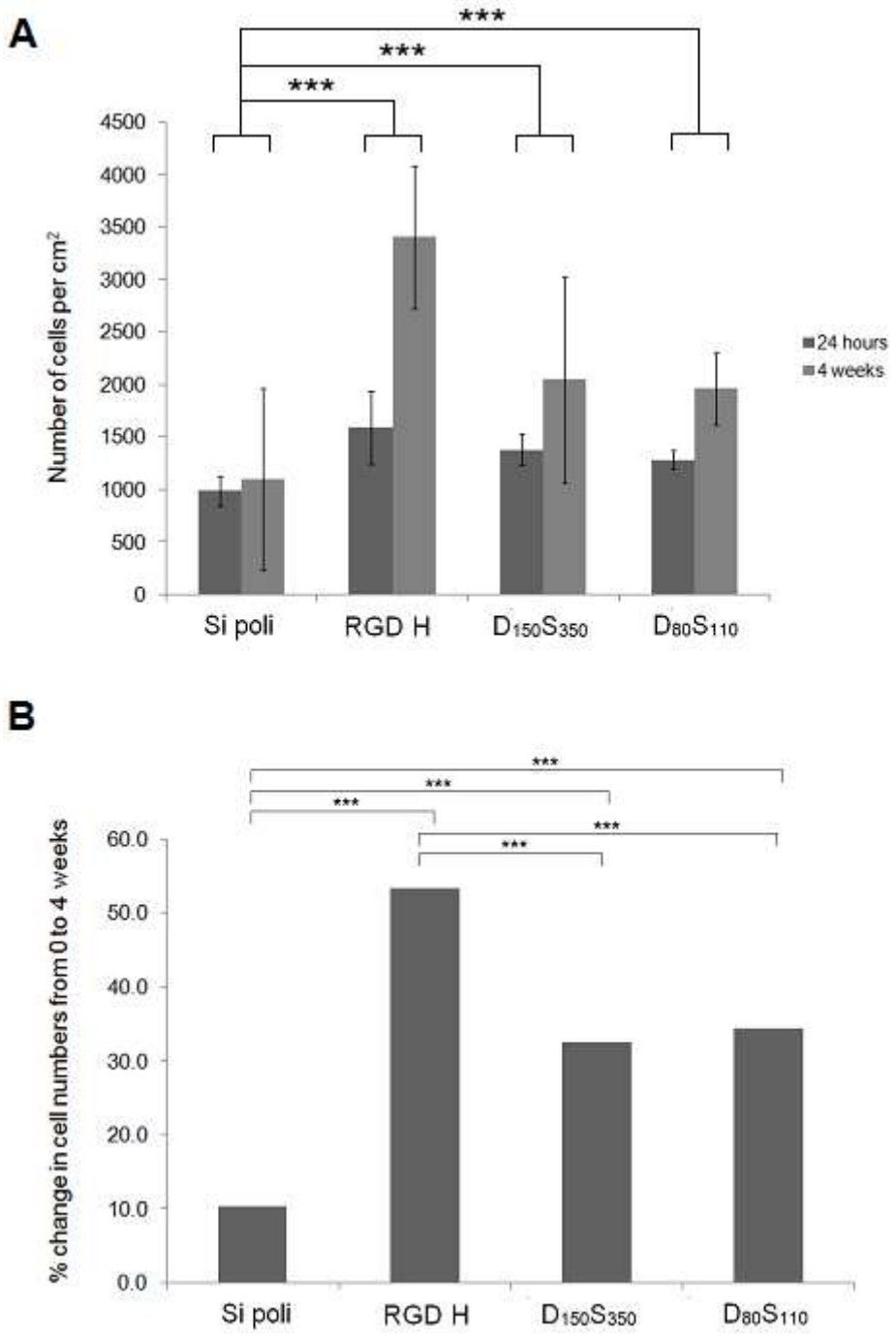

Figure IV.24 – hMSC adhesion and proliferation analysis on RGD-grafted surfaces and non-functionalized control. (A) The number of adherent cells per cm² was counted for each substrate at 24 hours and 4 weeks post-seeding. The RGD samples showed obvious increases in cell count, indicative of cell spreading, while limited spreading is seen on Si poli. (B) The rate of cell proliferation from 0 to 4 weeks in culture is expressed as percentage change in cell numbers. Cells on RGD H proliferated significantly better than on both $D_{150}S_{350}$ and $D_{80}S_{110}$; * represents a *p*-value of less than 0.05.**

Cell proliferation and differentiation are extremely coordinated processes that may synergistically determine the fate of stem cells. The results of cell proliferation may serve as an indicator for the presence of hMSC differentiation. Many previous studies have established an inverse relationship between cell proliferation and differentiation, suggesting that cells exist in a high proliferative state before entering a differentiation phase, where proliferation is slowed and ultimately halted in terminally differentiated cells [260-262]. In light of this relationship, we may be able to temporarily propose that since hMSC proliferation is lower on $D_{150}S_{350}$ and $D_{80}S_{110}$ compared with RGD H, that some cells on nanopatterned surfaces have indeed begun the differentiation process and may even be terminally differentiated. Contrarily, hMSCs on RGD H may continue to retain their proliferative capacity without differentiating into any specific mature cell type. This suggestion is very preliminary and will need precise studies of differentiation itself, which will be presented and discussed in Chapter IV.2.5.

2.2 hMSC morphology and spreading

Cell shape and morphology were observed at each condition (except for Si PEO) in terms of average cell spreading area and F-actin stress fiber organization (Figure IV.25 and Figure IV.26). Visually, we noticed that cells that adhered on Si poli samples seem to be smaller in size and lacked defined cytoskeletal organization, whereas on RGD H samples, cells are larger with a more organized cytoskeletal structure as revealed by the arrangement of the stress fibers. $D_{150}S_{350}$ and $D_{80}S_{110}$ show a mixture of cell shapes and sizes, but cytoskeletal arrangement remains organized with defined stress fibers.

To observe the formation of FAs, we stained for vinculin, an important protein that is found at the site of integrin-mediated FAs. We are interested in the behavior of FAs on the various surfaces and whether nanostructured surface chemistry has an effect on the maturation of FAs. Figure IV.25 highlights the typical appearance of FAs found on each type of surface with magnified views of selected regions shown in Figure IV.25A to D. Overall, FAs on Si poli (Figure IV.25A) were little to none, while RGD H exhibited thin clusters of vinculin both around the periphery (Figure IV.25B) and around the nucleus of the cell. In contrast, FAs were observed almost exclusively around the cell periphery

on $D_{150}S_{350}$ (Figure IV.25C) and $D_{80}S_{110}$ (Figure IV.25D), with longer, thicker, and more pronounced clusters, representing points of locally concentrated integrin clustering. Notably, FAs on RGD H are arranged in a seemingly random fashion, whereas on $D_{150}S_{350}$ and $D_{80}S_{110}$, the elongated FAs are aligned along the orientation of the stress fibers (Figure IV.26).

Herein, unlike conventional studies involving physical nanotopography, we prepared materials with chemical nanopatterns, providing a bioactive stage for the induction of specific cell response. We first noted that projected hMSC area is significantly larger on all RGD-grafted surfaces compared to the bare silicon control, after 24 hours in culture (Figure IV.21). RGD, being an adhesion-promoting motif, provides the platform for anchorage between the cells and the material. With the presence of RGD, an adherent cell is able to extend its cytoskeleton and probe into its surroundings while bare Si samples, without such mediator, result in poor adhesion in comparison. Cell shape is also a factor that determines survival and apoptosis, as extensively demonstrated in literature [80, 192, 263-266]. Flat cells that are allowed to spread tend to proliferate and undergo normal cell functions while rounded cells that are restricted from spreading generally undergo apoptosis. The viability of a cell, therefore, is dependent on its ability to anchor onto a substrate. Our observations of hMSC adhesion is consistent with the trend, as the cells appear to be much more spread on RGD-grafted surfaces compared with Si poli or Si PEO surfaces (Figure IV.21) in terms of area and morphology. The significant increase in hMSC area on RGD H, $D_{150}S_{350}$, and $D_{80}S_{110}$ surfaces (shown later in Figure IV.26 and Figure IV.27A) are similar to results published elsewhere [267]. Additionally, a simple cell count (Figure IV.23) confirms that indeed more cells survived on surfaces when they are allowed to adhere and spread.

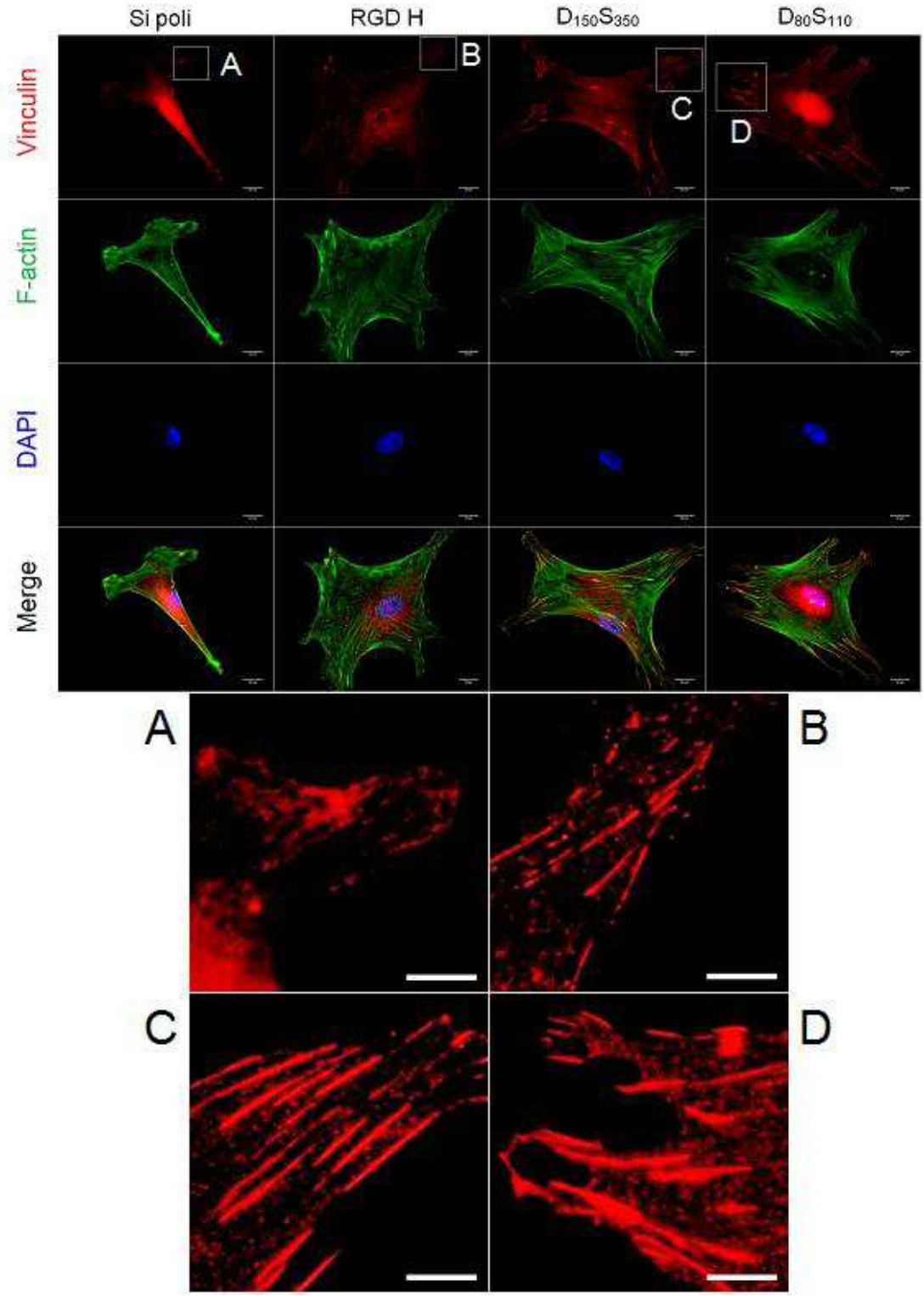

Figure IV.25 – Typical hMSC morphologies on RGD-grafted surfaces and non-functionalized control, with magnified FAs. Cells were immunofluorescently stained and imaged at 24 hours post-seeding with vinculin in red, actin cytoskeleton in green, and nucleus in blue. Top: scale bar = 20 µm; Magnified FAs: scale bar = 10 µm. Experiments were performed in duplicates (n = 2 samples per condition).

2.3 Assessment of contact area and focal adhesion size

hMSCs imaged at high magnification are shown in Figure IV.26. Quantification of projected cell area after 24 hours in culture gave average values of 4566 ± 2182 μm^2, 8240 ± 2243 μm^2, 7940 ± 3219 μm^2, and 7351 ± 2342 μm^2 for Si poli, RGD H, $D_{150}S_{350}$, and $D_{80}S_{110}$, respectively (Figure IV.27A), confirming our observations of cell size.

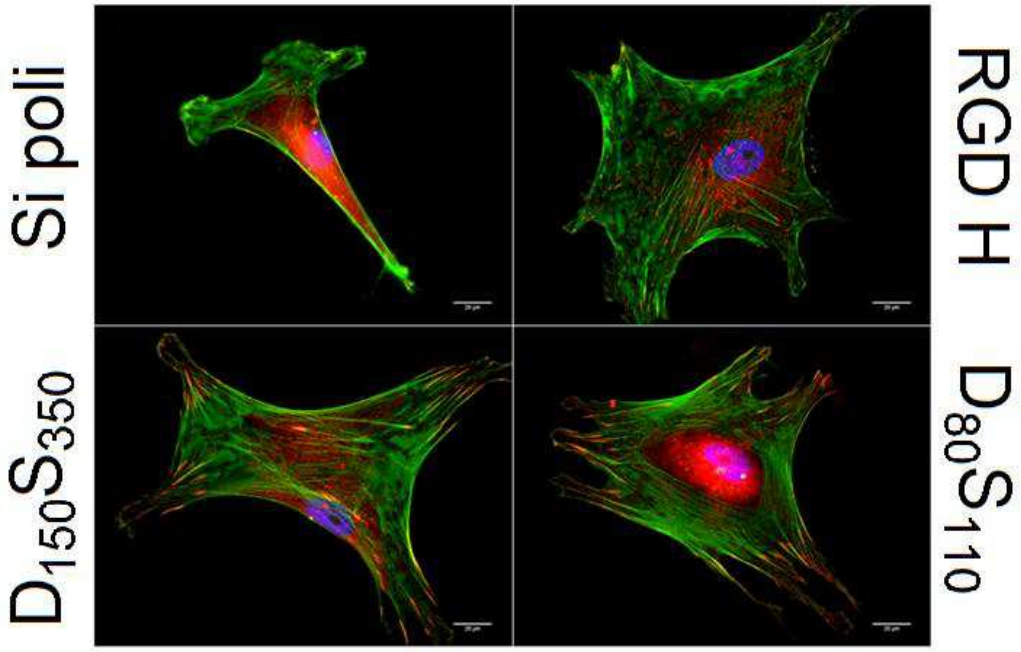

Figure IV.26 – Analysis of hMSC morphology, spreading, and area on RGD-grafted surfaces and non-functionalized control. Cells were immunofluorescently stained and imaged at 24 hours post-seeding with vinculin in red, actin cytoskeleton in green, and nucleus in blue; scale bar = 20 µm. Experiments were performed in duplicates (n = 2 samples per condition).

Further investigation in integrin-mediated adhesion is carried out, in particular the interaction between the cell and material through staining for vinculin, an integrin-related protein. Quantification of the total area of FAs in each cell was carried out on all fluorescent images to characterize the FA-mediated cell-material contact. In terms of total area of FAs per cell, the average values obtained are 196 ± 47 μm^2, 450 ± 42 μm^2, 501 ± 49 μm^2, and 506 ± 51 μm^2 for Si poli, RGD H, $D_{150}S_{350}$ and $D_{80}S_{110}$, respectively (Figure IV.27B). In accordance with the visual observations of FAs presented previously

in Figure IV.25, the limited formation of FAs on Si poli is confirmed by the low total FA area calculated. Moreover, the total area of FAs is greater on patterned substrates compared to the controls, which may indicate a larger degree of cell-material contact. However, such conclusion must also take into account the cell spread area, as a larger cell would naturally have a higher total FA area.

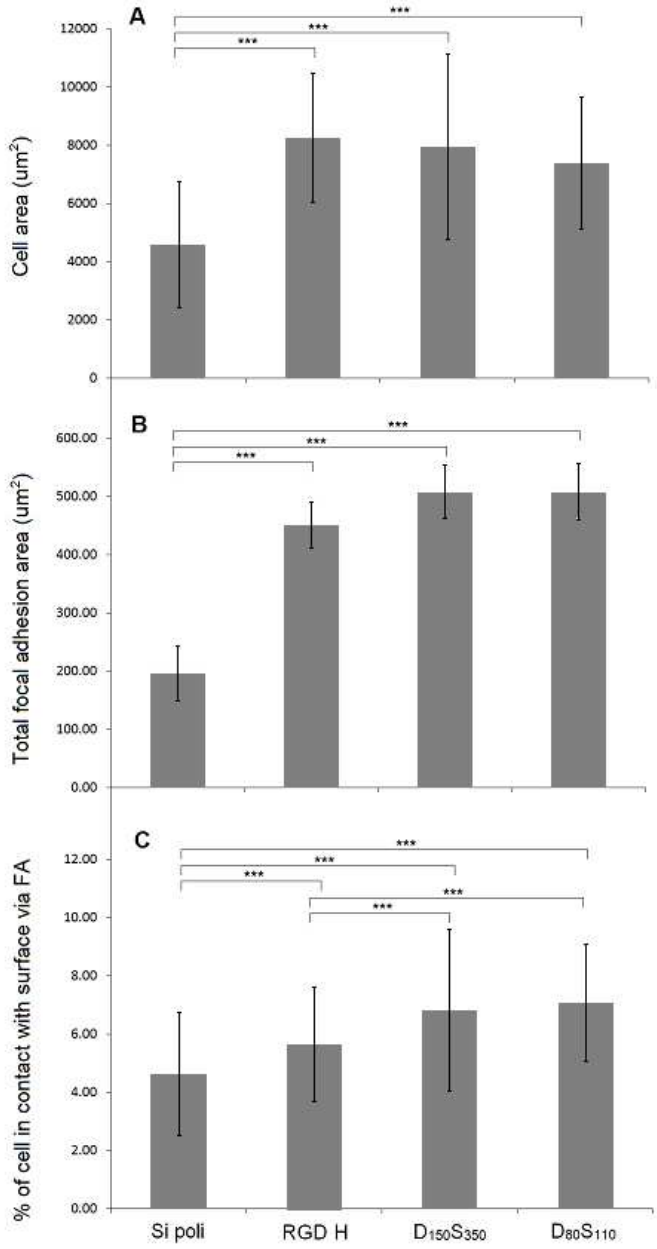

Figure IV.27 – Quantification of cell area, total FA area, and cell-material contact area on RGD-grafted surfaces and non-functionalized control, 24 hours post-seeding, in (A), (B), and (C), respectively; * represents a *p*-value of < 0.05.**

It would be ambiguous and misleading to analyze certain parameters, such as projected cell area and total FA area, individually without making a connection between the two. Since FAs are indicative of direct cell contact with the material, we looked at the degree of attachment between the cell and substrate by relating it to cell area. To normalize FA area with cell spread area, we expressed the total FA area per cell as a percentage of the total cell spread area (Figure IV.27C) to more accurately represent the cell-material contact area that is mediated via integrin-regulated FAs. We note values of 4.59%, 5.59%, 6.82%, and 7.02% for Si poli, RGD H, $D_{150}S_{350}$, and $D_{80}S_{110}$, respectively. While only minute differences exist between the two nanopatterned surfaces, we noticed that the difference in contact area is significant comparing polished silicon with the RGD-grafted surfaces (whether nanopatterned or not). Furthermore, significance is seen while comparing RGD H to either of the two nanopatterns. The difference in adhesive behavior between the homogeneous and nanopatterned samples is attributed to the dynamics of FA formation, where efficient integrin clustering leads to the maturation of FA points (Figure IV.25A to D).

The study of hMSC behavior on nanopatterned surfaces offers insights on several levels. Mature FAs have been shown to stretch along the direction of actin stress fiber elongation [81, 148, 268]. Morphologically, on $D_{150}S_{350}$ and $D_{80}S_{110}$ surfaces, FAs are formed in a fibrillar shape and concentrated around the edge of the cell. They are well-aligned with the stress fibers found in the cytoskeleton, serving as anchors that maintain fiber tension. On the other hand, FAs on homogeneous RGD orient in a random and disordered way, without the fibrillar configuration and profound cytoskeletal alignment observed on nanopatterned surfaces. Since cytoskeletal contractility is implicated in cellular signal transduction, the alignment of fibril-shaped contacts with stress fibers may upregulate this contractility through tension caused by the pulling action of FAs, in turn affecting cell phenotype.

The morphology and spreading of hMSCs and their surface attachment via integrin-mediated FAs can be coupled to reach several hypotheses related to cell differentiation, which will be explored in detail later in this chapter. In general, hMSCs undergo differential functions following cellular adhesion. Their response to external stimuli, like topography and mechanical forces, induce changes in cellular programming

that lead to their development into mature cell types [159]. The osteoblastic differentiation pathway of hMSCs is shown in Figure IV.28.

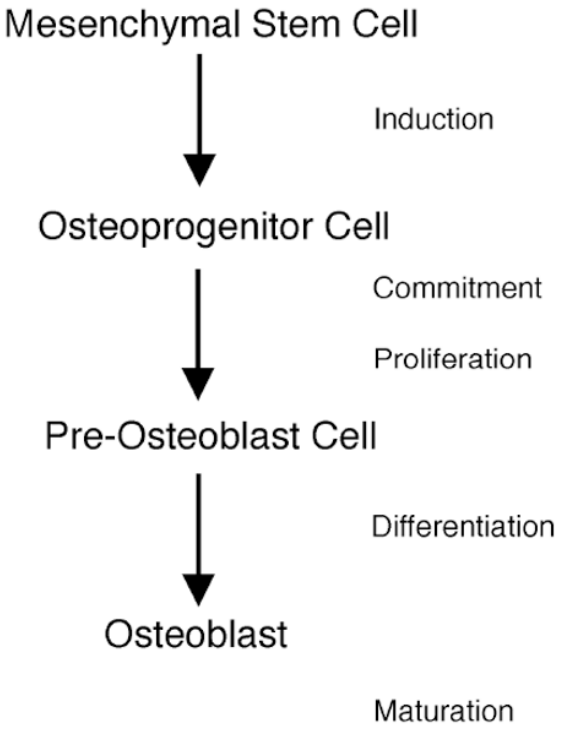

Figure IV.28 – The osteoblastic differentiation pathway of hMSCs. Induced hMSCs become osteoprogenitor cells, entering a stage of commitment with a high proliferative capacity. Differentiation follows and results in development into fully mature osteoblasts [159].

Cell adhesion leads to a reorganization of the cytoskeleton in terms of F-actin stress fibers. Within adherent cells, there are contractility-based machineries that facilitate cell motility [159]. A parameter that is closely related to the differentiation of hMSCs is the tension that is sustained in the actin stress fibers and the cytoskeletal contractility that contributes as a result. Intracellular forces and stress are important determinants of cell fate because the magnitude and dynamics of an applied force will remodel cell morphology. Depending on whether intracellular tension is maintained or not, a stem cell will take on various conformations and follow different pathways of commitment [82]. In the case of hMSCs, they are able to differentiate into osteoblasts or adipocytes, among other cell types [63, 188]. Osteoblasts are a type of high tension phenotype, generally flat and well-spread. On the other hand, adipocytes appear round

and unspread with a lack of intracellular tension. By controlling the organization of the actin stress fibers, it is possible to tune cell differentiation based on tension [82, 87].

Efficient cell adhesion is a criterion for directed cell differentiation, as integrin molecules act as a platform for transmembrane signaling, including mechanisms that drive osteospecific differentiation [159]. The onset of stable cell adhesion requires the clustering of integrins and their receptors which, when mature, establish FAs and enhance adhesive strength. FAs in turn regulate mechanotransduction between the cell and the extracellular matrix (ECM), since they are the points of cell-ECM (or cell-material) contact [148, 149, 269]. Indeed, cytoskeletal arrangement and organization are directly linked to the formation of FAs, evidently as FAs anchor at the ends of stress fibers and align in the direction of stress fiber elongation [81, 148, 268]. In turn, FAs also become elongated in the process of establishing firm adhesions with a surface. Consequently, FAs must be mature and stable enough in order to support the tension required for the osteoblastic phenotype. As introduced in Chapter I.5, adhesion complexes can be classified into different types based on size, chemical composition, and stability. If cell adhesion is primarily mediated by sparse focal complexes, which are transient and unstable, mechanotransductive events are greatly reduced [159]. hMSCs that use many small adhesions may permit a more dynamic interaction with the surrounding environment (ECM or substrates), in turn contributing to the retention of self-renewal instead of promoting differentiation [163]. In terms of osteospecific differentiation, the formation of mature FAs is a primary requirement as they are able to sustain intracellular tension which is transmitted via the actin stress fibers [163].

Considering these interrelated factors that influence cell fate, we may hypothesize that since cell-material contact is more prominent on nanopatterned peptide-grafted surfaces (Figure IV.27C), that it may play a role in favoring hMSC differentiation, since increased interaction of cells with the ECM positively influences mechanotransduction. The morphology of the stress fibers on the nanopatterned surfaces can also shed some light on the eventual behavior of the hMSCs. As previously mentioned and shown in Figure IV.26, long, defined, and well-organized stress fibers are found throughout hMSCs on $D_{150}S_{350}$ and $D_{80}S_{110}$, while on RGD H, cells seem to exhibit less cytoskeletal organization. This organization is almost completely absent on bare silicon controls. Moreover, the alignment of fibril-shaped FAs at the extremes of

stress fibers in the direction of elongation is present only on the two nanopatterned substrates, and not on RGD H. On the homogeneous control, FAs are randomly oriented and distributed within the cell. These correlated behaviors of FAs and actin stress fibers may indicate that hMSCs on nanopatterned peptide-grafted surfaces take on a more "high-tension" morphology relative to the homogeneous controls, as enabled by the ability of the cytoskeletal structure and adhesion complexes to sustain intracellular tension [163]. The ensemble of evidence, along with the cell proliferation analysis in the previous section, continues to support the hypothesis that osteogenic differentiation may be enhanced on $D_{150}S_{350}$ and $D_{80}S_{110}$ in comparison with RGD H.

2.4 Maturation of focal adhesion

To further implicate the role of integrin clustering in FA formation, we counted the number of FAs formed in each cell and quantified the average area of each FA (Figure IV.29). While FA count is lower on both nanopatterns compared with RGD H, the average FA area follows an inverse trend (higher on nanopatterns and lower on RGD H). For each type of material, the individual FAs are then classified based on their area: > 25 um^2, 10 – 25 um^2, 5 – 10 um^2, and < 5 um^2. FAs with an area of greater than 5 μm^2 are considered to be mature. Figure IV.30A is a typical cell that exhibits FAs in the first three classes. Magnified views of FAs are shown in Figure IV.30B to D for FA areas of 25 um^2, 10 um^2, and 5 um^2, respectively. Figure IV.30E expresses the number of FAs in each class (except for < 5 um^2) as a percentage of the total FA count for each material. Evidently, both $D_{150}S_{350}$ and $D_{80}S_{110}$ had more FAs in each class compared with the homogeneous surfaces, whether polished or RGD-grafted. Large FAs were more abundant in nanopatterns compared with homogeneous surfaces, with a 48% increase for FA areas > 25 μm^2, 33% increase for FA areas between 10 and 25 μm^2, and a 15% increase for FA areas between 5 and 10 μm^2. This result complements the results of total FA area and cell-material contact area. Since nanopatterned surfaces have a higher percentage of FAs with large areas, it is reasonable to say that the total FA area should also be higher (and is indeed the case as shown) and in parallel, that the cell-material contact area is higher on nanopatterned surfaces. These results also point to a general trend that integrins and their receptors are able to cluster more efficiently on

nanopatterned surfaces, readily enabling stable FAs to form. As previously discussed, nanopatterns have a positive effect on cell-material contact area, and the data obtained from measuring individual FA area reaffirm the role of mature FAs in cell adhesion.

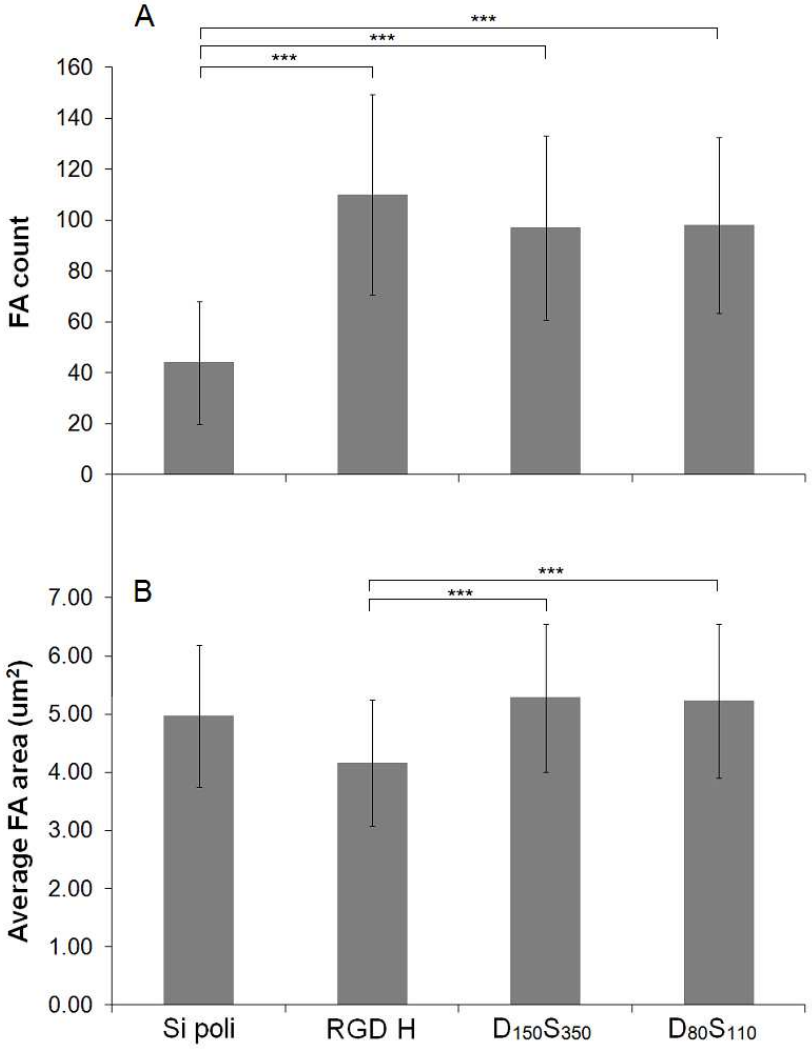

Figure IV.29 – Quantification of FA count and average FA area on RGD-grafted surfaces and non-functionalized control, 24 hours post-seeding, in (A) and (B), respectively; * represents a *p*-value of < 0.05.**

Further classification of adhesion complexes < 5 μm² is presented in Figure IV.31. The percentages of complexes between 2 – 5 μm², shown in Figure IV.31A, are relatively constant across all substrates, while complexes < 2 μm² are slightly more abundant on homogeneous controls than nanopatterned surfaces. Figure IV.31B is an overview of all adhesion complexes on all substrate surfaces.

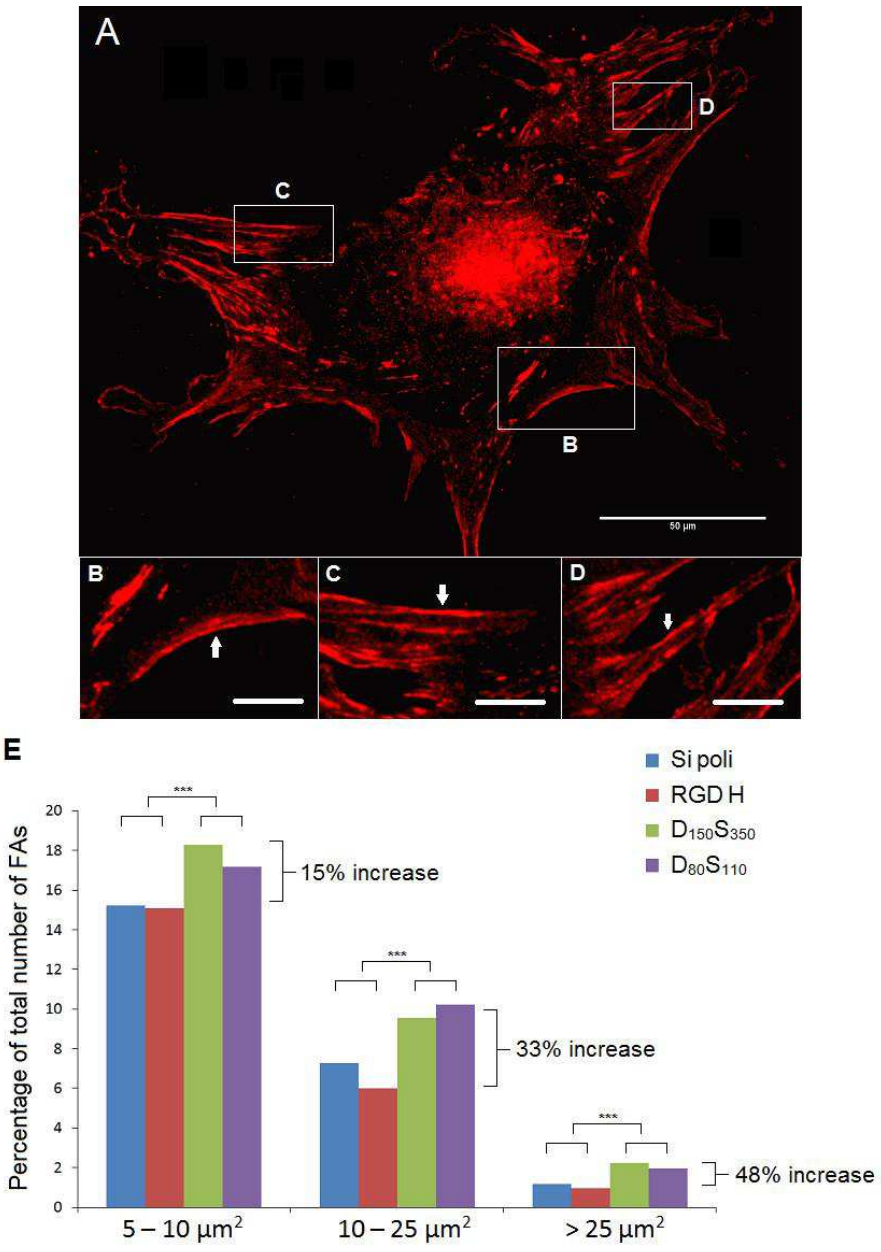

Figure IV.30 – Focal adhesion area analysis on RGD-grafted surfaces and non-functionalized control. (A) A hMSC expressing vinculin staining in red; scale bar = 50 µm. Examples of FAs with areas of (B) 25 µm², (C) 10 µm², and (D) 5 µm² are shown in the magnified views; scale bar = 10 µm. Mature FAs are sorted into classes: > 25 µm², 10 – 25 µm², and 5 – 10 µm². The number of FAs (vinculin clusters) in each class is expressed as a percentage of the total number of FAs for a material and plotted in (E). Many more large FAs were noticed in nanopatterns compared with homogeneous surfaces, with a 48% increase for FA areas > 25 µm², 33% increase for FA areas between 10 and 25 µm², and a 15% increase for FA areas between 5 and 10 µm². Two sample t-tests were used to compare significant difference between the percentages; * represents a *p*-value of less than 0.05.**

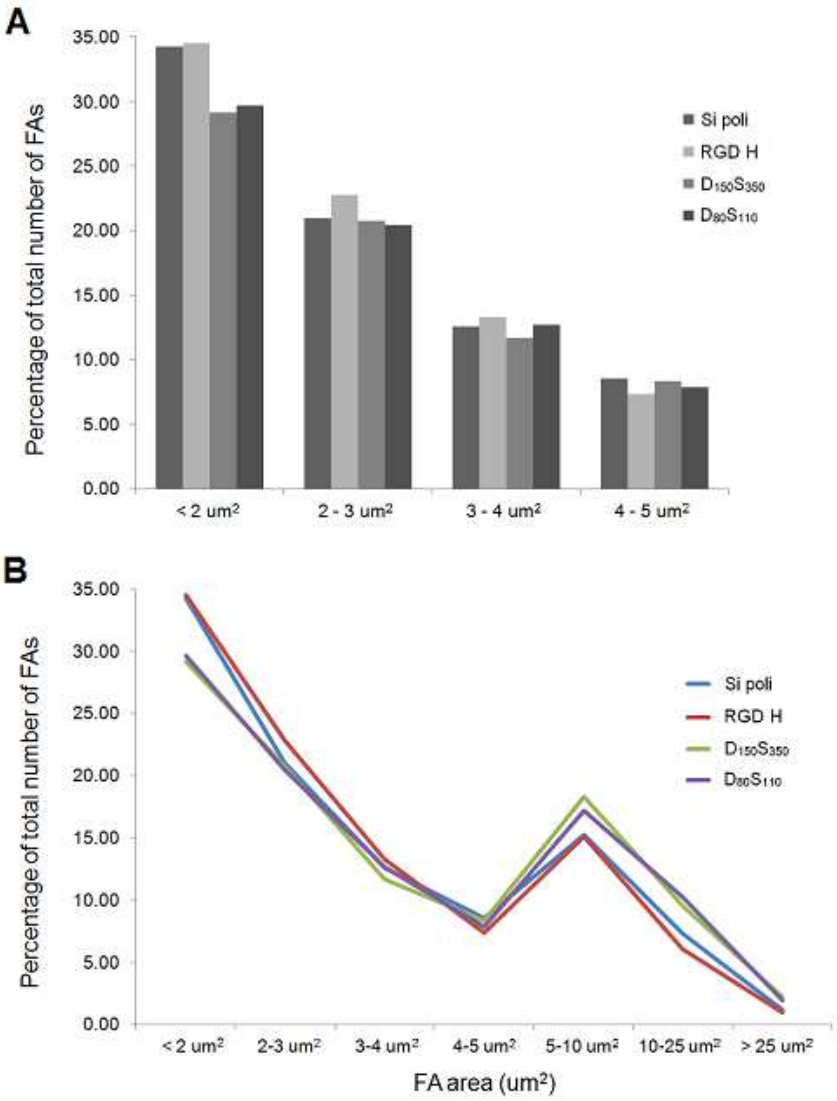

Figure IV.31 – Classification of adhesion complexes based on area. (A) Focal complexes with areas of less than 5 μm² are further broken down into groups with the number of FAs in each group expressed as a percentage of the total number of FAs for a particular type of material. (B) Overview of all adhesion complexes on all substrate surfaces.

The quantification of integrin clustering and classification based on the size of adhesion complexes yield important implications in studying the relationship between cell adhesion and differentiation. A recent report by Biggs *et al.* quantified adhesion complex formation and distribution in human osteoblasts, classifying different types of complexes based on size [270]. In this study, human osteoblasts were cultured on substrates with different types of surface topography and the length of each adhesion

structure was measured. These structures were grouped into three classes: focal complexes (FXs) are structures that are less than 1 μm in length; focal adhesions (FAs) are structures within the range of 1 μm to 5 μm in length; and super mature adhesions (SMAs) are structures greater than 5 μm in length (Figure IV.32). By observing the frequency of adhesion structures on each type of topography and monitoring specific gene expression, Biggs *et al.* established a link between integrin-related cellular adhesion and skeletal stem cell differentiation. Both square and hexagonal nanopit arrays disrupt adhesion formation and cellular spreading in human osteoblasts, in turn preventing osteospecific differentiation in skeletal stem cells. On the other hand, osteospecific differentiation and function were more pronounced on the 100 μm grooves through the upregulation of osteospecific genes. It is also worthwhile to note that on the 10 μm grooves, where adhesion seems to be severely inhibited, adipogenic differentiation was observed. Taken together, there is clear evidence presented in this study that the degree of adhesion maturation is significantly implied in the regulation of signaling pathways, eventually affecting cell differentiation [270].

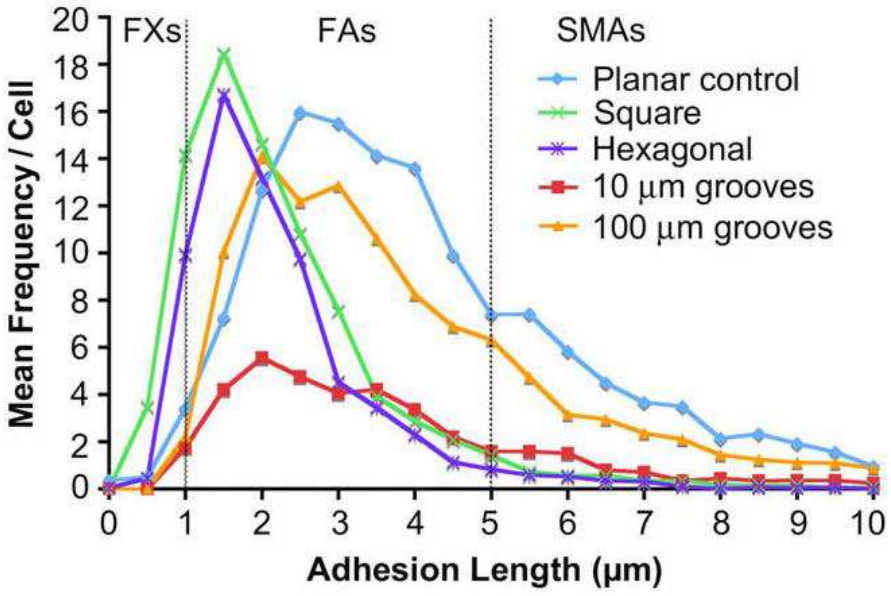

Figure IV.32 – Classification of adhesion complexes based on length, in a study done by Biggs et al. Adhesion structures smaller than 1 μm in length are termed "focal complexes" (FXs), those between 1 μm and 5 μm in length are termed "focal adhesions" (FAs), and those greater than 5 μm in length are termed "super mature adhesions" (SMAs) [270].

In our experiments, we employed a similar strategy of classifying FAs based on size. However, instead of using length, we used FA area as the classification standard, as was the case in a number of publications [44, 92, 268, 271]. Assuming that FAs have an approximate width of 1 μm, which is more or less the case (see Figure IV.30 for comparison), we can equate the two methods of classification. While Biggs *et al.* defined structures greater than 5 μm as super mature adhesions, we consider FAs with an area of greater than 5 μm^2 as "mature". Below 5 μm^2, objects are considered to be "focal complexes".

With regards to this classification, we made some general observations about FAs. Below 5 μm^2, focal complex numbers are relatively constant when comparing the different substrate conditions, as shown in detail in Figure IV.31A, while above 5 μm^2, focal complexes become mature FAs and are more predominant on nanopatterned surfaces as opposed to homogeneous controls, which is an inverse trend from that of the 4 – 5 μm^2 classification. Since the percentages of adhesion complexes with areas of less than 5 μm^2 are relatively constant across all substrate conditions, and taking into account the previous observations on hMSC morphology, spreading, and contact with material discussed previously, we can implicate that FA maturation and stabilization is a main criterion that drives changes in cell dynamics. In other words, the prominent increase in FA maturation on nanopatterned RGD-grafted surfaces ($D_{150}S_{350}$ and $D_{80}S_{110}$) relative to homogeneous controls (RGD H and Si poli) is a key behavior in inducing and directing cell mechanotransduction.

The evident difference in FA maturation between homogeneous controls and nanopatterned peptide dots can be attributed to the way that integrins bind with RGDs on the material surfaces. On homogeneous RGD-grafted surfaces, since the RGD peptide is present throughout the surface, a cell can randomly choose where it will attach. Consequently, integrin-related adhesion between the cell and the RGD peptide is not regulated, and the clustering of integrin is not ensured. On nanopatterned RGD-grafted surfaces, however, the RGD peptides are concentrated in the nanodots in an ordered and predictable manner. Since the background of the nanodots is covered with a cell-repellent PEO silane, when cells are cultured on these nanopatterned surfaces, they must probe their surroundings in search of regions where they are allowed to adhere, in other words, the RGD-grafted nanodots. Because of this restriction, the integrins are

confined within the nanodots, ensuring their proximity to each other and leading to a high degree of clustering. This integrin clustering in turn results in the formation of FAs, which explains the higher number of large adhesion structures on the nanopatterns compared to the homogeneous surfaces. FAs can then continue to recruit integrin units and cause a "fusion" effect to occur, where multiple FAs combine to form super mature FAs, as we have shown in Figure IV.30.

Indeed, the implications of the high proportions of mature FAs on nanopatterns on hMSC differentiation should not be neglected. As pointed out recently by Tsimbouri *et al.* (and mentioned earlier), adhesion complexes must lengthen, mature, and stabilize in order to support contractile cell morphologies with high levels of intracellular tension, in turn inducing osteogenesis to occur [163]. The maturation of FAs on our nanopatterns, as indicated by the profound increase in large FAs, is a preliminary indication that hMSCs cultured on these surfaces are present in a higher contractile state than those on the homogeneous controls. The result may be that osteogenesis will be favored on nanopatterns for the reasons related to FA conformation and the sustainability of intracellular tension.

Much comprehensive work related to FAs and cell behavior has been conducted in an attempt to firmly establish the role of FAs in directing cell function. Well-known studies by the research group of Spatz have set a solid foundation for the importance of integrin clustering in cell adhesion by defining the range between 58 nm and 73 nm as the optimal spacing between individual integrin ligands for the formation of FAs [162]. Consequently, above an integrin spacing of 73 nm, integrin activation is severely hindered and the formation of FAs and actin stress fibers is reduced, resulting in limited cell adhesion and spreading. This phenomenon was later demonstrated by related studies that confirmed the observation of a universal length scale for integrin clustering and activation and was extended to include effects of adhesion ligand order [124] and possible impact on hMSC differentiation [223].

In our work, our peptide domains are on a larger scale such that more than one integrin can ligate with each nanodot. The spacing between individual integrins, therefore, is not the issue at hand, like the studies mentioned previously. In short, the interest of our work lies in whether the clustering of integrin ligands present at different length scales can have an effect on cell adhesion and cell differentiation. We

have shown that even though the peptide nanodot are spaced at 350 nm and 110 nm for the two nanopatterns, the clustering of integrins on each nanodot is sufficient to promote adhesion despite the spacing.

However, no difference in cell adhesion has been observed between $D_{150}S_{350}$ and $D_{80}S_{110}$, whether in terms of cell spreading, FA count, total FA area, average FA area, cell-material contact, and percentage of mature FAs. The lack of difference is due to the length scale at which the peptide nanodots are present, which allows integrin clustering to happen regardless of whether the nanodot diameter is 150 nm or 80 nm. It has been demonstrated that clustering occurs when a minimum of five [71] or six [206] integrins form a group. While the diameter of each integrin is approximate 8 to 12 nm [162], the dimensions of the nanodots far surpasses the minimum threshold for integrin clustering, and so efficient clustering occurs equally on both $D_{150}S_{350}$ and $D_{80}S_{110}$ with no preferential adhesive behavior on either nanopattern. We propose that by decreasing the nanodot diameter D and/or by increasing the interdot gap width S of the nanopatterns, differences in cell adhesion will begin to become apparent.

Whether differentiation is truly affected solely by the integrin clustering effect, however, remains to be explored. Nanoscale surface cues, such as the RGD nanopatterns presented in this study, might have important indications in tissue-specific hMSC differentiation. Previous reports have proven that chemical patterning [82], material stiffness [87], and nanotopographical cues [123] all play roles in hMSC differentiation. The ensemble of these studies indicates that even slight changes in the hMSC environment is sufficient to promote a change in cell behavior, further extending the need to study the function of the stem cell niche. The induction of hMSC differentiation through contact with a material occurs through the formation of mature FAs, which in turn impacts cytoskeletal tension as FAs act as anchoring points between the cytoskeleton and a material surface. Consequently, changes in cytoskeletal tension indirectly affect a cell's mechanotransductive pathways, as demonstrated by cell response to material stiffness or external stress, for example [87, 272]. In our case, the presence of nanopatterned chemical cues also contributes to this change in cytoskeletal tension. Additionally, it has been shown that changes in cytoskeletal tension in response to surface nanocues could influence interphase nucleus organization, thus affecting cellular gene expression [273]. The changes in cytoskeletal tension result in changes in

cell morphology, as was seen in our study. We observe that specific maturation of FAs and the interaction of FAs with the cytoskeleton lead to different conformations of FA-based proteins, such as vinculin. Recruitment and activation of FAs induce these effects, as shown by the activation of vinculin binding via the unfolding of single talin rods, a process which forms part of the cellular mechanotransduction mechanism [274, 275].

2.5 STRO-1 expression of hMSC activity

As FAs have a direct effect on cell mechanotransduction and signaling pathways [150, 154, 159], we hypothesized that since FAs behave differently on homogeneous and nanopatterned surfaces, the commitment of hMSCs should be also affected. To investigate whether differences in FA formation and behavior induce changes in hMSC differentiation, we cultured hMSCs on the same types of materials (Si poli, RGD H, $D_{150}S_{350}$, $D_{80}S_{110}$) for 4 weeks to allow the cells to proliferate. At 4 weeks, cells were fixed and stained for STRO-1, a mesenchymal stem cell specific marker, by immunofluorescence and observed visually (Figure IV.33A to D). The STRO-1 fluorescence signal was then quantified by measuring the mean signal density of each cell (Figure IV.33E). We noted a decrease in STRO-1 expression at 4 weeks on homogeneous surfaces grafted with RGD, and again a decrease on nanopatterned RGD-grafted surfaces. Statistic analysis revealed significance between Si poli and all RGD-grafted surfaces, while the difference between the nanopatterns and homogeneous RGD is also significant. A decrease in STRO-1 activity implies that hMSC population has decreased over 4 weeks on nanopatterns relative to both homogeneous controls. While a part of the population is still STRO-1 positive (hence retaining its “stemness”) the decrease indicates that more cells have differentiated on nanopatterns than homogeneous controls.

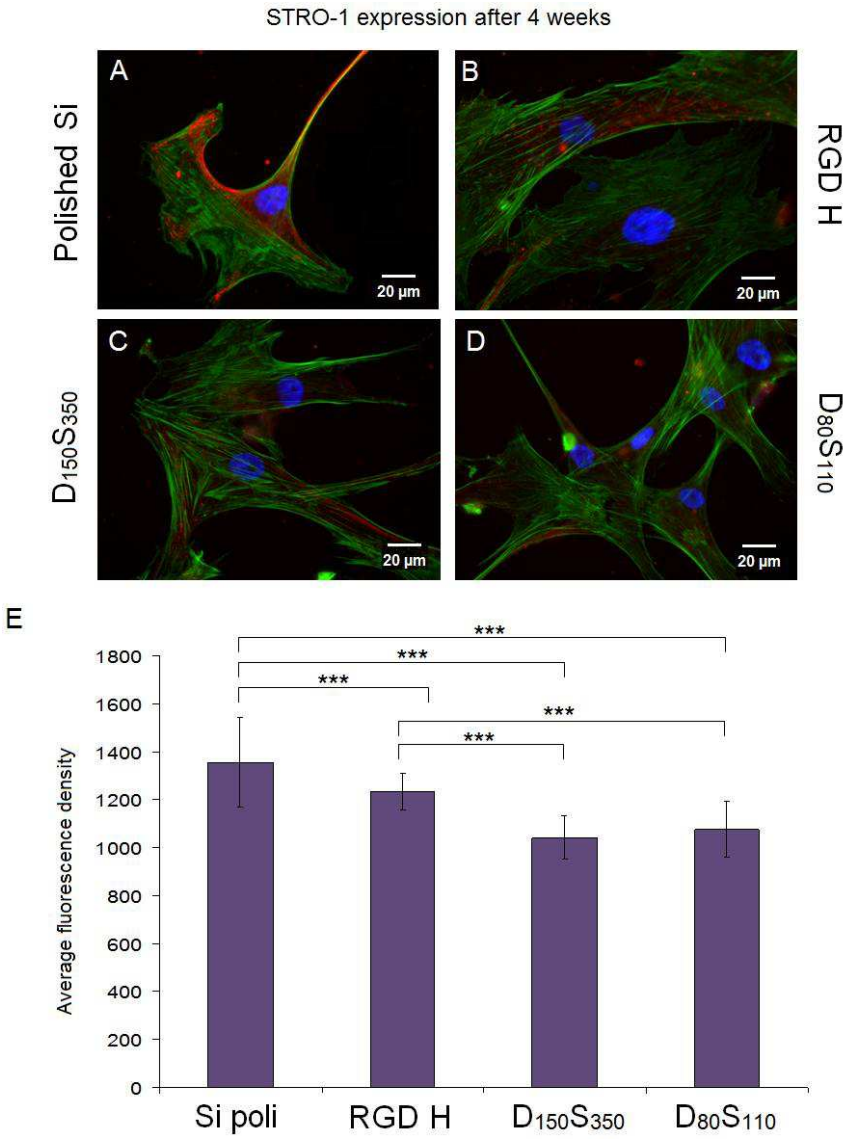

Figure IV.33 – Commitment studies of hMSCs 4 weeks post-seeding on RGD-grafted surfaces and non-functionalized control. (A) – (D) STRO-1, a hMSC marker, is immunofluorescently stained and shown in red, with F-actin stained in green and cell nucleus in blue; scale bar = 20 µm. (E) The amount of STRO-1 present in the cell is expressed as average fluorescent density, normalized with the number of cells (50 per condition); * represents a *p*-value of less than 0.05. Experiments were performed in duplicates (n = 2 samples per condition).**

We attempted to establish a direct link between FA activity and hMSC commitment in order to draw a preliminary conclusion. The decrease in STRO-1 expression on $D_{150}S_{350}$ and $D_{80}S_{110}$ relative to RGD H (Figure IV.33E) is a sign that cells are less "stem" on nanopatterns than homogeneously grafted RGD surfaces after 4 weeks in culture, thus indicating that they have differentiated into a mature cell lineage.

Previously, we have evaluated hMSC proliferation during the 4 weeks in culture (Figure IV.24) and found that hMSCs on nanopatterned RGD-grafted surfaces showed a lower proliferation profile compared with the homogeneous RGD control. We can attribute this observation to the idea that cell differentiation and proliferation follow an inverse relationship. Stem cells and terminally differentiated cells proliferate very slowly at a limited capacity, while progenitor cells enter a stage of high proliferative capacity before differentiation [276]. In fact, the decision of cells to differentiate occurs in the G1 phase of the cell cycle [260, 277]. In turn, the process of differentiation from progenitor cells into specialized cells involves a restricted proliferative capacity, which ultimately leads to cell cycle exit [260]. A look into the specific process of osteoblast differentiation by Quarles *et al.* revealed that clonal murine calvarial MC3T3-E1 cells undergo distinct stages throughout their development in a time-dependent manner. Initially, these cells participate in active replication while remaining as immature osteoblasts, as confirmed by the lack of alkaline phosphate expression and mineral deposition on the ECM. When the cells reach confluence, they enter cell growth arrest. Downregulation of further proliferation is initiated as osteoblastic functions begin to express, including the production of alkaline phosphatase, deposition of a collagenous ECM, and the mineralization of the ECM [278]. These claims are further supported by studies which show that the inhibition of proliferation results in an increase in osteoblastic phenotype markers, such as osteopontin and osteocalcin [261, 262].

2.6 Staining of lineage-specific markers

Since we predicted that increased FA maturation and cell-material contact on nanopatterned surfaces upregulates osteoblastic differentiation of hMSCs, we performed histochemical staining to see if any specific differentiation has occurred. As hMSCs are able to differentiate into osteoblasts and adipocytes (among other cell types), we chose two standard types of stains to detect differentiation into these lineages, as is often done in literature to compare lineage-specific behavior [82, 83, 92]. Figure IV.34 illustrates the results of ALP and Oil Red O staining on hMSCs cultured on different surfaces for 24 hours and 2 weeks.

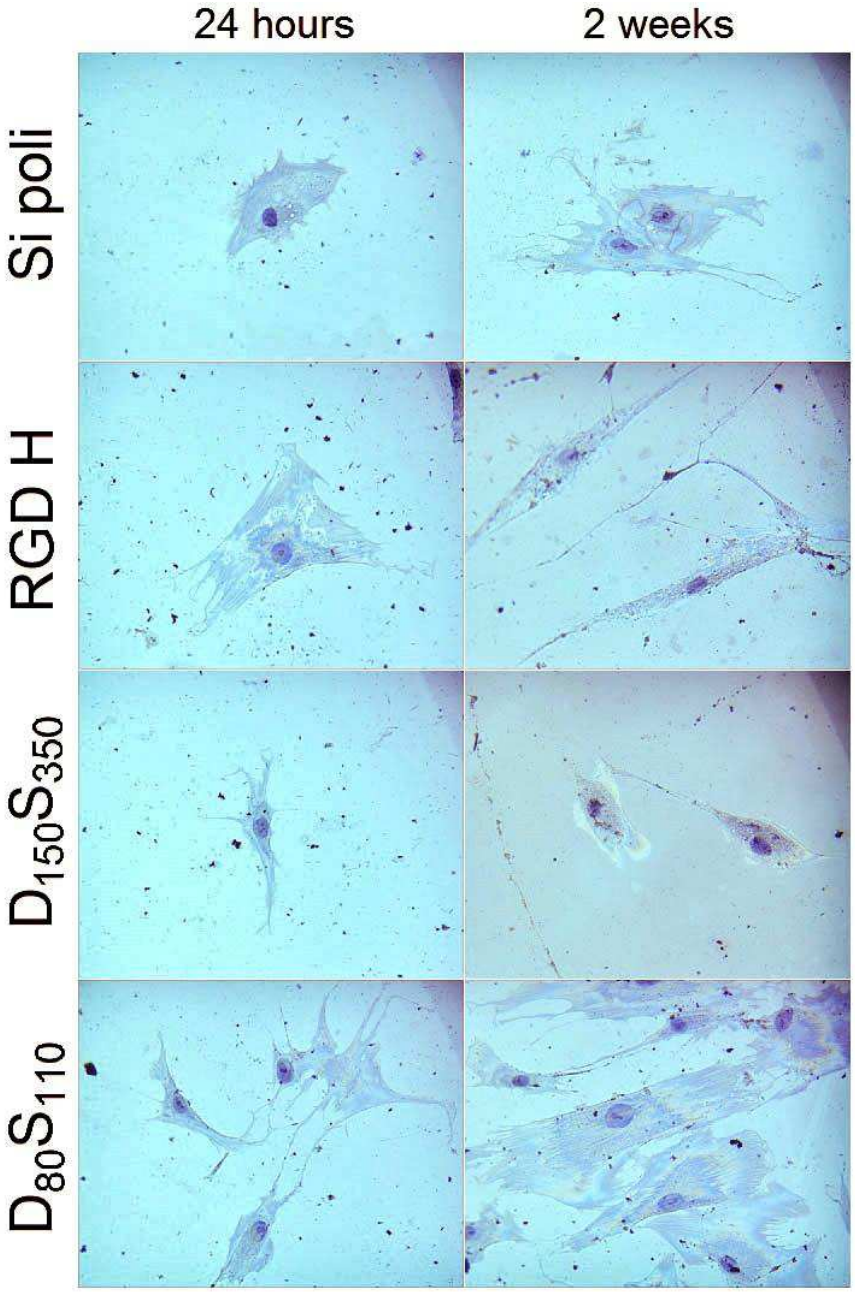

Figure IV.34 – Alkaline phosphatase (ALP) and Oil Red O staining for osteoblastic and adipogenic differentiation, respectively. ALP is expressed in osteoblasts while Oil Red O stains for fat and lipid deposits present in adipocytes. Positive staining for osteoblasts and adipocytes, if present, show up in purple and red, respectively. Experiments were performed in duplicates (n = 2 samples per condition).

First, we stained for alkaline phosphatase (ALP), an enzyme which indicates bone formation as it plays a role in bone mineralization [279, 280]. When applied on cells or tissues, positive ALP staining appears blue-purple and is a sign of osteogenic

differentiation. Next, we stained for fat and lipid deposits using Oil Red O, a fat-soluble diazo dye. When applied on cells or tissues, positive Oil Red O staining appears dark red and is a sign of adipogenic differentiation. At 24 hours post-seeding, no osteoblasts or adipocytes were detected as shown by the lack of purple or red cells on any surface, which is expected. At 2 weeks post-seeding, still no osteoblasts or adipocytes were detected, indicating that neither osteogenic nor adipogenic differentiation has occurred on any surface.

We then performed immunofluorescence staining and evaluated the expression of osterix, a transcription factor for osteogenic differentiation [281], and osteopontin, an important protein in the process of bone formation [165]. We wanted to see whether any sign of osteospecific differentiation has occurred when hMSCs have been cultured for 2 weeks on RGD surfaces, both homogeneous and nanopatterned. These results are shown in Figure IV.35 with the quantification of relative fluorescence expression shown in Figure IV.36. After being cultured for 2 weeks, hMSCs apparently expressed both osterix and osteopontin on all surfaces, including the control Si poli, as displayed by the red signal in Figure IV.35. However, there was no significant difference in the quantitative analysis between any substrates at for either osterix or osteopontin, indicating a lack of preferred osteospecific differentiation that is on any surface.

We have hypothesized earlier (Chapters IV.2.3 and IV.2.4) that hMSCs cultured on nanopatterned ($D_{150}S_{350}$ and $D_{80}S_{110}$) RGD-grafted surfaces would promote osteogenesis in comparison with homogeneous controls, based on analysis of cytoskeletal tension, stress fiber arrangement, and FA maturation. However, osteospecific differentiation staining yields negative results and it appears that at 2 weeks, no osteospecific differentiation has occurred. The results of immunofluorescence are logical in relations to the observations made previously through ALP staining. ALP is an early marker of ECM maturation (which is a criterion for bone development) and is expressed at the end of the osteoprogenitor proliferative stage and at the onset of osteoblast differentiation [262]. Osteopontin is expressed later in bone development as mineralization begins. Hence, if ALP is not observed, osteopontin should not have been observed as well since ALP expression precedes osteopontin expression. This is the case as shown in Figure IV.34 and Figure IV.36. A possible explanation could be that 2 weeks is not sufficient for hMSCs to enter osteogenic differentiation. We may be at the brink of

the proliferative period at 2 weeks, but a slightly longer culture time would be required to verify whether the osteogenic stage is reached or not.

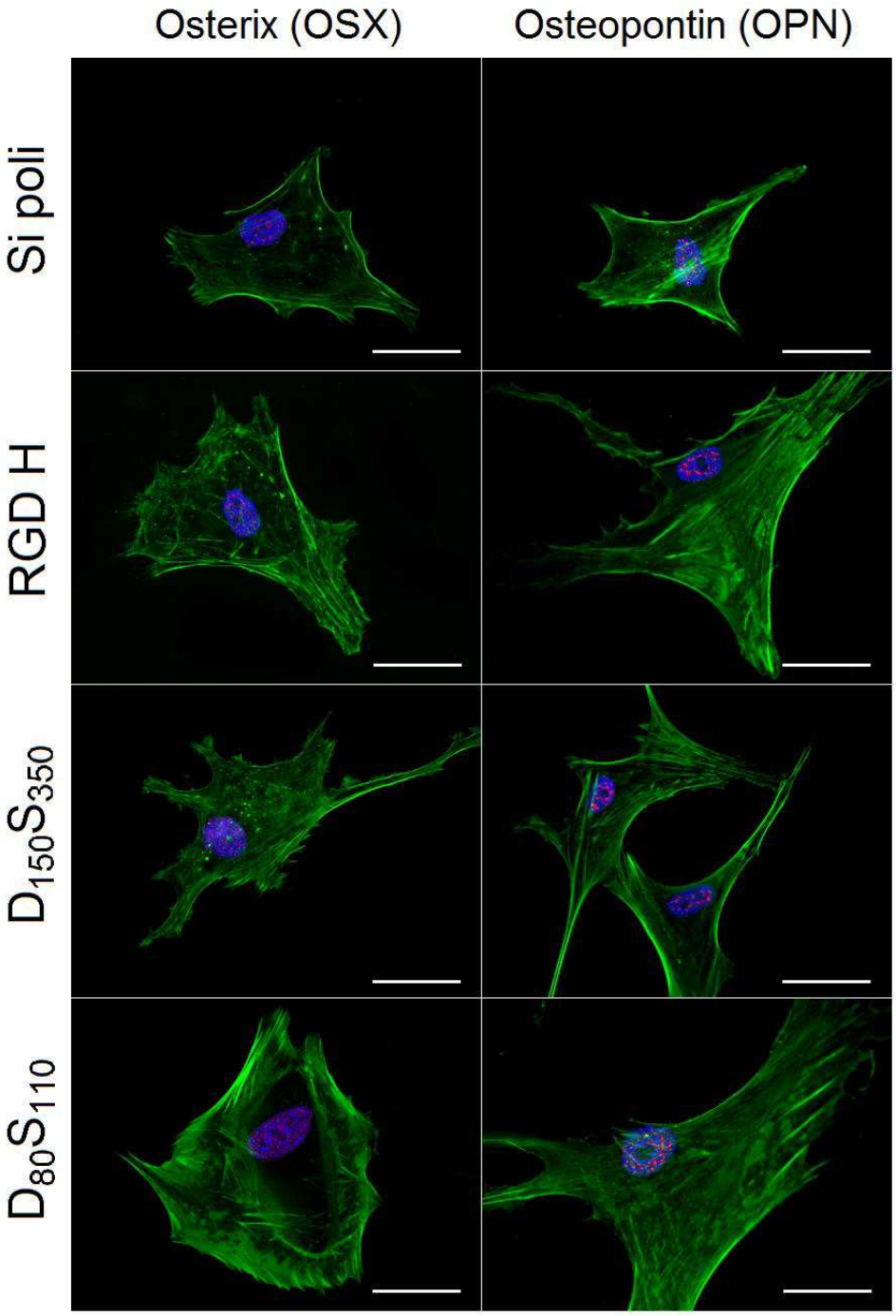

Figure IV.35 – Immunofluorescent staining for osterix and osteopontin at 2 weeks post-seeding on RGD-grafted surfaces and non-functionalized control with osterix or osteopontin in red, actin cytoskeleton in green, and nucleus in blue; scale bar = 50 µm. Experiments were performed in duplicates (n = 2 samples per condition).

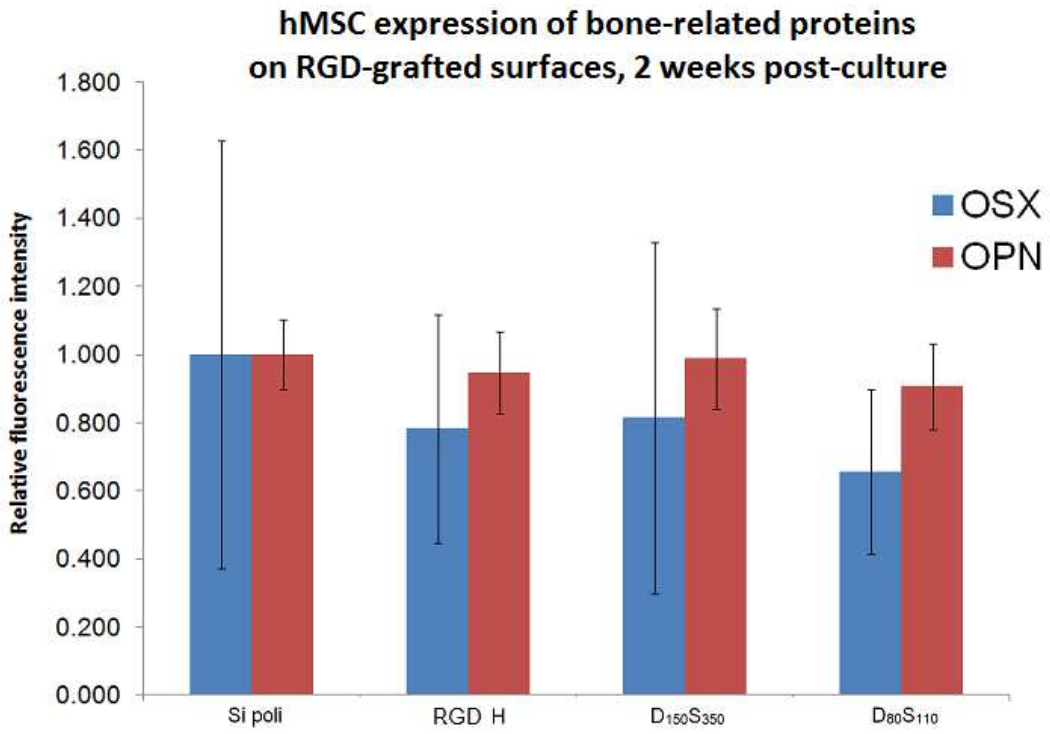

Figure IV.36 – hMSC expression of osterix (OSX) and osteopontin (OPN) on RGD-grafted surfaces and non-functionalized control is evaluated at 2 weeks post-seeding. Data is presented as relative fluorescent intensity between different substrates for osterix and osteopontin. At 2 weeks, no significant differences were observed for either osterix or osteopontin on any surface.

Going a step further, we speculated that since hMSCs were able to differentiate into mature phenotypes other than osteoblasts and adipocytes, that RGD-grafted nanopatterns may have directed them into any of the other possible lineages, in particular neurons and cartilage (chondrocytes) [5, 63]. To test whether this was the case, we performed immunofluorescence staining of lineage-specific proteins on hMSCs cultured for 2 weeks. We chose to mark tubulin β-3, a mature neuronal marker [122, 282], and SOX9, a transcription factor for cartilage gene expression [283, 284]. The results are shown in Figure IV.37. In these two cases, no expression of protein was detected through immunofluorescence, which disproves the speculation of either neuronal or chondrogenic differentiation. Again, the lack of any specific hMSC differentiation could simply be because 2 weeks of culture time is insufficient for cell commitment. Due to several technical difficulties in our experimental conditions, we were not able to perform hMSC culture for differentiation assessment for longer than 2

weeks in this part of the study. However, we intend to experiment with longer culture times (4 weeks or even up to 8 weeks) in future works.

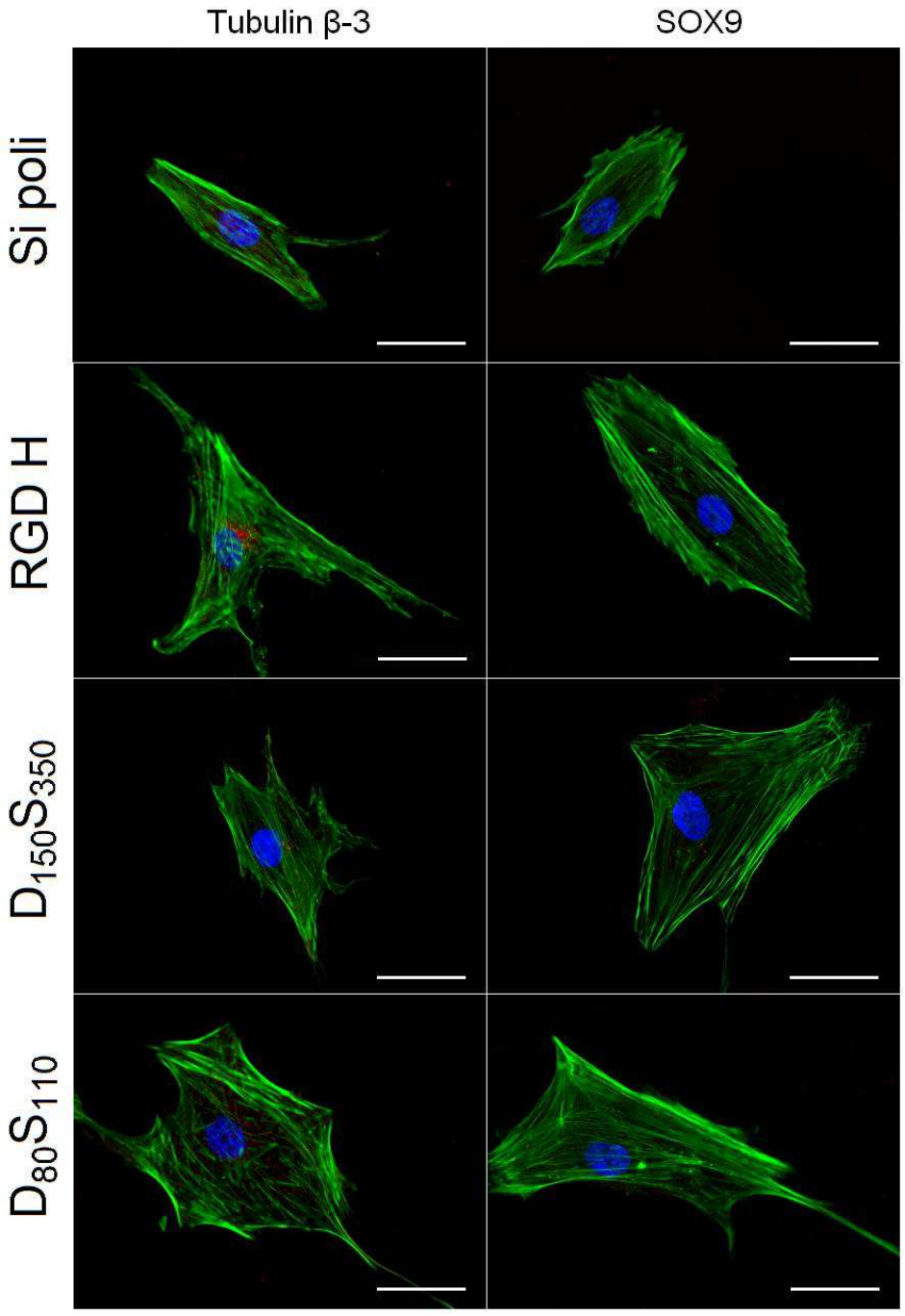

Figure IV.37 – Immunofluorescent staining for tubulin β-3 and SOX9 at 2 weeks post-seeding on RGD-grafted surfaces and non-functionalized control with tubulin β-3 or SOX9 in red, actin cytoskeleton in green, and nucleus in blue; scale bar = 50 µm. Experiments were performed in duplicates (n = 2 samples per condition).

3. Influence of mBMP-2 on hMSC adhesion and differentiation

3.1 Motivation of using mimetic BMP-2 peptide

Bone morphogenetic proteins (BMPs) play a very important role in osteoblastic differentiation and bone formation (Chapter I.3.4). Growth factors such as BMPs are present in insoluble forms *in vivo* and interact strongly with components of the extracellular matrix (ECM) [115, 285]. However, growth factors used in research are often employed in soluble forms instead of being "matrix-bound". There is ongoing debate as to whether a soluble approach should be preferred over surface immobilization in terms of eliciting the function of BMPs. Some researchers believe that BMP receptor internalization is a key requirement for its activation, and hence advocate the soluble approach. Others argue that the development of biomaterial surface functionalization methods that allow growth factors to be immobilized and matrix-bound has made it possible to mimic physiological ECM more efficiently, even if internalization is limited.

Mimetic BMP peptides (mBMPs) have been used in research to mimic *in vivo* microenvironment [51, 285]. Specifically, one area of research that our group has focused on throughout the past few years is the effect of surface-immobilized mBMPs on the osteogenic differentiation of human mesenchymal stem cells (hMSCs). The design of mBMPs was carried out through detailed structural studies of the binding interfaces between the mBMPs and their receptors [286]. In particular, a 21-amino acid sequence was selected as the region responsible for the interaction of BMP-2 with receptor II, forming the basis of our mimetic peptide [51]. These mBMP-2 peptides were subsequently grafted onto polyethylene terephthatalate (PET) surfaces to study their influence on pre-osteoblast differentiation [51]. Recently, the potential implications of matrix rigidity on hMSC differentiation was also investigated by grafting mBMP-2 on a poly(acrylamide-co-acrylic acid) hydrogel of varying stiffnesses and coupling the effects of mechanical and chemical signals to modulate cell fate [53].

In the latter study, which deals with matrix stiffness, the results show that at low rigidity (13 – 17 kPa), hMSCs tend toward myogenic differentiation whereas at high rigidity (45 – 49 kPa), hMSCs tend toward osteogenic differentiation. Chemical grafting

of soft and stiff matrices with mBMP-2 yields only osteogenic differentiation regardless of stiffness. Moreover, when grafted on extremely soft gels (0.5 – 3.5 kPa), the mBMP-2 had no effect on hMSC differentiation. A very interesting observation was made with regards to the actin stress fiber organization on these extremely soft gels (Figure IV.38), which could be indicative of the adaptation of hMSCs on very soft substrates [53].

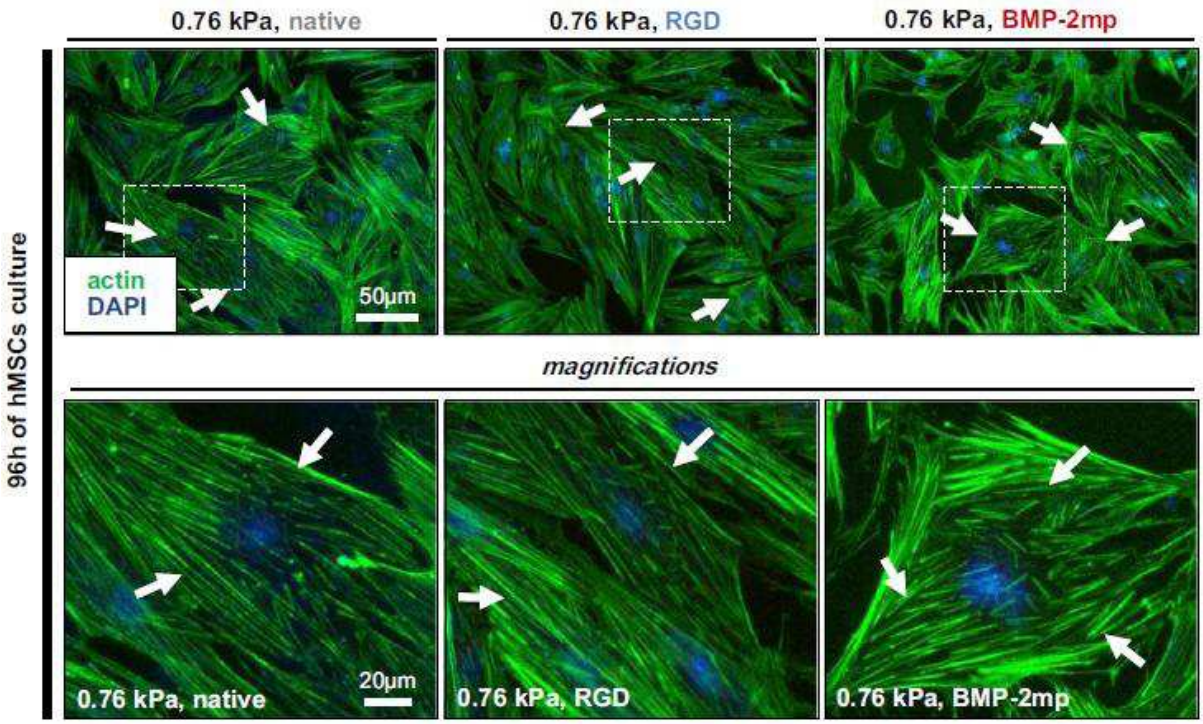

Figure IV.38 – hMSC cytoskeletal organization on low stiffness RGD- or mBMP-grafted hydrogel. Actin was stained in green and nuclei were stained in blue. A very particular stress fiber assembly and reorganization was observed on these soft hydrogels as indicated by white arrows [53].

In short, previous studies in our group illustrated the successful grafting of mBMP-2 onto PET surfaces and demonstrated the functionality of these peptides by showing their promotion of osteogenic differentiation. In this thesis, we apply the surface grafting strategies used previously in combination with chemical nanopatterning in order to bring a new parameter into view – nanodistribution. The results and perspectives are detailed in the following sections.

3.2 hMSC adhesion and spreading on mBMP-grafted surfaces

To demonstrate the compatibility of the nanoimprinting method with different types of peptides, we used a cysteine-containing mBMP-2 with the 21-amino acid sequence CKLPKLSTAPSELSGISTLYL. This peptide was grafted on the same surfaces as described in Chapter IV.1.1. Here, Si poli is the bare silicon control as before, BMP H is silicon homogeneous grafted with mBMP-2, and $D_{150}S_{350}$ and $D_{80}S_{110}$ are the two nanopatterns with dimensions as mentioned in Chapter III.2.1, grafted with mBMP-2. After 24 hours of culturing hMSCs on the four surfaces, their adhesive behaviors were evaluated and shown in Figure IV.39.

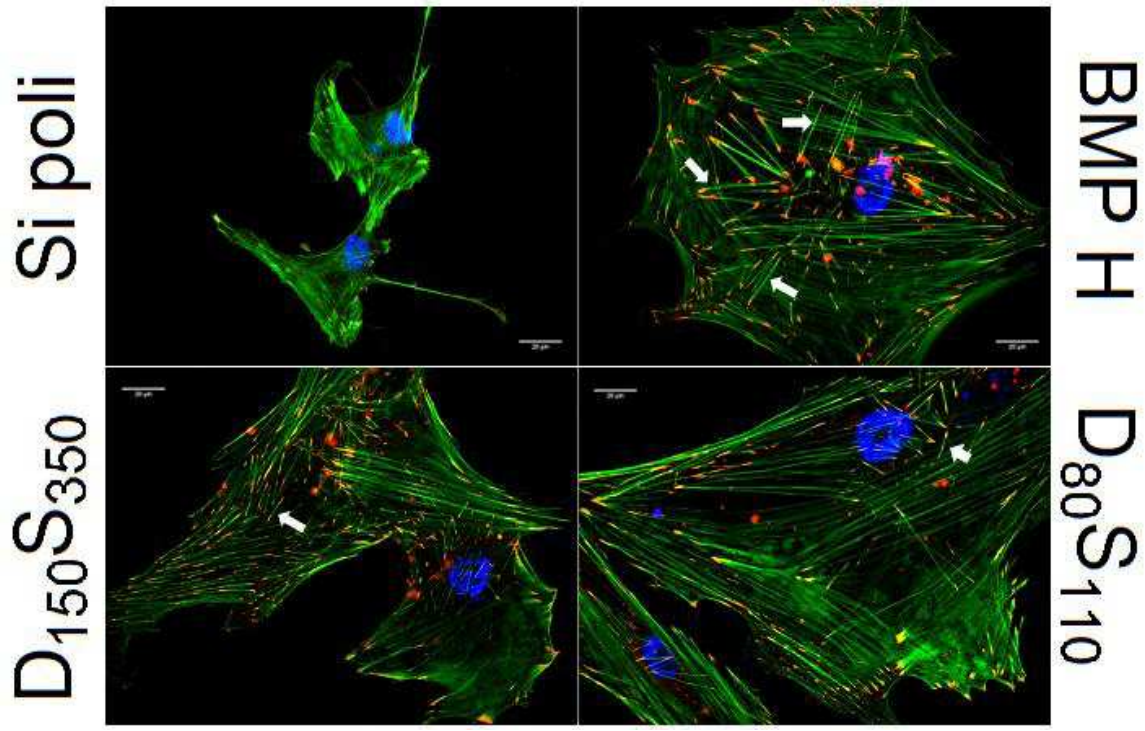

Figure IV.39 – Analysis of hMSC morphology and focal adhesion formation on mBMP-grafted surfaces and non-functionalized control. Cells were immunofluorescently stained and imaged at 24 hours post-seeding with vinculin in red, actin cytoskeleton in green, and nucleus in blue; scale bar = 20 µm. White arrows point to short, fragmented actin stress fibers. Experiments were performed in duplicates (n = 2 samples per condition).

Herein, we verify that our technique of nanopatterning and surface functionalization not only works with RGD peptides, but also with mimetic peptides of

growth factors, such as BMP-2. A general observation can be drawn by taking a look at Figure IV.39, which shows the adhesive behaviors of hMSCs on mBMP-grafted surfaces and the non-grafted control, and comparing it with Figure IV.26 in Chapter IV.2.3, corresponding to RGD-grafted surfaces.

First, we note the radically different organization of the cytoskeleton in the two different cases (Figure IV.26 for RGD and Figure IV.39 for mBMP-2). On RGD-grafted surfaces, hMSC cytoskeletal organization was well-defined on nanopatterns, presenting clear actin stress fibers anchored by large, mature focal adhesions (FAs). This organization is still present on homogeneous RGD, but to a lesser degree than the nanopatterns. Conversely, the hMSC cytoskeleton on mBMP-grafted surfaces seems to take on a completely different organization. This change in organization is very evident in cells cultured on mBMP-grafted surfaces (Figure IV.39), where short, thin fragments of the cytoskeleton are observed in the center of the cell. The length of these actin fragments are on the range of 10 to 50 μm, and their appearance, noted by the white arrows, is especially prominent on the homogeneous mBMP-grafted surface. These fragments are also present on the nanopatterned mBMP-grafted surfaces, but to a lesser degree than the homogeneous substrate. They are absent on the bare silicon control. These short actin fragments are aligned in random directions on mBMP-grafted surfaces without any particularly evident trend in orientation. On the RGD-grafted surfaces, whether homogeneous or nanopatterned, these short actin fragments have not been observed (Figure IV.26). The actin stress fibers here closely resemble the ones presented in Figure IV.38, corresponding to the previously published results of hMSCs on very soft mBMP-grafted hydrogels [53].

3.3 Quantification of cell area and focal complex behaviors

Next, we examined the effects of mBMP-grafting on cell spreading by quantifying the total hMSC area on each surface, as performed for RGD-grafted surfaces in Chapter IV.2.3. The results are depicted in Figure IV.40. Quantification of projected hMSC area after 24 hours in culture gave average values of 5823 ± 3187 μm^2, 12862 ± 5489 μm^2, 10331 ± 3062 μm^2, and 9709 ± 5677 μm^2 for Si poli, BMP H, $D_{150}S_{350}$, and $D_{80}S_{110}$, respectively. Indeed, the observation is similar to those discussed in Figure IV.27 for

RGD, where peptide grafting significantly increases the amount of cell spreading and in turn enlarges cell area. Moreover, if we compare the degree to which the two peptides increase cell spreading relative to non-functionalized controls, we find that mBMP-2 actually induces a much larger cell area than RGD. Average cell area on BMP H is around 50% greater than RGD H, and average cell area on mBMP-grafted $D_{150}S_{350}$ and $D_{80}S_{110}$ are around 30% greater than their RGD counterparts (see Figure IV.27A and Figure IV.40 for RGD and mBMP-2, respectively).

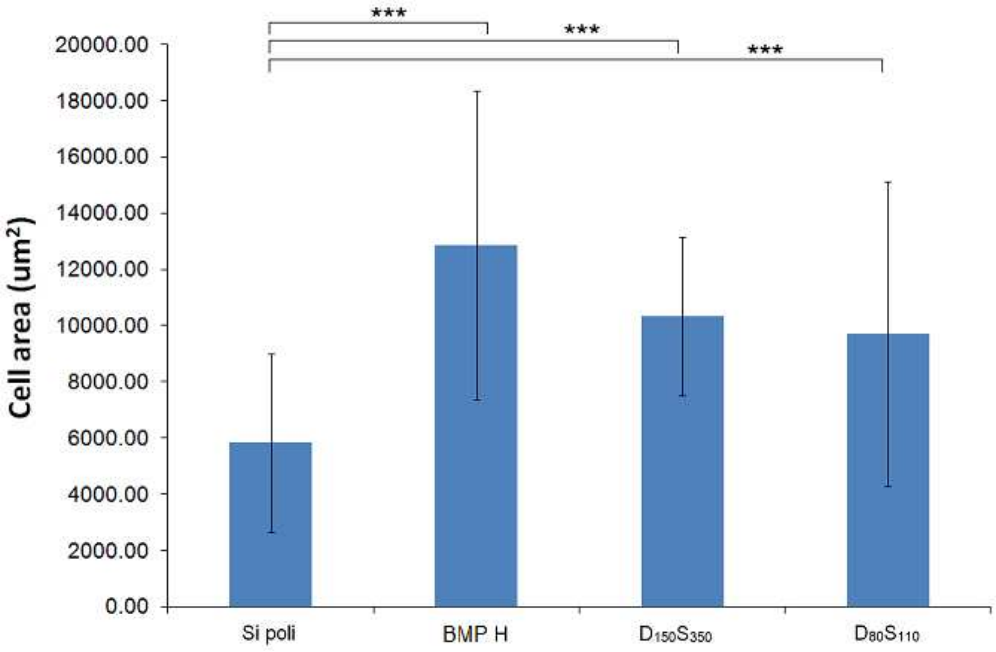

Figure IV.40 – Quantification of cell area on mBMP-grafted surfaces and non-functionalized control, 24 hours post-seeding; * represents a *p*-value of < 0.05.**

More importantly, we can take a look at the distribution of adhesion sites on the mBMP-grafted surfaces. Similar to the experiments done with RGD peptides, we stained for vinculin, an integrin-related protein that regulates FA activity. Immediately, it is clear that there is a significant difference between the way cell adhesions are formed on RGD- and mBMP-grafted surfaces. Adhesion complexes on BMP-grafted surfaces, appearing in red in Figure IV.39, are much shorter and thinner as well as more diffuse than the ones found on RGD (Figure IV.26). These focal complexes are formed as punctate points instead of fibrillar clusters on RGD. In other words, no sign of integrin clustering and FA maturation is found on any mBMP-grafted surface. While mature,

fibril-shaped FAs were found to align in the elongated direction of actin stress fibers on RGD substrates, focal complexes on mBMP substrates also seem to localize at the extremes of actin stress fibers, specifically anchoring the ends of the short actin fragments mentioned earlier. Unlike nanopatterned RGD-grafted surfaces, where FAs are localized at the edges of hMSCs, focal complexes distribute evenly about hMSCs cultured on nanopatterned mBMP-grafted surfaces. This behavior is similar on BMP H as well, where focal complexes are numerous and found all over the cell, and is possibly due to the random organization of the short actin fragments found within the cell.

We performed detailed quantitative analysis of the focal complexes present on mBMP-grafted surfaces by measuring some of the variables already quantified on RGD-grafted surfaces. These variables include focal complex count per cell (67 ± 39, 183 ± 71, 148 ± 58, and 152 ± 69 for Si poli, BMP H, $D_{150}S_{350}$, and $D_{80}S_{110}$, respectively), total focal complex area per cell (252 ± 118 μm^2, 664 ± 274 μm^2, 491 ± 152 μm^2, and 511 ± 194 μm^2 for Si poli, BMP H, $D_{150}S_{350}$, and $D_{80}S_{110}$, respectively), and average focal complex area (4.0 ± 1.0 μm^2, 3.6 ± 0.6 μm^2, 3.5 ± 0.8 μm^2, and 3.5 ± 0.8 μm^2 for Si poli, BMP H, $D_{150}S_{350}$, and $D_{80}S_{110}$, respectively). This set of data is plotted in Figure IV.41.

In Chapter IV.2.4, we have already defined “mature” FAs as adhesion structures with an individual area of 5 μm^2 or greater. Structures with an area below the threshold of 5 μm^2 are defined as “focal complexes”. Since we have not found any adhesion structures on mBMP-grafted surfaces with an area greater than 5 μm^2, we can assert that FAs do not form, and only focal complexes are present on these surfaces. From Figure IV.41, we see that mBMP grafting significantly increases the number of focal complexes found in each cell as well as the total focal complex area, whether the surface is nanopatterned or not. These results mirror those found for RGD grafting. However, in terms of average area of individual focal complexes, there is no difference between the Si poli control and the mBMP-grafted surfaces.

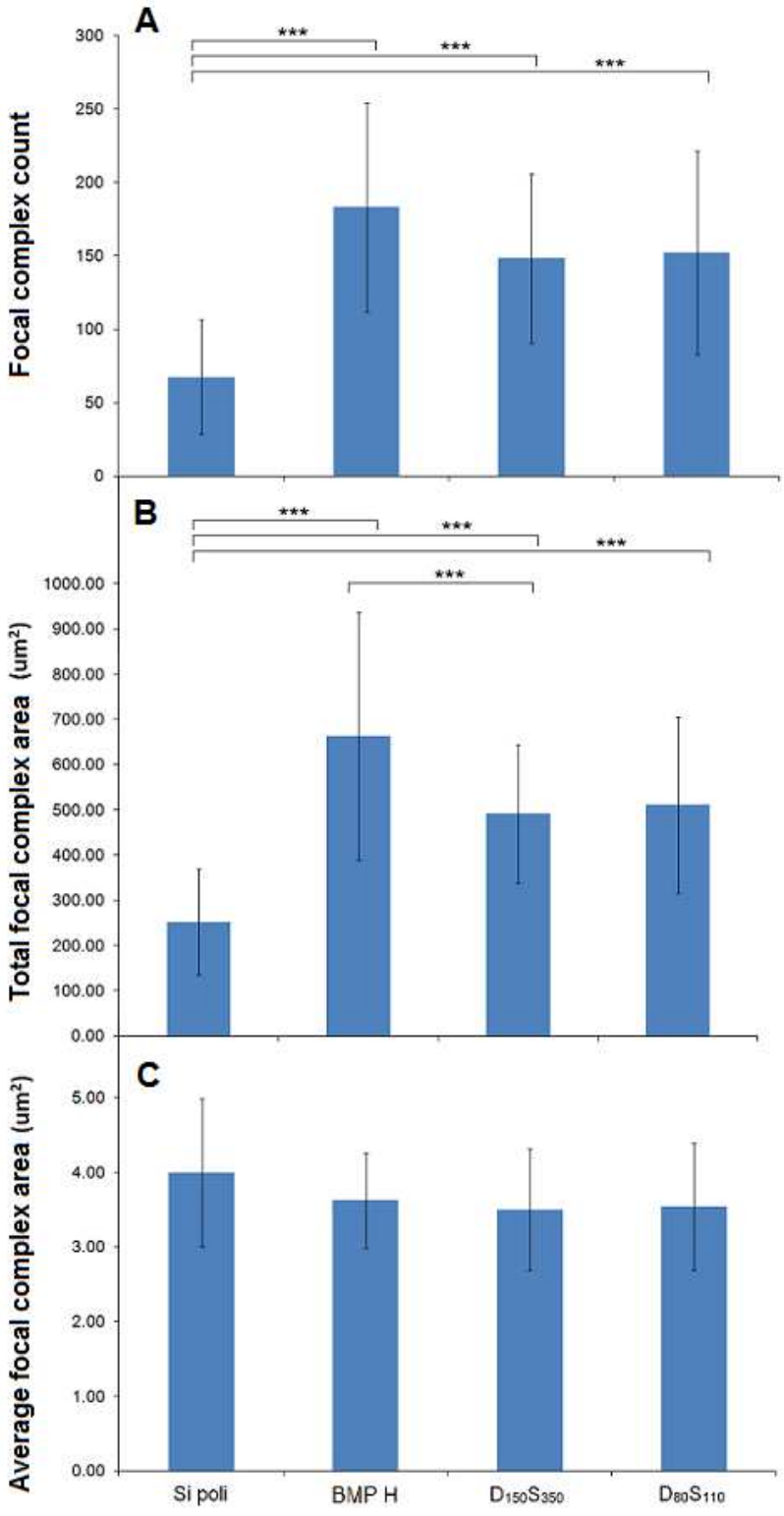

Figure IV.41 – Quantification of FA count, total FA area, and average FA area on mBMP-grafted surfaces and non-functionalized control, 24 hours post-seeding, in (A), (B), and (C), respectively; * represents a *p*-value of < 0.05.**

3.4 Comparison of RGD- and mBMP-grafted surfaces

A comparative analysis is performed between the RGD- and mBMP-grafted surfaces. Results from Chapter IV.2 are combined with data from Chapter IV.3 in a comprehensive assessment, shown in Table IV.8.

Table IV.8 – Comparison of cell behavior on RGD- and mBMP-grafted surfaces ± standard deviation

	RGD ± SD		mBMP-2 ± SD		% change
Cell area (μm²)	Si poli	4566 ± 2182	Si poli	5824 ±3187	28
	RGD H	8240 ± 2243	BMP H	12862 ± 5489	56
	$D_{150}S_{350}$	7940 ± 3219	$D_{150}S_{350}$	10331 ± 3062	30
	$D_{80}S_{110}$	7351 ± 2342	$D_{80}S_{110}$	9709 ± 5677	32
Adhesion structure count	Si poli	44 ± 24	Si poli	67 ± 39	52
	RGD H	110 ± 39	BMP H	183 ± 71	66
	$D_{150}S_{350}$	97 ± 36	$D_{150}S_{350}$	148 ± 58	53
	$D_{80}S_{110}$	98 ± 35	$D_{80}S_{110}$	152 ± 69	55
Total area of adhesion structures (μm²)	Si poli	196 ± 47	Si poli	252 ± 118	29
	RGD H	450 ± 42	BMP H	664 ± 274	48
	$D_{150}S_{350}$	507 ± 49	$D_{150}S_{350}$	491 ± 152	-3
	$D_{80}S_{110}$	506 ± 51	$D_{80}S_{110}$	511 ± 194	1
Average area of adhesion structure (μm²)	Si poli	5.0 ± 1.2	Si poli	4.0 ± 1.0	-20
	RGD H	4.1 ± 1.1	BMP H	3.6 ± 0.6	-13
	$D_{150}S_{350}$	5.2 ± 1.3	$D_{150}S_{350}$	3.5 ± 0.8	-34
	$D_{80}S_{110}$	5.2 ± 1.3	$D_{80}S_{110}$	3.5 ± 0.8	-32

At a glance, we note that while comparing RGD with mBMP-2 surfaces, the differences in percentage changes between $D_{150}S_{350}$ and $D_{80}S_{110}$ are minute for every parameter that was analyzed. However, the differences in percentage changes between peptide-grafted homogeneous surfaces and nanopatterns are generally quite large. These observations indicate three points. First, RGD and mBMP-2 definitely affect hMSC adhesive behavior in different ways, quite apparently demonstrated by the percentage differences between the two peptides. Second, nanopatterns influence hMSC adhesive

behavior in a different manner from homogeneous surfaces because of the noticeable difference in percentage changes. Third, the two nanopatterned surfaces, $D_{150}S_{350}$ and $D_{80}S_{110}$, seem to affect hMSC adhesive behavior in similar ways. They yield very close values for all four parameters that were measured, regardless of the peptide that was grafted, and in turn, very close values for percentage differences between RGD and mBMP-2. The last point may suggest that there is an unknown threshold in the design of our nanopatterns that has not been discovered. Thus, the two nanopatterns that were fabricated in this study are effectively in the same "realm" of nanodomains and hence have the same effect on hMSCs.

Another interesting observation that was made while comparing the RGD- and mBMP-grafted surfaces is that nanopatterned RGD surfaces induced FA maturation and stabilization while maturation is non-existent on any mBMP-2 substrate. The average area of each adhesion complex is significantly larger on nanopatterned RGD (either $D_{150}S_{350}$ or $D_{80}S_{110}$) while comparing with RGD H (Figure IV.29B), but the average area of each adhesion complex is the same on homogeneous and nanopatterned mBMP-2 (Figure IV.41C). Moreover, the average area of adhesion complexes on all mBMP-grafted surfaces is less than 4 μm^2, confirming that they are focal complexes that have not matured and perhaps will not mature.

3.5 hMSC differentiation on mBMP-grafted surfaces

As done in Chapter IV.2.6 for the RGD sample set, we performed immunofluorescence staining and evaluated the hMSC expression of osterix and osteopontin on mBMP-grafted surfaces 4 days post-culture. These results are shown in Figure IV.42 with the quantification of relative fluorescence expression shown in Figure IV.43. After being cultured for 4 days, hMSCs apparently expressed both osterix and osteopontin on all surfaces, including the control Si poli, as displayed by the red signal in Figure IV.42. Morphologically, hMSCs on BMP H still exhibit the same type of actin stress fiber organization, as observed earlier, but this organization is much less apparent on $D_{150}S_{350}$ and $D_{80}S_{110}$, 4 days post-culture.

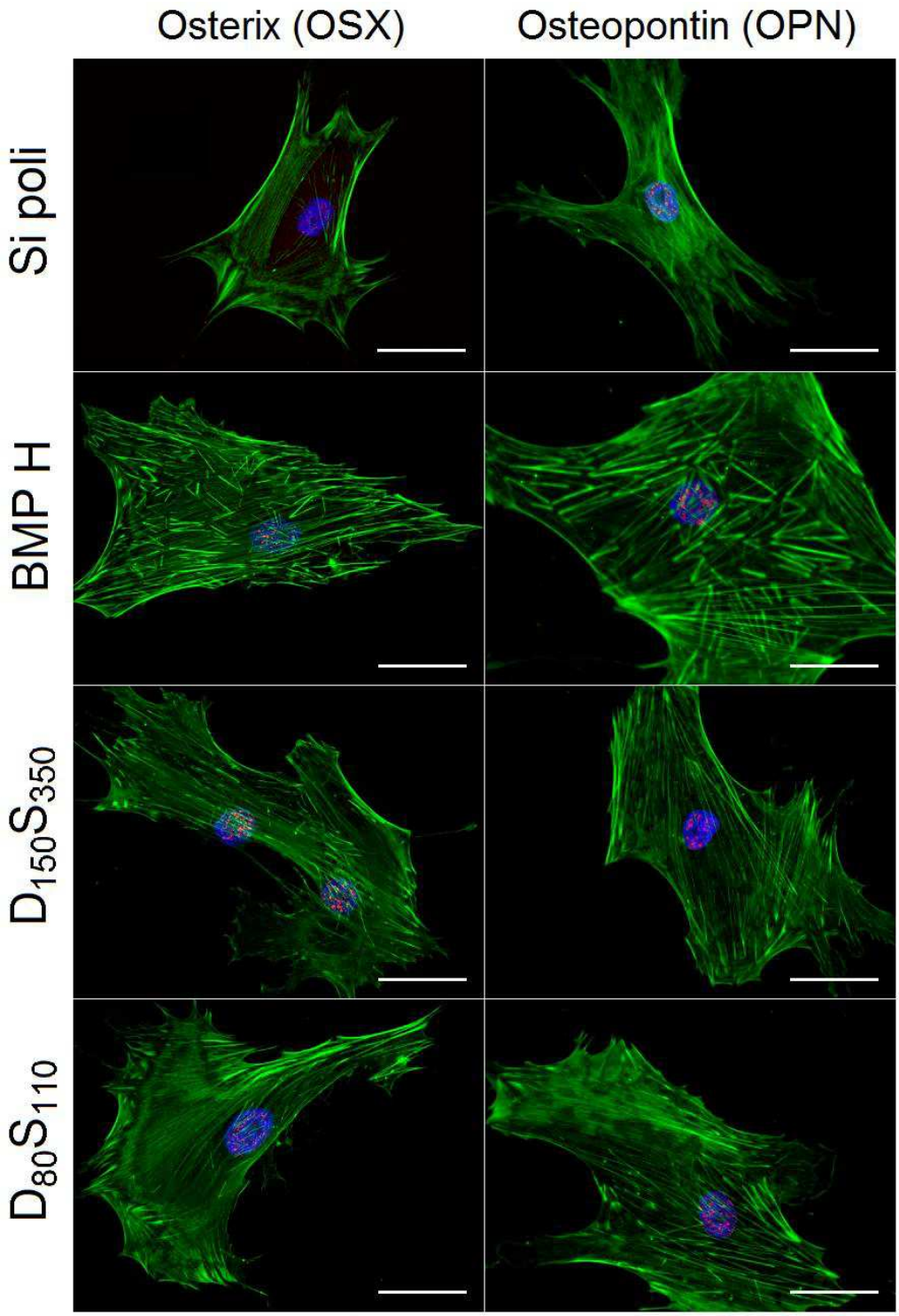

Figure IV.42 – Immunofluorescent staining for osterix and osteopontin at 4 days post-seeding on mBMP-grafted surfaces and non-functionalized control with osterix or osteopontin in red, actin cytoskeleton in green, and nucleus in blue; scale bar = 50 µm. Experiments were performed in duplicates (n = 2 samples per condition).

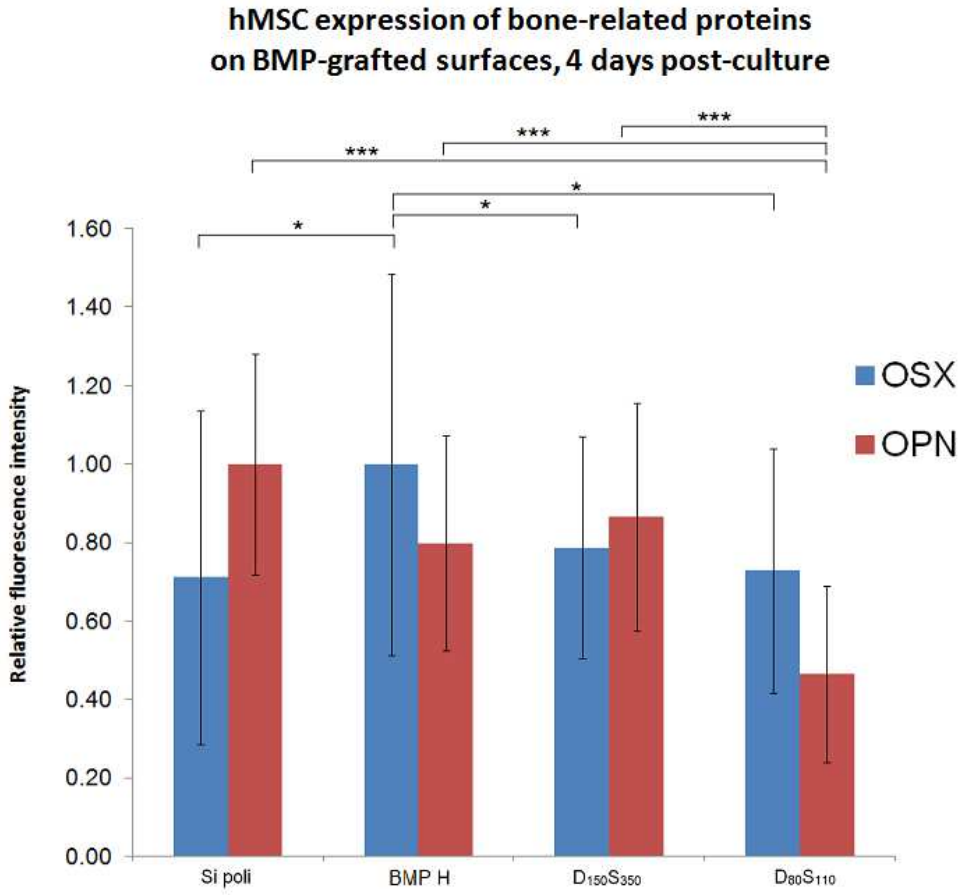

Figure IV.43 – hMSC expression of osterix (OSX) and osteopontin (OPN) on mBMP-grafted surfaces and non-functionalized control is evaluated at 4 days post-seeding. Data is presented as relative fluorescent intensity between different substrates for osterix and osteopontin; * represents a *p*-value of < 0.05 for osterix analysis; * represents a *p*-value of < 0.05 for osteopontin analysis.**

Osterix levels are significantly higher on homogeneous mBMP-grafted surfaces, compared with Si poli, but not on nanopatterned ones (Figure IV.43). hMSCs on BMP H exhibit the highest osterix expression, showing statistical significance while comparing with Si poli, $D_{150}S_{350}$, and $D_{80}S_{110}$. However, osteopontin shows a trend that is quite different from osterix, as hMSCs on mBMP-grafted surfaces seem to express lower levels of osteopontin than Si poli. The mixed trend between osterix and osteopontin presents a problem for the interpretation of the results, as the raw preliminary results are very ambiguous. Again, this may be due to insufficient culture time for cell commitment, making it difficult to see clear differences at early time points. Thus at the moment, a thorough analysis of hMSC osteogenic commitment on mBMP-grafted surfaces cannot be made.

3.6 Implications and perspectives

Through our experiments using mBMP-grafted silicon, both homogeneous and nanopatterned ($D_{150}S_{350}$ and $D_{80}S_{110}$) we have obtained preliminary results with regards to the effects of mBMP-2 surface grafting. In summary, mBMP-2 promotes cell spreading and the formation of adhesion structures. Cell area, adhesion structure count, and total adhesion area are all greater when compared with respective RGD-grafted substrates, both homogeneous and nanopatterned. However, mBMP-2 does not induce the formation of mature FAs on any surfaces, whether homogeneous or nanopatterned. Instead, adhesion is formed via small, point-like structures that we define as focal complexes. In addition, grafting of mBMP-2 on silicon yields a cytoskeletal organization characterized by short fragments of actin stress fibers, in accordance with a previous publication [53]. Finally, osteospecific differentiation on mBMP-grafted surfaces cannot be affirmed due to the mixed expression profiles of osterix and osteopontin, two important proteins in bone formation.

We initially proposed that promoted FA maturation would lead to increased osteogenesis [163, 270]. However, our results are not conclusive. In order to advance the study, we propose the study of hMSC differentiation at longer time points (4 weeks and 8 weeks). We also propose study the effect of mixing RGD and mBMP-2 peptides on the same surface. It would be interesting to evaluate hMSC adhesion and differentiation on homogeneous surfaces grafted with a mix of RGD and mBMP-2, also nanopatterned surfaces with RGD in the patterned regions and mBMP-2 in the background, and vice versa. Without these further experiments, it is difficult to make a definite conclusion related to hMSC differentiation.

In terms of the results that we have obtained, we draw several hypotheses to try to explain these observed behaviors, particularly with regards to the lack of FA maturation on mBMP-grafted surfaces and the mechanisms behind hMSC-mBMP-2 interaction.

Hypothesis #1 – BMP-2 and integrin receptors interact synergistically

As we have presented in Chapter I.3.4 and I.5.3, BMPs function by binding to a series of receptors. These ligand-receptor interactions are in fact related to integrin-mediated adhesion as the activation of growth factor receptors may trigger integrin receptors, and vice versa.

The fact that integrin receptors and BMP-2 receptors are interconnected is supported by our observations of hMSC adhesion on the mBMP-grafted surfaces. Compared with Si poli controls, there is a clear increase in focal complex count and total focal complex area (for BMP H), indicating that integrin function is largely upregulated. We can relate this observation to the study of Crouzier *et al.*, where the functions of soluble BMP-2 and matrix-bound BMP-2 (trapped within a polyelectrolyte film) were compared (see Chapter I.5.3 for summary of published results). The mBMP-2 used in our experiments is also matrix-bound. In fact, it is more bound than the film-trapped BMP-2 due to the direct immobilization of our peptides onto our substrate surface, which eliminates any possibility of diffusion. According to Figure I.16, when growth factor receptors (such as BMP-2 receptors) bind to their matrix-bound ligands, they are in close proximity with adhesion receptors. An interchange of signals occurs between the two receptors, hence causing cell adhesion to be upregulated on BMP-grafted surfaces [115]. This phenomenon may have been the reason that adhesion is greatly promoted on our mBMP-grafted surfaces, providing an explanation to the ample points of adhesion present as well as the enhanced cell spreading (greater than RGD).

Hypothesis #2 – Adhesion on mBMP-grafted surfaces depends on diverse factors

Even though hMSCs form adhesion complexes on nanopatterned mBMP-grafted surfaces, unlike the nanopatterned RGD-grafted surfaces, the adhesion complexes do not mature. One possible explanation for the lack of mature FAs on nanopatterned mBMP surfaces is the nature of hMSCs on RGD- and mBMP-grafted surfaces, which are inherently different. RGD is a ligand for which integrin is a receptor, and so the presence of RGD on a material surface directly induces ligand-receptor interactions, giving rise to focal complexes which in time become mature FAs. In short, the main function of RGD is to facilitate cell adhesion. mBMP-2, however, only indirectly induces the formation of

focal complexes, taking into account the cooperation between integrin and mBMP receptors [115, 164, 166, 167]. Hence, the formation of focal complexes on mBMP-grafted surfaces will depend on various factors, such as the distribution of mBMP-2, the availability of BMP-2 receptors, the proximity of mBMP-2 receptors to integrin receptors, and the efficiency of mBMP-2 receptors in stimulating integrin receptor activity. Given these considerations, and knowing that mBMP-2 induction of cell adhesion is an indirect process (as opposed to direct induction by RGD-receptor binding), it is possible that integrin function is downregulated on mBMP-grafted nanopatterns compared with RGD-grafted nanopatterns. Moreover, it is unlikely that mature FAs would be able to form on mBMP-grafted nanopatterns. RGD peptides are present on nanopatterns at specifically defined regions, and thus the induction of FAs is possible because integrins bind to immobilized RGD peptides with a high degree of spatial certainty. On mBMP-grafted nanopatterns, while mBMP-2 is spatially confined, the induced points of integrin receptor binding are random and unpredictable. Thus, it would be very unlikely for integrins to be able to cluster and form mature FAs, as it is also very difficult to control integrin binding with the nanodistribution of mBMP-2.

Considering this hypothesis, it would be very interesting to study surfaces that are functionalized with a mixture of RGD and mBMP-2. As shown before, osteoblastic markers are upregulated on surfaces grafted with both RGD and mBMP-2 [51]. Taking into account the results of FA maturation on the nanopatterned RGD-grafted surfaces and the difference in focal complex configuration on mBMP-grafted surfaces, using a mixture of the two peptides would provide further indications of the behaviors of FAs in relations to osteogenic differentiation. In addition, culture times of more than 4 days will be required in prospective experiments to ensure that hMSCs have enough time to go through the commitment process.

Hypothesis #3 – Peptides change hMSC's perception of surface stiffness

Because substrate elasticity and stiffness affect the fate of hMSCs [84, 87], there may be some implication related to the cell's perception of surface stiffness involved in the behavior of hMSCs on the different bioactive surfaces (nanostructured or not). Soft matrices cause the internalization of integrins [167], resulting in the formation of diffuse focal complexes instead of mature FAs [87]. Returning to our results, on both

RGD H and BMP H, points of adhesion are small and distributed sparsely. Cytoskeletal arrangement can also provide information about hMSC interaction with its surroundings. Disorganized, diffused actin filaments were observed on RGD H and are especially noticeable on BMP H with the appearance of short actin fragments, agreeing with literature observations for hMSCs on soft substrates [53, 87]. The size and conformation of integrin-mediated adhesion structures on our homogeneous peptide-grafted surfaces could be an indication that the peptides indeed alter the hMSC's sensitivity to its environment.

In this work, we have been unable to precisely evaluate the mechanical properties of our modified surfaces, and so we could not provide firm evidence that indicates the impact of mechanical cues on the behavior of hMSCs. This work can be followed with AFM-based single molecule force spectroscopy to evaluate precisely the mechanical interactions with surface-immobilized peptide chains in order to explain nanometric phenomena at the cell-peptide interface.

V. Conclusions and Perspectives

In this study, we fabricated bioactive nanopatterns functionalized with an RGD peptide or a mimetic BMP-2 peptide (mBMP-2). Homogeneous controls and nanopatterned peptide-grafted surfaces were characterized using a variety of techniques for monolayer thickness, molecular density, elemental composition, chemical topography, chemical contrast, and surface energy. Human mesenchymal stem cells (hMSCs) were cultured on homogeneous controls and nanopatterned RGD- or mBMP-grafted surfaces for various time points and their adhesion and differentiation behaviors were observed. Specifically, we evaluated cell spreading, cell morphology, cytoskeletal organization, cell-material contact, focal adhesion conformation and maturation, and stem cell commitment. The general conclusions are as follows.

Regarding materials preparation and surface functionalization

Through the development of our surface nanopatterning and functionalization method, we demonstrated that large-area (1 cm^2 x 1 cm^2) surfaces of ordered arrays of nanodots can be fabricated on silicon substrates using nanoimprint lithography. This area scale was not achievable by previously used techniques of nanofabrication, such as electron beam lithography. Next, peptides of varying lengths were successfully grafted onto the silicon substrates using a three-step functionalization process, through silane chemistry and maleimide-mediated reactions.

The validations of nanopatterning and peptide functionalization were undertaken using several surface characterization techniques at each step of the preparation process. First, the grafting of peptides was evidenced by fluorescence visualization. X-ray reflectivity analysis reveals that as the functionalization process progresses, monolayer thickness increases while molecular density decreases with the successive addition of each molecule (silane, cross-linker, and peptide). Next, X-ray photoelectron spectroscopy confirms expected elemental compositions on the substrate surface following each step. In terms of nanopattern characterization, atomic force microscopy allows clear visualization of the chemical topography and contrast between peptide-grafted nanopatterns and the PEO background. Finally, contact angle analysis shows an effect of RGD-grafting on the surface energy of the material.

Regarding RGD-grafted surfaces

hMSCs were cultured on bare silicon controls and RGD-grafted surfaces, whether homogeneous or nanopatterned ($D_{150}S_{350}$ and $D_{80}S_{110}$). More hMSCs adhered on RGD-grafted surfaces compared with bare silicon controls (Si poli), but the proliferation rate is higher on homogeneous RGD-grafted surfaces (RGD H) compared with nanopatterns ($D_{150}S_{350}$ and $D_{80}S_{110}$). Also, RGD-grafted surfaces increase cell spreading (cell area) relative to Si poli, demonstrating the RGD's role in mediating and promoting cell attachment to a surface

In terms of hMSC morphology, cytoskeletal organization is more defined on nanopatterned RGD-grafted surfaces ($D_{150}S_{350}$ and $D_{80}S_{110}$), with more organized actin stress fibers. This observation is complemented by the different organizations of focal adhesions (FAs), which are scarce on Si poli while numerous on RGD-grafted surfaces. On RGD H, FAs are found both in the center and around the edges of cells, whereas on nanopatterns, FAs are found almost exclusively around the edges of cells. Also, FAs tend to anchor at the ends of stress fibers and align in the direction of elongation of stress fibers, supporting intracellular tension. In turn, cell-material contact is significantly improved on nanopatterned surfaces compared with homogeneous controls. A closer look at the behavior of FAs revealed that mature FAs, with areas of greater than 5 μm^2, are much more numerous on nanopatterned surfaces compared with homogeneous controls.

In terms of hMSC differentiation, at 4 weeks post-culture, STRO-1 expression has decreased on nanopatterns relative to homogeneous controls, indicating that cells are less "stem" on nanopatterns ($D_{150}S_{350}$ and $D_{80}S_{110}$). However, lineage-specific assays of differentiation indicated that at 2 weeks post-culture, no sign of lineage-specific differentiation was detected.

Regarding mBMP-grafted surfaces

hMSCs were cultured on bare silicon controls and mBMP-grafted surfaces, whether homogeneous or nanopatterned ($D_{150}S_{350}$ and $D_{80}S_{110}$). It appears that cell spreading is enhanced on mBMP-grafted surfaces compared with Si poli. The number of

adhesion structures formed also increased. However, interestingly on mBMP-grafted surfaces, whether nanopatterned or not, no mature FAs form. Rather, small, point-like focal complexes form and are scattered around the cell. In addition, cytoskeletal organizations of hMSCs cultured on mBMP-grafted surfaces are very different from what was observed on RGD-grafted surfaces. Instead of long, organized stress fibers, short actin stress fiber fragments were observed around the hMSC on mBMP-grafted surface, which were not previously observed on RGD-grafted surfaces.

In terms of hMSC differentiation, results of osteogenic marker (osterix and osteopontin) expression are ambiguous and not sufficient to draw a conclusion with regards to osteogenic differentiation on the various surfaces.

Perspectives and future work

Explore the effects of a range of feature sizes with nanofabrication: Since no differences in hMSC behavior were observed between the $D_{350}S_{150}$ and $D_{80}S_{110}$ peptide nanodots, we plan to fabricate peptide-grafted nanopatterns, using nanoimprint lithography, with other dimensions (for example, nanodots with a pitch spacing greater than 500 nm and with a diameter smaller than 80 nm) to study whether there is a "threshold" where nanopattern dimensions can more potently affect hMSC adhesion and differentiation.

Study specific mechanical interactions between hMSCs and surface-immobilized peptide chains: We propose AFM-based single molecule force spectroscopy as a technique to perform on peptide thin films to evaluate the elastic properties of functionalized surfaces in order to probe the effects of peptide immobilization on hMSC adhesion and differentiation.

Determine whether the nanodistribution of surface chemical cues can influence hMSC differentiation (in addition to adhesion): We plan to perform differentiation tests at longer time points (4 weeks or 8 weeks) to ensure that the timing is sufficient for hMSC commitment. We also plan to add experimental controls using soluble factors in culture media that promote either osteogenic or adipogenic differentiation.

Understand the crosstalk between integrin and BMP-2 receptors and their synergistic effects on hMSC adhesion and differentiation: We will attempt to functionalize silicon surfaces with a mixture of RGD and mBMP-2. Homogeneous surfaces with this mixture can be prepared as well as nanopatterned surfaces. For nanopatterns, prepare RGD nanodots with mBMP-2 as the background, and vice versa, to evaluate the interaction between integrin and BMP receptors and their influence on hMSC adhesion and differentiation.

Appendices

Appendix 1: Scientific communications

(Includes scientific publications, oral presentations, and poster presentations.)

Appendix 2: Ultra nanoindentation analysis of mechanical properties

(Work done in collaboration with industry partner Rescoll to test the mechanical properties of peptide thin films, including hardness and elastic modulus.)

Appendix 3: Abbreviations

(Abbreviations used throughout the text of the thesis.)

A.1 Scientific communications

Scientific publications

Zhe A. Cheng, Omar F. Zouani, Karine Glinel, Alain M. Jonas, Marie-Christine Durrieu. *Bioactive chemical nanopatterns impact mesenchymal stem cell fate*. **Nano Letters**, 2013. **13**(8): p. 3923-9.

Zhe A. Cheng, Omar F. Zouani, Karine Glinel, Alain M. Jonas, Marie-Christine Durrieu. *Bioactive nanoimprint lithography: A study of human mesenchymal stem cell behavior and fate*. **MEDICON 2013 Proceedings**, 2013.

Olivier Deschaume, Delphine Magnin, Zhe A. Cheng, Colette Douchamps, Pierre Labbé, Sami Yunus, Marie-Christine Durrieu, Bernard Nysten, Karine Glinel, Sophie Demoustier, Alain M. Jonas. *Grafting Density and Activity of Peptides and Proteins Grafted onto Silane Layers and Polyelectrolyte Multilayers*. 2013. *Submitted*.

Oral presentations

Zhe A. Cheng, Omar F. Zouani, Karine Glinel, Alain M. Jonas, Marie-Christine Durrieu. *Bioactive Surface Preparation Using Nanoimprint Lithography: A Stem Cell Study*. **European Society of Biomaterials 2013**, Madrid, Spain, 2013.

Zhe A. Cheng, Omar F. Zouani, Karine Glinel, Alain M. Jonas, Marie-Christine Durrieu. *Nanoimprint lithography and surface functionalization for bioactive surface preparation and stem cell studies*. **E-MRS Spring Meeting 2013**, Strasbourg, France, 2013.

Zhe A. Cheng, Omar F. Zouani, Karine Glinel, Alain M. Jonas, Marie-Christine Durrieu. *Influence of nanopatterned biomaterial surfaces on mesenchymal stem cell behaviours*. **Young Scientists Symposium**, Bordeaux, France, 2012.

Zhe A. Cheng, Karine Glinel, Alain M. Jonas, Marie-Christine Durrieu. *RGD peptides nanopatterning on biomaterial surfaces using nanoimprint for cell adhesion and differentiation studies*. Colloque **Interface Vivant/Matériaux NanoStructurés**, Clermont-Ferrand, France, 2011.

Zhe A. Cheng, Karine Glinel, Alain M. Jonas, Marie-Christine Durrieu. *Biological Multi-Functionalization and Micro/Nanopatterning of Biomaterials*. **IDS-FunMat Training School 2011**, Sesimbra, Portugal, 2011.

Poster presentations

Zhe A. Cheng, Omar F. Zouani, Karine Glinel, Alain M. Jonas, Marie-Christine Durrieu. *Biological Multi-Functionalization and Micro/Nanopatterning of Biomaterials*. **IDS-FunMat Training School 2013**, Annecy, France, 2013.

Zhe A. Cheng, Omar F. Zouani, Karine Glinel, Alain M. Jonas, Marie-Christine Durrieu. *RGD peptide nanopatterning for mesenchymal stem cell adhesion studies*. **9th World Biomaterials Congress**, Chengdu, China, 2012. (Recipient of the "Rapid fire poster presentation" award.)

Zhe A. Cheng, Omar F. Zouani, Karine Glinel, Alain M. Jonas, Marie-Christine Durrieu. *Biological Multi-Functionalization and Micro/Nanopatterning of Biomaterials*. **Journée de l'École doctorale des sciences chimiques**, Bordeaux, France, 2012.

Zhe A. Cheng, Omar F. Zouani, Karine Glinel, Alain M. Jonas, Marie-Christine Durrieu. *Biological Multi-Functionalization and Micro/Nanopatterning of Biomaterials*. **IDS-FunMat Training School 2012**, Anglet, France, 2012.

Naresh Saha, Zhe A. Cheng, Karine Glinel, Claire Monge, Catherine Picart, Marie-Christine Durrieu, Alain M. Jonas. *Preparation of Nano/Micro-Patterned Surfaces for Cell Adhesion Studies*. **Annual Meeting of the Belgian Polymer Group (BPG 2011)**, Houffalize, Belgium, 2011.

A.2 Ultra nanoindentation analysis of mechanical properties

Ultra nanoindentation (UN) is a non-destructive characterization technique that measures the mechanical properties of a material at its extreme surface. Using UN, the hardness and elastic modulus (Young's modulus) of thin films on the range of 10 to 100 nm in thickness can be determined. For instance, it is possible to evaluate the properties of coatings applied onto a material surface or chemical monolayers resulting from surface modification, as is the case for the peptides (RGD and mBMP) in our study. UN experiments were performed by the industry partner Rescoll in France. A Berkovich ultra nanoindentation apparatus (CSM Instruments, Peseux, Switzerland) was used to measure surface mechanical properties, including hardness and elastic modulus, on peptide-modified substrates. The tests were performed with the following parameters: Approaching velocity = 1 μm/min; type of charge = quasi static; charging time = 30 seconds; maximal force = 15 – 25 – 50 and 100 μN depending on the cycles; pause at maximal charge = 10 seconds; decharging time = 30 seconds. Results were obtained using the "Oliver & Pharr" method with a theoretical Poisson coefficient of 0.4 for the calculation of elastic modulus.

The operating principles of UN are described as follows, according to the Oliver and Pharr model (Figure A.1) [287, 288]. An indenter tip approaches a thin film modified substrate surface vertically from the top (Figure A.1A). As the tip contacts the surface, it exerts a pre-defined perpendicular load/force P which allows the tip to penetrate the thin film, reaching a depth of h (h_{max} in Figure A.1B) at maximum loading (P_{max}). The depth of penetration is a function of the magnitude of the applied force, the geometry of the indenter tip, and the intrinsic mechanical properties of the thin film. As the magnitude of the applied force increases, so does the depth of penetration. At P_{max}, the tip is allowed to unload and retract. However, due to elastic and plastic deformation of the substrate and the thin film, the tip does not retract completely to the initial surface but in turn rests at a final displacement h_f (Figure A.1B). The various parameters obtained from this loading and unloading process allow hardness and elastic modulus to be calculated through a series of complex operation and formulae [287]. These parameters include:

P = perpendicular loading force

P_{max} = maximum loading force exerted

a = radius of contact circle

Φ = half angle of indenter

h = depth of penetration/displacement

h_{max} = displacement at P_{max} (full loading)

h_c = contact depth at full loading

$h_s = h_{max} - h_c$ = surface displacement ("sink-in") at contact perimeter

h_f = final displacement after unloading

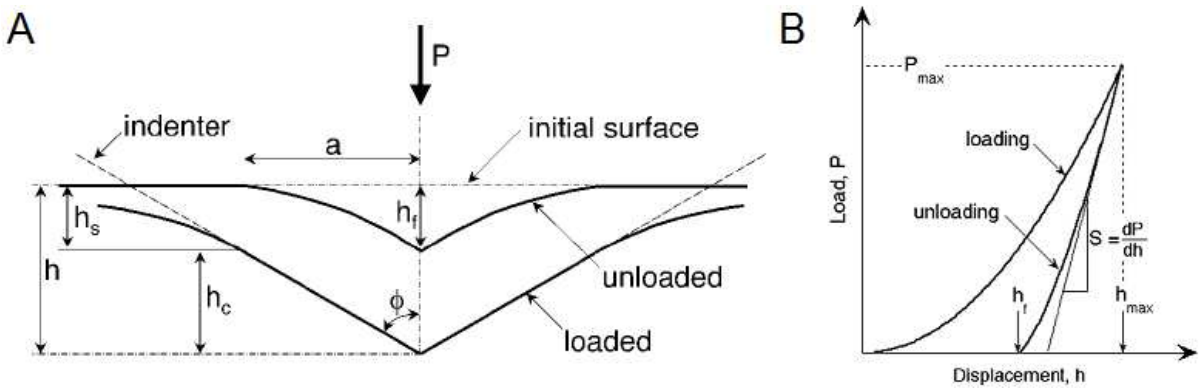

Figure A.1 – Oliver and Pharr model of ultra nanoindentation. The schematic of indenter loading and unloading is shown in (A) with the various parameters that are measured, while the relationship between loading force P and displacement h (penetration depth) during loading and unloading is depicted in (B) [287].

Since the displacement h is proportional to the loading force P, at a given applied force, the indenter will penetrate the surface thin film deep enough to feel the substrate. At this point, substrate effects on hardness and elastic modulus measurements cannot be neglected, and the calculations are further complicated. Generally, different loading forces are tested and the maximum loading force is chosen such that substrate effects are not involved. For very soft thin films, the maximum displacement h_{max} should not exceed 10% of the film thickness in order to limit the measurement to "film only" properties [289, 290]. In other words, $h_{max}/t \leq 0.1$ where t = the thickness of the thin film. Above this threshold, it is likely that substrate effects will interfere with the analysis. Figure A.2 illustrates the effects of intrinsic substrate properties on the measurement of thin film mechanical properties. Here, a soft film is deposited onto a stiff substrate. Several indenter displacements (corresponding to different loading forces) are trialed. Below h_4, output of mechanical properties is constant, implying that

we are still within the regime of "film only" properties. Above h_4, however, substrate effects are taken into account as the indenter begins to feel the stiffer substrate lying underneath the film being measured. Consequently, a maximum displacement h_{max} (and its corresponding P_{max}) should be chosen between h_1 and h_4 to ensure that "film only" properties are calculated and unaffected by substrate properties.

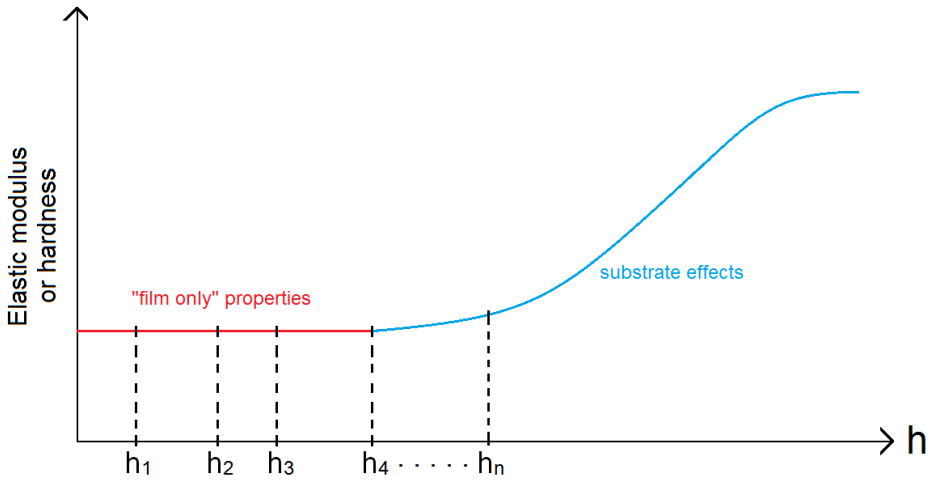

Figure A.2 – Substrate effects on measurement of thin film properties obtained using ultra nanoindentation. Different values of h are tested (from h_1 to h_n), where each h corresponds to a different perpendicular loading force P_{max} exerted by the indenter. Below h_4, the mechanical property (elastic modulus or hardness) remains constant as the indenter is penetrating within the "film only" regime. Above h_4, the outputted value of elastic modulus or hardness is influenced by substrate effects. To obtain information related only to the thin film, h should be chosen such that it does not exceed h_4.

For our UN tests, perpendicular loading forces (P) ranging from 15 to 100 µN were applied to three substrates: bare, polished Si (Si poli), silicon homogeneously grafted with a GRGDSPC peptide (Si + RGD, 7 amino acids), and silicon homogeneously grafted with a mimetic BMP-2 peptide (Si + BMP, 21 amino acids). The substrates were subjected to a force loading-unloading cycle where the maximum displacement of the indenter at full loading and final displacement after retraction were recorded. The loading-unloading profiles of each substrate at various loading forces (P_{max}) are shown in Figure A.3, Figure A.4, and Figure A.5 (see Figure A.1B for typical appearance of loading-unloading curve).

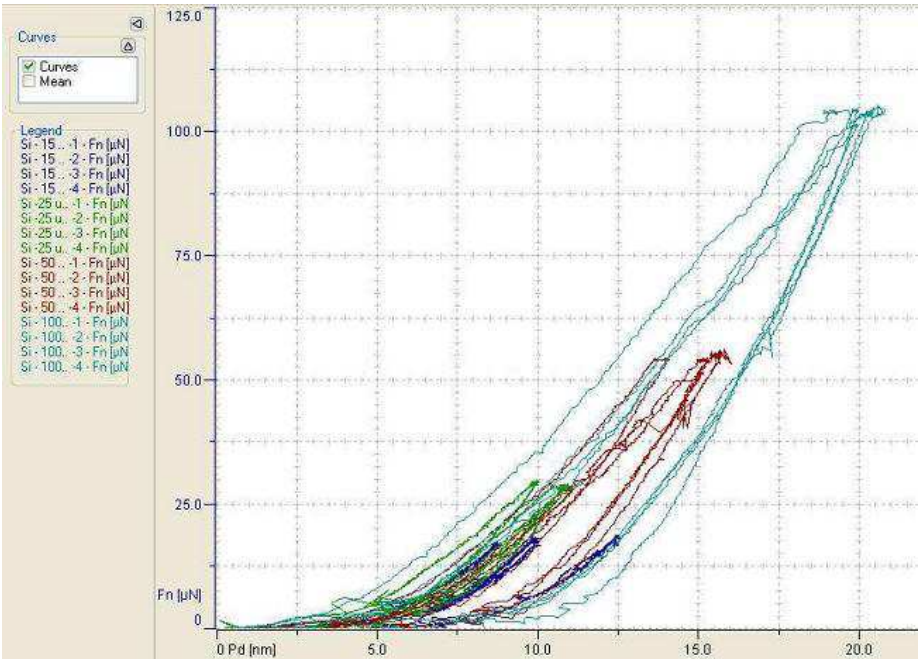

Figure A.3 – UN loading-unloading curves for Si at various loading forces. X-axis = displacement in nm; Y-axis = loading force in µN. Blue: P_{max} = 15 µN; green: P_{max} = 25 µN; red: P_{max} = 50 µN; aqua: P_{max} = 100 µN.

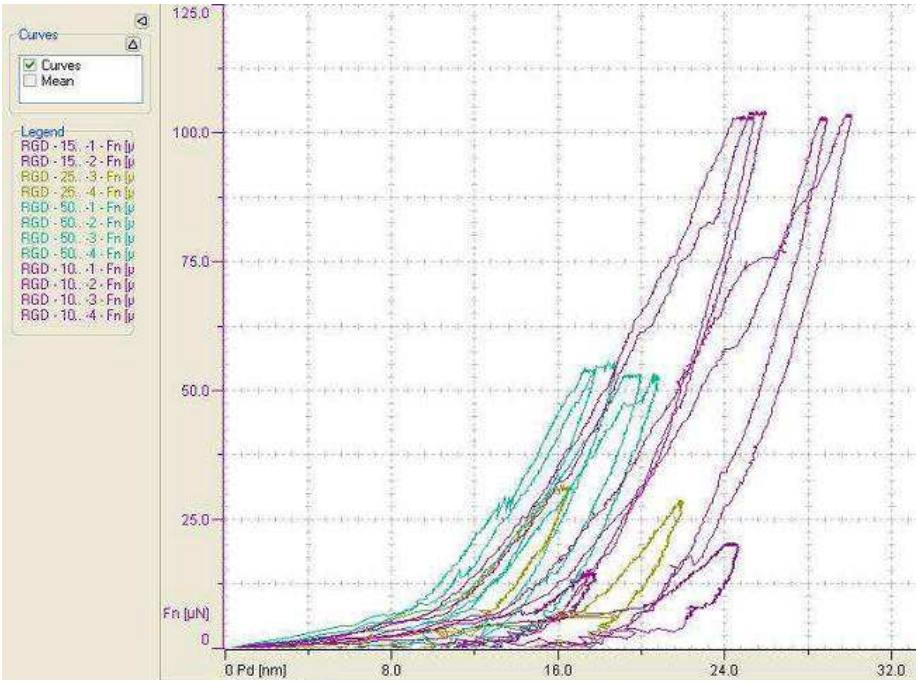

Figure A.4 – UN loading-unloading curves for Si + RGD at various loading forces. X-axis = displacement in nm; Y-axis = loading force in µN. Dark purple: P_{max} = 15 µN; yellow: P_{max} = 25 µN; aqua: P_{max} = 50 µN; light purple: P_{max} = 100 µN.

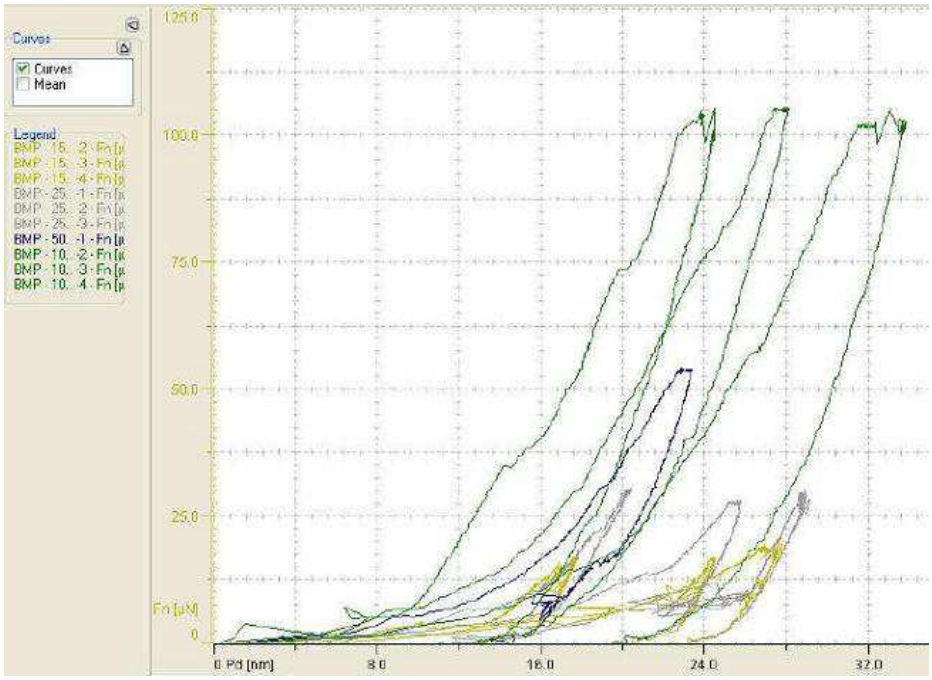

Figure A.5 – UN loading-unloading curves for Si + mBMP at various loading forces. X-axis = displacement in nm; Y-axis = loading force in µN. Yellow: P_{max} = 15 µN; gray: P_{max} = 25 µN; blue: P_{max} = 50 µN; green: P_{max} = 100 µN.

Using the parameters measured from the above figures and the known input parameters, the hardness and elastic modulus of the three substrates can be calculated using the equations developed in the Oliver and Pharr model [287]. The resulting profiles for hardness and elastic modulus are shown in Figure A.6 and Figure A.7, respectively.

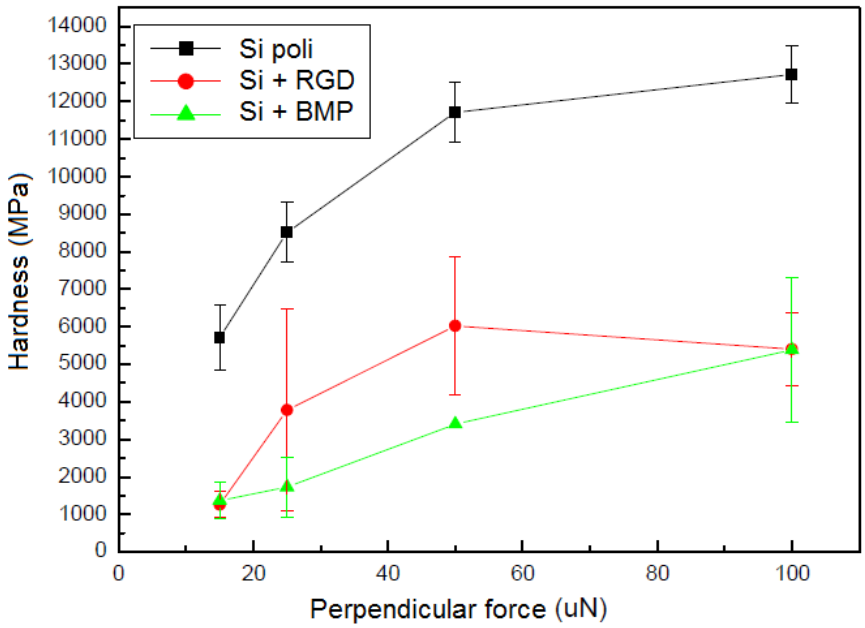

Figure A.6 – Changes in hardness with increasing perpendicular loading force. While both peptide-modified substrates exhibit lower hardness values than the silicon reference, substrate effects are apparent and "peptide only" properties cannot be extracted.

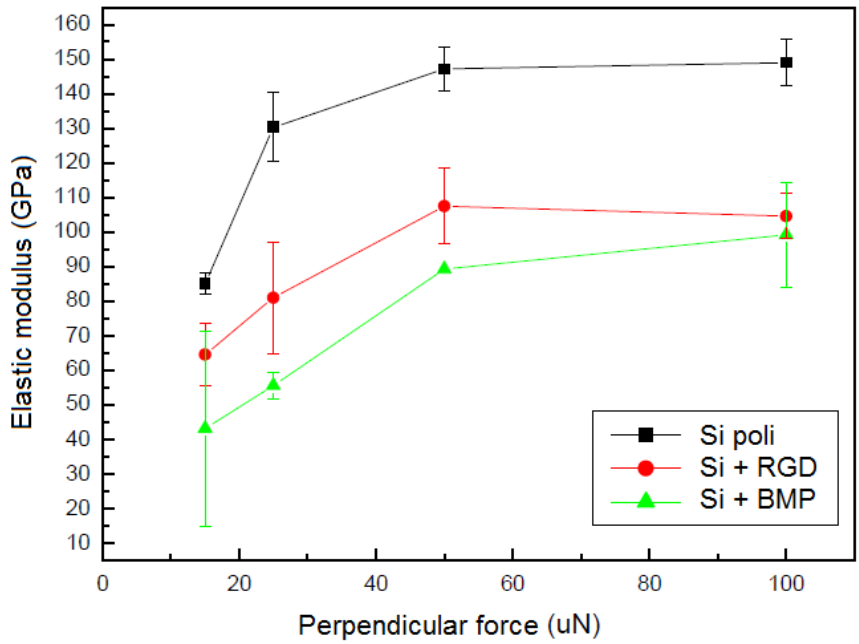

Figure A.7 – Changes in elastic modulus with increasing perpendicular loading force. While both peptide-modified substrates exhibit lower elastic modulus values than the silicon reference, substrate effects are apparent and "peptide only" properties cannot be extracted.

From the two figures, we see a distinct difference in hardness and elastic modulus between the bare silicon reference and the two peptide-modified substrates. For bare silicon, there is a progressive increase in hardness and elastic modulus before reaching an asymptotic regime. The low values of hardness and elastic modulus prior to the asymptote is due to the presence of an oxide layer on the silicon substrate and possible impurities within the layer. Beyond that, we get an average value of 13 GPa for hardness and 149 GPa for elastic modulus, which agree with literature values for conventional untreated silicon [291-294].

For the two peptide-modified surfaces, we see the same trends, yet the values of hardness and elastic modulus do not reach that of the bare silicon and remain lower. There is a clear difference between either modified surface with the bare silicon, which is to be expected as the peptides are much softer than the silicon substrate. Substrate effects on peptide properties are apparent here. As we see in Figure A.6 and Figure A.7, above a loading force of 15 μN, which was the weakest force attainable with our ultra nanoindentation device, the data already exhibit substrate effects as illustrated in Figure A.2. That is to say, even a force of 15 μN is too strong and the indenter has penetrated deep enough within the peptide layer (either RGD or mBMP-2) such that substrate effects cannot be neglected. This is logical because as previously analyzed by XRR (Table IV.1), the thicknesses of the grafted RGD and mBMP-2 monolayers are 1.19 nm and 1.86 nm, respectively. To accurately measure “peptide only” properties, h_{max} should ideally be less than 10% of the monolayer thickness, i.e. 1.19 Å and 1.86 Å for RGD and mBMP-2, respectively. Yet, taking a look at the loading-unloading curves (Figure A.3, Figure A.4, and Figure A.5), the lowest displacement attainable at a maximum load of 15 μN is on the range of 20 to 30 nm, which is much higher than the accepted h_{max}. The "film only" regime requires forces much smaller than 15 μN, which unfortunately is the limit of detection with UN. The peptides are too thin to be measured with the indenter as it directly penetrates into the substrate, bypassing the "film only" regime in Figure A.2. Therefore, “peptide only” mechanical properties cannot be extracted from this technique.

A.3 Abbreviations

AFM – Atomic force microscopy

APDMS – 3-aminopropyldimethylethoxysilane

(m)BMP – (mimetic) Bone morphogenetic protein

ECM – Extracellular matrix

FA – Focal adhesion

(h)MSC – (human) Mesenchymal stem cell

NIL – Nanoimprint lithography

OPN – Osteopontin

OSX – Osterix

PEO – Poly(ethylene oxide)

RGD – Arginine-glycine-aspartic acid

SMP – 3-succinimidyl-3-maleimidopropionate

UN – Ultra nanoindentation

XPS – X-ray photoelectron spectroscopy

XRR – X-ray reflectivity

References

1. Langer, R. and J.P. Vacanti, *Tissue Engineering.* Science, 1993. **260**(5110): p. 920-926.
2. Quarto, R., et al., *Repair of large bone defects with the use of autologous bone marrow stromal cells.* The New England Journal of Medicine, 2001. **344**(5): p. 385-386.
3. Torok, E., et al., *Primary human hepatocytes on biodegradable poly(l-lactic acid) matrices: a promising model for improving transplantation efficiency with tissue engineering.* Liver Transplantation, 2011. **17**(2): p. 104-14.
4. Freed, L.E., et al., *Neocartilage formation in vitro and in vivo using cells cultured on synthetic biodegradable polymers.* Journal of Biomedical Materials Research, 1993. **27**: p. 11-23.
5. Caplan, A.I., *Adult Mesenchymal Stem Cells for Tissue Engineering Versus Regenerative Medicine.* Journal of Cellular Physiology, 2007. **213**: p. 341-347.
6. Tuan, R.S., G. Boland, and R. Tuli, *Adult mesenchymal stem cells and cell-based tissue engineering.* Arthritis Research and Therapy, 2003. **5**(1): p. 32-45.
7. Mason, C. and P. Dunnill, *A brief definition of regenerative medicine.* Future Medicine, 2008. **3**(1): p. 1-5.
8. Griffith, L.G. and G. Naughton, *Tissue engineering--current challenges and expanding opportunities.* Science, 2002. **295**(5557): p. 1009-14.
9. Burke, J.F., et al., *Successful Use of a Physiologically Acceptable Artificial Skin in the Treatment of Extensive Burn Injury.* Annals of Surgery, 1981. **194**(4): p. 413-428.
10. L'Heureux, N., T.N. McAllister, and L.M. de la Fuente, *Tissue-Engineered Blood Vessel for Adult Arterial Revascularization.* New England Journal of Medicine, 2007. **357**(14): p. 1451-1453.
11. Sharma, B., et al., *Human cartilage repair with a photoreactive adhesive-hydrogel composite.* Science Translational Medicine, 2013. **5**(167): p. 167ra6.
12. Stevens, M., *Biomaterials for bone tissue engineering.* Materials Today, 2008. **11**(5): p. 18-25.
13. Petite, H., et al., *Tissue-engineered bone regeneration.* Nature Biotechnology, 2000. **18**: p. 959-963.
14. Porter, J.R., T.T. Ruckh, and K.C. Popat, *Bone tissue engineering: a review in bone biomimetics and drug delivery strategies.* Biotechnology Progress, 2009. **25**(6): p. 1539-60.
15. Dimitriou, R., et al., *Complications following autologous bone graft harvesting from the iliac crest and using the RIA: a systematic review.* Injury, 2011. **42 Suppl 2**: p. S3-15.
16. Nodarian, T., et al., *Iliac crest bone graft harvesting complications: A case of liver herniation.* Orthopaedics & Traumatology: Surgery & Research, 2010. **96**(5): p. 593-6.
17. Damien, C.J. and J.R. Parsons, *Bone Graft and Bone Graft Substitutes: A Review of Current Technology and Applications.* Journal of Applied Biomaterials, 1991. **2**: p. 187-208.
18. Salgado, A.J., O.P. Coutinho, and R.L. Reis, *Bone tissue engineering: state of the art and future trends.* Macromolecular Bioscience, 2004. **4**(8): p. 743-65.
19. Meijer, G.J., et al., *Cell-Based Bone Tissue Engineering.* PLoS Medicine, 2007. **4**(2): p. 260-264.
20. Marolt, D., M. Knezevic, and G.V. Novakovic, *Bone tissue engineering with human stem cells.* Stem Cell Research & Therapy, 2010. **1**(2): p. 10-19.
21. Liao, S., C.K. Chan, and S. Ramakrishna, *Stem cells and biomimetic materials strategies for tissue engineering.* Materials Science and Engineering: C, 2008. **28**(8): p. 1189-1202.
22. Khademhosseini, A., et al., *Microscale technologies for tissue engineering and biology.* Proceedings of the National Academy of Sciences of the United States of America, 2006. **103**(8): p. 2480-7.
23. Parida, P., A. Behera, and S.C. Mishra, *Classification of Biomaterials used in Medicine.* International Journal of Advances in Applied Sciences, 2012. **1**(3): p. 125-129.
24. Lee, C.H., A. Singla, and Y. Lee, *Biomedical applications of collagen.* International Journal of Pharmaceutics, 2001. **221**: p. 1-22.

25. Kim, B.S. and D.J. Mooney, *Development of biocompatible synthetic extracellular matrices for tissue engineering.* Trends in Biotechnology, 1998. **16**(5): p. 224-230.
26. Place, E.S., et al., *Synthetic polymer scaffolds for tissue engineering.* Chemical Society Reviews, 2009. **38**(4): p. 1139-51.
27. Alvarez, K. and H. Nakajima, *Metallic Scaffolds for Bone Regeneration.* Materials, 2009. **2**(3): p. 790-832.
28. Hench, L.L., *Bioceramics: From Concept to Clinic.* Journal of the American Ceramics Society, 1991. **74**(7): p. 1487-1510.
29. Thamaraiselvi, T.V. and S. Rajeswari, *Biological Evaluation of Bioceramics - A Review.* Trends in Biomaterials and Artificial Organs, 2004. **18**(1): p. 9-17.
30. Best, S.M., et al., *Bioceramics: Past, present and for the future.* Journal of the European Ceramic Society, 2008. **28**(7): p. 1319-1327.
31. Narayan, R., *Metallic Biomaterials.* 2009.
32. Niinomi, M., *Metallic biomaterials.* Journal of Artificial Organs, 2008. **11**(3): p. 105-10.
33. Long, M. and H.J. Rack, *Titanium alloys in total joint replacement - a materials science perspective.* Biomaterials, 1998. **19**: p. 1621-1639.
34. Henriques, V.A.R., et al., *Production of Titanium Alloys for Advanced Aerospace Systems by Powder Metallurgy.* Materials Research, 2005. **8**(4): p. 443-446.
35. Le Guehennec, L., et al., *Surface treatments of titanium dental implants for rapid osseointegration.* Dental Materials, 2007. **23**(7): p. 844-54.
36. Hanawa, T., *In vivo metallic biomaterials and surface modification.* Materials Science and Engineering: A, 1999. **267**: p. 260-266.
37. Ratner, B.D. and S.J. Bryant, *Biomaterials: where we have been and where we are going.* Annual Review of Biomedical Engineering, 2004. **6**: p. 41-75.
38. Boivin, M.C., et al., *Human saphenous vein endothelial cell adhesion and expansion on micropatterned polytetrafluoroethylene.* Journal of Biomedical Materials Research Part A, 2013. **101**(3): p. 694-703.
39. Cunha, A., et al., *Wetting behaviour of femtosecond laser textured Ti–6Al–4V surfaces.* Applied Surface Science, 2013. **265**: p. 688-696.
40. Das, R.K., et al., *Influence of Nanohelical Shape and Periodicity on Stem Cell Fate.* ACS Nano, 2013.
41. Chollet, C., et al., *RGD peptides grafting onto poly(ethylene terephthalate) with well controlled densities.* Biomolecular Engineering, 2007. **24**(5): p. 477-82.
42. Chollet, C., et al., *Impact of peptide micropatterning on endothelial cell actin remodeling for cell alignment under shear stress.* Macromolecular Bioscience, 2012. **12**(12): p. 1648-59.
43. Lei, Y., et al., *Peptide immobilization on polyethylene terephthalate surfaces to study specific endothelial cell adhesion, spreading and migration.* Journal of Materials Science: Materials in Medicine, 2012. **23**(11): p. 2761-72.
44. Lei, Y., et al., *Geometrical microfeature cues for directing tubulogenesis of endothelial cells.* PLoS One, 2012. **7**(7): p. e41163.
45. Lei, Y., et al., *Modulation of lumen formation by microgeometrical bioactive cues and migration mode of actin machinery.* Small, 2013. **9**(7): p. 1086-95.
46. Nguyen, M.N., et al., *Impact of RGD nanopatterns grafted onto titanium on osteoblastic cell adhesion.* Biomacromolecules, 2012. **13**(3): p. 896-904.
47. Pichavant, L., et al., *pH-controlled delivery of gentamicin sulfate from orthopedic devices preventing nosocomial infections.* Journal of Controlled Release, 2012. **162**(2): p. 373-81.
48. Porte-Durrieu, M.C., et al., *Cyclo-(DfKRG) peptide grafting onto Ti-6Al-4V: physical characterization and interest towards human osteoprogenitor cells adhesion.* Biomaterials, 2004. **25**(19): p. 4837-46.
49. Porte-Durrieu, M.C., et al., *Development of RGD peptides grafted onto silica surfaces: XPS characterization and human endothelial cell interactions.* Journal of Biomedical Materials Research, 1999. **46**(3): p. 368-375.

50. Saut, O., et al., *Modeling of the migration of endothelial cells on bioactive micropatterned polymers.* Mathematical Biosciences and Engineering, 2013. **10**(4): p. 997-1015.
51. Zouani, O.F., et al., *Differentiation of pre-osteoblast cells on poly(ethylene terephthalate) grafted with RGD and/or BMPs mimetic peptides.* Biomaterials, 2010. **31**(32): p. 8245-53.
52. Zouani, O.F., et al., *Altered nanofeature size dictates stem cell differentiation.* Journal of Cell Science, 2012. **125**(Pt 5): p. 1217-24.
53. Zouani, O.F., et al., *Effect of BMP-2 from matrices of different stiffnesses for the modulation of stem cell fate.* Biomaterials, 2013. **34**(9): p. 2157-66.
54. Zouani, O.F., Y. Lei, and M.C. Durrieu, *Pericytes, Stem-Cell-Like Cells, but not Mesenchymal Stem Cells are Recruited to Support Microvascular Tube Stabilization.* Small, 2013.
55. Cheng, Z.A., et al., *Bioactive chemical nanopatterns impact human mesenchymal stem cell fate.* Nano Letters, 2013. **13**(8): p. 3923-9.
56. Mieszawska, A.J. and D.L. Kaplan, *Smart biomaterials - regulating cell behavior through signaling molecules.* BMC Biology, 2010. **8**(59): p. 1-3.
57. Karkkainen, M.J. and T.V. Petrova, *Vascular endothelial growth factor receptors in the regulation of angiogenesis and lymphangiogenesis.* Oncogene, 2000. **19**: p. 5598-5605.
58. Nourse, M.B., et al., *VEGF induces differentiation of functional endothelium from human embryonic stem cells: implications for tissue engineering.* Arteriosclerosis, Thrombosis, and Vascular Biology, 2010. **30**(1): p. 80-9.
59. Gomez, N., et al., *Immobilized nerve growth factor and microtopography have distinct effects on polarization versus axon elongation in hippocampal cells in culture.* Biomaterials, 2007. **28**(2): p. 271-84.
60. Javed, F., et al., *Significance of the platelet-derived growth factor in periodontal tissue regeneration.* Archives of Oral Biology, 2011. **56**(12): p. 1476-84.
61. Yang, H., W. Hong, and L. Dong, *A controlled biochemical release device with embedded nanofluidic channels.* Applied Physics Letters, 2012. **100**(15): p. 153510.
62. Chollet, C., et al., *The effect of RGD density on osteoblast and endothelial cell behavior on RGD-grafted polyethylene terephthalate surfaces.* Biomaterials, 2009. **30**(5): p. 711-20.
63. Pittenger, M.F., *Multilineage Potential of Adult Human Mesenchymal Stem Cells.* Science, 1999. **284**(5411): p. 143-147.
64. Coelho, M.J. and M.H. Fernandes, *Human bone cell cultures in biocompatibility testing, Part II: effect of ascorbic acid, b-glycerophosphate and dexamethasone on osteoblastic differentiation.* Biomaterials, 2000. **21**: p. 1095-1102.
65. Jaiswal, N., et al., *Osteogenic Differentiation of Purified, Culture-Expanded Human Mesenchymal Stem Cells In Vitro.* Journal of Cellular Biochemistry, 1997. **64**: p. 295-312.
66. Tenenbaum, H.C. and J.N.M. Heersche, *Differentiation of Osteoblasts and Formation of Mineralized Bone in Vitro.* Calcified Tissue International, 1982. **34**: p. 76-79.
67. Klemm, D.J., et al., *Insulin-induced adipocyte differentiation. Activation of CREB rescues adipogenesis from the arrest caused by inhibition of prenylation.* The Journal of Biological Chemistry, 2001. **276**(30): p. 28430-5.
68. Franceschi, R.T., *The Role of Ascorbic Acid in Mesenchymal Differentiation.* Nutrition Reviews, 1992. **50**(3): p. 65-70.
69. Hersel, U., C. Dahmen, and H. Kessler, *RGD modified polymers: biomaterials for stimulated cell adhesion and beyond.* Biomaterials, 2003. **24**(24): p. 4385-4415.
70. Ruoslahti, E., *RGD and other recognition sequences for integrins.* Annual Review of Cell and Developmental Biology, 1996. **12**: p. 697-715.
71. Maheshwari, G., et al., *Cell adhesion and motility depend on nanoscale RGD clustering.* Journal of Cell Science, 2000. **113 (Pt 10)**: p. 1677-86.
72. Gao, J., et al., *A neuroinductive biomaterial based on dopamine.* Proceedings of the National Academy of Sciences of the United States of America, 2006. **103**(45): p. 16681-6.
73. Fan, V.H., et al., *Tethered epidermal growth factor provides a survival advantage to mesenchymal stem cells.* Stem Cells, 2007. **25**(5): p. 1241-51.

74. Oberpenning, F., et al., *De novo reconstitution of a functional mammalian urinary bladder by tissue engineering.* Nature Biotechnology, 1999. **17**: p. 149-155.
75. Shinoka, T., et al., *Tissue engineering heart valves: Valve leaflet replacement study in a lamb model.* The Annals of Thoracic Surgery, 1995. **60**: p. S513-S516.
76. Heath, C.A., *Cells for tissue engineering.* Trends in Biotechnology, 2000. **18**(1): p. 17-19.
77. Atala, A., *Engineering tissues, organs and cells.* Journal of Tissue Engineering and Regenerative Medicine, 2007. **1**(2): p. 83-96.
78. Chollet, C., et al., *Impact of RGD micro-patterns on cell adhesion.* Colloids and Surfaces B Biointerfaces, 2010. **75**(1): p. 107-14.
79. Weiss, P. and B. Garber, *Shape and Movement of Mesenchyme Cells as Functions of the Physical Structure of the Medium. Contributions to a Quantitative Morphology.* Proceedings of the National Academy of Sciences of the United States of America, 1952. **38**(3): p. 264-280.
80. Chen, C.S., *Geometric Control of Cell Life and Death.* Science, 1997. **276**(5317): p. 1425-1428.
81. Chen, C.S., et al., *Cell shape provides global control of focal adhesion assembly.* Biochemical and Biophysical Research Communications, 2003. **307**(2): p. 355-361.
82. McBeath, R., et al., *Cell Shape, Cytoskeletal Tension, and RhoA Regulate Stem Cell Lineage Commitment.* Developmental Cell, 2004. **6**: p. 483-495.
83. Kilian, K.A., et al., *Geometric cues for directing the differentiation of mesenchymal stem cells.* Proceedings of the National Academy of Sciences of the United States of America, 2010. **107**(11): p. 4872-7.
84. Discher, D.E., P.A. Janmey, and Y. Wang, *Tissue Cells Feel and Respond to the Stiffness of Their Substrate.* Science, 2005. **310**: p. 1139-1143.
85. Gumbiner, B.M., *Cell Adhesion: The Molecular Basis of Tissue Architecture and Morphogenesis.* Cell, 1996. **84**: p. 345-357.
86. Ruoslahti, E. and J.C. Reed, *Anchorage Dependence, Integrins, and Apoptosis.* Cell, 1994. **77**: p. 477-478.
87. Engler, A.J., et al., *Matrix elasticity directs stem cell lineage specification.* Cell, 2006. **126**(4): p. 677-89.
88. Flanagan, L.A., et al., *Neurite branching on deformable substrates.* Neuroreport, 2002. **13**(18): p. 2411-2415.
89. Engler, A.J., et al., *Myotubes differentiate optimally on substrates with tissue-like stiffness: pathological implications for soft or stiff microenvironments.* The Journal of Cell Biology, 2004. **166**(6): p. 877-87.
90. Garcia, A.J. and C.D. Reyes, *Bio-adhesive Surfaces to Promote Osteoblast Differentiation and Bone Formation.* Journal of Dental Research, 2005. **84**(5): p. 407-413.
91. Saha, K., et al., *Substrate modulus directs neural stem cell behavior.* Biophysical Journal, 2008. **95**(9): p. 4426-38.
92. Fu, J., et al., *Mechanical regulation of cell function with geometrically modulated elastomeric substrates.* Nature Methods, 2010. **7**(9): p. 733-6.
93. Winer, J.P., et al., *Bone Marrow-Derived Human Mesenchymal Stem Cells Become Quiescent on Soft Substrates but Remain Responsive to Chemical or Mechanical Stimuli.* Tissue Engineering Part A, 2009. **15**(1): p. 147-154.
94. Guilak, F., et al., *Control of stem cell fate by physical interactions with the extracellular matrix.* Cell Stem Cell, 2009. **5**(1): p. 17-26.
95. Wang, N., J.D. Tytell, and D.E. Ingber, *Mechanotransduction at a distance: mechanically coupling the extracellular matrix with the nucleus.* Nature Reviews, 2009. **10**: p. 75-82.
96. Wang, N., J.P. Butler, and D.E. Ingber, *Mechanotransduction Across the Cell Surface and Through the Cytoskeleton.* Science, 1993. **260**(5111): p. 1124-1127.
97. Riveline, D., et al., *Focal contacts as mechanosensors: externally applied local mechanical force induces growth of focal contacts by an mDia1-dependent and ROCK-independent mechanism.* Journal of Cell Biology, 2001. **153**(6): p. 1175-86.

98. Nava, M.M., M.T. Raimondi, and R. Pietrabissa, *Controlling self-renewal and differentiation of stem cells via mechanical cues.* Journal of Biomedicine and Biotechnology, 2012. **2012**: p. 797410.
99. Kurpinski, K., et al., *Anisotropic mechanosensing by mesenchymal stem cells.* Proceedings of the National Academy of Sciences of the United States of America, 2006. **103**(44): p. 16095-100.
100. Subramony, S.D., et al., *The guidance of stem cell differentiation by substrate alignment and mechanical stimulation.* Biomaterials, 2013. **34**(8): p. 1942-53.
101. Lee, J.H., et al., *Cell behaviour on polymer surfaces with different functional groups.* Biomaterials, 1993. **15**(9): p. 705-711.
102. Ruoslahti, E. and M.D. Pierschbacher, *New Perspectives in Cell Adhesion: RGD and Integrins.* Science, 1987. **238**(4826): p. 491-197.
103. Huang, H., et al., *Enhanced Osteoblast Functions on RGD Immobilized Surface.* Journal of Oral Implantology, 2003. **29**(2): p. 73-79.
104. Kantlehner, M., et al., *Surface Coating with Cyclic RGD Peptides Stimulates Osteoblast Adhesion and Proliferation as well as Bone Formation.* ChemBioChem, 2000. **1**: p. 107-114.
105. Balasundaram, G. and T.J. Webster, *Increased osteoblast adhesion on nanograined Ti modified with KRSR.* Journal of Biomedical Materials Research Part A, 2007. **80**(3): p. 602-11.
106. Kim, J.W., et al., *Effect of RGDS and KRSR peptides immobilized on silk fibroin nanofibrous mats for cell adhesion and proliferation.* Macromolecular Research, 2010. **18**(5): p. 442-448.
107. Schuler, M., et al., *Comparison of the response of cultured osteoblasts and osteoblasts outgrown from rat calvarial bone chips to nonfouling KRSR and FHRRIKA-peptide modified rough titanium surfaces.* Journal of Biomedical Materials Research Part B: Applied Biomaterials, 2009. **91**(2): p. 517-27.
108. Sawyer, A.A., K.M. Hennessy, and S.L. Bellis, *The effect of adsorbed serum proteins, RGD and proteoglycan-binding peptides on the adhesion of mesenchymal stem cells to hydroxyapatite.* Biomaterials, 2007. **28**(3): p. 383-92.
109. Linkhart, T.A., S. Mohan, and D.J. Baylink, *Growth Factors For Bone Growth And Repair: IGF, TGFB And BMP.* Bone, 1996. **19**(1): p. 1S-12S.
110. Lieberman, J.R., A. Daluiski, and T.A. Einhorn, *The Role of Growth Factors in the Repair of Bone.* The Journal of Bone and Joint Surgery, 2002. **84A**(6): p. 1032-1044.
111. Schmitt, J.M., et al., *Bone Morphogenetic Proteins: An Update on Basic Biology and Clinical Relevance.* Journal of Orthopaedic Research, 1999. **17**: p. 269-278.
112. Yin, H., et al., *Characterization of ligand-binding properties of the human BMP type II receptor extracellular domain.* Journal of Molecular Biology, 2008. **378**(1): p. 191-203.
113. ten Dijke, P., et al., *Controlling cell fate by bone morphogenetic protein receptors.* Molecular and Cellular Endocrinology, 2003. **211**(1-2): p. 105-113.
114. Liu, F., et al., *Human type II receptor for bone morphogenetic proteins (BMPs): extension of the two-kinase receptor model to the BMPs.* Molecular and Cellular Biology, 1995. **15**(7): p. 3479-3486.
115. Crouzier, T., et al., *Presentation of BMP-2 from a soft biopolymeric film unveils its activity on cell adhesion and migration.* Advanced Materials, 2011. **23**(12): p. H111-8.
116. Kim, S.H., J. Turnbull, and S. Guimond, *Extracellular matrix and cell signalling: the dynamic cooperation of integrin, proteoglycan and growth factor receptor.* Journal of Endocrinology, 2011. **209**(2): p. 139-51.
117. Murakami, N., et al., *Repair of segmental defects in rabbit humeri with titanium fiber mesh cylinders containing recombinant human bone morphogenetic protein-2 (rhBMP-2) and a synthetic polymer.* Journal of Biomedical Materials Research, 2002. **62**(2): p. 169-174.

118. Hartung, A., et al., *Different routes of bone morphogenic protein (BMP) receptor endocytosis influence BMP signaling.* Molecular and Cellular Biology, 2006. **26**(20): p. 7791-805.
119. Balloni, S., et al., *Effects of Titanium Surface Roughness on Mesenchymal Stem Cell Commitment and Differentiation Signaling.* The International Journal of Oral & Maxillofacial Implants, 2009. **24**(4): p. 627-635.
120. Wilkinson, C.D., et al., *The use of materials patterned on a nano- and micro-metric scale in cellular engineering.* Materials Science and Engineering: C, 2002. **19**: p. 263-269.
121. Yim, E.K., et al., *Nanotopography-induced changes in focal adhesions, cytoskeletal organization, and mechanical properties of human mesenchymal stem cells.* Biomaterials, 2010. **31**(6): p. 1299-306.
122. Yim, E.K., S.W. Pang, and K.W. Leong, *Synthetic nanostructures inducing differentiation of human mesenchymal stem cells into neuronal lineage.* Experimental Cell Research, 2007. **313**(9): p. 1820-9.
123. Dalby, M.J., et al., *The control of human mesenchymal cell differentiation using nanoscale symmetry and disorder.* Nature Materials, 2007. **6**(12): p. 997-1003.
124. Huang, J., et al., *Impact of order and disorder in RGD nanopatterns on cell adhesion.* Nano Letters, 2009. **9**(3): p. 1111-6.
125. Park, J., et al., *Nanosize and Vitality: TiO2 Nanotube Diameter Directs Cell Fate.* Nano Letters, 2007. **7**(6): p. 1686-1691.
126. Oh, S., et al., *Stem cell fate dictated solely by altered nanotube dimension.* Proceedings of the National Academy of Sciences of the United States of America, 2009. **106**(7): p. 2130-5.
127. Zhao, L., et al., *Suppressed primary osteoblast functions on nanoporous titania surface.* Journal of Biomedical Materials Research Part A, 2011. **96**(1): p. 100-7.
128. Clarke, B., *Normal bone anatomy and physiology.* Clinical Journal of the American Society of Nephrology, 2008. **3 Suppl 3**: p. S131-9.
129. Bosman, F.T. and I. Stamenkovic, *Functional structure and composition of the extracellular matrix.* The Journal of Pathology, 2003. **200**(4): p. 423-8.
130. Gelse, K., *Collagens—structure, function, and biosynthesis.* Advanced Drug Delivery Reviews, 2003. **55**(12): p. 1531-1546.
131. Lieff, J., *Proteins in the Neuron Shape is Function.* 2012.
132. Arima, Y. and H. Iwata, *Effects of surface functional groups on protein adsorption and subsequent cell adhesion using self-assembled monolayers.* Journal of Materials Chemistry, 2007. **17**(38): p. 4079.
133. Sengupta, D. and S.D. Heilshorn, *Protein-Engineered Biomaterials: Highly Tunable Tissue Engineering Scaffolds.* Tissue Engineering Part B, 2010. **16**(3): p. 285-293.
134. Fields, G.B., et al., *Proteinlike Molecular Architecture: Biomaterial Applications for Inducing Cellular Receptor Binding and Signal Transduction.* Biopolymers Peptide Science, 1998. **47**(2): p. 143-151.
135. Hlady, V.V. and J. Buijs, *Protein adsorption on solid surfaces.* Current Opinion in Biotechnology, 1996. **7**(1): p. 72-7.
136. Lhoest, J.-B., et al., *Fibronectin adsorption, conformation, and orientation on polystyrene substrates studied by radiolabeling, XPS, and ToF SIMS.* Journal of Biomedical Materials Research, 1997. **41**(1): p. 95-103.
137. Keselowsky, B.G., D.M. Collard, and A.J. Garcia, *Surface chemistry modulates fibronectin conformation and directs integrin binding and specificity to control cell adhesion.* Journal of Biomedical Materials Research Part A, 2003. **66A**(2): p. 247-259.
138. Garcia, A.J., M.D. Vega, and D. Boettiger, *Modulation of Cell Proliferation and Differentiation through Substrate-dependent Changes in Fibronectin Conformation.* Molecular Biology of the Cell, 1999. **10**(3): p. 785-798.
139. Dettin, M., et al., *Effect of synthetic peptides on osteoblast adhesion.* Biomaterials, 2005. **26**(22): p. 4507-15.

140. Collier, J.H. and T. Segura, *Evolving the use of peptides as components of biomaterials.* Biomaterials, 2011. **32**(18): p. 4198-4204.
141. Beutner, R., et al., *Biological nano-functionalization of titanium-based biomaterial surfaces: a flexible toolbox.* Journal of the Royal Society Interface, 2010. **7 Suppl 1**: p. S93-S105.
142. Kowalczynska, H.M., et al., *Fibronectin adsorption and arrangement on copolymer surfaces and their significance in cell adhesion.* Journal of Biomedical Materials Research Part A, 2005. **72**(2): p. 228-36.
143. Toworfe, G.K., et al., *Fibronectin adsorption on surface-activated poly(dimethylsiloxane) and its effect on cellular function.* Journal of Biomedical Materials Research Part A, 2004. **71**(3): p. 449-61.
144. Zhou, Z. and M.E. Meyerhoff, *Preparation and characterization of polymeric coatings with combined nitric oxide release and immobilized active heparin.* Biomaterials, 2005. **26**(33): p. 6506-17.
145. Wong, L.S., F. Khan, and J. Mickelfield, *Selective Protein Covalent Immobilization: Strategies and Applications.* Chemical Reviews, 2009. **109**: p. 4025-4053.
146. Giancotti, F.G., *Integrin Signaling.* Science, 1999. **285**(5430): p. 1028-1033.
147. Takada, Y., X. Ye, and S. Simon, *The integrins.* Genome Biology, 2007. **8**(5): p. 215.
148. Adams, J.C., *Cell-matrix contact structures.* Cellular and Molecular Sciences, 2001. **58**(3): p. 371-92.
149. Geiger, B., J.P. Spatz, and A.D. Bershadsky, *Environmental sensing through focal adhesions.* Nature Reviews Molecular Cell Biology, 2009. **10**(1): p. 21-33.
150. Geiger, B. and A. Bershadsky, *Assembly and mechanosensory function of focal contacts.* Current Opinion in Cell Biology, 2001. **13**(5): p. 584-92.
151. Jones, J.L. and R.A. Walker, *Integrins a role as cell signalling molecules.* Journal of Clinical Pathology, 1999. **52**: p. 208-213.
152. Geiger, B., et al., *Vinculin, an intracellular protein localized at specialized sites where microfilament bundles terminate at cell membranes.* Proceedings of the National Academy of Sciences of the United States of America, 1980. **77**(7): p. 4127-4131.
153. Miyamoto, S., et al., *Integrin function: molecular hierarchies of cytoskeletal and signaling molecules.* The Journal of Cell Biology, 1995. **131**(3): p. 791-805.
154. Geiger, B., et al., *Transmembrane extracellular matrix-cytoskeleton crosstalk.* Nature Reviews, 2001. **2**: p. 793-805.
155. Nobes, C.D. and A. Hall, *Rho, Rac, and Cdc42 GTPases Regulate the Assembly of Multimolecular Focal Complexes Associated with Actin Stress Fibers, Lamellipodia, and Filopodia.* Cell, 1995. **81**: p. 53-62.
156. Alexandrova, A.Y., et al., *Comparative dynamics of retrograde actin flow and focal adhesions: formation of nascent adhesions triggers transition from fast to slow flow.* PLoS One, 2008. **3**(9): p. e3234.
157. Choi, C.K., et al., *Actin and alpha-actinin orchestrate the assembly and maturation of nascent adhesions in a myosin II motor-independent manner.* Nature Cell Biology, 2008. **10**(9): p. 1039-50.
158. Schwartz, M.A., *Integrins and extracellular matrix in mechanotransduction.* Cold Spring Harbor Perspectives in Biology, 2010. **2**(12): p. a005066.
159. Biggs, M.J. and M.J. Dalby, *Focal adhesions in osteoneogenesis.* Proceedings of the Institution of Mechanical Engineers, 2010. **224**(12): p. 1441-1453.
160. Zamir, E., et al., *Dynamics and segregation of cell-matrix adhesions in cultured fibroblasts.* Nature Cell Biology, 2000. **2**: p. 191-196.
161. Morgan, M.R., M.J. Humphries, and M.D. Bass, *Synergistic control of cell adhesion by integrins and syndecans.* Nature Reviews Molecular Cell Biology, 2007. **8**(12): p. 957-69.
162. Arnold, M., et al., *Activation of integrin function by nanopatterned adhesive interfaces.* Chemphyschem, 2004. **5**(3): p. 383-8.

163. Tsimbouri, P.M., et al., *Using Nanotopography and Metabolomics to Identify Biochemical Effectors of Multipotency.* ACS Nano, 2012. **6**(11): p. 10239-10249.
164. Xiao, G., et al., *Bone Morphogenetic Proteins, Extracellular Matrix, and Mitogen-Activated Protein Kinase Signaling Pathways Are Required for Osteoblast-Specific Gene Expression and Differentiation in MC3T3-E1 Cells.* Journal of Bone and Mineral Research, 2002. **17**(1): p. 101-110.
165. Lecanda, F., L.V. Avioli, and S.L. Cheng, *Regulation of Bone Matrix Protein Expression and Induction of Differentiation of Human Osteoblasts and Human Bone Marrow Stromal Cells by Bone Morphogenetic Protein-2.* Journal of Cellular Biochemistry, 1997. **67**: p. 386-398.
166. Lai, C.F. and S.L. Cheng, *Alphavbeta integrins play an essential role in BMP-2 induction of osteoblast differentiation.* Journal of Bone and Mineral Research, 2005. **20**(2): p. 330-40.
167. Du, J., et al., *Integrin activation and internalization on soft ECM as a mechanism of induction of stem cell differentiation by ECM elasticity.* Proceedings of the National Academy of Sciences of the United States of America, 2011. **108**(23): p. 9466-71.
168. Caplan, A.I., *Mesenchymal Stem Cells.* Journal of Orthopaedic Research, 1991. **9**: p. 641-650.
169. Fuchs, E., T. Tumbar, and G. Guasch, *Socializing with the Neighbors: Stem Cells and Their Niche.* Cell, 2004. **116**: p. 769-778.
170. Minguell, J.J., A. Erices, and P. Conget, *Mesenchymal Stem Cells.* Experimental Biology and Medicine, 2001. **226**: p. 507-520.
171. Moore, K.A. and I.R. Lemischka, *Stem cells and their niches.* Science, 2006. **311**(5769): p. 1880-5.
172. Petersen, B.E., *Bone Marrow as a Potential Source of Hepatic Oval Cells.* Science, 1999. **284**(5417): p. 1168-1170.
173. Wilson, A. and A. Trumpp, *Bone-marrow haematopoietic-stem-cell niches.* Nature Reviews Immunology, 2006. **6**(2): p. 93-106.
174. Bjornson, C.R., *Turning Brain into Blood: A Hematopoietic Fate Adopted by Adult Neural Stem Cells in Vivo.* Science, 1999. **283**(5401): p. 534-537.
175. Kennea, N.L. and H. Mehmet, *Neural stem cells.* The Journal of Pathology, 2002. **197**(4): p. 536-50.
176. Potten, C.S. and R.J. Morris, *Epithelial stem cells in vivo.* Journal of Cell Science, 1988. **10**: p. 45-62.
177. Marshman, E., C. Booth, and C.S. Potten, *The intestinal epithelial stem cell.* BioEssays, 2002. **24**(1): p. 91-98.
178. Thomson, J.A., *Embryonic Stem Cell Lines Derived from Human Blastocysts.* Science, 1998. **282**(5391): p. 1145-1147.
179. Shamblott, M.J., et al., *Derivation of pluripotent stem cells from cultured human primordial germ cells.* Proceedings of the National Academy of Sciences of the United States of America, 1998. **95**: p. 13726-13731.
180. Reubinoff, B.E., et al., *Embryonic stem cell lines from human blastocysts: somatic differentiation in vitro.* Nature Biotechnology, 2000. **18**: p. 399-404.
181. Yin, T. and L. Li, *The stem cell niches in bone.* Journal of Clinical Investigation, 2006. **116**(5): p. 1195-201.
182. Kolf, C.M., E. Cho, and R.S. Tuan, *Mesenchymal stromal cells. Biology of adult mesenchymal stem cells: regulation of niche, self-renewal and differentiation.* Arthritis Research and Therapy, 2007. **9**(1): p. 204.
183. Scadden, D.T., *The stem-cell niche as an entity of action.* Nature, 2006. **441**(7097): p. 1075-9.
184. Sun, Y., C.S. Chen, and J. Fu, *Forcing stem cells to behave: a biophysical perspective of the cellular microenvironment.* Annual Review of Biophysics, 2012. **41**: p. 519-42.
185. Peerani, R. and P.W. Zandstra, *Enabling stem cell therapies through synthetic stem cell-niche engineering.* Journal of Clinical Investigation, 2010. **120**(1): p. 60-70.

186. Watt, F.M., *Out of Eden: Stem Cells and Their Niches.* Science, 2000. **287**(5457): p. 1427-1430.
187. Barry, F.P. and J.M. Murphy, *Mesenchymal stem cells: clinical applications and biological characterization.* The International Journal of Biochemistry & Cell Biology, 2004. **36**(4): p. 568-84.
188. Caplan, A.I., *Mesenchymal Stem Cells: The Past, the Present, the Future.* Cartilage, 2009. **1**(1): p. 6-9.
189. Whitesides, G.M., et al., *Soft Lithography in Biology and Biochemistry.* Annual Review of Biomedical Engineering, 2001. **3**: p. 335-373.
190. Kane, R.S., et al., *Patterning proteins and cells using soft lithography.* Biomaterials, 1999. **20**: p. 2363-2376.
191. Tan, J.L., J. Tien, and C.S. Chen, *Microcontact Printing of Proteins on Mixed Self-Assembled Monolayers.* Langmuir, 2002. **18**: p. 519-523.
192. Chen, C.S., et al., *Micropatterned Surfaces for Control of Cell Shape, Position, and Function.* Biotechnology Progress, 1998. **14**: p. 356-363.
193. Kim, E., Y. Xia, and G.M. Whitesides, *Polymer microstructures formed by moulding in capillaries.* Nature Biotechnology, 2002. **376**(581-584).
194. Delamarche, E., *Patterned Delivery of Immunoglobulins to Surfaces Using Microfluidic Networks.* Science, 1997. **276**(5313): p. 779-781.
195. Chiu, D.T., et al., *Patterned deposition of cells and proteins onto surfaces by using three-dimensional microfluidic systems.* Proceedings of the National Academy of Sciences of the United States of America, 2000. **97**(6): p. 2408-13.
196. Trkov, S., et al., *Micropatterned three-dimensional hydrogel system to study human endothelial-mesenchymal stem cell interactions.* Journal of Tissue Engineering and Regenerative Medicine, 2010. **4**(3): p. 205-15.
197. Yap, F.L. and Y. Zhang, *Protein and cell micropatterning and its integration with micro/nanoparticles assembly.* Biosensors and Bioelectronics, 2007. **22**(6): p. 775-88.
198. Tan, J. and W.M. Saltzman, *Biomaterials with hierarchically defined micro- and nanoscale structure.* Biomaterials, 2004. **25**(17): p. 3593-601.
199. Yan, C., J. Sun, and J. Ding, *Critical areas of cell adhesion on micropatterned surfaces.* Biomaterials, 2011. **32**(16): p. 3931-3938.
200. Chen, W., et al., *Nanotopography Influences Adhesion, Spreading, and Self-Renewal of Human Embryonic Stem Cells.* ACS Nano, 2012. **6**(5): p. 4094-4103.
201. Yim, E.K.F. and K.W. Leong, *Significance of synthetic nanostructures in dictating cellular response.* Nanomedicine: Nanotechnology, Biology and Medicine, 2005. **1**(1): p. 10-21.
202. Nie, Z. and E. Kumacheva, *Patterning surfaces with functional polymers.* Nature Materials, 2008. **7**: p. 277-290.
203. Norman, J.J. and T.A. Desai, *Methods for Fabrication of Nanoscale Topography for Tissue Engineering Scaffolds.* Annals of Biomedical Engineering, 2006. **34**(1): p. 89-101.
204. Vieu, C., et al., *Electron beam lithography: resolution limits and applications.* Applied Surface Science, 2000. **164**: p. 111-117.
205. Christman, K.L., V.D. Enriquez-Rios, and H.D. Maynard, *Nanopatterning proteins and peptides.* Soft Matter, 2006. **2**(11): p. 928.
206. Arnold, M., et al., *Cell interactions with hierarchically structured nano-patterned adhesive surfaces.* Soft Matter, 2009. **5**(1): p. 72-77.
207. Dalby, M.J., N. Gadegaard, and C.D.W. Wilkinson, *The response of fibroblasts to hexagonal nanotopography fabricated by electron beam lithography.* Journal of Biomedical Materials Research Part A, 2008. **84A**(4): p. 973-979.
208. Kulangara, K., et al., *Nanotopography as modulator of human mesenchymal stem cell function.* Biomaterials, 2012. **33**(20): p. 4998-5003.
209. Chou, S.Y., P.R. Krauss, and P.J. Renstrom, *Imprint Lithography with 25-Nanometer Resolution.* Science, 1996. **272**(5258): p. 85-87.

210. Gates, B.D., et al., *New Approaches to Nanofabrication: Molding, Printing, and Other Techniques.* Chemical Reviews, 2005. **105**: p. 1171-1196.
211. Long, B.K., B.K. Keitz, and C.G. Willson, *Materials for step and flash imprint lithography (S-FIL®).* Journal of Materials Chemistry, 2007. **17**(34): p. 3575.
212. Guo, L.J., *Nanoimprint Lithography: Methods and Material Requirements.* Advanced Materials, 2007. **19**(4): p. 495-513.
213. Yu, Z., S.J. Schablitsky, and S.Y. Chou, *Nanoscale GaAs metal–semiconductor–metal photodetectors fabricated using nanoimprint lithography.* Applied Physics Letters, 1999. **74**(16): p. 2381.
214. Wu, W., et al., *Large area high density quantized magnetic disks fabricated using nanoimprint lithography.* Journal of Vacuum Science & Technology B, 1998. **16**(6): p. 3825-3829.
215. Wang, J., et al., *Fabrication of a new broadband waveguide polarizer with a double-layer 190 nm period metal-gratings using nanoimprint lithography.* Journal of Vacuum Science & Technology B, 1999. **17**(6): p. 2957-2960.
216. Falconnet, D., et al., *A Novel Approach to Produce Protein Nanopatterns by Combining Nanoimprint Lithography and Molecular Self-Assembly.* Nano Letters, 2004. **4**(10): p. 1909-1914.
217. Engel, E., et al., *Mesenchymal stem cell differentiation on microstructured poly (methyl methacrylate) substrates.* Annals of Anatomy, 2009. **191**(1): p. 136-44.
218. Franco, D., et al., *Control of initial endothelial spreading by topographic activation of focal adhesion kinase.* Soft Matter, 2011. **7**(16): p. 7313.
219. Abdul Kafi, M., et al., *Cell adhesion, spreading, and proliferation on surface functionalized with RGD nanopillar arrays.* Biomaterials, 2012. **33**(3): p. 731-9.
220. Dalby, M.J., et al., *Osteoprogenitor response to semi-ordered and random nanotopographies.* Biomaterials, 2006. **27**(15): p. 2980-7.
221. Curran, J.M., et al., *Introducing dip pen nanolithography as a tool for controlling stem cell behaviour: unlocking the potential of the next generation of smart materials in regenerative medicine.* Lab Chip, 2010. **10**(13): p. 1662-70.
222. Lutz, R., et al., *Nano-stenciled RGD-gold patterns that inhibit focal contact maturation induce lamellipodia formation in fibroblasts.* PLoS One, 2011. **6**(9): p. e25459.
223. Frith, J.E., R.J. Mills, and J.J. Cooper-White, *Lateral spacing of adhesion peptides influences human mesenchymal stem cell behaviour.* Journal of Cell Science, 2012. **125**(Pt 2): p. 317-27.
224. Killops, K.L., et al., *Nanopatterning Biomolecules by Block Copolymer Self-Assembly.* ACS Macro Letters, 2012. **1**(6): p. 758-763.
225. Dellinger, J.G., J. Cesarano, 3rd, and R.D. Jamison, *Robotic deposition of model hydroxyapatite scaffolds with multiple architectures and multiscale porosity for bone tissue engineering.* Journal of Biomedical Materials Research Part A, 2007. **82**(2): p. 383-94.
226. Keilhoff, G., et al., *Transdifferentiated mesenchymal stem cells as alternative therapy in supporting nerve regeneration and myelination.* Cellular and Molecular Neurobiology, 2006. **26**(7-8): p. 1235-52.
227. Arys, X., A. Laschewsky, and A.M. Jonas, *Ordered Polyelectrolyte "Multilayers". 1. Mechanisms of Growth and Structure Formation: A Comparison with Classical Fuzzy "Multilayers".* Macromolecules, 2001. **34**: p. 3318-3330.
228. Bollinne, C., et al., *Density Perturbations in Polymers Near a Solid Substrate: An X-ray Reflectivity Study.* Macromolecules, 1999. **32**: p. 4719-4724.
229. Daillant, J. and A. Gibaud, *X-Ray and Neutron Reflectivity : Principles and Applicaitons.* Springer : Berlin, 1999.
230. Lekner, J., *Theory of Reflection of Electromagnetic and Particle Waves.* Martinus Nijhoff Publishers : Dordrecht, 1987.

231. Cecchet, F., et al., *One Step Growth of Protein Antifouling Surfaces: Monolayers of Poly(ethylene oxide) (PEO) Derivatives on Oxidized and Hydrogen-Passivated Silicon Surfaces.* Langmuir, 2006. **22**: p. 1173-1181.
232. Pei, X., et al., *Correlation between the structure and wettability of photoswitchable hydrophilic azobenzene monolayers on silicon.* Langmuir, 2011. **27**(15): p. 9403-12.
233. Qi, J., M. Oppenheimer, and P. Sobrado, *Fluorescence Polarization Binding Assay for Aspergillus fumigatus Virulence Factor UDP-Galactopyranose Mutase.* Enzyme Research, 2011. **2011**: p. 513905.
234. Pallandre, A., et al., *Binary Nanopatterned Surfaces Prepared from Silane Monolayers.* Nano Letters, 2004. **4**(2): p. 365-371.
235. Swift, P., *Adventitious Carbon - The Panacea for Energy Referencing?* Surface and Interface Analysis, 1982. **4**(2): p. 47-51.
236. Kahn, F.J., *Orientation of liquid crystals by surface coupling agents.* Applied Physics Letters, 1973. **22**(8): p. 386.
237. Davis, D.H., et al., *Immobilization of RGD to <111> silicon surfaces for enhanced cell adhesion and proliferation.* Biomaterials, 2002. **23**: p. 4019-4027.
238. Dupres, V., C. Verbelen, and Y.F. Dufrene, *Probing molecular recognition sites on biosurfaces using AFM.* Biomaterials, 2007. **28**(15): p. 2393-402.
239. Jandt, K.D., *Atomic force microscopy of biomaterials surfaces and interfaces.* Surface Science, 2001. **491**: p. 303-332.
240. Hugel, T. and M. Seitz, *The Study of Molecular Interactions by AFM Force Spectroscopy.* Macromolecular Rapid Communications, 2001. **22**(13): p. 989-1016.
241. Curtis, A. and C.D. Wilkinson, *Topographical control of cells.* Biomaterials, 1997. **18**: p. 1573-1583.
242. Weisenhorn, A.L., et al., *Deformation and height anomaly of soft surfaces studied with an AFM.* Nanotechnology, 1993. **4**: p. 106-113.
243. Muller, D.J. and A. Engel, *The Height of Biomolecules Measured with the Atomic Force Microscope Depends on Electrostatic Interactions.* Biophysical Journal, 1997. **73**: p. 1633-1644.
244. Jiao, Y. and T.E. Schaffer, *Accurate Height and Volume Measurements on Soft Samples with the Atomic Force Microscope.* Langmuir, 2004. **20**: p. 10038-10045.
245. Bruker, *Common Approaches to Tip Functionalization for AFM-Based Molecular Recognition Measurements.* 2010.
246. Putman, C.A.J., et al., *Tapping mode atomic force microscopy in liquid.* Applied Physics Letters, 1994. **64**(18): p. 2454-2456.
247. Dong, M., et al., *AFM-based force spectroscopy measurements of mature amyloid fibrils of the peptide glucagon.* Nanotechnology, 2008. **19**(38): p. 384013.
248. Picart, C., et al., *Measuring mechanical properties of polyelectrolyte multilayer thin films: Novel methods based on AFM and optical techniques.* Colloids and Surfaces A: Physicochemical and Engineering Aspects, 2007. **303**(1-2): p. 30-36.
249. Puchner, E.M. and H.E. Gaub, *Force and function: probing proteins with AFM-based force spectroscopy.* Current Opinion in Structural Biology, 2009. **19**(5): p. 605-14.
250. Lai, H.C., et al., *The influence of surface energy on early adherent events of osteoblast on titanium substrates.* Journal of Biomedical Materials Research Part A, 2010. **93**(1): p. 289-96.
251. Bernard, S.A., et al., *Bone cell-materials interactions and Ni ion release of anodized equiatomic NiTi alloy.* Acta Biomaterialia, 2011. **7**(4): p. 1902-12.
252. Zhao, G., et al., *High surface energy enhances cell response to titanium substrate microstructure.* Journal of Biomedical Materials Research Part A, 2005. **74**(1): p. 49-58.
253. Lampin, M., et al., *Correlation between substratum roughness and wettability, cell adhesion, and cell migration.* Journal of Biomedical Materials Research, 1997. **36**(1): p. 99-108.

254. Hallab, N.J., et al., *Evaluation of Metallic and Polymeric Biomaterial Surface Energy and Surface Roughness Characteristics for Directed Cell Adhesion.* Tissue Engineering, 2001. **7**(1): p. 55-71.
255. Fan, C.-W. and S.-C. Lee, *Surface Free Energy Effects in Sputter-Deposited WNx Films.* Materials Transactions, 2007. **48**(9): p. 2449-2453.
256. Carré, A., *Polar interactions at liquid/polymer interfaces.* Journal of Adhesion Science and Technology, 2007. **21**(10): p. 961-981.
257. Fowkes, F.M., *Determination of interfacial tensions, contact angles, and dispersion forces in surfaces by assuming additivity of intermolecular interactions in surfaces.* The Journal of Physical Chemistry, 1962. **66**(2): p. 382.
258. Cunliffe, D., et al., *Bacterial Adhesion at Synthetic Surfaces.* Applied and Environmental Microbiology, 1999. **65**(11): p. 4995-5002.
259. Chai, C., J. Lee, and P. Takhistov, *Direct detection of the biological toxin in acidic environment by electrochemical impedimetric immunosensor.* Sensors (Basel), 2010. **10**(12): p. 11414-27.
260. Zhu, L. and A.I. Skoultchi, *Coordinating cell proliferation and differentiation.* Current Opinion in Genetics & Development, 2001. **10**: p. 91-97.
261. Malaval, L., et al., *Kinetics of Osteoprogenitor Proliferation and Osteoblast Differentiation In Vitro.* Journal of Cellular Biochemistry, 1999. **74**: p. 616-627.
262. Stein, G.S., J.B. Lian, and T.A. Owen, *Relationship of cell growth to the regulation of tissue-specific gene expression during osteoblast differentiation.* The FASEB Journal, 1990. **4**(3111-3123).
263. Re, F., et al., *Inhibition of Anchorage-dependent Cell Spreading Triggers Apoptosis in Cultured Human Endothelial Cells.* The Journal of Cell Biology, 1994. **127**(2): p. 537-546.
264. Huang, S. and D.E. Ingber, *Shape-dependent control of cell growth, differentiation, and apoptosis: switching between attractors in cell regulatory networks.* Experimental Cell Research, 2000. **261**(1): p. 91-103.
265. Häcker, G., *The morphology of apoptosis.* Cell and Tissue Research, 2000. **301**(1): p. 5-17.
266. Folkman, J. and A. Moscona, *Role of cell shape in growth control.* Nature, 1978. **273**(345-349).
267. Lee, M.H., et al., *Adhesion of MC3T3-E1 cells to RGD peptides of different flanking residues: detachment strength and correlation with long-term cellular function.* Journal of Biomedical Materials Research Part A, 2007. **81**(1): p. 150-60.
268. Balaban, N.Q., et al., *Force and focal adhesion assembly: a close relationship studied using elastic micropatterned substrates.* Nature Cell Biology, 2001. **3**: p. 466-472.
269. Wang, Y.K. and C.S. Chen, *Cell adhesion and mechanical stimulation in the regulation of mesenchymal stem cell differentiation.* Journal of Cellular and Molecular Medicine, 2013. **17**(7): p. 823-32.
270. Biggs, M.J., et al., *The use of nanoscale topography to modulate the dynamics of adhesion formation in primary osteoblasts and ERK/MAPK signalling in STRO-1+ enriched skeletal stem cells.* Biomaterials, 2009. **30**(28): p. 5094-103.
271. Han, S.J., et al., *Decoupling substrate stiffness, spread area, and micropost density: a close spatial relationship between traction forces and focal adhesions.* Biophysical Journal, 2012. **103**(4): p. 640-8.
272. Chowdhury, F., et al., *Material properties of the cell dictate stress-induced spreading and differentiation in embryonic stem cells.* Nature Materials, 2010. **9**(1): p. 82-8.
273. Dalby, M.J., et al., *Nanotopographical stimulation of mechanotransduction and changes in interphase centromere positioning.* Journal of Cellular Biochemistry, 2007. **100**(2): p. 326-38.
274. Grashoff, C., et al., *Measuring mechanical tension across vinculin reveals regulation of focal adhesion dynamics.* Nature, 2010. **466**(7303): p. 263-6.
275. del Rio, A., et al., *Stretching Single Talin Rod Molecules Activates Vinculin Binding.* Science, 2009. **323**: p. 638-641.

276. Discher, D.E., D.J. Mooney, and P.W. Zandstra, *Growth factors, matrices, and forces combine and control stem cells.* Science, 2009. **324**(5935): p. 1673-7.
277. Golding, B., et al., *Inverse relationship between proliferation and differentiation in a human TNP-specific B cell line.* The Journal of Immunology, 1988. **131**: p. 2564-2568.
278. Quarles, L.D., et al., *Distinct Proliferative and Differentiated Stages of Murine MC3T3-E1 Cells in Culture: An In Vitro Model of Osteoblast Development.* Journal of Bone and Mineral Research, 1992. **7**(6): p. 683-692.
279. Hessle, L., et al., *Tissue-nonspecific alkaline phosphatase and plasma cell membrane glycoprotein-1 are central antagonistic regulators of bone mineralization.* Proceedings of the National Academy of Sciences of the United States of America, 2002. **99**(14): p. 9445-9.
280. Golub, E.E. and K. Boesze-Battaglia, *The role of alkaline phosphatase in mineralization.* Current Opinion in Orthopaedics, 2007. **18**: p. 444-448.
281. Tai, G., et al., *Differentiation of Osteoblasts from Murine Embryonic Stem Cells by Overexpression of the Transcriptional Factor Osterix.* Tissue Engineering, 2004. **10**(9/10): p. 1456-1466.
282. Toma, J.G., et al., *Isolation of multipotent adult stem cells from the dermis of mammalian skin.* Nature Cell Biology, 2001. **3**: p. 778-784.
283. Indrawattana, N., et al., *Growth factor combination for chondrogenic induction from human mesenchymal stem cell.* Biochemical and Biophysical Research Communications, 2004. **320**(3): p. 914-9.
284. Bi, W., et al., *Sox9 is required for cartilage formation.* Nature Genetics, 1999. **22**: p. 85-89.
285. Zouani, O.F., et al., *Insights into the osteoblast precursor differentiation towards mature osteoblasts induced by continuous BMP-2 signaling.* Biology Open, 2013.
286. Saito, A., et al., *Activation of osteo-progenitor cells by a novel synthetic peptide derived from the bone morphogenetic protein-2 knuckle epitope.* Biochimica et Biophysica Acta (BBA) - Proteins and Proteomics, 2003. **1651**(1-2): p. 60-67.
287. Oliver, W.C. and G.M. Pharr, *Measurement of hardness and elastic modulus by instrumented indentation: Advances in understanding and refinements to methodology.* Journal of Materials Research, 2003. **19**(1): p. 3-20.
288. Pharr, G.M., *Measurements of mechanical properties by ultra-low load indentation.* Materials Science and Engineering: A, 1998. **253**: p. 151-159.
289. Oliver, W.C. and G.M. Pharr, *An improved technique for determining hardness and elastic modulus using load and displacement sensing indentation experiments.* Journal of Materials Research, 1992. **7**(6): p. 1564-1583.
290. Saha, R. and W.D. Nix, *Effects of the substrate on the determination of thin film mechanical properties by nanoindentation.* Acta Materialia, 2002. **50**: p. 23-38.
291. Sharpe, W.N., B. Yuan, and R. Vaidyanathan, *Measurements of Young's modulus, Poisson's ratio, and tensile strength of polysilicon.* Micro Electro Mechanical Systems, 1997: p. 424-429.
292. Boyd, E.J. and D. Uttamchandani, *Measurement of the Anisotropy of Young's Modulus in Single-Crystal Silicon.* Journal of Microeletromechanical Systems, 2012. **21**(1): p. 243-249.
293. Pethicai, J.B., R. Hutchings, and W.C. Oliver, *Hardness measurement at penetration depths as small as 20 nm.* Philosophical Magazine A, 1983. **48**(4): p. 593-606.
294. Leistner, A.J., A.C. Fischer-Cripps, and J.M. Bennett, *Indentation hardness and modulus of the surface of a large superpolished single-crystal silicon sphere.* Optical Materials and Structures Technologies, 2003. **5179**: p. 215-222.

ABSTRACT

The aim of biomaterials design is to create an artificial environment that mimics the in vivo extracellular matrix (ECM) for optimized cell interactions. A precise synergy between the scaffolding material, bioactivity, and cell type must be maintained in an effective biomaterial. In this work, we present a technique of nanofabrication that creates chemically nanopatterned bioactive silicon surfaces for cell studies. Using nanoimprint lithography, RGD and mimetic BMP-2 peptides were covalently grafted onto silicon as nanodots of various dimensions, resulting in a nanodistribution of bioactivity. To study the effects of spatially distributed bioactivity on cell behavior, mesenchymal stem cells (MSCs) were cultured on these chemically modified surfaces, and their adhesion and differentiation were studied. We observe that peptide nanodots induce differences in MSC behavior in terms of cytoskeletal organization, actin stress fiber arrangement, focal adhesion (FA) maturation, and MSC commitment in comparison with homogeneous control surfaces. In particular, FA area, distribution, and conformation were highly affected by the presence of peptide nanopatterns. Additionally, RGD and mimetic BMP-2 peptides influenced cellular behavior through different mechanisms that resulted in changes in cell spreading and FA maturation. These findings have remarkable implications that contribute to the understanding of cell-ECM interactions for clinical biomaterials applications.

RÉSUMÉ

De façon optimale, un biomatériel devrait présenter aux cellules une structure similaire à la matrice extracellulaire (MEC) naturelle de chaque tissu pour que les cellules puissent s'organiser et former un tissu valide. Toutefois, cette approche idéale est difficilement réalisable de par la complexité à mimer précisément la structure de la MEC de façon synthétique, et de par le faible niveau de connaissance des interactions entre matériaux biomimétiques et cellules. Cet objectif peut être atteint en associant des cellules, des facteurs biologiques à un biomatériau sur lequel ces cellules peuvent se développer pour reconstruire le tissu natif. Le défi à relever est la synthèse de matériaux capables de reproduire ou d'identifier ces signaux susceptibles d'orienter les cellules vers un comportement choisi. Les nanotechnologies sont sans conteste aujourd'hui d'exellents outils pour produire des matériaux structurés capables de mimer le MEC et d'amener une bioactivité. Dans cette étude, nous avons créé des surfaces bioactives nanostructurées en combinant la nanolithographie et la fonctionnalisation de surface en greffant des peptides susceptibles de favoriser l'adhésion (RGD) ou la différenciation (bone morphogenetic protein 2 (BMP-2)) de des cellules souches mésenchymateuses (CSM). Nous montrons que la nanodistribution des peptides induit une bioactivité qui a un impact sur l'organisation du cytosquelette, la conformation des fibres de stress d'actine, la maturation des adhésions focales (AFs), et l'engagement des CSM. En particulier, l'aire, la distribution, et la conformation des AFs sont affectées par la présence de cette nanobioactivité. Par ailleurs, la présence des peptides RGD et BMP-2 modifient le comportement cellulaire par des voies et des mécanismes différents ce qui entraine des changements au niveau de l'étalement cellulaire et de la maturation des AFs. Ces résultats permettent de contribuer à une meilleure compréhension des interactions cellules-MEC pour les applications cliniques de ces dispositifs de plus haute fonctionnalité.